Multi-Orbital Physics in Materials with Strong Electronic Correlations: Hund's Coupling and Inter-Shell Interactions

Jakob Steinbauer

▶ **To cite this version:**

Jakob Steinbauer. Multi-Orbital Physics in Materials with Strong Electronic Correlations: Hund's Coupling and Inter-Shell Interactions. Strongly Correlated Electrons [cond-mat.str-el]. Université Paris Saclay (COmUE), 2019. English. NNT: 2019SACLX068 . tel-02435008

HAL Id: tel-02435008

https://theses.hal.science/tel-02435008v1

Submitted on 10 Jan 2020

HAL is a multi-disciplinary open access archive for the deposit and dissemination of scientific research documents, whether they are published or not. The documents may come from teaching and research institutions in France or abroad, or from public or private research centers.

L'archive ouverte pluridisciplinaire **HAL**, est destinée au dépôt et à la diffusion de documents scientifiques de niveau recherche, publiés ou non, émanant des établissements d'enseignement et de recherche français ou étrangers, des laboratoires publics ou privés.

université PARIS-SACLAY

NNT : 2019SACLX068

Thèse de doctorat

Multi-Orbital Physics in Materials with Strong Electronic Correlations: Hund's Coupling and Inter-Shell Interactions

Thèse de doctorat de l'Université Paris-Saclay
préparée à École Polytechnique

École doctorale n°564 Physique en Ile-de-France (EDPIF)
Spécialité de doctorat : Physique

Thèse présentée et soutenue à Palaiseau, le 24.10.2019, par

JAKOB STEINBAUER

Composition du Jury :

Marcelo Rozenberg Directeur de Recherche, LPS, Orsay (France)	Président
David Jacob Chargé de Recherche, EHU/UPV, San Sebastian (Espagne)	Rapporteur
Serge Florens Directeur de Recherche, Institut Néel, Grenoble (France)	Rapporteur
Luca de' Medici Professeur, ESPCI, Paris (France)	Examinateur
Mark van Schilfgaarde Professeur, King's College, London (Royaume-Uni)	Examinateur
Silke Biermann Professeur, École Polytechnique, Palaiseau (France)	Directeur de thèse

Für Alexander und seine kindliche Neugier …

Abstract

The central topic of this thesis is the physics of strongly correlated electronic systems. The study of such systems is motivated by the prospect of gaining a better understanding of the nature of correlated materials, which feature some of the most fascinating phenomena of condensed matter physics and promise a wealth of technological applications. Among these phenomena, we find exotic transport properties including metal-insulator transitions, superconductivity, charge-, spin-, or orbital ordering, and many more. From the perspective of theory, these materials are described as interacting quantum many-body systems. While the basic theory is well established, an exact solution to these problems is intractable, and in most cases simply impossible to obtain. It is for this reason, that theoretical progress mainly relies on the study of simplified model systems. In the context of strongly correlated materials, the most famous of these is probably the Hubbard model, a minimal lattice model that only considers a single electron orbital per site. Despite its simplicity, it incorporates many of the effects mentioned before. Most prominently it describes the localization of conduction electrons when the effective Coulomb repulsion, parametrized by the Hubbard interaction U, dominates over the kinetic energy of the electrons, thus causing a metal-insulator transition. For the description of more realistic systems, however, a single orbital description is a crude over-simplification. In this case, more complex multi-orbital models have to be considered, containing even richer physics.

In this thesis, we investigate the physics of multi-orbital models, especially focusing on two aspects associated with such systems:

First, we consider the effect of enhanced orbital degeneracy and Hund's exchange coupling – which parametrizes the reduction of the effective on-site Coulomb interaction for electrons with parallel spins. After giving a detailed review of the current state of the research, we focus on some of the remaining open questions. More specifically, we investigate the influence of Hund's exchange coupling on the nature of the doping driven metal-insulator transition. As in the single-orbital Hubbard model, the transition is found to be of first-order within dynamical mean-field theory, with a coexistence region where two solutions can be stabilized. We show that in the presence of Hund's exchange coupling, the insulating phase is adiabatically connected to a phase of bad metal character. Furthermore, we examine the fate of spin-spin correlations in the vicinity of the phase transition.

The second emphasis of the thesis is on the effect of inter-shell interactions. The electronic structure of realistic systems is determined by the interplay of many different electrons of different orbital characters. In many cases, a faithful modeling requires the consideration of more than only

one type of orbital. An example would be the famous cuprate superconductors, where oxygen p-states hybridize – and interact – with copper d-states. The problem is that, as soon as inter-shell interactions are taken into account, such models become rather challenging to solve. For this reason, such interactions are mostly neglected, and little is known about their influence on the systems under consideration. In this thesis, we perform a detailed study of the effects of inter-shell interactions, by considering a minimal multi-orbital model system. The results are then compared to different approximation schemes. While common Hartree-Fock approximations perform rather well in the metallic phase, they are found to break down at the metal-insulator transition. This motivates us to develop a new, hybrid method, combining quantum Monte Carlo with the analytic slave rotor method, which allows an improved description in this regime.

In the final chapter of the thesis, we leave the realm of solid-state physics, to study strong correlations in molecules. More specifically, we construct a minimal model that captures the essence of the spin-crossover in organometallic molecules, thus providing a better understanding of the underlying physics. The model is then combined with input from density functional theory, to study the spin-state switching in Ni-porphyrin molecules. In this context, we demonstrate the importance of charge-transfer in the determination of the spin-state. Finally, we propose a spin-crossover mechanism based on mechanical strain, which could find an application in spintronic devices.

Résumé

Le sujet central ce cette thèse est la physique des systèmes électroniques fortement corrélés. L'étude de ces systèmes est motivée par la perspective d'approfondir notre compréhension des matériaux corrélés. Ceux-ci présentent certains des phénomènes les plus fascinants de la physique de la matière condensée, laissant ainsi entrevoir un large éventail d'applications techniques. Parmi ces phénomènes, on citera des propriétés de transport exotiques, telles que les transitions métal/isolant, la supraconductivité, l'ordre de charge, de spin ou des degrés de liberté orbitalaires... Du point de vue théorique, on modélise ces matériaux par des systèmes quantiques en interaction. Bien que la théorie fondamentale de ces systèmes soit bien connue, une solution exacte des problèmes quantiques est très difficile, voire, la plupart du temps, impossible à obtenir. C'est pour cette raison que le progrès théorique s'appuie sur l'étude de systèmes modèles plus simples. Dans le contexte des matériaux fortement corrélés, c'est probablement le modèle de Hubbard qui est le plus connu. Il s'agit d'un modèle minimal sur réseau discrétisé et constitué d'une seule orbitale électronique. Malgré sa simplicité, ce modèle contient beaucoup des effets cités ci-avant. Il est notamment connu pour rendre compte de la localisation des électrons de conduction, lorsque la répulsion effective de Coulomb, paramétrisée par l'interaction de Hubbard "U", domine l'énergie cinétique des électrons, entraînant ainsi une transition métal/isolant. Cependant, pour la plupart des systèmes réels, la description via des modèles ne contenant qu'une seule orbitale électronique est une simplification trop abrupte. Dans ce cas, il faut considérer des modèles multi-orbitalaires, qui peuvent rendre compte d'une physique plus riche.

Dans cette thèse, nous étudions la physique des modèles multi-orbitalaires, en nous concentrant particulièrement sur deux aspects importants associés à ces systèmes :

Premièrement, nous considérons l'effet de l'augmentation de la dégénérescence orbitalaire, et du couplage d'échange de Hund. Ce dernier paramétrise la réduction de l'interaction de Coulomb effective entre électrons sur le même site et de spins parallèlles. Après une revue détaillée de l'état actuel de la recherche, nous nous concentrons sur quelques questions encore ouvertes. Plus particulièrement, nous étudions l'influence du couplage d'échange de Hund sur la nature de la transition de métal/isolant stimulée par le dopage du système. Ainsi que pour le modèle de Hubbard à une seule orbitale, nous trouvons que la transition est du premier ordre selon la théorie du champ moyen dynamique (DMFT), avec une région de coexistence où deux solutions peuvent être stabilisées. Nous démontrons qu'en présence du couplage d'échange de Hund, la phase isolante est adiabatiquement

connectée à une phase de caractère “mauvais métal”. De plus, nous étudions le sort des corrélations entre spins à proximité de la transition de phase.

Le deuxième accent de cette thèse est mis sur l’effet des interactions inter-couches. La structure électronique des systèmes réel est déterminée par l’interaction des électrons de couches orbitalaires différentes. Donc souvent, une description fidèle de la physique exige de considérer plus d’une orbitale. Un exemple serait le cas des célèbres supraconducteurs cuprates, où la physique dépend crucialement de l’hyrbidisation et interaction entre orbitales de type d des atomes de cuivre et celles de type p des atomes d’oxygène. Malheureusement, l’inclusion des interactions inter-couches rend le problème encore plus difficile à résoudre. C’est pour cette raison que la plupart du temps, ces interactions sont ignorées, et on sait peu de choses de leur influence sur les systèmes physiques. Dans cette thèse, nous étudions l’effet des interactions inter-couches, en considérant un modèle multi-orbital minimaliste. Alors que les approximations de type Hartree-Fock fournissent des résultats satisfaisants dans le cas d’un remplissage incommensurable, ils donnent des résultats peu fiables dans les autres régimes, surtout autour de la transition de phase métal/isolant. Cela nous conduit à proposer une nouvelle méthode hybride, qui est une combinaison entre une approche de Monte-Carlo et la méthode des “rotateurs esclaves”, cette dernière étant une technique analytique. La nouvelle méthode est ensuite évaluée dans plusieurs régimes de paramètres, et fournit des résultats prometteurs.

Dans le dernier chapitre de cette thèse, nous quittons le domaine de la physique des solides pour étudier l’effet des fortes corrélations dans les molécules. Plus particulièrement, nous construisons un modèle minimaliste qui reprend l’essence de la transition de spin dans des molécules organo-métalliques, permettant ainsi de mieux comprendre la physique sous-jacente. Ensuite, le modèle est appliqué avec des paramètres extraits de la théorie de la fonctionnelle de la densité (DFT), pour étudier le changement d’état de spin dans des molécules de porphyrine de nickel. Dans ce contexte, nous démontrons l’importance du transfert de charge pour déterminer l’état de spin. Finalement, nous proposons un mécanisme de “spin-crossover”, induit par la tension mécanique, qui pourrait trouver une application dans des appareils spintroniques.

Table of contents

Part I

Introduction

Chapter 1

The Electronic Quantum Many-Body Problem

1.1 Many-body physics

Traditionally, physics is associated with the quest for the fundamental, microscopic laws of nature. To this day, this aspect of the subject attracts most of the public attention, and probably remains the driving motivation for the youth to consider this subject at university. Indeed, the past progress is impressive. From the demystification of planetary motion, to the understanding of the fundamentals of chemistry, we are now at a point where we consider only three fundamental theories. The Dirac- and Yang-Mills theories of fermions and bosons, respectively, interwoven in the framework of quantum field theories, offer a precise description of (so far) any experimentally accessible microscopic physical phenomenon. On the other hand, the theory of general relativity successfully describes the fabrics of space-time on a macroscopic level. Beyond these, countless theories emerged in the pursuit of unification; experimental confirmation for any of those, however, still seems beyond the horizon.

The philosophy of many body physics is a very different one. Here, we are interested in the description and understanding of "emerging phenomena"; that means, complex phenomena, that arise from the interaction of many particles – usually of the order $\sim 6 \times 10^{23}$. In contrast to the picture outlined above, this approach is rather reductionist. For the description of most of the systems surrounding us, starting from the most fundamental theories is neither important, nor practical – what is the value of an equation if you cannot solve it? To obtain a quantitative description of all the phenomena of condensed matter theory and chemistry, it is in fact sufficient to consider only the electrostatic interaction between electrons an nuclei, ignoring the inner structure of the latter ones. More specifically, the physics of most solid-state systems, gases and liquids is well described by the

Schrödinger equation[140], considering the following Hamiltonian

$$\begin{aligned} H &= T_{nuc} + T_e + V_{e-e} + V_{e-nuc} + V_{nuc-nuc} \\ &= -\sum_{i=1}^{N_{nuc}} \frac{\hbar}{2M_i}\nabla_{R_i}^2 - \sum_{i=1}^{N_e} \frac{\hbar}{2m_i}\nabla_{r_i}^2 \\ &+ \frac{e^2}{4\pi\varepsilon_0}\left[\sum_{i=1}^{N_e}\sum_{j=1}^{i}\frac{1}{|r_i - r_j|} - \sum_{i=1}^{N_e}\sum_{j=1}^{N_{nuc}}\frac{Z_j}{|r_i - R_j|} + \sum_{i=1}^{N_{nuc}}\sum_{j=1}^{i}\frac{Z_i Z_j}{|R_i - R_j|}\right] . \end{aligned} \tag{1.1}$$

Here, $\hbar = h/(2\pi)$ is the reduced Planck constant, e is the electron charge, ε_0 is the vacuum electric permittivity and r_i, R_i are the position of the electrons and nuclei, respectively. The two kinetic terms T_{nuc} and T_e correspond to the movement of the atomic cores of mass M_i and the electrons of mass m_i, respectively. The potential energy is composed of the repulsive interactions among the electrons (V_{e-e}) and between different nuclei of charge Z_i/Z_j ($V_{nuc-nuc}$), as well as the attractive interaction between electrons and nuclei of charge Z_j (V_{e-nuc}). The one-body part of this Hamiltonian[1] can be derived by considering the non-relativistic limit of the Dirac equation[42]; when expanding the equation up to order $1/c^2$, one also gets a spin-orbit coupling term (among others), which couples the electron spin to the magnetic moment induced by the angular momentum of the electron. Throughout this thesis we will, however, ignore such terms.

Despite its conceptual simplicity, the *many body* Hamiltonian (1.1) remains a challenge to theorists. This is the famous *many body problem*. If the number of atoms in a typical macroscopic systems is $\sim 6 \times 10^{23}$, the number of electrons will usually be even an order of magnitude larger (which, at this point does not make any difference), so an exact diagonalization of the corresponding Hamiltonian matrix is out of question. Even small systems are hard to tackle; with some exceptions, such as the hydrogen atom, no analytic solution can be obtained, and one thus relies on approximations and/or numerical methods.

A standard approximation that is applied to Hamiltonian (1.1) is the so-called Born-Oppenheimer approximation [27]. It is based on the significant difference of mass between the electrons and the nuclei, which implies that the dynamics of the two can be effectively decoupled. From the electron's point of view, the much heavier nuclei appear fixed, only contributing a static potential. Applying this approximation, our Hamiltonian simplifies substantially

$$\begin{aligned} H &= T_e + V_{e-e} + V_{e-nuc} \\ &= -\sum_{i=1}^{N_e} \frac{\hbar}{2m_i}\nabla_{r_i}^2 + \frac{e^2}{4\pi\varepsilon_0}\left[\sum_{i=1}^{N_e}\sum_{j=1}^{i}\frac{1}{|r_i - r_j|} - \sum_{i=1}^{N_e}\sum_{j=1}^{N_{nuc}}\frac{Z_j}{|r_i - R_j|}\right] . \end{aligned} \tag{1.2}$$

Despite this simplification, the problem is, in general, still too hard to solve. Over the course of the decades, however, a rich set of techniques was developed to find approximate solutions to the problem. Most notably are the Hartree-Fock method[68], as well as density functional theory

[1] The two-body Coulomb interaction is obtained by considering coupling via photonic exchange.

(DFT)[76, 89]. The Hartree-Fock method approximates the eigenstates of the many-body system by an antisymmetrized product of single-particle states – the Slater determinant. DFT, on the other hand, is based on the fact[76] that the ground-state properties of any system can be described as a functional of the electron density only. It is not hard to see, that this is a great simplification: For a mole of carbon atoms with $\sim 7.2 \times 10^{24}$ electrons, DFT reduces the dimensionality of the problem from $\sim 2.2 \times 10^{25}$ down to 3.

Despite their success, both techniques have some drawbacks. While in principle DFT provides the exact ground state of a system, it does not give any information about the corresponding excitation spectrum. Furthermore, in order to calculate the exact ground-state from DFT, one would need to know the exact exchange-correlation potential which is, in general, not known. In practice, approximations like the local density approximation (LDA)[89] or the generalized gradient approximation (GGA)[100] have to be considered; however, within these approximations, electronic correlations are taken into account only to a limited extent. The latter deficiency is even more severe for the Hartree-Fock method, which completely neglects Coulomb correlations. This is especially problematic when considering strongly correlated systems.

1.2 Strongly correlated electron systems

Casually speaking, systems with strong electronic correlations are systems, in which the dynamics of each electron is strongly influenced by those of the other electrons. Considering the form of the many-body Hamiltonian (1.2) introduced in the last section, one would therefore assume that any system with a sufficient density of atoms should be strongly correlated, due to the long-range character of the Coulomb force. It might come as a surprise, however, this is not the case, as we shall elaborate with two examples.

In compounds, where bonding is of ionic character, such as for instance in NaCl, the electrons are tightly confined to the proximity of the nuclei. Corresponding solid state systems are typically band insulators, exhibiting weak electronic correlations.

On the other side of the spectrum, there are metals like for instance aluminum, in which the long-range Coulomb interaction is effectively screened by the conduction electrons. At low temperatures, most metals can be effectively described by Landau's Fermi liquid theory[99, 98]. Fermi liquid theory is based on the assumption that, upon "slowly turning on" interactions between electrons, the original, non-interacting ground state adiabatically transforms into the ground state of the interacting system. Instead of considering the original, bare electrons, one is then working with complex linear combinations of those – the so-called quasi particles (see Fig. 1.1 for an illustration). They have the same momentum, charge and spin as the original electrons; their dynamic properties, however, such as their mass and magnetic moment, are renormalized by the interactions. While quasi-particle excitations generally decay after a certain time, their lifetime diverges quadratically close to the Fermi level, such that in this vicinity they behave as long-lived particles. The long quasi particle lifetime goes along with a well defined energy-momentum relation. In this sense, such a picture is consistent with

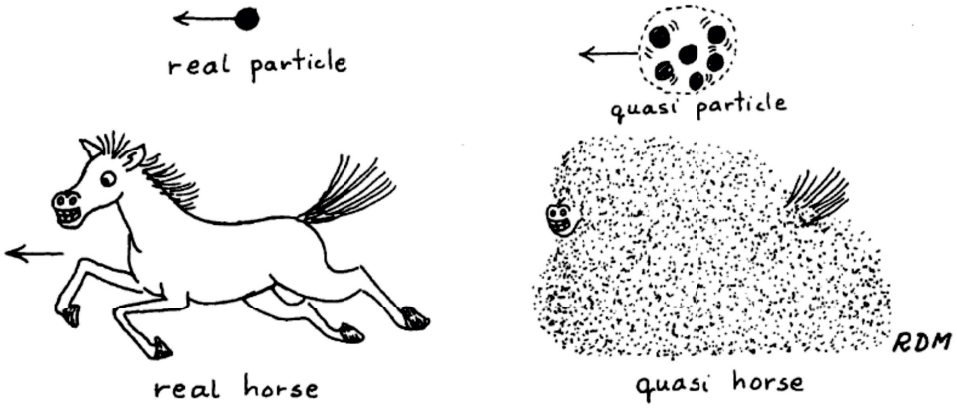

Fig. 1.1 The quasi particle concept, as illustrated by R. D. Mattuck [111].

band-theory – a single-particle theory – which states that the single-particle momentum in a periodic lattice system is a good quantum number, with the corresponding eigenstates forming extended bands.

Already in the early days of solid-state physics, however, it was realized that for certain classes of materials, electronic band theory fails to provide an accurate description. The prototypical example is the case of NiO; a transition metal oxide (TMO) which, according to band theory, should be a metal due to the partially filled d-shell of the Nickel atoms. Yet experimentally, this compound was found to be an insulator[37], with an antiferromagnetic ground state. It didn't take long, until an explanation was found[118], claiming that it was the large effective Coulomb interaction between electrons on different atomic sites, that prevents any itinerancy. This is an example of strong electronic correlations; the behavior of any single electron is strongly influenced by that of all other electrons.

Since the discovery of such "Mott insulating materials", a wealth of other phenomena associated with strong correlations were found. Aside from metal insulator transitions and other exotic transport properties – as for instance corresponding to bad metallic states – they include satellite features in spectroscopic measurements, charge-, spin -, and orbital ordering and, most prominently, unconventional superconductivity.

Apart from the fascinating effects emerging in strongly correlated systems, they pose a major challenge to theory. Since all standard band-theory type approaches fail, the motivation to describe these systems sparked many new developments, such as simple, effective models to describe the relevant physics, and new methods to tackle certain many-body Hamiltonians.

1.3 The tight binding approximation and the Hubbard Model

In weakly correlated metals, such as the above-mentioned aluminum, the valence electrons are strongly delocalized, and the corresponding wave functions rather resemble Bloch waves than atomic orbitals. On the other hand, a description in terms of free electrons is not well adapted for systems like ionic crystals or materials with covalent bonds.

In the latter case, it is often useful to consider a picture, in which the system's Hamiltonian is spanned by localized, atomic orbitals, the overlap of which allows "hopping" of electrons. This is the so-called tight-binding method, a simple, yet useful technique to approach the electronic structure of solid-state systems (for an extensive and detailed introduction, consider [53]).

The notion of "tight binding model" usually refers to non-interacting lattice models. In this sense, the electron-electron interaction V_{e-e} in (1.2) is ignored, and the tight binding Hamiltonian might be conveniently written in second quantization

$$H_{TB} = -\sum_{i\neq j,mm'\sigma} t_{ij,mm'} c^{\dagger}_{im\sigma} c_{jm'\sigma} + \sum_{im\sigma} \varepsilon_m c^{\dagger}_{im\sigma} c_{im\sigma} \ , \tag{1.3}$$

where i,j are the site indices and m,m' those of the local orbitals $|\chi_m\rangle$. The hopping amplitude corresponds to the matrix element $t_{ij,mm'} = -\langle \chi_{im\sigma}|T_e + V_{e-nuc}|\chi_{jm'\sigma}\rangle$ (the sign is a matter of convention); the second parameter ε_m correspond to the bare atomic energy levels $\langle \chi_{im\sigma}|T_e + V_{e-nuc}|\chi_{im\sigma}\rangle$. Using an infinite number of local atomic orbitals, the tight binding Hamiltonian (1.3) is a faithful representation of the one-body Hamiltonian $H = T_e + V_{e-nuc}$. In practice, however, it is necessary to truncate the Hilbert space in order to perform calculations.

While the tight binding model (1.3) describes a one-body theory, it can be easily extended to incorporate many-body effects. To this means, we introduce an additional term, that accounts for the Coulomb interaction

$$H = -\sum_{i\neq j,mm'\sigma} t_{ij,mm'} c^{\dagger}_{im\sigma} c_{jm'\sigma} + \sum_{im\sigma} \varepsilon_m c^{\dagger}_{im\sigma} c_{im\sigma} + \frac{1}{2} \sum_{\substack{ijkl \\ mm'nn' \\ \sigma\sigma'}} V^{ijkl}_{mm'nn'} c^{\dagger}_{im\sigma} c^{\dagger}_{jn\sigma'} c_{ln'\sigma'} c_{km'\sigma} \ . \tag{1.4}$$

Here, we introduced the Coulomb matrix, defined as

$$\begin{aligned} V^{ijkl}_{mm'nn'} &= \langle \chi_{im\sigma}\chi_{jn\sigma'}|V_{e-e}|\chi_{km'\sigma}\chi_{ln'\sigma'}\rangle \\ &= \iint \mathrm{d}^3r\mathrm{d}^3r' \chi^*_{m\sigma}(\mathbf{r}-\mathbf{R}_i)\chi^*_{n\sigma'}(\mathbf{r}'-\mathbf{R}_j) W(|\mathbf{r}-\mathbf{r}'|)\chi_{n'\sigma'}(\mathbf{r}'-\mathbf{R}_l)\chi_{m'\sigma}(\mathbf{r}-\mathbf{R}_k) \ , \end{aligned} \tag{1.5}$$

where $W(|\mathbf{r}-\mathbf{r}'|)$ is the screened Coulomb potential[2]. Despite its simple form, there is still no hope for tackling Hamiltonian (1.4) without the application of some major simplifications:

- In most cases, a qualitative - or even quantitative description of the relevant physics can already be obtained from a drastically reduced set of local basis functions.

[2] In momentum space, the screened Coulomb potential may be defined as $W(\mathbf{q}) = V(\mathbf{q})\varepsilon^{-1}(\mathbf{q})$, where $V(\mathbf{q})$ and $\varepsilon(\mathbf{q})$ are the bare Coulomb interaction and the dielectric function in momentum space; $\mathbf{q}$ is the momentum. Note that is a simplification; more precisely, one would have to consider the partially screened Coulomb potential that does not take into screening from the electrons in the energy range covered by the model (1.4). In the context of deriving low energy models for realistic materials calculations, the partially screened Coulomb potential might be calculated using techniques like cRPA[9].

- Usually, Coulomb matrix elements connecting more than two different orbitals are small; therefore only elements of the type $V_{mm'mm'}$ or $V_{mm'm'm}$ are considered.
- The Coulomb interaction between electrons from neighboring sites is usually much weaker than onsite interactions. On one hand, this is due to the rapid decay of orbital wave functions; on the other hand, it is because of the rapid decay of the Coulomb interaction due to screening[3] $W(r) \sim e^{-r}/r$. For these reasons, often only the onsite terms

$$U_{mm'nn'} = \delta_{ij}\delta_{jk}\delta_{kl}V^{ijkl}_{mm'nn'} \tag{1.7}$$

  are kept.

Considering the most simple case of a single orbital per site, these approximations lead us to the (in)famous Hubbard model [79]

$$H = -\sum_{i\neq j\sigma} t_{ij}c^\dagger_{i\sigma}c_{j\sigma} + \varepsilon_0\sum_{i\sigma} c^\dagger_{i\sigma}c_{i\sigma} + U\sum_i c^\dagger_{i\uparrow}c^\dagger_{i\downarrow}c_{i\downarrow}c_{i\uparrow}\,. \tag{1.8}$$

This is the prototypical model for strongly correlated systems. Despite its simplicity, it incorporates many of the phenomena that arise from strong electronic correlations. It is able to predict the localization of electrons in certain systems which, according to band theory, should be metallic, as in the case of NiO mentioned above. Furthermore, it received increased interest in the context of the *cuprate* high-temperature superconductors, following argumentations [4] that this simple model might already incorporate the relevant physics of these systems.

Beside pure model considerations, multi-orbital versions of the Hubbard model enjoy increasing popularity in the context of *ab-initio* calculations. In this sense, the model can be applied together with first principles methods like DFT: The latter technique is used to obtain an "uncorrelated" band structure, which is then fitted to an appropriate one- or multi-orbital tight binding model, that captures the relevant features close to the Fermi level. A Hubbard-like interaction is introduced to account for the Coulomb interaction[4], and the model is then solved within one of the various techniques available (as discussed in the following). Such approaches involve some subtleties, such as the problem of the "double counting" of correlations that were already considered by DFT. However, they allow to retain accurate results and spectral properties even for systems with strong electronic correlations.

[3] Within the linearized Thomas-Fermi theory (see [62] for a pedagogic introduction), the dielectric function is $\varepsilon(\mathbf{q}) = 1 + \frac{k_s^2}{\mathbf{q}^2}$ with the Thomas-Fermi wave vector k_s. This would result in a screened potential of Yukawa form

$$W(|\mathbf{r}|) = \frac{e^2}{4\pi\varepsilon_0|\mathbf{r}|}e^{-k_s|\mathbf{r}|}\,, \tag{1.6}$$

with e being the electron charge and ε_0 the vacuum permittivity.

[4] The evaluation of the effective Hubbard interaction is actually far from trivial, and various techniques – most notably the cRPA [9, 114, 122, 115] – have been developed to achieve this in a consistent manner.

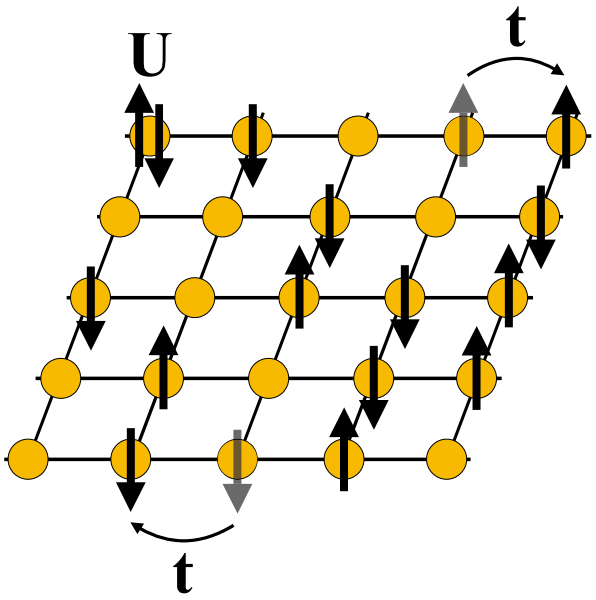

Fig. 1.2 Sketch of the Hubbard model.

1.4 Dynamical mean-field theory

Shortly after the introduction of the Hubbard model, is was shown that an exact solution can be obtained for the one-band case in one dimension[106]. For most applications in solid-state theory, however, one is interested in higher dimensional cases. Here, no analytic solution can be obtained, and even numeric approaches prove difficult, as can be anticipated for instance by considering the option of exact diagonalization. For the 2-dimensional Hubbard model, truncating the (otherwise infinite) lattice to a grid of 2×2 sites yields a Hamiltonian matrix is of rank 256; however, for a 3×3 grid this size increases to $\sim 2.6 \times 10^5$ and for 4×4 the rank is $\sim 4.3 \times 10^9$. Even though there exist efficient algorithms to find the dominant eigenvalues (such as the Lanczos algorithm [97]), it is clear that other routes have to be considered.

Standard perturbation theory might work well in the limiting cases of weak interaction U, as well as close to the atomic limit. However, such perturbative approaches will fail in the strongly correlated intermediate regime, relevant for many interesting materials. Various re-summation schemes have been developed to overcome these shortcomings, but their validity is often limited; usually, they only become exact in "exotic" limits such as infinite spin degeneracy (the *non-crossing approximation* [96]).

A different approach is provided by *dynamical mean-field theory*[55] (DMFT). The following discussion is inspired by the review of the inventors of this technique [57], which we recommend for a more detailed study.

1.4.1 Weiss mean-field theory

As the name indicates, the basic idea of DMFT is rooted in the well-known Weiss mean-field theory (MFT). The idea of Weiss MFT is best illustrated by considering the Ising model, a model of classical spins on a periodic lattice, defined by

$$H = -J\sum_{\langle ij\rangle} S_i S_j - h\sum_i S_i \,. \tag{1.9}$$

Here, the first sum runs only over neighboring spins $S_i \in \{-1/2, 1/2\}$ and h is an external field. The mean-field theory is then introduced by applying the approximating $S_i S_j = (\langle S_i\rangle + \Delta S_i)(\langle S_j\rangle + \Delta S_j) \approx \langle S_i\rangle \langle S_j\rangle + \langle S_i\rangle \Delta S_j + \Delta S_i \langle S_j\rangle$, where $\Delta S_i = S_i - \langle S_i\rangle$. This makes the original Hamiltonian split into identical, independent and local mean-field Hamiltonians of the form

$$H^{MF} = -h_{eff} S_0 \,, \tag{1.10}$$

with the Weiss field $h_{eff} = h + \sum_{\langle 0j\rangle} J\langle S_j\rangle$, and where we dropped any constant terms. Applying this mean-field approximation, the partition function is approximated by its saddle-point contribution only. To see this explicitly, one might introduce bosonic fields ϕ_{ij} to decouple the Ising spins

$$H = \sum_{\langle ij\rangle} (S_i + S_j)\phi_{ij} + \frac{1}{J}\sum_{\langle ij\rangle} \phi_{ij}^2 - h\sum_i S_i \,. \tag{1.11}$$

The mean-field solution now follows from extremizing the corresponding action with respect to a constant field $\bar{\phi}_{ij}$, which yields $2\bar{\phi}_{ij} = J\langle S_i + S_j\rangle$, leading to (1.10).

The interesting thing about mean-field theory is that it becomes exact in the limit of infinite coordination. This can be seen rather intuitively from the decoupled expression (1.11). Increasing the lattice coordination Z, which quantifies the number of nearest neighbors around each site. In order to keep the kinetic energy finite, the coupling J thus has to be rescaled as

$$J = \frac{J^*}{Z} \,, \tag{1.12}$$

where J^* is kept constant.
Considering Eq. (1.11), one can then show that the Boltzmann weight of fluctuations around the mean-field solution $\Delta\phi_{ij} = \phi_{ij} - \bar{\phi}_{ij}$ is

$$P \sim \exp\left\{-\frac{Z}{J^*}\sum_{\langle ij\rangle} \Delta\phi_{ij}^2\right\} \,, \tag{1.13}$$

and thus vanishes as $Z \to \infty$.

In its spirit, DMFT is closely related to Weiss mean-field theory. However, it goes beyond its classical counterpart by taking into account quantum fluctuations. DMFT is designed to provide an

approximation to general Hubbard-type models (1.4) with local interactions (1.7). For the sake of simplicity, however, we illustrate its functioning by considering the simple one-orbital Hubbard model

$$H = -\sum_{\langle ij\rangle} t_{ij} c^{\dagger}_{i\sigma} c_{j\sigma} - \mu \sum_{i} c^{\dagger}_{i\sigma} c_{i\sigma} + U \sum_{i} n_{i\uparrow} n_{i\downarrow} \,, \tag{1.14}$$

which is equivalent to (1.8) with $\varepsilon_0 = 0$, $n_\sigma = c^{\dagger}_{\sigma} c_{\sigma}$ and nearest-neighbor hoppings only. Dynamical mean-field theory approximates the physics of this Hamiltonian by an effective action which, in imaginary time formalism, reads

$$S_{eff} = -\iint_0^{\beta} \mathrm{d}\tau \mathrm{d}\tau' \sum_{\sigma} c^{\dagger}_{\sigma}(\tau) \mathscr{G}_0^{-1}(\tau - \tau') c_{\sigma}(\tau') + U \int \mathrm{d}\tau \, n_{\uparrow}(\tau) n_{\downarrow}(\tau) \,. \tag{1.15}$$

As before, this action is local in space. The crucial difference, however, is that the constant Weiss field h_{eff} of classical MFT was exchanged by a dynamic quantity $\mathscr{G}_0^{-1}$, effectively taking into account quantum fluctuations. Before we proceed to define the equations that determine this dynamic Weiss field, it is instructive and interesting to consider the approximations necessary to arrive at the effective action (1.15).

1.4.2 Scaling in infinite dimensions

As classical mean-field theory, DMFT becomes exact in the limit of infinite lattice coordination. In order to demonstrate this, we first need to establish some basic relations concerning the scaling of the Hubbard model parameters and Green's functions in this limit.

The imaginary time lattice Green's function is defined as

$$G_{ij}(\tau) = -\left\langle T c_i(\tau) c^{\dagger}_j(0) \right\rangle \,; \tag{1.16}$$

it describes the amplitude of an electron being created at site j at $\tau = 0$, and being annihilated at (i,τ). With the above definition, $G_{ij}(\tau = 0^-) = \left\langle c^{\dagger}_j c_i \right\rangle$ corresponds to the hopping amplitude of an electron from site i to site j. Since the Hubbard model (1.14) conserves the total particle number, electrons cannot be destroyed, but can only "hop" from one place to another. In this sense, summing the probabilities of an electron to hop from site 0 to any other site should yield unity

$$\sum_j |G_{0j}(\tau = 0^-)|^2 = 1 \,. \tag{1.17}$$

This simple argument can be used to evaluate the dimensional scaling of the Green's function. Even if we increase the dimension, the cumulative hopping probability (1.17) must remain equal to one. Thus, since $\sum_{\langle 0j\rangle} = Z = 2d$ (for a square lattice), we can deduce that

$$G_{0j}(\tau) \sim \frac{1}{\sqrt{Z}}. \tag{1.18}$$

In this spirit, one could argue that the electron propagation from site i to any other site j involves at least $||i-j||_1$ hopping processes (where $||\cdot||_1$ is the Manhattan metric), and should therefore scale as $\sim (1/\sqrt{Z})^{-||i-j||_1}$. For a more detailed discussion, see [154, 112].

On the other hand, the kinetic energy of the model is given by

$$E_{kin} = -t \sum_{\langle ij \rangle} \left\langle c_i^\dagger c_j \right\rangle \,. \tag{1.19}$$

When increasing the dimension of the system, the hopping parameter t has to be rescaled, since otherwise the kinetic energy largely dominates over the interaction energy and the model becomes trivial. From the scaling of the Green's function (1.18), it is easy to deduce that t should scale as

$$t \to \frac{t^*}{\sqrt{Z}} \,, \tag{1.20}$$

in order to keep E_{kin} of the same order of magnitude, i.e. finite. Here, t^* refers to the bare, unscaled parameter. An alternative derivation considers the central limit theorem, and can be found in [57, 13].

1.4.3 The cavity construction

To derive the DMFT effective action, it is useful to work with a functional integral formalism. In this language, the Hubbard model (1.14) can be written as

$$S = \int_0^\beta \mathrm{d}\tau \sum_{\langle ij \rangle, \sigma} c_{i\sigma}^\dagger(\tau) \left(\partial_\tau \delta_{ij} - \mu - t_{ij}\right) c_{j\sigma}(\tau) + U \int \mathrm{d}\tau \sum_i n_{i\uparrow}(\tau) n_{i\downarrow}(\tau) \,, \tag{1.21}$$

where we implicitly assume that the operators $c_\sigma^\dagger$,c_σ are replaced by Grassmann variables.

The goal is now to construct an effective action $S_{eff}[c_{0\sigma}^\dagger, c_{0\sigma}]$ for a single lattice site, which we label by the index 0. Formally, this corresponds to

$$\frac{1}{Z_{eff}} e^{-S_{eff}[c_{0\sigma}^\dagger, c_{0\sigma}]} = \frac{1}{Z} \int \prod_{i \neq 0 \sigma} \mathrm{D}c_{i\sigma}^\dagger \mathrm{D}c_{i\sigma} e^{-S} \,. \tag{1.22}$$

Following the derivation in [57], we will split the action S into three contributions

$$S = S_0 + S^{(0)} + \Delta S \,, \tag{1.23}$$

where S_0 is the part from the impurity only

$$S_0 = \int_0^\beta \mathrm{d}\tau \sum_\sigma c_{0\sigma}^\dagger(\tau)(\partial_\tau - \mu) c_{0\sigma}(\tau) + U \int \mathrm{d}\tau \, n_{0\uparrow}(\tau) n_{0\downarrow}(\tau) \,, \tag{1.24}$$

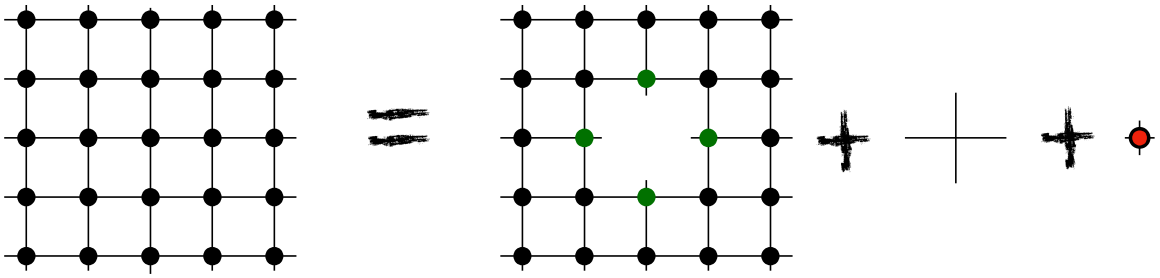

Fig. 1.3 Sketch of the cavity construction. The left site represents the Hubbard model without the impurity and the corresponding hopping terms; the middle and right parts consider hopping to the impurity and the impurity itself. Nearest neighbors of the impurity are colored in red; note that propagation from one of these to another includes at least two hopping processes.

$S^{(0)}$ considers the rest of the lattice, excluding the impurity and any hopping to it

$$S^{(0)} = \int_0^\beta \mathrm{d}\tau \sum_{\langle ij\rangle\neq 0,\sigma} c^\dagger_{i\sigma}(\tau)\left((\partial_\tau-\mu)\delta_{ij}-t_{ij}\right)c_{j\sigma}(\tau)+U\int \mathrm{d}\tau \sum_{i\neq 0} n_{i\uparrow}(\tau)n_{i\downarrow}(\tau)\,, \tag{1.25}$$

and ΔS contains the hopping parts connecting the impurity with the rest of the lattice

$$\Delta S = -\int_0^\beta \mathrm{d}\tau \sum_{\langle 0j\rangle,\sigma}\left(c^\dagger_{0\sigma}(\tau)t_{0j}c_{j\sigma}(\tau)+c^\dagger_{j\sigma}(\tau)t_{j0}c_{0\sigma}(\tau)\right)\,. \tag{1.26}$$

Then, the right side of (1.22) can be expanded in ΔS

$$\frac{e^{-S_0}}{Z}\int\prod_{i\neq 0\sigma}\mathrm{D}c^\dagger_{i\sigma}\mathrm{D}c_{i\sigma}\left(1-\Delta S+\frac{1}{2}(\Delta S)^2-\ldots\right)e^{-S^{(0)}} = e^{S_0}\frac{Z^{(0)}}{Z}\left(1-\langle\Delta S\rangle+\frac{1}{2}\left\langle(\Delta S)^2\right\rangle-\ldots\right)\,, \tag{1.27}$$

where the average values are taken with respect to the cavity action $S^{(0)}$. Since we are working with fermionic systems, only contributions with equal numbers of $c^\dagger_{i\neq 0}$ and $c_{i\neq 0}$ Grassmann variables will yield non-vanishing expectation values, such that we can discard the first, third, fifth, etc. order terms in the expansion.

Now let us have a closer look at the second and fourth order terms. The contribution quadratic in ΔS reads

$$\begin{aligned}\frac{1}{2}\left\langle(\Delta S)^2\right\rangle &= -\iint_0^\beta \mathrm{d}\tau\mathrm{d}\tau' \sum_\sigma c^\dagger_{0\sigma}(\tau)c_{0\sigma}(\tau')\sum_{\langle 0i\rangle,\langle 0j\rangle} t_{0j}t_{i0}\left\langle c^\dagger_{i\sigma}(\tau')c_{j\sigma}(\tau)\right\rangle \\ &= \iint_0^\beta \mathrm{d}\tau\mathrm{d}\tau' \sum_\sigma c^\dagger_{0\sigma}(\tau)c_{0\sigma}(\tau')\sum_{\langle 0i\rangle,\langle 0j\rangle} t_{0j}t_{i0}G^{(0)}_{ji}(\tau-\tau')\,,\end{aligned} \tag{1.28}$$

where the prefactor $1/2$ is canceled by the two different non-vanishing contributions from squaring ΔS. As we increase the dimension of the system, the number of elements in the second sum increases as $\sim d^2$ (since we sum over all nearest neighbors twice). On the other hand, $t_{0j}t_{i0} \sim 1/d$ and $G^{(0)}_{j0} \sim (1/\sqrt{d})^{||j-i||_1} \sim 1/d$, since propagation from one nearest neighbor to another involves at least two hopping processes, such that $||j-i||_1 \geq 2$ (see Fig. 1.3). This means, that the overall dimensional scaling of the second order contribution is $\sim \mathcal{O}(1)$, and therefore survives the limit $d \to \infty$.

The fourth order terms consist of two contributions. On one hand, we have the disconnected terms

$$\begin{aligned}\frac{1}{4!}\left\langle (\Delta S)^4 \right\rangle &= \frac{4\cdot 3}{4!} \iint \iint_0^\beta \mathrm{d}\tau \mathrm{d}\tau' \, \mathrm{d}\tau'' \mathrm{d}\tau''' \sum_{\sigma\sigma'} c^\dagger_{0\sigma}(\tau) c_{0\sigma}(\tau') c^\dagger_{0\sigma'}(\tau'') c_{0\sigma'''}(\tau''') \\ &\quad \times \sum_{ijkl} t^4 \left\langle c^\dagger_{i\sigma}(\tau') c_{j\sigma}(\tau) \right\rangle \left\langle c^\dagger_{k\sigma}(\tau'') c_{l\sigma}(\tau''') \right\rangle \\ &= \frac{1}{2} \left(\iint_0^\beta \mathrm{d}\tau \mathrm{d}\tau' \sum_\sigma c^\dagger_{0\sigma}(\tau) c_{0\sigma}(\tau') \sum_{\langle 0i\rangle, \langle 0j\rangle} t_{0j} t_{i0} G^{(0)}_{ji}(\tau - \tau') \right)^2 ,\end{aligned} \tag{1.29}$$

where, for simplicity we set $t_{ij} = t\delta_{\langle ij\rangle}$ and the indices i, j, k, l run over all nearest neighbors of the impurity. The prefactor of $4 \cdot 3$ corresponds to the number of different combinations for combining two operators. In the last line, it becomes clear that this corresponds just to the second order term to the power of two; therefore it has the same scaling.

The connected contribution, on the other hand, is characterized by a different dimensional scaling. This can be seen as the following. As for the disconnected diagrams, the four summations over the nearest neighbors will scale as $\sim d^4$, and the hopping parameters give $t^4 \sim 1/d^2$. The connected two-particle Green's function $G^{(0)}_{ijkl}(\tau, \tau', \tau'', \tau''')$, however, will scale as $\sim (1/\sqrt{d})^{||i-j||_1} \times (1/\sqrt{d})^{||i-k||_1} \times (1/\sqrt{d})^{||i-l||_1}$, since additional propagator lines are needed to connect the diagram. Again, $||i-j||_1 \geq 2$ (equally for k, l), such that the net scaling is $\sim 1/d$.

Likewise, it can be shown, that all connected diagrams of higher order vanish in the limit $d \to \infty$. Re-summing the remaining connected diagrams, one therefore arrives at the effective action

$$S_{eff} = S_0 - \iint_0^\beta \mathrm{d}\tau \mathrm{d}\tau' \sum_\sigma c^\dagger_{0\sigma}(\tau) c_{0\sigma}(\tau') \sum_{\langle 0i\rangle, \langle 0j\rangle} t_{0j} t_{i0} G^{(0)}_{ji}(\tau - \tau') \, . \tag{1.30}$$

This gives us an explicit expression for the DMFT Weiss function, which, transformed to Matsubara space, reads

$$\mathcal{G}_0^{-1}(i\omega) = i\omega + \mu - \sum_{\langle i0\rangle, \langle 0j\rangle} t_{i0} t_{0j} G^{(0)}_{ji}(i\omega) = i\omega + \mu - \Delta(i\omega) \, , \tag{1.31}$$

where we introduced the *hybridization function* $\Delta(i\omega)$. This is a remarkable result. It means, that in the limit of infinite dimensions, all local quantities – such as local propagators, susceptibilities etc. – are exactly defined by the local action (1.30).

The effective action (1.30) has a simple interpretation (see [55]) in the form of an Anderson impurity model [3], defined by

$$H = -\mu \sum_{\sigma} c_{\sigma}^{\dagger} c_{\sigma} + U n_{\uparrow} n_{\downarrow} + \sum_{k\sigma} (V_k c_{\sigma}^{\dagger} b_{k\sigma} + h.c.) + \sum_{k\sigma} \varepsilon_k^b b_{k\sigma}^{\dagger} b_{k\sigma} \,, \tag{1.32}$$

where k labels the infinite number of bath sites of energy ε_k^b; V_k parametrizes the strength of the hybridization with the impurity. In this sense, the hybridization function emerges from integrating out the bath sites

$$\Delta(i\omega) = \sum_k \frac{V_k V_k^*}{i\omega - \varepsilon_k^b} \,. \tag{1.33}$$

1.4.4 DMFT self consistency equations

Expression (1.30) still includes Green's functions from the cavity action $S^{(0)}$, which are awkward to handle. Upon expanding the Green's function in t_{ij} (see [57]), one can, however, relate it to the full Green's function

$$G_{ij}^{(0)} = G_{ij} - \frac{G_{i0} G_{0j}}{G_{00}} \,. \tag{1.34}$$

The Green's function itself can be expressed via the self energy Σ

$$G_{ij}(i\omega) = \sum_{\mathbf{k}} \frac{e^{-i(\mathbf{r}_i - \mathbf{r}_j)\cdot\mathbf{k}}}{i\omega + \mu - \varepsilon(\mathbf{k}) - \Sigma(i\omega, \mathbf{k})} \,, \tag{1.35}$$

which in the limit $d \to \infty$ becomes local[120]

$$\lim_{d\to\infty} \Sigma_{ij}(i\omega) = \Sigma(i\omega) \,, \tag{1.36}$$

as can be demonstrated with similar arguments as the ones used for the derivation of the Weiss field (see [57] for more details).

Putting everything together by plugging (1.34) into (1.31), one finally arrives as

$$\mathscr{G}_0^{-1}(i\omega) = \Sigma(i\omega) + \left(\sum_{\mathbf{k}} \frac{1}{i\omega + \mu - \varepsilon(\mathbf{k}) - \Sigma(i\omega)} \right)^{-1} = \Sigma(i\omega) + G_{00}^{-1}(i\omega) \,. \tag{1.37}$$

Despite being local, the Weiss field $\mathscr{G}_0^{-1}(i\omega)$ takes into account the structure of the lattice, which is encoded in the lattice dispersion $\varepsilon(\mathbf{k})$.

This leads to a self-consistency scheme.

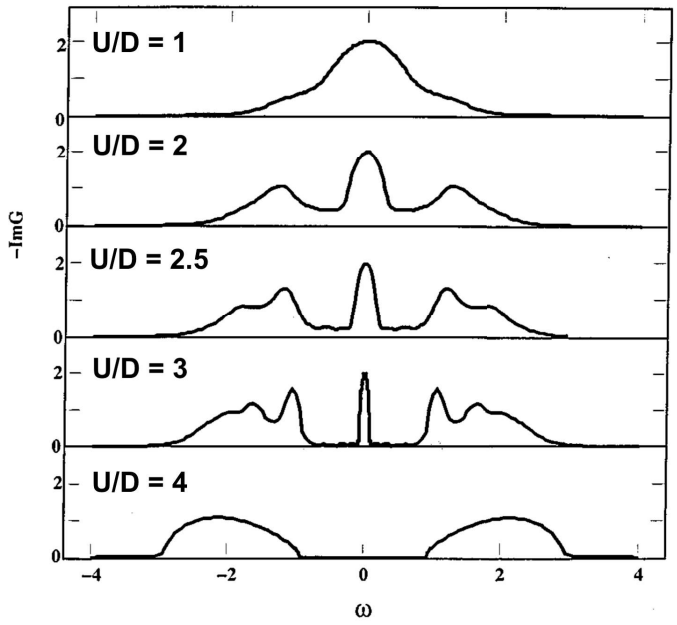

Fig. 1.4 DMFT spectral functions $\pi DA(\omega)$ at zero temperature, for different interaction strengths. The DMFT equations were solved within the iterated perturbation theory approximation[55].

1. Starting from an initial guess for the Weiss function $\mathcal{G}^{-1}_{0,old}(i\omega)$, we can calculate the local Green's function

$$G_{loc}(i\omega) = G_{00}(i\omega) \tag{1.38}$$

from the effective action (1.30).

2. Using the Dyson equation (1.37), we can calculate the self energy

$$\Sigma(i\omega) = \mathcal{G}^{-1}_{0,old}(i\omega) - G^{-1}_{loc}(i\omega)\ . \tag{1.39}$$

3. This self energy is then used to create a new Weiss field

$$\mathcal{G}^{-1}_{0,new}(i\omega) = \Sigma(i\omega) + \left(\sum_{\mathbf{k}} \frac{1}{i\omega + \mu - \varepsilon(\mathbf{k}) - \Sigma(i\omega)}\right)^{-1}\ , \tag{1.40}$$

which takes into account the structure of the lattice via $\varepsilon(\mathbf{k})$. This Weiss field is then used to construct a new effective action, and the process starts over again, until convergence.

In the limit of infinite dimensions, the effective action (1.30) yields the exact local Green's function, and the scheme will, therefore, converge to the exact solution.

All the considerations that flow into to the derivation of dynamical mean-field theory are non-perturbative. The scheme, therefore, remains valid independently of the interaction strength U. This

non-perturbative character makes it possible to study phenomena in all regimes of the phase diagram. Most prominently, it is able to capture the Mott metal insulator transition. This can be seen in Fig. 1.4, which shows the spectral function of the infinite dimensional single-orbital Hubbard model on the Bethe lattice with half bandwidth D at zero temperature. The DMFT equations were solved within the iterated perturbation theory approximation. As it can be seen from the upper panels with $U/D = 1, 2, 2.5, 3$, it gives the expected results in the weakly- and strongly-correlated metallic phase, describing the formation of a Kondo peak ($U/D = 3$), which finally disappears in the insulating phase ($U/D = 4$). In Hubbard-like systems with finite connectivity Z, the DMFT results will deviate from the exact solution of the corresponding model. Independently of the connectivity (or dimension), however, we retain the correct results in the non-interacting, as well as in the atomic limit, as can be easily checked.

The formalism, as presented above, was derived for paramagnetic systems. However, the theory can be extended to systems with long-range order [58, 57] or superconductivity [56, 57].

Finally, the success of dynamical mean-field theory is strongly related to the availability of efficient solvers for the corresponding effective many-body problem. The action (1.30) still describes an interacting, highly non-trivial problem. However, lots of analytic and numeric techniques have been developed to treat the Anderson impurity model[55, 64, 50, 166].

Chapter 2

Slave Particle Techniques

2.1 The need for light-weight techniques

The last decades have seen enormous progress in the theoretical treatment of strongly correlated electron systems. On one hand, these advances can be attributed to the development of methods like the dynamical mean-field theory[57] (which we already discussed in a previous chapter) and its numerous extensions[75, 24, 150, 12], density-matrix renormalization group methods[164, 138], quantum Monte Carlo methods[149, 151, 165], self-energy functional theory[134], etc. On the other hand there has been a major improvement on the computational side, with the development of powerful impurity solvers and effective algorithms.
However impressive these new methods are, they come along with an ever increasing demand for computational resources and a surplus of complexity rendering calculations rather costly.
It is for this reason, that light-weight analytic methods are of special interest: First of all, they provide an effective way to scan the high dimensional phase space spanned by the multiple parameters of various models. Apart from that, and maybe even more importantly, they often allow for a more intuitive way of understanding the underlying physics . Finally, they can be used in combination with other methods, like quantum Monte Carlo, either as an approximation to decrease the computational cost, or to consider effects that are, otherwise, hard to tackle numerically.

2.2 Auxiliary particle techniques - an overview

This section is supposed to provide a short overview over the most important auxiliary particle techniques, with the aim of allowing for a direct comparison.

2.2.1 Schwinger bosons

Historically, the idea of replacing fermionic operators with auxiliary variables comes from the study of spin systems[23]. Indeed, it is straight forward to show that one can recover the original spectrum

of a SU(2) spin Hamiltonian by replacing the components of the spin operator $\hat{\vec{S}}$ by combinations of two bosonic operators $[a, a^\dagger] = 1$ and $[b, b^\dagger] = 1$ that respect the spin algebra. This is done by replacing

$$S^+ = a^\dagger b \tag{2.1}$$

$$S^- = b^\dagger a \tag{2.2}$$

$$S^z = \frac{1}{2}(a^\dagger a - b^\dagger b) \,, \tag{2.3}$$

with the constraint

$$a^\dagger a + b^\dagger b = 2S \,, \tag{2.4}$$

which is commonly treated by using Lagrange multipliers. The ladder operators are constructed according to the standard definition $S^\pm = S^x \pm iS^y$.

An introduction to the subject considering an application to the Heisenberg model can be found in [10].

2.2.2 Slave bosons I - The infinite U Anderson model

In the context of strongly correlated electron systems, auxiliary-boson or "slave-boson" methods were originally proposed for the infinite-U Anderson model[16, 32]. Such a model can e.g. be motivated by considering the mixed-valence problem. In a mixed-valence crystal, the rare-earth ions on each lattice site can exist in two or more valence states, and the f-electrons hybridize with an extended band of free conduction (bath) electrons. Considering only a single correlated lattice site, this leads us to

$$H = H_f + H_{bath} + H_{hyb} \,, \tag{2.5}$$

where

$$H_f = \sum_\sigma \varepsilon_f f_\sigma^\dagger f_\sigma \tag{2.6}$$

describes the valence f electrons,

$$H_{bath} = \sum_{k\sigma} \varepsilon_k c_{k\sigma}^\dagger c_{k\sigma} \tag{2.7}$$

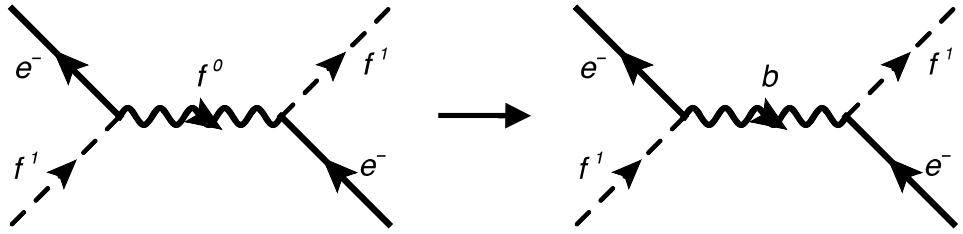

Fig. 2.1 Diagrammatic representation of the slave boson method in the infinite U Anderson model. Graphic inspired by [33].

describes the free conduction electrons[1] and

$$H_{hyb} = \sum_{k\sigma} \left(V_k c^\dagger_{k\sigma} P_0 f_\sigma + h.c. \right) \tag{2.8}$$

describes the hybridization term. The purpose of the operator P_0 is to project onto states with no f-electrons, reminiscent of the $U \to \infty$ limit, in which no double occupancy survives. The physical signification becomes even clearer when explicitly writing the combination $P_0 f_\sigma = |0\rangle\langle\sigma| = X_\sigma$, where we introduced the Hubbard operator X_σ. When attempting to solve Hamiltonian (2.5), one is confronted with the problem that there is no Wick's theorem for the Hubbard operators $X_\sigma / X^\dagger_\sigma$, so conventional quantum-field theory techniques will not be applicable.

A solution to this problem has been proposed by Coleman [32], who suggested that the unoccupied f-level state f^0 could be reinterpreted as a bosonic state with the corresponding energy. In this sense, the model would be re-formulated as

$$H = \sum_{k\sigma} \varepsilon_k c^\dagger_{k\sigma} c_{k\sigma} + \sum_{k\sigma} \left(V_k c^\dagger_{k\sigma} f_\sigma b^\dagger + h.c. \right) + \varepsilon_f \sum_\sigma f^\dagger_\sigma f_\sigma + \lambda \left(\sum_\sigma f^\dagger_\sigma f_\sigma + b^\dagger b - Q \right) . \tag{2.9}$$

The last term includes a Lagrange multiplier λ and was introduced to ensure that the overall occupation of f-electrons plus bosons is one. Setting $Q = 1$, it ensures that there is no boson as long as the f-level occupation is one, and exactly one boson when the f-level is empty. Hence, such approaches are known as slave boson techniques, since the behavior of the auxiliary boson is dictated by its electronic "master".

Note that

$$\hat{Q} = \sum_\sigma f^\dagger_\sigma f_\sigma + b^\dagger b \tag{2.10}$$

is a conserved quantity $[H, \hat{Q}] = 0$; for this reason, it is sufficient to consider a static Lagrange multiplier $\lambda(\tau) \equiv \lambda$. This is a feature of all slave-particle theories, and will be discussed in more

[1] Note that throughout most of this thesis, conduction/bath electrons will be denoted with the letter "b". Here, we use the label "c", in order to avoid confusion with the slave boson fields, for which the name "b" seems more appropriate.

detail in the context of the slave rotor method. Furthermore, the existence of a conserved, local charge leads to a gauge theory.

Re-writing the Hamiltonian in such a way leads to a new many-body model, which is not less complex then the previous one. However, re-expressing the original infinite-U model in terms with bosonic operators results in a theory, that can be treated with standard field-theoretical methods. Quite often, valuable insights can already be gained by considering a simple mean-field approximation – decoupling the bosonic and fermionic degrees of freedom. In this sense, the hybridization is renormalized by the bosonic condensate $V_k \to V_k \langle b \rangle$, consistent with the narrowing of the f-level resonance from the Kondo effect.

2.2.3 Slave bosons II - Kotliar Ruckenstein

The slave boson approach to the mixed valence problem, as it formulated by Coleman in 1984[32], gave a first glimpse of the potential of such techniques. In its original version, however, the approach is limited to infinite interaction strengths U. This drawback was overcome with a new technique, developed by Kotliar and Ruckenstein [93] only two years later, in 1986.

The goal of this method is to provide analytic approximations to the Hubbard model

$$H = -\sum_{ij\sigma} f^\dagger_{i\sigma} f_{j\sigma} + U \sum_i n_{i\uparrow} n_{i\downarrow} \,. \tag{2.11}$$

The basic idea of Kotliar and Ruckenstein was to introduce four auxiliary bosons, corresponding to the four basis states of the local Hilbert space

$$|e\rangle_i \rightleftharpoons |0\rangle_i \quad , \quad |p_\sigma\rangle_i \rightleftharpoons |\sigma\rangle_i \quad \text{and} \quad |d\rangle_i \rightleftharpoons |\uparrow\downarrow\rangle_i \,. \tag{2.12}$$

These states are created (destroyed) by the bosonic operators $e^\dagger_i$ (e_i), $p^\dagger_{i\sigma}$ ($p_{i\sigma}$) and $d^\dagger_i$ (d_i), which must obey the constraints

$$1 \stackrel{!}{=} e^\dagger_i e_i + \sum_\sigma p^\dagger_{i\sigma} p_{i\sigma} + d^\dagger_i d_i \,, \tag{2.13}$$

$$f^\dagger_{i\sigma} f_{i\sigma} \stackrel{!}{=} p^\dagger_{i\sigma} p_{i\sigma} + d^\dagger_i d_i \,, \; \sigma \in \{\uparrow, \downarrow\} \,. \tag{2.14}$$

These constraints are easily understood. The first one ensures proper normalization of the local states, and can be seen as a completeness-relation: The local site can be either empty ($e^\dagger_i e_i = 1$), with one electron of spin σ ($p^\dagger_{i\sigma} p_{i\sigma} = 1$), doubly occupied ($d^\dagger_i d_i = 1$), or in any linear combination of those; however, the normalization must be ensured. The second constrained ensures that the dynamics of the bosonic operators corresponds to the original fermions.

The Hubbard model can then be re-written as

$$\begin{aligned} H = &-\sum_{ij\sigma} f^\dagger_{i\sigma} f_{j\sigma} z^\dagger_{i\sigma} z_{j\sigma} + U \sum_i d^\dagger_{i\sigma} d_{i\sigma} \\ &+ \sum_i \lambda_i \left(e^\dagger_i e_i + \sum_\sigma p^\dagger_{i\sigma} p_{i\sigma} + d^\dagger_i d_i - 1 \right) + \sum_{i,\sigma} \lambda^\sigma_i \left(f^\dagger_{i\sigma} f_{i\sigma} - p^\dagger_{i\sigma} p_{i\sigma} - d^\dagger_i d_i \right) , \end{aligned} \tag{2.15}$$

with $z_{i\sigma} = e^\dagger p_{i\sigma} + p^\dagger_{i\bar{\sigma}} d_i$. Lagrange multipliers were introduced to enforce the constraints (2.13). The meaning of the operators z_i can be easily understood. If the bosonic state, on which it is acting is $|\sigma\rangle_i = |p_\sigma\rangle_i$, it destroys the state, replacing it with $|0\rangle_i = |e\rangle_i$. If, however the initial state is doubly occupied $|\uparrow\downarrow\rangle_i = |d\rangle_i$, it is replaced by $|\bar{\sigma}\rangle_i = |p_{\bar{\sigma}}\rangle_i$.

Despite the formulation with this choice of operator $z_{i\sigma}$ being faithful, it suffers from a drawback. In the simplest mean-field approximation, the bosonic part of the Hamiltonian is first decoupled from the fermionic degrees of freedom. The bosonic lattice problem is then further simplified and treated in local mean-field theory. Within such an approximation, the bosonic operators "condense" to complex numbers, and the conduction band is renormalized by $\left\langle z^\dagger_{i\sigma} \right\rangle \langle z_{j\sigma} \rangle = z^2$. Employing this approximation, one might check if one recovers the correct results in the non-interacting limit $U = 0$, where this renormalization should become unity $z^2 = 1$. Considering the case of half filling, it is easy to show (see [93]), that the condensed amplitudes are $e^2 = p^2_\sigma = d^2 = 1/4$, in accordance with (2.13). This, however, leads to

$$\left\langle z^\dagger_{i\sigma} \right\rangle \langle z_{j\sigma} \rangle = e^2 p^2_\sigma + d^2 p^2_{\bar{\sigma}} + 2ed\, p_\sigma p_{\bar{\sigma}} = \frac{1}{4} . \tag{2.16}$$

In order to resolve this problem, one can consider the improved expressions

$$\tilde{z}_{i\sigma} = (1 - d^\dagger_i d_i - p^\dagger_{i\sigma} p_{i\sigma})^{-1/2} z_{i\sigma} (1 - e^\dagger_i e_i - p^\dagger_{i\bar{\sigma}} p_{i\bar{\sigma}})^{-1/2} . \tag{2.17}$$

Within the physical subspace, defined by the constraints (2.13), these operators have the same eigenvalues and eigenvectors as $z_{i\sigma}$. Indeed, if this operator is applied on the states $|\sigma\rangle_i$ or $|d\rangle_i$, the additional terms are unity, while for $|\bar{\sigma}\rangle_i$ or $|e\rangle_i$, they yield zero. Substituting these improved expressions into Hamiltonian (2.15), we get a model which, within mean-field approximation, gives the correct results in the non-interacting limit.

One of the successes of the Kotliar Ruckenstein slave boson formulation was that its mean-field solution reproduce the results from the Gutzwiller approximation, therefore establishing a basis for systematic further corrections. However, it does not explicitly incorporate spin-rotation invariance; an issue that has been adressed in [104, 54]). Furthermore, more recent developments consider rotational invariant multi-orbital extensions, such as [102].

2.3 The slave rotor technique

2.3.1 The orbitally degenerate Hubbard Model

The basic principle of methods like the slave-boson technique by Kotliar and Ruckenstein is to introduce an auxiliary boson for each state in the local Hamiltonian. In case of the single-orbital Hubbard model, the local Hilbert space consists of only 4 states and such a method can be applied easily. In the case of multi-orbital models, however, it is clear that this might not be the most economic approach.

To be more specific, let us consider the N-fold orbitally degenerate Hubbard model

$$H = H_0 + H_{int} = -\sum_{ij,m\sigma} t_{ij} d^\dagger_{im\sigma} d_{jm\sigma} + \frac{U}{2}\sum_i \left(\sum_{m\sigma} d^\dagger_{im\sigma} d_{im\sigma} - \frac{N}{2} \right)^2 , \tag{2.18}$$

with $m = 1 \ldots (N/2)$ and $\sigma = \uparrow, \downarrow$. The crucial observation is, that the interacting part of this Hamiltonian does not depend on the local electronic configuration. It only depends on the total number of electrons Q per site, with an interaction energy

$$E_Q = \frac{U}{2}\left(Q - \frac{N}{2} \right)^2 . \tag{2.19}$$

For this reason, it is tempting to replace this rather complicated combination of fermionic operators by some sort of auxiliary "number operator", counting the overall local occupation. One could think of achieving this by introducing a single bosonic variable for each lattice site, replacing $d^\dagger_{im\sigma} \to f^\dagger_{im\sigma} b^\dagger_i$ and $d_{im\sigma} \to f_{im\sigma} b_i$, such that the Hamiltonian transforms to

$$H = -\sum_{ij,m\sigma} t_{ij} f^\dagger_{im\sigma} f_{jm\sigma} b^\dagger_i b_j + \frac{U}{2}\sum_i \left(b^\dagger_i b_i - \frac{N}{2} \right)^2 . \tag{2.20}$$

This naive approach, however, leads to a couple of problems: First of all, the new composite operators cannot obey the canonical anti-commutation relations $\{f^\dagger_{im\sigma} b^\dagger_i, f_{im\sigma} b\} = f^\dagger_{im\sigma} f_{im\sigma} b^\dagger_i b_i + f_{im\sigma} f^\dagger_{im\sigma} (b^\dagger_i b_i + 1) = b^\dagger_i b_i - f^\dagger_{im\sigma} f_{im\sigma} + 1 \stackrel{!}{=} 1$ for all fillings, since the resulting constraint $b^\dagger_i b_i \stackrel{!}{=} f^\dagger_{im\sigma} f_{im\sigma}$ is in contradiction with $b^\dagger_i b_i = \sum_{m\sigma} f^\dagger_{im\sigma} f_{im\sigma}$. Furthermore, after performing a mean-field decoupling, one is confronted with the more practical problem: The bosonic part of the Hamiltonian itself contains terms of quartic order and can not be solved easily.

A more successful approach to tackle the Hubbard Model with large degeneracy has been derived by S. Florens et al.[50, 51]. Instead of bosons, they suggested to use a $U(1)$ quantum rotor to describe the total electronic charge[2].
In this representation, the physical electron fields $d^\dagger_{m\sigma}$ are expressed in terms of auxiliary fermions

[2] A similar idea has been applied in the context of the Coulomb blockade[47].

$f^{\dagger}_{m\sigma}$ and an $U(1)$ quantum rotor, represented by an angular variable $\theta \in [0, 2\pi]$

$$d^{\dagger}_{m\sigma} = f^{\dagger}_{m\sigma} e^{i\theta} \quad , \quad d_{m\sigma} = f_{m\sigma} e^{-i\theta}; \tag{2.21}$$

where the objects $e^{i\theta}/e^{-i\theta}$ have the function of ladder operators, raising/lowering the angular momentum by one unit. As in any slave particle theory, the new operators act on an enlarged Hilbert space, in which any physical state is uniquely represented by an auxiliary state

$$|\sigma_1 ... \sigma_Q\rangle_d \rightarrow |\sigma_1 ... \sigma_Q\rangle_f \otimes |Q - N/2\rangle_\theta \ . \tag{2.22}$$

with

$$|Q - N/2\rangle_\theta = e^{i\theta} \cdots e^{i\theta} \, |-N/2\rangle_\theta = (e^{i\theta})^Q \, |-N/2\rangle_\theta \ , \tag{2.23}$$

where the state $|Q - N/2\rangle_\theta$ is an eigenstate of the angular momentum operator $\hat{L} = -i\partial_\theta$

$$\hat{L} \, |Q - N/2\rangle_\theta = (Q - N/2) \, |Q - N/2\rangle_\theta \ . \tag{2.24}$$

Rewriting the physical states in this way, we identify the total electron number Q as corresponding to the angular momentum of the quantum rotor. It is, therefore, possible to rewrite the interacting part of (2.18) in terms of our new variables, by replacing the sum of the electron density operators

$$\sum_{m\sigma} n_{m\sigma} - \frac{N}{2} \rightarrow \hat{L} \, . \tag{2.25}$$

Applying this substitution to the Hamiltonian (2.18)

$$H = - \sum_{ij,m\sigma} t_{ij} f^{\dagger}_{im\sigma} f_{jm\sigma} e^{i\theta_i} e^{-i\theta_j} + \frac{U}{2} \hat{L}^2 \, , \tag{2.26}$$

we can replace a complicated two-body operator, quartic in the electron fields, by a much simpler kinetic term, acting on the rotors. Replacing the electron density by the rotor angular momentum works fine, as long as we are dealing with physical states of the form (2.22). However, the enlarged Hilbert space will also accommodate unphysical states where the number of auxiliary fermions Q does not match the rotor angular momentum ℓ and the substitution (2.25) cannot be applied. In order to retrieve the physics of the original system, we therefore have to find a way to exclude unphysical states with $Q \neq \ell$. This is a problem, that concerns all slave-particle methods. The standard way to solve it is by defining an operator

$$\hat{Q}_i = \left(\sum_{m\sigma} n^f_{im\sigma} - \frac{N}{2} - \hat{L}_i \right) \, , \tag{2.27}$$

that measures the difference of the number of electrons and the angular momentum $Q-\ell$ on the lattice site i. This operator commutes with the Hamiltonian (2.26)

$$\begin{aligned}\left[H,\hat{Q}_k\right] = &-\sum_{ij,m\sigma} t_{ij}\left(-\delta_{ik}f^{\dagger}_{im\sigma}f_{jm\sigma}+\delta_{jk}f^{\dagger}_{im\sigma}f_{jm\sigma}\right)e^{i\theta_i}e^{-i\theta_j}\\ &+\sum_{ij,m\sigma} t_{ij}f^{\dagger}_{im\sigma}f_{jm\sigma}\left(-\delta_{ik}e^{i\theta_i}e^{-i\theta_j}+\delta_{jk}e^{i\theta_i}e^{-i\theta_j}\right)=0\,,\end{aligned} \tag{2.28}$$

making it a time independent quantity. Since the expectation value of $\hat{Q}_i$ is non-zero only for unphysical states, we can use it to construct a projection operator that eliminates unphysical states. Not caring about normalization, this operator reads

$$\hat{P}=\prod_i\left(\int \mathrm{d}\lambda_i e^{-i\lambda_i\hat{Q}_i}\right)\,. \tag{2.29}$$

Thanks to the property (2.28), it is sufficient to define one Lagrange multiplier λ_i for every lattice site, independent of time.
We are now ready to calculate any expectation value as

$$\left\langle\hat{O}\right\rangle=\frac{\mathrm{Tr}\left\{e^{-\beta H}\hat{P}\hat{O}\right\}}{\mathrm{Tr}\left\{e^{-\beta H}\hat{P}\right\}}=\frac{\mathrm{Tr}\left\{\prod_i\left(\int \mathrm{d}\lambda_i\right)e^{-\beta H-i\sum_i\lambda_i\hat{Q}_i}\hat{O}\right\}}{\mathrm{Tr}\left\{\prod_i\left(\int \mathrm{d}\lambda_i\right)e^{-\beta H-i\sum_i\lambda_i\hat{Q}_i}\right\}}\,. \tag{2.30}$$

In practice, however, integrating over all Lagrange multipliers would only lead us back to a problem that is as complex as the original one, and nothing is won. Instead, we restrict ourselves to the saddle point values h_i of λ_i

$$\prod_i\left(\int \mathrm{d}\lambda_i\right)e^{-\beta H-i\sum_i\lambda_i\hat{Q}_i}\to e^{-\beta H+\beta\sum_i h_i\hat{Q}_i}\,, \tag{2.31}$$

where he have set $h_i=-i\lambda_i/\beta$ (allowing complex values for the saddle-point value is a common strategy to access a larger class of saddle-point solutions). The specific value of h is evaluated by minimizing the free energy corresponding to the Hamiltonian

$$H=-\sum_{ij,m\sigma}t_{ij}f^{\dagger}_{im\sigma}f_{jm\sigma}e^{i\theta_i}e^{-i\theta_j}+\frac{U}{2}\hat{L}^2-\sum_i h_i\left(\sum_{m\sigma}n^f_{im\sigma}-\frac{N}{2}-\hat{L}_i\right)\,, \tag{2.32}$$

leading to the intuitive saddle-point condition

$$\sum_m\left\langle n^f_{im\sigma}\right\rangle_H-\frac{N}{2}\stackrel{!}{=}\left\langle\hat{L}_i\right\rangle_H\,. \tag{2.33}$$

Finally, if there is no additional, inhomogeneous potential, the saddle point values will be site-independent $h_i=h$.

Physical observables as the single particle Greeens' function can then be calculated, by replacing the electronic operators by their composite substitutes (2.21) and calculating the expectation value with respect to the slave rotor Hamiltonian (2.32)

$$G^d_{m\sigma}(\tau) = -\left\langle T d_{m\sigma}(\tau) d^\dagger_{m\sigma}(0)\right\rangle = -\left\langle T f_{m\sigma}(\tau) f^\dagger_{m\sigma}(0) e^{-i(\theta(\tau)-\theta(0))}\right\rangle . \tag{2.34}$$

2.3.2 Mean-field solution to the Hubbard model

Applying the slave-rotor formalism allowed us to the eliminate the electron interaction term. Unfortunately however, we had to trade it for a hopping term that explicitly couples the fermionic to the slave rotor ladder operators.

Here, we have to make a second approximation. Assuming that the fluctuations of the charge (represented by the rotor variable) "live" on a different energy scale than fluctuations of the spin, we can decouple the Hamiltonian (2.32) in a mean-field fashion

$$H \approx H_f + H_\theta , \tag{2.35}$$

with

$$H_f = -\sum_{ij.m\sigma} t_{ij} f^\dagger_{im\sigma} f_{jm\sigma} \left\langle e^{i(\theta_i-\theta_j)}\right\rangle_\theta - (\mu + h)\sum_{im\sigma} n^f_{im\sigma} \tag{2.36}$$

$$H_\theta = -\sum_{ij.m\sigma} t_{ij} \left\langle f^\dagger_{im\sigma} f_{jm\sigma}\right\rangle_f e^{i(\theta_i-\theta_j)} + h\sum_i \hat{L}_i + \frac{U}{2}\sum_i \hat{L}_i^2 . \tag{2.37}$$

This implies, that the original partition function splits into two parts

$$Z = \mathrm{Tr}\{e^{-\beta H}\} \to \mathrm{Tr}\{e^{-\beta H_f}\}\mathrm{Tr}\{e^{-\beta H_\theta}\} = Z_f Z_\theta , \tag{2.38}$$

and that physical observables, as the Greens' function (2.34), will factorize

$$G^d_{m\sigma}(\tau) \to -\left\langle T f_{m\sigma}(\tau) f^\dagger_{m\sigma}(0)\right\rangle_f \left\langle e^{-i(\theta(\tau)-\theta(0))}\right\rangle_\theta = G^f_{m\sigma}(\tau) G^\theta_{m\sigma}(\tau) . \tag{2.39}$$

Self-consistently evaluating the expectation values in (2.36) and (2.37) corresponds to solving a set of mean-field equations. After a solution is obtained (ensuring that the saddle point constraint (2.33) is fulfilled) we can calculate any physical observable as an expectation value taken with the mean-field Hamiltonian(2.35). Evaluating the expectation value $\left\langle f^\dagger_{im\sigma} f_{jm\sigma}\right\rangle_f$ is done most easily, since the Hamiltonian H_f can be diagonalized trivially by transforming it into momentum space. Unfortunately, there is no simple way to diagonalize H_θ, so we have to consider a different approach.

We follow the strategy in [51] and tackle the problem by applying a second mean-field decoupling to

the rotor Hamiltonian H_θ

$$H_\theta^{MF} = -\sum_{ij,m\sigma} t_{ij} \left\langle f_{im\sigma}^\dagger f_{jm\sigma} \right\rangle_f \left(e^{i\theta_i} \left\langle e^{-i\theta_j} \right\rangle + \left\langle e^{i\theta_i} \right\rangle e^{-i\theta_j} \right) + h\sum_i \hat{L} + \frac{U}{2}\sum_i \hat{L}_i^2 \,. \tag{2.40}$$

This last approximation drastically reduces the complexity of the problem and leaves us with the task of solving an effective single-site problem. We can, therefore, eliminate the site indices and write

$$H_\theta^{MF} = -K\cos\theta + h\hat{L} + \frac{U}{2}\hat{L}^2 \,, \tag{2.41}$$

with

$$K = 2\sum_{jm\sigma} t_{ij} \left\langle f_{im\sigma}^\dagger f_{jm\sigma} \right\rangle_f \langle\cos\theta\rangle_\theta = 2N\sum_j t_{ij} \left\langle f_i^\dagger f_j \right\rangle_f \langle\cos\theta\rangle_\theta \,, \tag{2.42}$$

where, in the last step, we assumed all auxiliary fermions of index $m\sigma$ to be identical. In addition, the expectation value in (2.36) factorizes to

$$\left\langle e^{i(\theta_i-\theta_j)} \right\rangle_\theta \to \langle\cos\theta\rangle_\theta^2 = \mathscr{Z} \,, \tag{2.43}$$

which we recognize as the quasi-particle renormalization $\mathscr{Z}$ (not to be confused with the partition function Z).
In summary, we are left to solve the following mean-field equations

$$\begin{aligned} K &= 2N\langle\cos\theta\rangle_\theta \sum_{i\omega\mathbf{k}} \frac{\varepsilon(\mathbf{k})}{i\omega+\mu+h-\mathscr{Z}\varepsilon(\mathbf{k})} \\ &= 2N\langle\cos\theta\rangle_\theta \int \mathrm{d}\varepsilon D(\varepsilon)\varepsilon n_F[\mathscr{Z}\varepsilon-\mu+h] = 2N\langle\cos\theta\rangle_\theta \bar{\varepsilon}_{kin} \,, \end{aligned} \tag{2.44}$$

$$\mathscr{Z} = \langle\cos\theta\rangle_\theta^2 = \left(\frac{1}{Z_\theta} \mathrm{Tr}\{\cos\theta e^{-\beta H_\theta}\} \right)^2 \tag{2.45}$$

$$\left\langle \hat{L} \right\rangle_\theta = \sum_{m\sigma} \left\langle f_{m\sigma}^\dagger f_{m\sigma} \right\rangle_f - \frac{N}{2} = N\int \mathrm{d}\varepsilon D(\varepsilon) \left(n_F[\mathscr{Z}\varepsilon-\mu+h] - \frac{1}{2} \right) \,, \tag{2.46}$$

with $D(\varepsilon)$ being the density of states and $n_F[\varepsilon]$ the Fermi function.

The problem simplifies even further when solving (2.44)-(2.46) for a fixed electronic occupation $\bar{n} = \left\langle f^\dagger f \right\rangle$. Since the kinetic energy $\bar{\varepsilon}_{kin}$ is independent of $\mathscr{Z}$ i.e. only a function of the filling $\bar{n}$

$$\int \mathrm{d}\varepsilon D(\varepsilon)\varepsilon n_F[\mathscr{Z}\varepsilon-\mu+h] = \bar{\varepsilon}_{kin}(\bar{n}) \,, \tag{2.47}$$

the mean-field equations reduce to the problem of self-consistently evaluating $\langle\cos\theta\rangle_\theta$, with the constraint $\left\langle \hat{L} \right\rangle_\theta = N(\bar{n}-1/2)$.

Fig. 2.2 shows the quasi-particle renormalizations which we obtained from applying the slave rotor method in its mean-field approximation to the Hubbard model at half filling. The blue, solid

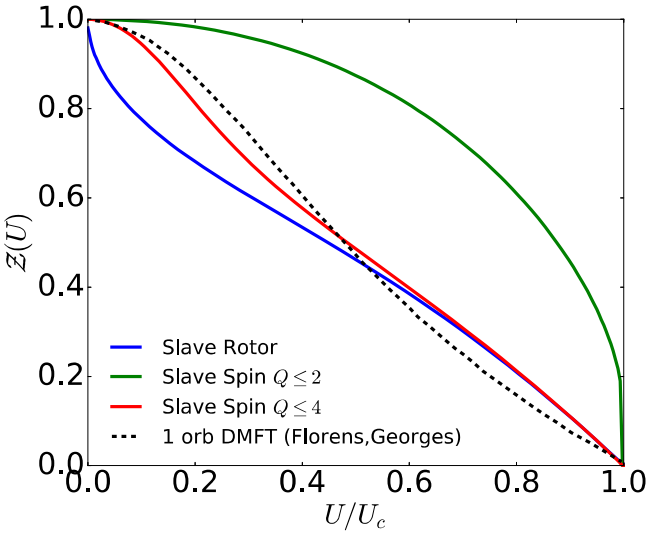

Fig. 2.2 Quasi-particle renormalization Z from the slave-rotor mean-field formalism, compared to the result from dynamical mean-field theory (DMFT)[51]. For the blue line, the full rotor spectrum with $Q \in (-\infty, +\infty)$ was taken into account, while for the green and the red lines, the spectrum was truncated at $Q \leq 2$ and $Q \leq 4$, respectively.

line corresponds to the result considering the full spectrum of the local rotor Hamiltonian, while the red and green lines were obtained from truncating the spectrum at $Q \leq 4$ and $Q \leq 2$, respectively (for detailed informations see Appendix A.1). Of course, the formalism can also be applied away from half filling. Fig. 2.3 shows a finite temperature phase diagram for the 2-orbital Hubbard model, which we obtained by using the slave rotor method, with the angular momentum spectrum truncated to $Q \leq 4$. The phase diagram faithfully captures the Mott metal-insulator transition at commensurate fillings, with the insulating lobes expanding to lower values of U away from half filling.

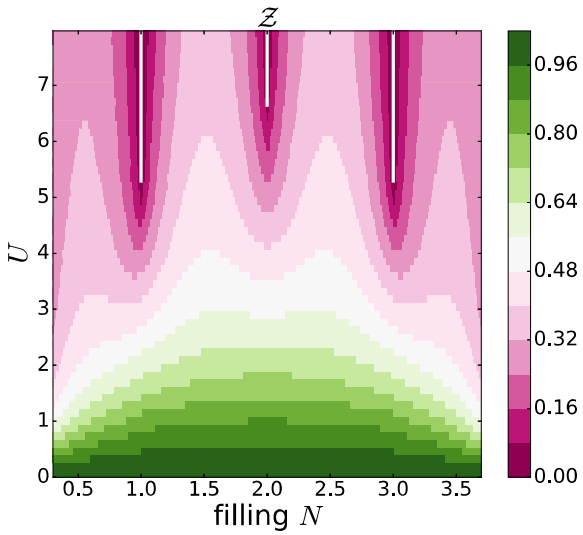

Fig. 2.3 Quasiparticle renormalization $\mathscr{Z}$ for the 2-orbital Hubbard model with semicircular DOS, calculated with the slave-rotor mean-field method, with a truncated rotor spectrum $Q \leq 4$ at $\beta t = 40$.

Part II

The Multi-Orbital Hubbard Model & Hund's Physics

Chapter 3

The Physics of Multi-Orbital Systems

3.1 Motivation

The concept of strongly correlated systems was already discussed in the introductory chapter. In this context, we introduced the Hubbard model[79] as a minimal system to describe strong correlations. The Hubbard model, although comprising only one orbital per site and parametrized, besides temperature, by merely three scalars (the hopping amplitude t, the on-site Coulomb interaction U and the chemical potential μ), incorporates many of the physical phenomena observed in strongly correlated materials. Most prominently, it allows to describe the interaction-driven localization of electrons, the so-called Mott transition[118].

The Mott phenomenon received ever more attention after the discovery of the *cuprate* high temperature superconductors[18], when it was clear that the parent compounds of these unconventional superconductors were Mott insulators. Early theoretical works suggested that the essence of the underlying physics may already be contained in the single-orbital Hubbard model[4] (although this was quickly disputed, as we shall see in the following chapter). In such a single band picture, strong correlations of the doped systems are understood to emerge from the proximity to the Mott insulator.

Unlike the cuprate systems, most materials possess more than a single active band at the Fermi level, and a single orbital description would lead to fundamentally wrong results. This is true for many of the early transition metal oxides (TMOs); an interesting example being the case of the $3d^1$ perovskites $SrVO_3$, $CaVO_3$, $LaTiO_3$ and $YTiO_3$. All four compounds possess a single valence electron, and modeling the compounds with a one orbital Hubbard model (with the corresponding interaction parameter and dispersion) would predict all of them to be insulators. In reality, however, only the latter two materials show a spectral gap at the Fermi level [127], while $SrVO_3$ and $CaVO_3$ are correlated metals [110]. In order to resolve this puzzle, we have to take into account the different effective orbital degeneracies of the systems. In $SrVO_3$ and $CaVO_3$, the valence electron occupies the 3-fold degenerate t_{2g} manifold, leading to a gain in kinetic energy and a higher critical Coulomb interaction, while in $LaTiO_3$ and $YTiO_3$ this degeneracy is lifted.

Other examples include the families of ruthenates, chalcogenides and, most prominently, the *iron*

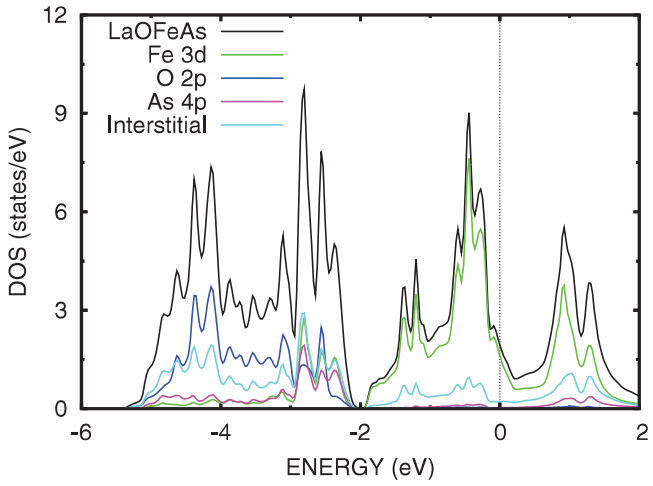

Fig. 3.1 Density of states of LaOFeAs within the generalized gradient approximation, from[72].

pnictide superconductors, that attracted much attention after their discovery in 2006[83, 84]. In these compounds, several bands, formed of the d-shell orbitals, cross the Fermi level (an example can be seen in Fig. 3.1, showing the density of states of LaOFeAs withing density functional theory) and hybridize with the ligands.

Considering multi-orbital many body models is thus a necessary step towards a more realistic description of many materials. Such models exhibit a wealth of new physical phenomena, emerging from the nature of multi-orbital interactions, or simply the increase in degeneracy, as in the example mentioned before. Most importantly, deriving the effective on-site Coulomb interaction in the case of multiple orbitals gives rise to a new energy scale, the so-called *Hund's exchange coupling* J. It quantifies the energy gain of putting electrons in a configuration with parallel spin, as compared to a configuration with anti-parallel spins.

This Hund's coupling J was found to be at the origin of various high-[39] and low-energy[148] effects, and is now generally accepted to be a central quantity in the theoretical description of many transition metal oxides of the 3d and 4d series. Systems with Hund's coupling can exhibit strong correlations while not being close to a Mott insulator. This led to the emergence of the notion of *Hund's metals*[Yin et al.], to designate materials in which correlations are due to Hund's coupling, rather than "Mottness" (i.e. the proximity to the Mott insulator).

The outline of this chapter is as follows. In the beginning, we shall discuss the on-site Coulomb matrix, that emerges in the multi-orbital case. In this context, we will introduce the concept of the Hund's exchange coupling, which, throughout the chapter, will remain at the center of our interest. In the following, we shall give a brief review of the physics that emerges from multi-band impurity models with Hund's interaction, and discuss the similarities and differences to the results from lattice models. Finally, we shall present results from calculations, investigating the effect of Hund's exchange coupling onto the metal to insulator transition.

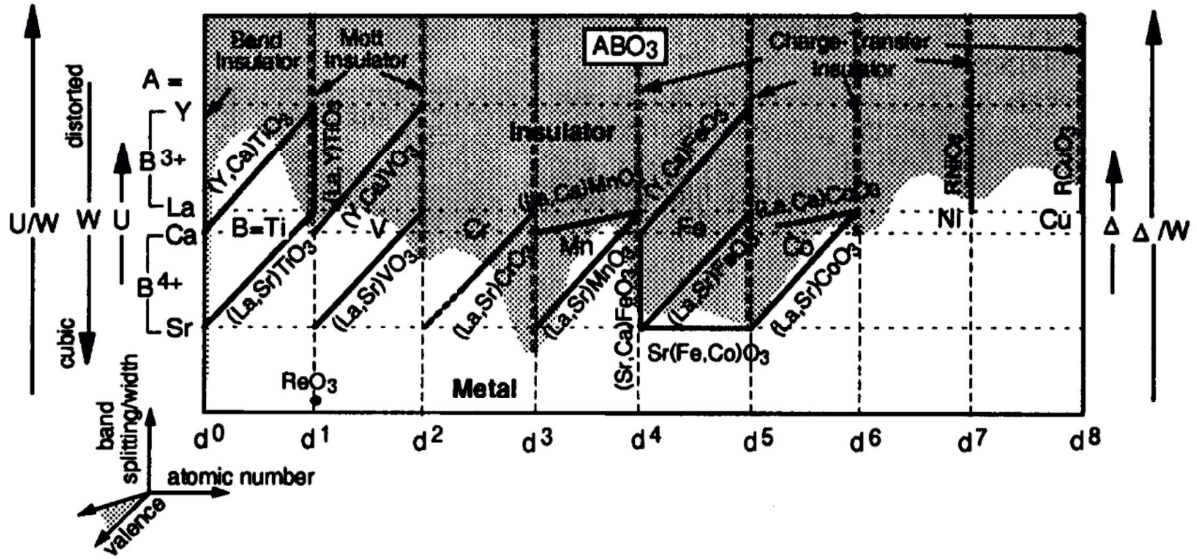

Fig. 3.2 "Map" of perovskite-type oxides (from [1], Fig. 1). The horizontal axis shows the d-band filling, marking the d-orbital configuration of the stochiometric compounds. According to the original description "Band-gap closure occurs along vertical lines: valence control is realized along oblique directions and atomic-number control along the horizontal direction." Despite what the figure suggests, it is known today that U/W alone does not describe the physical properties of most of the compounds displayed; in particular, one has to take into account Hund's exchange coupling and the effective orbital degenery. The decrease of the critical interaction U/W when going from d^1 to the d^3 compounds can be explained as a consequence of Hund's coupling.

3.2 The Coulomb matrix

In this section, we shall discuss the form of the Coulomb interaction for multi-orbital tight binding models.

Considering only local Coulomb interactions, such a Hamiltonian can be cast in the general form

$$\begin{aligned} H =& H_0 + H_{int} \\ =& -\sum_{ijmm'\sigma} t_{ijmm'} c^\dagger_{im\sigma} c_{jm'\sigma} + \frac{1}{2}\sum_i \sum_{mm'm''m'''\sigma\sigma'} V_{mm'm''m'''} c^\dagger_{im\sigma} c^\dagger_{im'\sigma'} c_{im''\sigma'} c_{im'''\sigma} \,. \end{aligned} \tag{3.1}$$

Here, $V_{m,m',m'',m'''}$ describes the matrix elements of the Coulomb interaction in the single particle basis, with

$$\begin{aligned} V_{mm'm''m'''} &= \left\langle m,m' \left| \hat{V}_{Coulomb} \right| m'',m''' \right\rangle \\ &= \iint \mathrm{d}\mathbf{r}\mathrm{d}\mathbf{r}' \phi^*_{m\sigma}(\mathbf{r}) \phi^*_{m'\sigma'}(\mathbf{r}') W(|\mathbf{r}-\mathbf{r}'|) \phi_{m'''\sigma'}(\mathbf{r}') \phi_{m''\sigma}(\mathbf{r}) \end{aligned} , \tag{3.2}$$

with the screened Coulomb potential $W(|\mathbf{r}-\mathbf{r}'|)$. Note that the interaction matrix does not depend on spin. This is due to the spin-conserving character of the Coulomb interaction.

Considering the 1-orbital system that we introduced in the previous chapter, the interaction matrix only has a single element

$$H_{int} = \frac{1}{2}\sum_{\sigma\sigma'} V c^\dagger_\sigma c^\dagger_{\sigma'} c_{\sigma'} c_\sigma = V c^\dagger_\uparrow c_\uparrow c^\dagger_\downarrow c_\downarrow \,, \tag{3.3}$$

where we omitted the site-index i.
In general, however, the interaction matrix V is a rank-4 tensor. In case of a M-orbital system, we are thus confronted with a matrix of M^4 elements. This means, that for a p-orbital system with $\ell = 1$ and $m \in \{-1,0,1\}$, the tensor has $3^4 = 81$ elements; for a d-electron system with $\ell = 3$ it is $5^4 = 625$ elements, etc. Clearly, working with such objects would cause major complications. Luckily, however, the number of independent elements of the Coulomb tensor is much smaller, due to symmetries of the interaction.

We can illustrate this by considering a p-orbital system with $\ell = 1$. Exploiting the rotational symmetry of the Coulomb interaction, it can be shown that the interaction tensor of the p-orbital system has only two independent parameters and can be written as

$$V_{mm'm''m'''} = U'\delta_{mm''}\delta_{m'm'''} + J(\delta_{mm'''}\delta_{m'm''} + \delta_{mm'}\delta_{m''m'''}) \,, \tag{3.4}$$

(for a detailed derivation see [53]).
Evaluating the matrix element for $m = m' = m'' = m'''$ yields the well-known relation

$$\left\langle m,m \middle| \hat{V}_{Coulomb} \middle| m,m \right\rangle \equiv U = U' + 2J \,, \tag{3.5}$$

while the values of U' and J can be retained by comparing expressions (3.2) and (3.4).

In the context of transition metal oxides, we will mainly be interested in correlations of the d shell (inter-shell interactions will be the topic of the following chapter). Even though the full d-shell is composed of five orbitals, crystal fields in the solid generally lift the rotational symmetry. In an octahedral crystal field, this results in two sub-manifolds – known as t_{2g} and e_g – comprised of three and two-orbitals, respectively. In both cases, the Coulomb interaction can be parametrized by only 3 independent integrals, which read

$$U = \left\langle m,m \middle| \hat{V}_{Coulomb} \middle| m,m \right\rangle = \iint \mathrm{d}\mathbf{r}\mathrm{d}\mathbf{r}' |\phi_{m\sigma}(\mathbf{r})|^2 V(|\mathbf{r}-\mathbf{r}'|) |\phi_{m\bar{\sigma}}(\mathbf{r}')|^2 \tag{3.6}$$

$$U' = \left\langle m,m' \middle| \hat{V}_{Coulomb} \middle| m,m' \right\rangle = \iint \mathrm{d}\mathbf{r}\mathrm{d}\mathbf{r}' |\phi_{m\sigma}(\mathbf{r})|^2 V(|\mathbf{r}-\mathbf{r}'|) |\phi_{m'\sigma'}(\mathbf{r}')|^2 \tag{3.7}$$

$$J = \left\langle m,m' \middle| \hat{V}_{Coulomb} \middle| m',m \right\rangle = \iint \mathrm{d}\mathbf{r}\mathrm{d}\mathbf{r}' \phi^*_m(\mathbf{r}) \phi^*_{m'\sigma}(\mathbf{r}') V(|\mathbf{r}-\mathbf{r}'|) \phi_m(\mathbf{r}') \phi_{m'\sigma}(\mathbf{r}) \,. \tag{3.8}$$

Note that here we used the unscreened potential $V(|\mathbf{r}-\mathbf{r}'|)$. This is because the parametrization Eq. (3.4) depends on the rotational symmetry of the interaction. While in solid state systems, the effective interaction will be screened, one often keeps the form Eq. (3.4), assuming that the screening is sufficiently isotropic.

With these interaction parameters, the t_{2g} interaction Hamiltonian takes the well-known Kanamori form [85]

$$\begin{aligned} H_{int} = U\sum_m n_{m\uparrow}n_{m\downarrow} + U'\sum_{m>m',\sigma} n_{m\sigma}n_{m'\bar{\sigma}} + (U'-J)\sum_{m>m'\sigma} n_{m\sigma}n_{m'\sigma} \\ - J\sum_{m>m'\sigma} c^\dagger_{m\sigma}c^\dagger_{m'\bar{\sigma}}c_{m'\sigma}c_{m\bar{\sigma}} + J\sum_{m>m'\sigma} c^\dagger_{m\sigma}c^\dagger_{m\bar{\sigma}}c_{m'\bar{\sigma}}c_{m'\sigma} \,, \end{aligned} \tag{3.9}$$

where the last two terms describe spin-flipping and pair-hopping, respectively.
Note that expressions (3.6)-(3.8) correspond to the general form derived for the interaction for a p-orbital system (3.4). Indeed, by requiring the system to be rotationally symmetric, we reproduce (3.5), i.e. $U' = U - 2J$. Relating the parameters in such a way, we can re-write (3.9) in a form that explicitly reveals its rotational symmetry (for a more detailed discussion, consider reference [59])

$$H_{int} = \frac{U-3J}{2}\hat{N}(\hat{N}-1) - 2J\hat{\vec{S}}^2 - \frac{J}{2}\hat{\vec{L}}^2 + \frac{5}{2}J\hat{N} \,, \tag{3.10}$$

where we introduced the total number operator

$$\hat{N} = \sum_{m\sigma} c^\dagger_{m\sigma}c_{m\sigma} \,, \tag{3.11}$$

and the total spin and angular momentum

$$\hat{\vec{S}} = \frac{1}{2}\sum_{m,\sigma\sigma'} c^\dagger_{m\sigma}\vec{\sigma}_{\sigma\sigma'}c_{m\sigma'} \,, \hat{L}_m = i\sum_{mm'\sigma} \varepsilon_{mm'm''}c^\dagger_{m'\sigma}c_{m''\sigma} \,. \tag{3.12}$$

If we consider the full d-orbital manifold, things get a bit more complicated. The following presentation follows Ref. [13], for a more detailed discussion, consider e.g. Ref. [143]); the case with crystal fields is discussed in [52]. To keep the discussion simple, we again consider the bare Coulomb interaction. In order to systematically derive the on-site interaction in this case, we re-write the Coulomb potential as

$$\frac{1}{|\mathbf{r}-\mathbf{r}'|} = \sum_{\ell=0}^{\infty}\frac{r_<^\ell}{r_>^{\ell+1}}\frac{4\pi}{2\ell+1}\sum_{m=-\ell}^{\ell} Y^*_{\ell m}(\theta,\varphi)Y_{\ell m}(\theta',\varphi') \,, \tag{3.13}$$

where we introduced the spherical harmonics $Y_{\ell m}$, and $r_</r_>$ designates the norm of the smaller/bigger of the vectors $\mathbf{r}$ and $\mathbf{r}'$. Likewise, we can write the hydrogen-like orbital of quantum numbers n,ℓ,m as

$$\langle r,\theta,\varphi\,|\,n,\ell,m\rangle = R_{n\ell}(r)Y^{\ell m}(\theta,\varphi) \,, \tag{3.14}$$

where we introduced the radial function

$$R_{n\ell}(r) = \sqrt{\left(\frac{2Z}{n}\right)^3 \frac{(n-\ell-1)!}{2n\left[(n+\ell)!\right]^3}} e^{-rZ/n} \left(\frac{2Zr}{n}\right)^{\ell} L_{n-\ell-1}^{2\ell+1}\left(\frac{2Zr}{n}\right) , \tag{3.15}$$

with the atomic number Z and $L_{n-\ell-1}^{2\ell+1}$ being the Laguerre polynomials of degree $n-\ell-1$.
This notation simplifies the calculation of the matrix element (3.2), since the integrals factorize into a radial and an angular component. Eventually, we get

$$\left\langle mm' \left| \hat{V}_{Coulomb} \right| m''m''' \right\rangle = \sum_{k=0}^{2\ell} a_k(m,m',m'',m''')F_k , \tag{3.16}$$

with

$$\begin{aligned} &a_k(m,m',m'',m''') \\ &\quad = \sum_{q=-k}^{k} \frac{4\pi}{2q+1} \int \mathrm{d}\Omega_1 Y_{\ell m}^*(\Omega_1) Y_{kq}^*(\Omega_1) Y_{\ell m''}(\Omega_1) \int \mathrm{d}\Omega_2 Y_{\ell m'}^*(\Omega_2) Y_{kq}(\Omega_2) Y_{\ell m'''}(\Omega_2) \end{aligned} , \tag{3.17}$$

and the radial Slater integrals

$$F_k = \iint \mathrm{d}r_1 \mathrm{d}r_2 \; r_1^2 r_2^2 R_{n\ell}^2(r_1) \frac{r_<^k}{r_>^{k+1}} R_{n\ell}^2(r_2) . \tag{3.18}$$

Even though the number of independent interaction parameters is bigger than in the three orbital case, we can organize the entries in a similar manner as before, by generalizing (3.7) and (3.8) to

$$U_{mm'} = \left\langle m,m' \left| \hat{V}_{Coulomb} \right| m,m' \right\rangle \tag{3.19}$$

$$J_{mm'} = \left\langle m,m' \left| \hat{V}_{Coulomb} \right| m',m \right\rangle . \tag{3.20}$$

Here, these quantities are matrices. Writing them in the basis $(z^2, x^2-y^2, xy, xz, yz)$ yields

$$J_{mm'} = \begin{bmatrix} 0 & J_2 & J_2 & J_4 & J_4 \\ J_2 & 0 & J_3 & J_1 & J_1 \\ J_2 & J_3 & 0 & J_1 & J_1 \\ J_4 & J_1 & J_1 & 0 & J_1 \\ J_4 & J_1 & J_1 & J_1 & 0 \end{bmatrix} , \tag{3.21}$$

while $U_{mm'}$ takes the familiar form

$$U_{mm'} = U_0 - 2J_{mm'} = \begin{bmatrix} U_0 & U_0-2J_2 & U_0-2J_2 & U_0-2J_4 & U_0-2J_4 \\ U_0-2J_2 & U_0 & U_0-2J_3 & U_0-2J_1 & U_0-2J_1 \\ U_0-2J_2 & U_0-2J_3 & U_0 & U_0-2J_1 & U_0-2J_1 \\ U_0-2J_3 & U_0-2J_1 & U_0-2J_1 & U_0 & U_0-2J_1 \\ U_0-2J_4 & U_0-2J_1 & U_0-2J_1 & U_0-2J_1 & U_0 \end{bmatrix} . \tag{3.22}$$

In order to define these new parameters, it is useful to introduce the averaged values

$$U_{avg} = \frac{1}{(2\ell+1)^2}\sum_{mm'} U_{mm'} = F_0 \tag{3.23}$$

$$J_{avg} = U_{avg} - \frac{1}{2\ell(2\ell+1)}\sum_{m\neq m'}(U_{mm'} - J_{mm'}) = \frac{F_2+F_4}{14} , \tag{3.24}$$

which are related to the Slater integrals F_0, F_2, F_4. The averaged interaction parameters are defined in such a way that they yield simple expressions for the mean-field part of the interaction Hamiltonian[1]. With these definitions, the other parameters in (3.21) and (3.22) read

$$U_0 = U_{avg} + \frac{8}{7}J_{avg} \tag{3.26}$$

$$J_1 = \frac{3}{49}F_2 + \frac{20}{441}F_4 \tag{3.27}$$

$$J_2 = -\frac{10}{7}J_{avg} + 3J_1 = -\frac{10}{7}J_{avg} + \frac{9}{49}F_2 + \frac{20}{147}F_4 \tag{3.28}$$

$$J_3 = \frac{30}{7}J_{avg} - 5J_1 = \frac{30}{7}J_{avg} - \frac{15}{49}F_2 - \frac{100}{441}F_4 \tag{3.29}$$

$$J_4 = \frac{20}{7}J_{avg} - 3J_1 = \frac{20}{7}J_{avg} - \frac{9}{49}F_2 - \frac{20}{147}F_4 . \tag{3.30}$$

Using these expressions, together with (3.21) and (3.22), we can finally write down the interaction Hamiltonian

$$\begin{aligned} H_{int} = &\sum_{mm'} U_{mm'} n_{m\uparrow} n_{m'\downarrow} + \sum_{m>m',\sigma} (U_{mm'} - J_{mm'}) n_{m\sigma} n_{m'\sigma} \\ &- \sum_{m>m'\sigma} J_{mm'} c^\dagger_{m\sigma} c^\dagger_{m'\bar{\sigma}} c_{m'\sigma} c_{m\bar{\sigma}} + \sum_{m>m'\sigma} J_{mm'} c^\dagger_{m\sigma} c^\dagger_{m\bar{\sigma}} c_{m'\bar{\sigma}} c_{m'\sigma} , \end{aligned} \tag{3.31}$$

which is a direct generalization of the three-orbital Kanamori Hamiltonian (3.9).
Note that interactions within the t_{2g} and e_g manifolds are defined by only two parameters each; U_0, J_1

[1] Following [35], the mean-field part of the interaction Hamiltonian can be written as

$$\langle H_{int}\rangle = U_{avg} N_\uparrow N_\downarrow + \frac{1}{2}(U_{avg} - J_{avg})\frac{2\ell}{2\ell+1}\sum_\sigma N_\sigma^2 , \tag{3.25}$$

with $N_\sigma = \sum_m \langle n_{m\sigma}\rangle$. This expression is known as the around mean-field (AMF) approximation to the double counting functional, and was originally derived in the context of the LDA+U scheme[6].

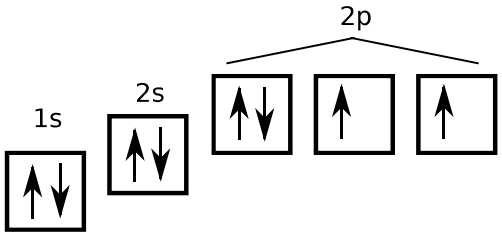

Fig. 3.3 Schematic representation for the electronic configuration of oxygen, obeying Hund's rules.

and U_0, J_2, respectively. This is consistent with the Kanamori interaction (3.9), note however, that these values are quite different from the averaged interaction parameters U_{avg} and J_{avg}.
Already when restricting ourselves to on-site interactions only, we implicitly made the assumption that the electrostatic field generated by the ions is effectively screened by the surrounding electrons. Screening effects also have to be taken into account in *ab-initio* calculations of the interaction parameters. Here, much progress has been made with the development of the *constrained random phase approximation* (cRPA)[9, 114, 122, 115], which allows to take into account screening from electron bands outside a certain energy window, for which the interacting low energy model shall be defined.
Most interestingly, screening effects increase the importance of the exchange interaction parametrized by J_{avg}, as it has been shown in [153]. For 3d systems, the theoretical bare value of the exchange term $J_{avg} = 0.81 + 0.080(Z-21)$ eV is only a small fraction of the bare value of $U_{avg} = 15.31 + 1.50(Z-21)$ eV. In the solid state context, however, F_0 is screened much more strongly than F_2 and F_4, such that empirically the interaction parameters are found [153] to be

$$J_{avg} = 0.59 + 0.075(Z-21) \text{ eV} \tag{3.32}$$

$$U_{avg} = 1.5 + 0.21(Z-21) \text{ eV} . \tag{3.33}$$

3.3 Atomic limit and Mott gap

Before considering the case of a solid state system, it is interesting and insightful to consider the physics that one obtains in the atomic limit.
Looking at the interaction Hamiltonian for the three orbital system (3.9), one can directly deduce the first and second Hund's rule of atomic physics:

1. First, maximize the total spin $\hat{S}^2$
2. Then, maximize the angular momentum $\hat{L}^2$

Fig. 3.3 shows the application of Hund's first and second rules to evaluate the electronic configuration of atomic oxygen: The four electrons of the p-shell arrange themselves in such a way that they maximize the total spin to $S = 1$ and the total angular momentum to $L = 1$.

In the context of a lattice system, the lowering of the atomic ground state configuration proportional to $\hat{\vec{S}}^2$ (and $\hat{\vec{L}}^2$) will have some significant consequences. To understand this, let us consider the example of a t_{2g} system with three orbitals. At half filling, the ground state configuration is defined by $N = 3$, $S = 3/2$, $L = 0$, and the corresponding interaction energy $\langle H_{int} \rangle$ can be obtained from (3.9), by using $\hat{\vec{S}}^2 = S(S+1)$ and $\hat{\vec{L}}^2 = L(L+1)$.

N	S	L	$E_{int}[N]$
3	3/2	0	$-7.5J$
2	1	1	$0.5U - 6.5J$
1	1/2	1	$2U - 8.5J$
0	0	0	$4.5U - 13.5J$

Table 3.1 Ground state configurations for the interaction part of the three orbital Kanamori model (3.9) (ignoring the non interacting, last term), labeled by the electron occupation N, the spin moment S and the orbital moment L. A chemical potential shift was added to enforce particle-hole symmetry $E_{int}[3+\Delta N] = E_{int}[3-\Delta N]$.

If we start from a system at half filling, taking one electron from one site to another will create two new atomic configurations with 1) $N = 2$, $S = 1$, $L = 1$ and 2) $N = 4$, $S = 1$, $L = 1$. Using Tab. 3.1, we can compare the energy of the initial state with the final one

$$\Delta_{at}[N = 3] \equiv E_{int}[N = 2] + E_{int}[N = 4] - 2E_{int}[N = 3] = U + 2J \,, \tag{3.34}$$

which tells us, that the energy difference is raised by the Hund's exchange coupling. Considering (3.31), one can deduce that the energy gap at half filling is $\Delta_{at}[N = M] = U + (M-1)J$ for a M orbital system.
If, on the other hand, we start out with a system at $N = 2$ or $N = 1$ (or the corresponding particle-hole symmetric fillings), we get

$$\Delta_{at}[N \neq 3] = U - 3J \,, \tag{3.35}$$

(this result is independent of the number of orbitals M). While J increases the energy cost corresponding to the charge transfer for systems at half filling, it decreases the energy difference at other fillings. These simple considerations turn out to be rather powerful to predict the influence of Hund's coupling on systems at different fillings.

Fig. 3.4 shows the influence of Hund's coupling on the quasiparticle weight Z for a three-orbital system with Kanamori-type interaction (3.9) for different commensurate fillings within *dynamical mean-field theory*, by de' Medici et al. . For large values of J, the results agree with the atomic limit considerations outlined before. At half filling $N = 3$, the critical value of U decreases upon increasing J; while increasing J at other commensurate fillings causes an increase in the critical interaction. This result on its own is rather interesting, since it provides a qualitative explanation of what is seen in the "map of perovskites" by Fujimori[1], Fig. 3.2. The "map" shows a decrease in the critical U

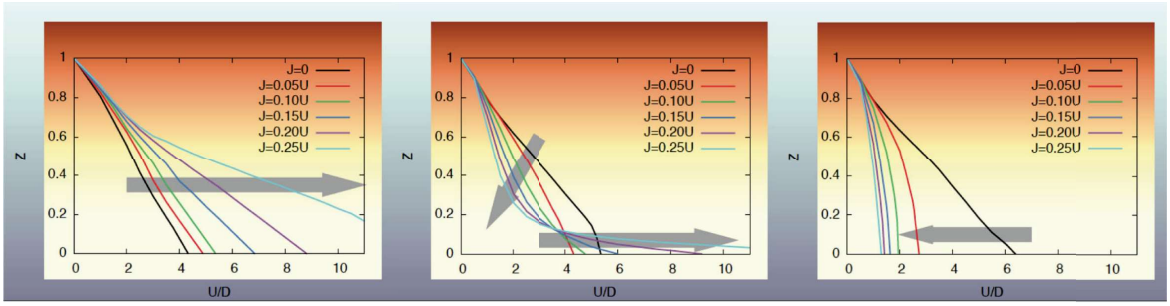

(a) $N = 1$ (b) $N = 2$ (c) $N = 3$

Fig. 3.4 Influence of Hund's exchange coupling on the quasiparticle renormalization Z as a function of U, by de' Medici et al. [39]. Panels (a), (b) and (c) show the results for $N = 1$, $N = 2$ and $N = 3$, respectively. The arrows indicate the influence of increasing J.

upon increasing the atomic number when going from d^1 ($SrVO_3$) to d^3 compounds ($SrMnO_3$). Such a behavior would be in contradiction with the predictions from a t_{2g} model with $J = 0$, where the critical U is supposed to be highest in the half filled case $N = 3$. Considering however the significant value of $J_{avg}/U_{avg} \approx 0.38$ (which follows from Eqs. (3.32), (3.33)), these findings are in perfect agreement with the theoretical expectations.

So far, we ignored the peculiar behavior the quasiparticle renormalization in the middle panel (b) for $N = 2$. Here, Hund's coupling seems to have two effects that oppose each other. For small to moderate values of the Hubbard interaction U (as compared to the critical value for $J = 0$), increasing J causes a significant increase in correlations, seen as a decrease in Z. On the other hand, increasing J above a certain value strongly enhances the critical U, as compared to the case without Hund's coupling. This can be explained by the fact that for a M-orbital system with filling $2M - 1 > N > 1$, Hund's coupling generally lowers the degeneracy of the atomic ground state. A lower degeneracy causes a decrease of the kinetic energy and a suppression of the coherence scale to lower energies.

The last point proved the obvious fact that a mere consideration of the multiplet structure is not sufficient to explain all the effects induced by Hund's exchange coupling. Indeed, "turning on" Hund's coupling has some major influences on the low energy physics of the systems under consideration.

Even though our final interest lies in the description of lattice systems, many of these effects can already be found in the corresponding quantum impurity models. For this reason, the next section will be dedicated to a brief discussion of these models in the multi-orbital case.

3.4 Physics of the impurity model

The main focus of this section considers the influence of enhanced degeneracy and Hund's coupling on the coherence of quantum impurity models. Before we discuss the case of multi-orbital models, let us start with a brief reminder on the one orbital Kondo problem.

3.4.1 One orbital Kondo physics

We already introduced the one orbital quantum impurity model in the previous chapter, in the context of DMFT. Historically, the model was proposed by Philip W. Anderson[3] to describe the formation of local moments in metals, a problem that had been studied by Friedel and Blandin[26]. These theoretical developments were motivated by experimental findings[31, 137], suggesting that it is the presence of magnetic moments, that causes the mysterious resistance minimum that was found when cooling gold, copper and other metals to low temperatures[38] (for an introduction with detailed historical information, see [33]).

The spin degenerate one orbital Anderson model describes an interacting quantum impurity in a sea of non-interacting bath sites

$$H = \sum_{k\sigma} \varepsilon_k b^\dagger_{k\sigma} b_{k\sigma} + \sum_{k\sigma} (V_k d^\dagger_\sigma b_{k\sigma} + h.c.) + \varepsilon^d n^d + U \left(n^d_\uparrow - \frac{1}{2}\right)\left(n^d_\downarrow - \frac{1}{2}\right) . \tag{3.36}$$

At first sight, there is no apparent connection to the physics of magnetic impurities. However, this changes when considering the case where $n^d = 1$ is the energetically favored occupation. In this case, we can apply a Schrieffer-Wolff[139] (for a detailed derivation, see Appendix B.1.1 and B.1.2) transformation to derive a low-energy Hamiltonian, in which fluctuations to the $n^d \in \{0,2\}$ high-energy states are considered in second order perturbation theory. This leads us to the famous Kondo model

$$H = \sum_{k\sigma} \varepsilon_k b^\dagger_{k\sigma} b_{k\sigma} + \sum_{k,k'} J_{k,k'} b^\dagger_{k\sigma} \vec{\sigma}_{\sigma\sigma'} b_{k'\sigma'} \cdot \vec{S}_d \ , \tag{3.37}$$

with $\vec{S}_d = \frac{1}{2} d^\dagger_\sigma \vec{\sigma}_{\sigma\sigma'} d_{\sigma'}$ (using the Einstein summation convention, $\vec{\sigma}_{\sigma\sigma'}$ being the vector of Pauli matrices, and

$$J_{k,k'} = V_k V^*_{k'} \left(\frac{1}{\varepsilon^d + U} - \frac{1}{\varepsilon^d} \right) \approx J_K \ , \tag{3.38}$$

where in the last step, we assumed that $V_k, V^*_{k'}$ are roughly constant. Historically, this model was first proposed by J. Kondo [90], and later rederived from the Anderson model by Schrieffer and Wolff[139].

The Kondo coupling J_K is an effective interaction scale, that is defined by the energy differences to the high energy states that were "integrated out". However, there's no reason to stop there. Upon lowering the temperature, thermal fluctuation will mainly occur in an ever smaller energy window around the Fermi surface. This means, that particle/hole excitations at the edges of the conduction band will become increasingly unlikely. For this reason, we may consider integrating out the states at the edges of the conduction band to derive a new, effective Hamiltonian. This Hamiltonian will be of the same form as (3.37), however with a renormalized coupling $J_K(D')$, which will depend on the

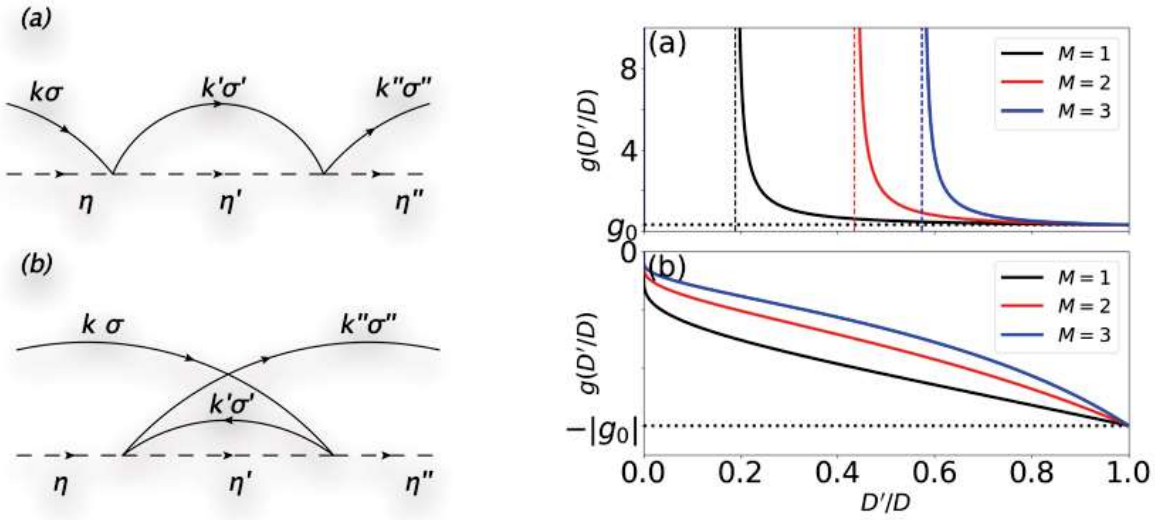

Fig. 3.5 Left panel: Second order diagrams contributing to the renormalization of the Kondo coupling. Right panel: Running coupling $g(D'/D)$ as function of the reduced bandwidth for different number M of orbitals, at half filling. The horizontal, dashed line marks the unrenormalized coupling g_0, while horizontal dashed lines mark the corresponding Kondo scales $T_K/D = \exp\{-1/2Mg_0\}$.

new, effective bandwidth D'

$$H = \sum_{|\varepsilon_k|<D',\sigma} \varepsilon_k b^\dagger_{k\sigma} b_{k\sigma} + \sum_{|\varepsilon_k|,|\varepsilon_{k'}|<D'} J_K(D') b^\dagger_{k\sigma} \vec{\sigma}_{\sigma\sigma'} b_{k'\sigma'} \cdot \vec{S}_d \,. \tag{3.39}$$

In the simplest case, known as the *poor man's scaling* approach[5, 169], the bandwidth is not renormalized back to its original width. Nevertheless, it gives valuable qualitative insights. The evolution of the renormalized coupling can be evaluated by calculating $\partial J_K(D')/\partial D'$ upon reducing the bandwidth by an infinitesimal energy $D' = D - \delta D$. This leads to a differential equation for the coupling, which, up to second order in perturbation theory (the corresponding diagrams are shown in the left panel of Fig. 3.5), reads

$$\frac{\partial g}{\partial \ln D'} = \beta(g) = -2g^2 + \mathscr{O}(g^3) \,. \tag{3.40}$$

Here, we introduced the beta function $\beta(g)$, depending on $g = \rho J_K$, with the density of states ρ (which, for the sake of simplicity, is set constant).

Solving this differential equation results in

$$g(D') = \frac{1}{2\ln\left(\frac{D'}{D}\right) + g_0^{-1}} \,, \tag{3.41}$$

with $g_0 = \rho J_K(D' = D)$. Now this equation is rather interesting. Apparently, the flow of the renormalized coupling depends on its initial sign. For ferromagnetic coupling $g_0 < 0$, reducing the bandwidth results in a reduction of the absolute value of $g(D')$ (as shown in the lower left panel (b) of

Fig. 3.5), such that in the limit $D'/D \to 0$, the impurity spin is decoupled from the bath.
For anti-ferromagnetic $g_0 > 0$, however, reducing the bandwidth increases the strength of the coupling, which eventually diverges (upper left panel (a) of Fig. 3.5) The scale at which the perturbative approximation is supposed to break down is known as the Kondo temperature; in case of the one orbital system it is

$$\frac{T_K}{D} = e^{-\frac{1}{2g_0}} = e^{-\frac{1}{2\rho J_K}} \ . \tag{3.42}$$

Even though these results are only obtained from second order perturbation theory, it has been shown – using the numerical renormalization group (NRG) technique[166] – that the coupling constant indeed diverges at low energy scales. The magnetic moment of the impurity is then screened by the conduction electrons, forming a non magnetic singlet. This means, that scattering of quasi-particles with energies around the Fermi level is suppressed, and the system undergoes a transition from incoherent to coherent.
The Kondo effect is an example of *asymptotic freedom*[61, 133]; a term that has been coined in the context of quantum chromodynamics. There, it is responsible for the reduction of the coupling between quarks and gluons at high energy scales, rendering perturbative approximations possible.

3.4.2 Multi-orbital Kondo physics

We now turn to the Kondo physics of multi-orbital systems. For this purpose, we consider a model with an interaction of the form (3.31), such that we can tune the Hund's coupling by changing $J_{mm'}$. Such models have been extensively studied in the literature[34, 126, 167, 123, 125, 124, 77]; the following discussion is supposed to give an overview over the most important results.

No Hund's Coupling, $J = 0$

In the case $J_{mm'} = 0$, we are dealing with the $SU(2M)$ symmetric M-orbital Hubbard model. The Kondo physics of this model was first studied by Coqblin and Schrieffer[34], in the context of investigating exchange interactions in alloys with cerium impurities. Performing a Schrieffer-Wolff transformation on the M-orbital system leads to the Coqblin-Schrieffer model

$$H = \sum_{k\alpha} \varepsilon_{k\alpha} b^\dagger_{k\alpha} b_{k\alpha} + J_K \sum_{k,k'} \sum_{\alpha\beta} b^\dagger_{k\alpha} b_{k'\beta} S_{\alpha\beta} \ . \tag{3.43}$$

As in [59], we used composite indices $\alpha = \{m, \sigma\}$ to improve readability, and $S_{\alpha\beta} \sim |\alpha\rangle\langle\beta|$. The interaction part of the Coqblin-Schrieffer model considers processes changing the spin- and orbital configuration of the impurity, leaving the overall occupation constant.
When calculating the beta function for a scaling analysis of the Kondo coupling, one can use the same diagrams as in the one-orbital case. In the M-orbital case, however, one has to consider additional

scattering channels. Considering the case of a half-filled system, the beta function reads

$$\frac{\partial g}{\partial \ln D'} = \beta(g) = -2Mg^2 + \mathscr{O}(g^3) \,, \tag{3.44}$$

which leads to an enhancement of the Kondo temperature

$$\frac{T_K}{D} = e^{-\frac{1}{2Mg_0}} = e^{-\frac{1}{2M\rho J_K}} \,. \tag{3.45}$$

This scenario is shown in the right panel of Fig. 3.5, which compares the flow of the couplings for three different numbers of orbitals $M \in \{1,2,3\}$. In case of anti-ferromagnetic g_0, the position of the critical $D' = T_K$ is clearly shifted to higher energies, as M is increased (upper right panel (a) of Fig. 3.5). This implies that in multi-orbital models, magnetic moments are already screened at higher temperatures, which means that coherence is generally increased, as compared to the one-orbital model.

With Hund's coupling, $J > 0$

We now turn to the case with finite, positive Hund's coupling (the case of negative J will not be considered here). This case was first investigated in detail by Okada and Yosida [126], who found that a positive Hund's exchange coupling generally decreases the coherence scale. This can be understood as follows by considering the following model

$$H = \sum_{km\sigma} \varepsilon_{km\sigma} b^\dagger_{km\sigma} b_{km\sigma} - J\left(\sum_m \vec{S}_m\right)^2 + J_K \sum_m b^\dagger_{km\sigma} \vec{\sigma}_{\sigma\sigma'} b_{k'm\sigma'} \cdot \vec{S}_m \,, \tag{3.46}$$

which is an adaption of the Coqblin-Schrieffer model, incorporating Hund's coupling (note that, in contrast to (3.43), the interaction part of this Hamiltonian conserves the individual orbital occupations; detailed investigations on this model can be found in [123]). Considering the case $J \to \infty$, the second term in (3.46) acts like a projector, eliminating all configurations that do not maximize the spin, characterized by $S = M/2$ for a M-orbital system. For infinite J the individual spins will be "locked" in the same direction[125], and we can replace

$$\vec{S}_m \to \frac{1}{M}\sum_m \vec{S}_m = \frac{1}{M}\vec{S}_{tot} \,, \tag{3.47}$$

such that

$$H_{J\to\infty} = \sum_{km\sigma} \varepsilon_{km\sigma} b^\dagger_{km\sigma} b_{km\sigma} + \frac{J_K}{M}\sum_m b^\dagger_{km\sigma} \vec{\sigma}_{\sigma\sigma'} b_{k'm\sigma'} \cdot \vec{S}_{tot} \,. \tag{3.48}$$

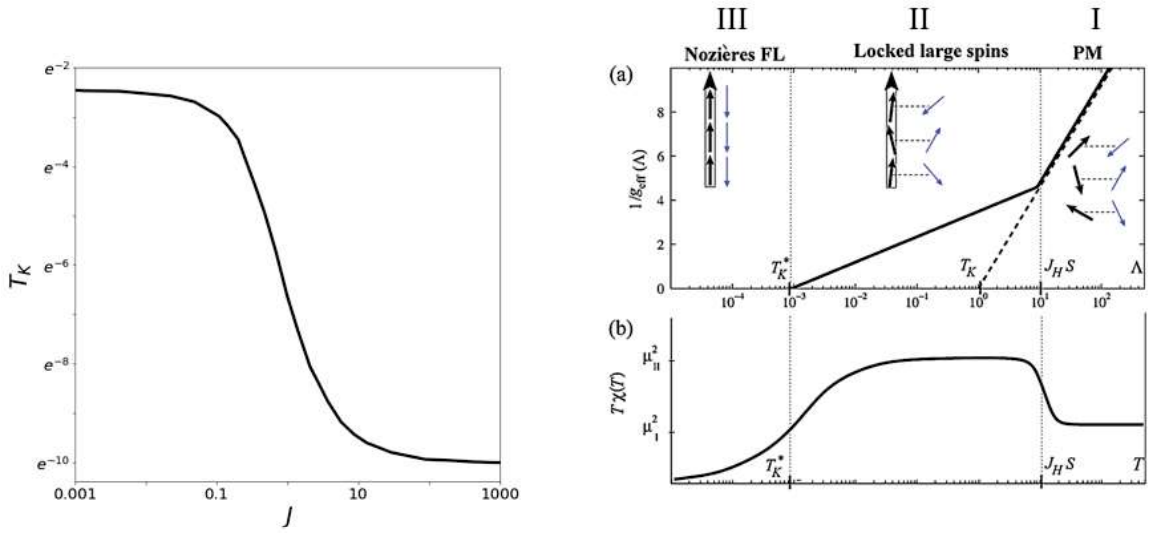

Fig. 3.6 Left panel: Kondo temperature as a function of Hund's exchange coupling for a two-orbital model (data extracted from Ref. [167], Fig. 3). Right panel: (a) Schematics showing the running coupling $g_{eff}(\Lambda) = J(\Lambda)\rho M_{eff}$ (in our notation, this corresponds to $g(\Delta') = J(\Delta')\rho M_{eff}$) as a function of the energy scale. In the region I, $M_{eff} = 1$ and the system is paramagnetic. In region II, the impurity spins align due to Hund's coupling, forming a large effective spin moment S. The boundary between region I and II is defined by the Hund's coupling times the effective spin. Finally in region III, the big, composite spin is screened by the conduction elections. (b) Depicts the evolution of the magnetic susceptibility, showing an enhancement in region II and screening in region III. The figure was taken from [124].

This means, that we are dealing with an effective Kondo system with a large local spin, and a reduced Kondo coupling J_K/M. Consequently, the Kondo Temperature is suppressed

$$T_K = e^{-\frac{M}{2g_0}} = e^{-\frac{M}{2\rho J_K}} \,. \tag{3.49}$$

It is interesting to compare the values of Kondo temperatures of the multi-orbital models with and without Hund's coupling to $T_K^{M=1}$ of the one-band model

$$\frac{T_K^{M,J=\infty}}{D} = e^{-\frac{M}{2\rho J_K}} < \frac{T_K^{M=1}}{D} = e^{-\frac{1}{2\rho J_K}} < \frac{T_K^{M,J=0}}{D} = e^{-\frac{1}{2M\rho J_K}} \,. \tag{3.50}$$

The left panel of Fig. 3.6 shows the evolution of the Kondo temperature of a two-orbital model within the poor man's coupling approach, as a function of Hund's coupling (the data has been extracted from Ref. [167], Fig. 3). The ratio of the limiting values is $\ln T_K^{M=2,J=0}/\ln T_K^{M=2,J=\infty} = 4 = 2^2$, confirming the prediction $T_K^{M,J=\infty}/D = (T_K^{M,J=0}/D)^{M^2}$ from the considerations presented before.
The right panel of Fig. 3.6 shows (a) the running coupling and (b) the magnetic susceptibility of the M-orbital model (3.46) as obtained from a two-loop renormalization group (RG) calculation. The calculation was performed in two different regimes. In the first one, labeled as "I", the bare

couplings J, J_K were taken according to (3.46), while in region II and III, the reduced bare coupling $J_K^* = J_K/M$ was considered in the renormalization group RG equations. The locked spin scenario has some interesting consequences on the magnetic susceptibility, as can be seen in the lower right panel (b) of Fig. 3.6. When changing from the paramagnetic to the "locked large spins" phase, the susceptibility is significantly increased, before it is finally screened by the conduction electrons at low temperatures.

3.4.3 Spin-orbit separation

While the "extended Kondo model" considered in the previous section 3.4.2 takes into account the effect of Hund's coupling, it does not correspond to the Hamiltonian that one would get upon performing a Schrieffer-Wolff transformation on a Kanamori-type model (3.9). As the Coqblin-Schrieffer model (3.43), such a model must contain orbital-changing terms $b^\dagger_{m'\sigma'} c_{m'\sigma'} c^\dagger_{m\sigma} b_{m\sigma}$ with $m \neq m'$, and will thus be more complex then (3.46).

Such a model was derived by Horvat et al. (see [77]), who performed a Schrieffer-Wolff transformation on a Hamiltonian with Kanamori interaction (3.9) (with and without the angular momentum term $\sim \hat{\vec{L}}^2$). For a M-orbital system with the full interaction (3.9), their resulting model can be cast in the form

$$\begin{aligned} H = {} & J_p \hat{N} + J_s \hat{\vec{S}} \cdot \hat{\vec{s}} + J_l \hat{\vec{L}} \cdot \hat{\vec{l}} + J_q \hat{Q}^\alpha \hat{q}^\alpha \\ & + J_{ls} \left(\hat{\vec{L}} \otimes \hat{\vec{S}} \right) \cdot \left(\hat{\vec{l}} \otimes \hat{\vec{s}} \right) + J_{qs} \left(\hat{Q}^\alpha \otimes \hat{\vec{S}} \right) \cdot \left(\hat{q}^\alpha \otimes \hat{\vec{s}} \right) , \end{aligned} \tag{3.51}$$

where we used capital letters for the impurity and lower letters for the bath degrees of freedom. Furthermore, we employed the notation $\hat{N} = \sum_{m\sigma} c^\dagger_{m\sigma} c_{m\sigma}$, $\hat{\vec{S}} = \frac{1}{2} \sum_m c^\dagger_{m\sigma} \vec{\sigma}_{\sigma\sigma'} c_{m\sigma'}$, $\hat{\vec{L}} = \sum_\sigma c^\dagger_{m\sigma} \vec{L}_{mm'} c_{m'\sigma}$ and $\hat{Q}^{\alpha=bc} = \frac{1}{2} \left(L^b_{im} L^c_{mj} + L^c_{im} L^b_{mj} \right) - \frac{2}{3} \delta_{bc} \delta_{ij}$, with $\vec{\sigma}$ the vector of the Pauli matrices and $\vec{L}_{mm'}$ the angular momentum matrices[2]. As before, the bare Kondo couplings J_p, J_s, J_l, J_q, J_{ls}, J_{qs} are defined by the energy differences between the states with N and $N \pm 1$ electrons; for an explicit form, we refer to [77].

Analyzing the flow of the model parameters (3.51) with the *poor man's scaling* approach, reveals that the spin- and orbital couplings change differently upon decreasing the bandwidth. At lowest

[2] For M=3, they are spin-1 matrices and read

$$L^x = \frac{1}{\sqrt{2}} \begin{bmatrix} 0 & 1 & 0 \\ 1 & 0 & 1 \\ 0 & 1 & 0 \end{bmatrix} , L^y = \frac{i}{\sqrt{2}} \begin{bmatrix} 0 & -1 & 0 \\ 1 & 0 & -1 \\ 0 & 1 & 0 \end{bmatrix} , L^z = \begin{bmatrix} 1 & 0 & 0 \\ 0 & 0 & 0 \\ 0 & 0 & -1 \end{bmatrix} . \tag{3.52}$$

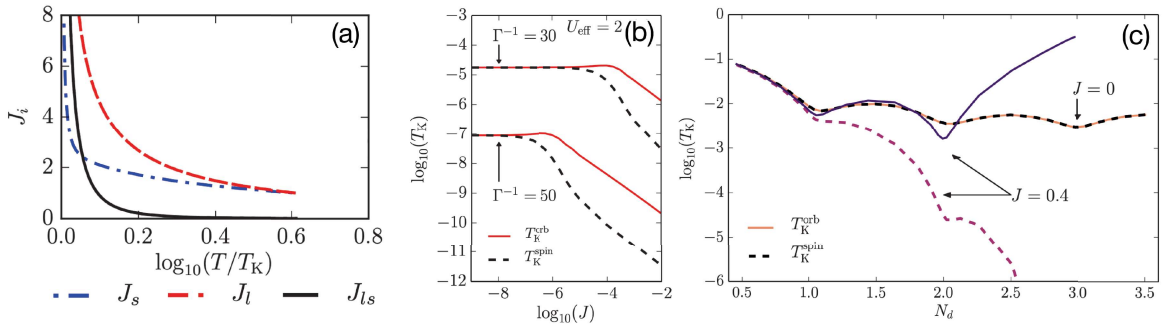

Fig. 3.7 Kondo physics of the 3-orbital Kanamori model, figures adopted from [77]. Panel (a): Results from *poor man's scaling* analysis, showing the flow of the spin-, orbit-, and "spin-orbit" couplings J_s, J_l, J_{ls}. The bare couplings were chosen as $J_s = J_l = J_q = 1$ and $J_{ls} = J_{qs} = J_s/100$. Panels (b) and (c): Results from an numerical renormalization group analysis. (b) shows the Kondo temperatures of the spin- and orbital d.o.f. as a function of the Hund's coupling J, for two different impurity-bath hybridization strengths Γ. (c) shows the evolution of the spin- and orbitals Kondo temperatures as a function of the impurity filling N_d, for two different values of J.

order, the scaling functions $\partial J_i/\partial \ln(D') = \beta_i$ for J_s and J_l read [77]

$$\beta_s = -\frac{1}{9}\left(3J_{ls}^2 + 5J_{qs}^2 + 9J_s^2\right) \tag{3.53}$$

$$\beta_l = -\frac{1}{4}\left(J_l^2 + 2J_{ls}^2 + 5(J_q^2 + 2J_{qs}^2)\right) \tag{3.54}$$

$$\beta_q = -\frac{3}{2}\left(J_l J_q + 2J_{ls}J_{qs}\right) . \tag{3.55}$$

When setting $J_q = J_l$ and the cross-terms to zero $J_{ls} = J_{qs} = 0$, the flow equations decouple and one can simply read off the different Kondo scales. In this case, $\beta_l/\beta_s = (3/2)J_l^2/J_s^2$, which displays the fact that J_l scales faster to high couplings (without even considering that $J_l > J_s$).

Considering the corresponding prefactors, this also holds true for finite J_{ls}, J_{qs}; as can be seen in panel (a) of Fig. 3.7, which shows the scaling of J_l, J_s and J_{ls} starting from the bare couplings $J_l = J_s = J_q = 1$ and $J_{ls} = J_{qs} = 1/100$. The results illustrate the slower running of the spin coupling J_s.

The results from the poor man's scaling analysis were confirmed by calculations using the numerical renormalization group (NRG) method[77]. Panel (b) and (c) show results, confirming the decoupling of the Kondo temperatures for the spin and orbital degrees of freedom for finite Hund's exchange coupling J. Most interestingly, the effect gets stronger upon approaching half filling, as can be seen in panel (c) in Fig. 3.7.

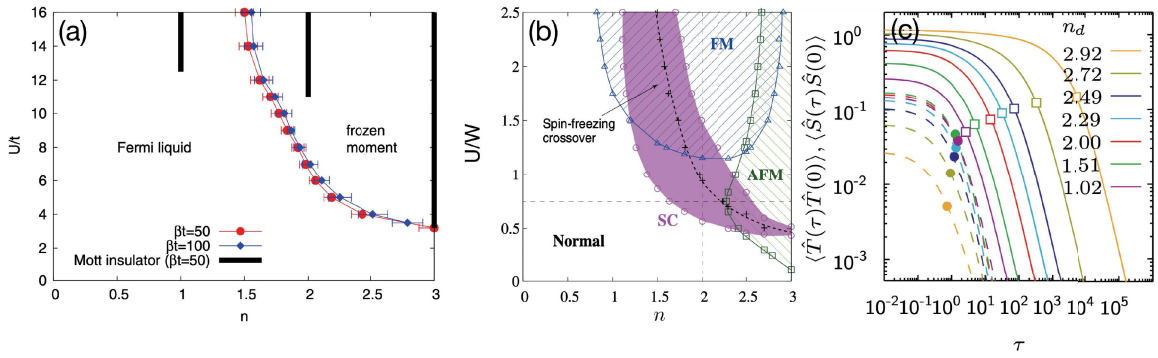

Fig. 3.8 Facettes of spin-freezing. (a) Occurence of the spin freezing phenomenon in the interaction-filling plane from [160]; for the three orbital model with spin rotational SU(2) symmetry ($\alpha = 1$). Black bars mark the Mott-insulating phase. (b) Interaction-filling phase diagram of the ferromagnetic (FM), anti-ferromagnetic (AFM) and superconducting phases from [78]; for the three orbital model with Ising spin anisotropy ($\alpha = 0$), marking the position of the spin-freezing crossover. Interaction in units of $W = 4t$, the inverse temperature is $\beta t = 100$. (c) Long time spin-spin $\left\langle \hat{S}(\tau)\hat{S}(0)\right\rangle$ (solid lines) and orbital-orbital $\left\langle \hat{T}(\tau)\hat{T}(0)\right\rangle$ (dashed lines) correlations from [147]; demonstrating that the spin-spin correlations do eventually decay. $U = 5$, $J = 1$ and $T = 0$.

3.5 Physics on the lattice

Beyond quantum impurity models, Hund's exchange coupling was found to have important consequences on the physics of multi-orbital lattice systems. Here, the method of choice is dynamical mean-field theory (DMFT) [57] (see Chapter 1.4), which treats the low-energy Kondo physics (described in the previous sections) and high-energy charge fluctuations on an equal footing. Some results from DMFT were already presented in Fig. 3.4, which demonstrates the ambivalent effect of Hund's exchange coupling on the quasiparticle renormalization. Even earlier, Werner et al. [160] discovered that Hund's coupling induces a range of interesting phenomena, like increased decoherence and non-Fermi liquid power-law behavior of the self-energies. In particular, they discovered a regime where spin-spin correlations do not decay – the "spin-freezing phenomenon", which we shall review in the following.

3.5.1 The spin-freezing phenomenon

Non-Fermi liquid power-law behavior of the self-energies, induced by Hund's coupling, was originally discussed in the context of the three-orbital Kanamori model [160] (ref. [159] then identified such behavior in realistic five-orbital calculations for iron pnictide compounds). There, it was observed to appear in a regime where spin-spin correlations $\langle S_z(0)S_z(\tau)\rangle$, with $S_z = \frac{1}{2}\sum_m (n_{m\uparrow} - n_{m\downarrow})$, do not decay at long times, a phenomenon, for which the notion of *spin-freezing* was coined.

The spin-freezing regime is particularly interesting, since it has been argued that it might explain the peculiar $\sigma_1 \sim \omega^{-1/2}$ behavior of the optical conductivity in $SrRuO_3$ and $CaRuO_3$ [91, 43, 103]. In models with spin anisotropy (Hamiltonian (4.2) with $\alpha < 1$), the spin-freezing phenomenon was found

to be related to emerging superconductivity [78] and furthermore suggested in [161] as a "universal mechanism underlying the physics of" various unconventional superconductors, such as cuprates, pnictates, ruthenates etc. Specifically, it is the strongly and slowly fluctuating magnetic moments at the spin-freezing crossover that could provide a pairing mechanism in these compounds.
Fig. 3.8 (a) shows the spin-freezing regime in the interaction-filling plane for the three-band model with spin-rotational symmetry $\alpha = 1$. The occurrence of a spin-triplet superconducting phase is closely related to the spin-freezing crossover, as can be seen in Fig. 3.8 (b). However, the spin-triplet pairing relies on an Ising spin anisotropy $\alpha < 1$.

More recently the spin-freezing effect was reexamined with the numerical renormalization group (NRG) method [148, 147], revealing that the spin-spin correlations are not actually frozen, but rather decay at exponentially long times, as is shown in Fig. 3.8 (c). Moreover, it was argued that the spin-freezing phenomenon, as the whole non Fermi liquid regime, are just different aspects of the spin-orbit separation, which we already discussed in the context of quantum impurity models (see Sec. 3.4.3). In this sense, spin-freezing appears in the intermediate regime $T_K^{spin} < T, |\omega| < T_K^{orb}$, where orbital degrees of freedom are screened to form a large local spin moment, that is only poorly screened by the conduction electrons.

Chapter 4

The Metal-Insulator Transition with Hund's Coupling

In this chapter, we present new insights on the effect of Hund's exchange coupling in the vicinity of the doping-driven metal-insulator transition, using *dynamical mean-field theory* (DMFT)[57], that we have obtained in this thesis. This project was done in collaboration with Luca de' Medici.

4.1 The model

We consider the M-orbital Hubbard model of the form

$$H = H_0 + H_{int} \ , \tag{4.1}$$

with

$$H_0 = -\sum_{ij,m\sigma} t_{ij} c^{\dagger}_{im\sigma} c_{jm\sigma} + \sum_{im\sigma} (\varepsilon_m - \mu) c^{\dagger}_{im\sigma} c_{im\sigma} + H_{int} \ , \tag{4.2}$$

$$\begin{aligned} H_{int} = {} & U \sum_{m} n_{m,\uparrow} n_{m,\downarrow} + U' \sum_{m>m'\sigma} n_{m\sigma} n_{m'\bar{\sigma}} + (U' - J) \sum_{m>m'\sigma} n_{m\sigma} n_{m'\sigma} \\ & + \alpha \left[J \sum_{m \neq m'} c^{\dagger}_{m\uparrow} c^{\dagger}_{m\downarrow} c_{m'\downarrow} c_{m'\uparrow} - J \sum_{m \neq m'} c^{\dagger}_{m\uparrow} c_{m\downarrow} c^{\dagger}_{m'\downarrow} c_{m'\uparrow} \right] \ , \end{aligned} \tag{4.3}$$

where $m \in \{1 \dots M\}$. We introduced a parameter α, which allows us to choose whether to consider ($\alpha = 1$) or discard ($\alpha = 0$) the effect of the spin-flip and pair-hopping terms.

Such models have been the subject of numerous studies, both on the model level[39, 49, 135, 148, 147, 160] and considering realistic materials[159, 71, Yin et al.]. In Sec. 3.3, we already discussed the influence of Hund's coupling on the Mott transition at commensurate fillings, by reviewing the results from [39]. In the following, we shall consider a different path in parameters space by doping such systems away from commensurate fillings.

For finite two-body interactions, Hamiltonian (4.2) cannot be diagonalized exactly and approximations have to be considered. Our method of choice is the DMFT (introduced Chapter 1.4), which keeps the information on the lattice and, locally, on the high-energy multiplet structure. This permits us to study the electronic properties from the itinerant to the localized regime, including the metal-insulator transition and correponding coexistence regions.

Some technical remarks. The single site quantum impurity model corresponding to the DMFT treatment is solved using continuous time quantum Monte Carlo (QMC) methods[64]. More specifically, we considered a hybridization expansion algorithm[162, 64], expanding the impurity action around the atomic limit. The calculations were performed using the TRIQS library[129], as well as an adaption of a code provided by Yusuke Nomura from University of Tokyo. Observables were usually obtained from 1.6×10^8 QMC measurements distributed on 40 cores.

In the following, we will focus on the physics of three- and two-orbital models, considering their relevance for t_{2g} and e_g systems. We are interested in the case of finite, positive Hund's couplings $J > 0$. Assuming rotational symmetry, we set $U' = U - 2J$. Throughout this chapter, the chemical potential will defined relative to the particle-hole point, such that $\mu = 0$ corresponds to the system at half filling.

The models are studied on the Bethe lattice with infinite coordination number, corresponding to a semi-circular density of states

$$\mathscr{D}(\omega) = \theta(2t - |\omega|)\frac{\sqrt{4t^2 - \omega^2}}{2\pi t^2} \,. \tag{4.4}$$

For all calculations presented in the following discussion, the hopping was set to $t = 1$; all other parameters are expressed in units of t.

4.2 Results

4.2.1 The phase diagram

We start by considering the most simple case of a two-orbital Hubbard model with density-density interactions only ($\alpha = 0$). The exhaustive studies that we performed on this system allow us to draw a phase diagram, which later on can be used for guidance in parameter space. Furthermore, it is insightful to compare such a phase diagram to the one obtained for the one-orbital model, which can be found in the literature[163].

Using the hopping amplitude t as the unit of energy, the one orbital Hubbard model can be parametrized by only two scalar variables U/t and μ/t. Including temperature, this results in a three dimensional phase diagram, as it is sketched in Fig. 4.1 (a). For particle-hole symmetry $\mu = \mu_1 = U/2$ and at constant temperature, the figure shows a metallic phase (marked as "M"), undergoing a first order phase transition to an insulator upon increasing the interaction strength U. The position of the first-order phase transition is marked by a red line; however if we were to increase U starting from a

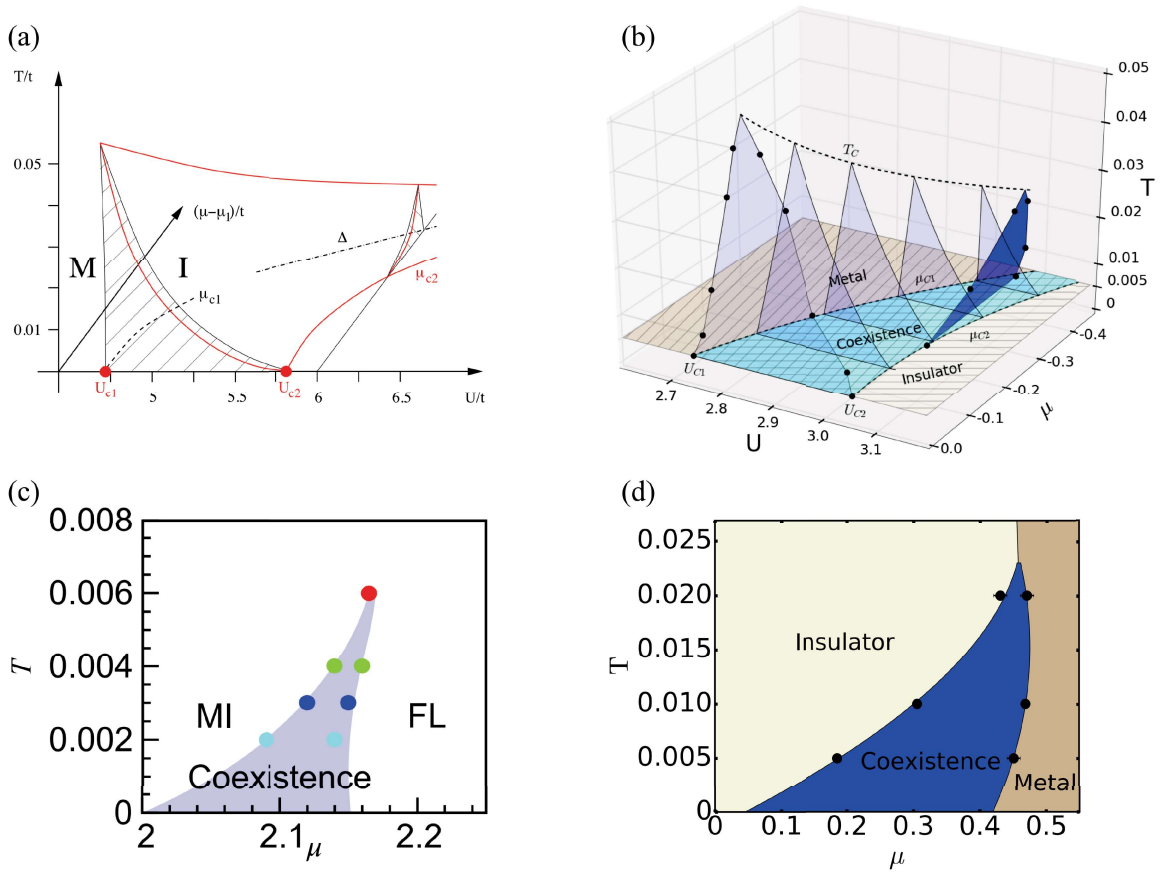

Fig. 4.1 (a) Sketch of the phase diagram of the one-orbital Hubbard model within single-site DMFT, from [163]. Thick, red, lines indicate the surface spanned by the first order phase transition; thin, black lines delimit the coexistence region.(b) Phase diagram of the two-orbital Hubbard model with density-density interactins $\alpha = 0$ and $J = 0.25U$. Black dots correspond to results from calculations, light-blue triangles schematically illustrate cuts through the coexistence region. (c) Coexistence region of the one-orbital Hubbard model in the (T, μ)-plane, at constant $U = 3.2$, from [156] (supplementary materials). Colored dots mark the calculated positions of the spinoidals. (d) Coexistence region of the two-orbital Hubbard model in the (T, μ)-plane, at constant $U = 3.06$. Black dots mark the calculated positions of the spinoidals.

metallic system, we would be able to stabilize a metallic solution up to the spinoidal U_{c2}. Conversely, if we started in the insulating phase (marked as "I"), such a solution could be stabilized down to the spinoidal U_{c1}. These spinoidals U_{c1} and U_{c2} span a coexistence region, in which both metallic and insulating solutions can be stabilized. As we shall see in the case of multi-orbital models, this causes many observables to undergo a hysteresis upon successively crossing the coexistence region from one side and then back from the other side. The coexistence region gets narrower upon increasing the temperature, until it vanishes at the critical temperature T_C. Away from particle-hole symmetric chemical potential $\mu = 0$ (note that the convention for μ in Fig. 4.1 (a) is different from the one used here), the spinoidals are shifted to stronger interactions and the coexistence region is narrowed.

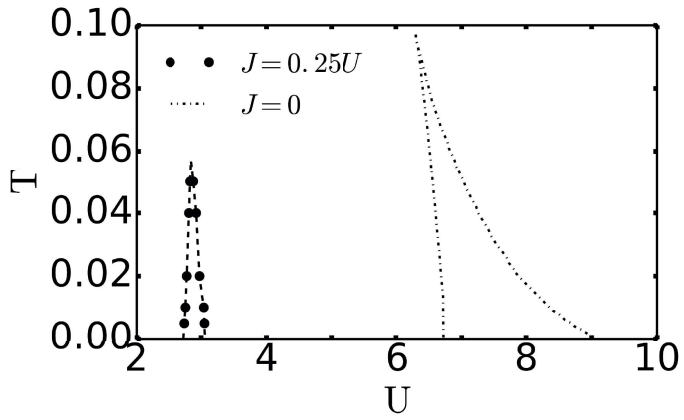

Fig. 4.2 Coexistence regions of the two-orbital Hubbard models with $J = 0$ (from [88]) and $J = 0.25U$.

The phase-diagram Fig. 4.1 (a) of the one-band model can be compared to panel (b) of the same figure, showing the results for the two-band Hubbard model with density-density interactions $\alpha = 0$ and Hund's exchange coupling $J = 0.25U$. As for the one-orbital model, we find a first-order metal-insulator transition with an extended coexistence region. The shape of the coexistence region in the particle-hole symmetric plane is different from the one-band case, however consistent with similar calculations including Hund's coupling[88] (and slightly reminiscent of the result obtained from cluster DMFT calculations for the 1-orbital Hubbard model; see [130]). Comparing however the cuts in the (T, μ)-planes Fig. 4.1 (c) and (d), the coexistence regions look rather similar.

A difference between panels (a) and (b) is the interaction strength, at which the phase transition occurs. For the model with Hund's coupling, the transition occurs at much lower values of U, a consequence of the effect that the exchange coupling has on the multiplet structure (see Sec. 3.3). This difference becomes even more pronounced when comparing the results to the two-orbital model with $J = 0$, as presented in Fig. 4.2. The model without Hund's coupling has $SU(4)$ symmetry, and enhanced-orbital fluctuations cause the Mott transition to occur at stronger Hubbard interaction, as compared to the model with Hund's coupling (as well as the one-band model). Hund's coupling quenches these orbital fluctuations, shifting the phase boundary in the opposite direction. Another remarkable difference considers the critical temperatures $T_c(J = 0) > T_c(J > 0)$, which is related to the different coherence scales for models with and without Hund's coupling (see Sec. 3.4.2).

4.2.2 The doping-driven metal-insulator transition

We shall now focus on the doping-driven Mott transition. Fig. 4.3 shows the particle number as a function of the chemical potential, comparing the results obtained from the two-orbital Hubbard model with (a) and without (b) Hund's coupling. In both cases, $n(\mu)$ is plotted for several values of the interaction strength U, while the temperatures are fixed to $\beta = 100$ (a) and $\beta = 25$ (b). The initial hybridization functions $\Delta(\tau)$ for the DMFT cycles were taken from previous calculations. Dots connected by solid lines correspond to solutions obtained by following the solutions of the metallic

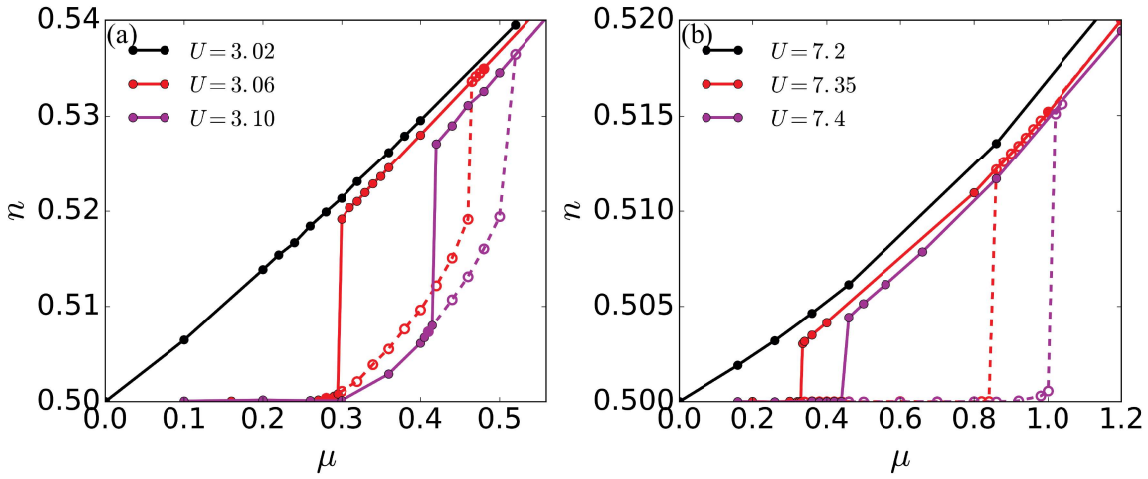

Fig. 4.3 Filling n per spin as a function of the chemical potential μ for the two-orbital model with $J = 0.25U$ (a) and without Hund's coupling $J = 0$ (b), for various Hubbard interactions U and $\beta = 100$ (a) and $\beta = 25$ (b). Solid(dashed) lines denote results starting from a metallic(insulating) initial configuration.

branch, starting in the highly doped regime and continuously reducing the chemical potential. Hollow dots connected by dashed lines, however, were obtained following the insulation branch upon doping away from the particle-hole symmetric point.

Comparing the results with and without J, reveals several differences. First of all, as for the results at constant $\mu = 0$, the energy range of the coexistence region is significantly reduced by Hund's coupling.

Much more remarkable, however, is the difference of the shape of the insulating branch. For $J = 0$, the insulating branch remains practically undoped in the entire range of chemical potentials up to μ_{C1}. Minor dopings close the spinoidal are also observed in the one-band model (see e.g. [92]) and are generally considered as a finite temperature effect. In the case of finite Hund's coupling, however, the insulating branches acquire notable dopings before the solutions become unstable. Results for the three-orbital case, exhibiting an even more remarkable extension of the insulating branches, can be found in the Appendix B.2.

In Fig. 4.4, we examine the nature of the two branches for $J = 0.25U$, by looking at the imaginary part of the self-energy and the Green's function at various values of μ, with $U = 3.06$, $\beta = 100$. For the insulating solutions obtained in the coexistence region ($\beta = 0.38$ and $\beta = 0.46$), one sees that the imaginary part of the Green's functions at the smallest Matsubara frequency $\mathrm{Im}[G(i\omega_0)]$ acquire rather large (negative) values. This implies a significant spectral weight at the Fermi level and suggests, that the "insulating" states are not insulating at all, but should rather be characterized as bad metals (however, we shall keep the notions "metallic" and "insulating" to differentiate between the two branches).

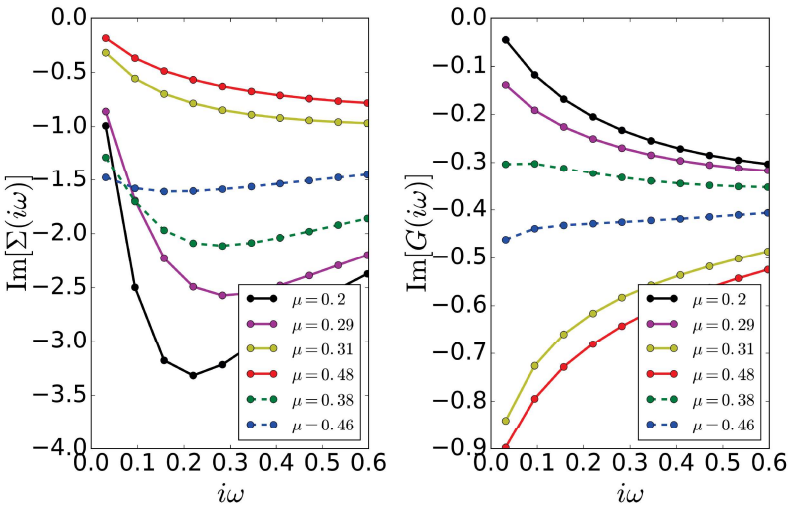

Fig. 4.4 Imaginary part of the self-energies (*left panel*) and Green's functions (*right panel*) for the two-orbital model with $U = 3.06$, $J = 0.25U$ and $\beta = 100$. Solid (dashed) lines denote simulations starting from a metallic (insulating) initial configuration.

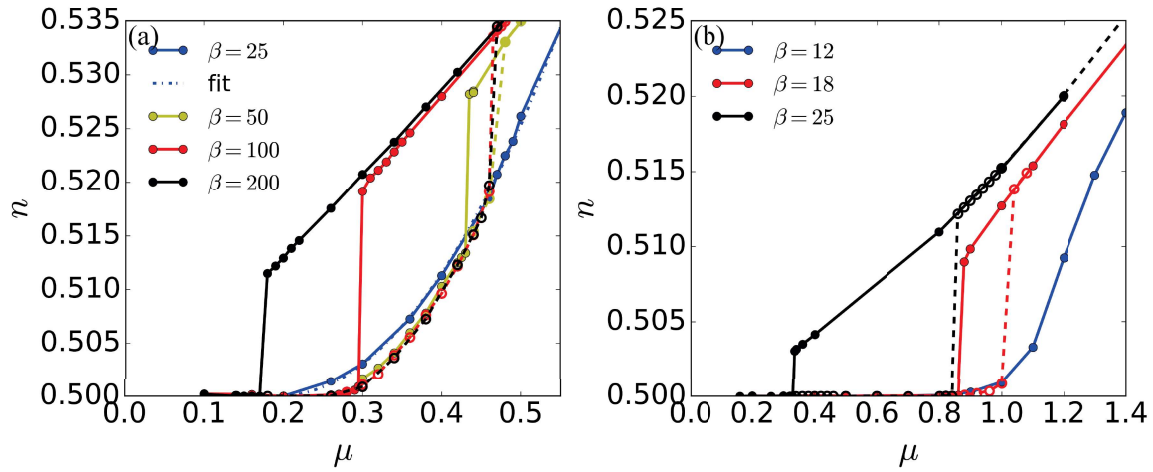

Fig. 4.5 *Left panel*: Filling n per spin as a function of μ in the two-orbital model, with $U = 3.06$ and $J = 0.25U$, for different temperatures $T = 1/\beta$. The curve for $\beta = 25$ has been fitted to $n = A(\mu - \mu_0)^2$, yielding $A = 0.27$, $\mu_0 = 0.19$. *Right panel*: Filling n per spin as a function of μ in the two-orbital model with $U = 7.35$, $J = 0$ for different temperatures $T = 1/\beta$. Solid (dashed) lines designate solutions starting from a metallic (insulating) configuration.

Table 4.1 Parameters obtained from fitting the filling to $n(\mu) = A(\mu - \mu_0)^2$. The last values for $\beta = \infty$ are extrapolated from a linear fit of $\mu_0(T)$ and $A(T)$.

β	μ_0	A
25	0.194	0.270
50	0.351	0.231
100	0.414	0.247
200	0.441	0.253
∞	0.460,	0.263

A similar behavior has been observed in[145, 146] for cluster models in two dimensions; however there, the reason for this was attributed to the effect of short-range spin correlations - considering that no similar behavior was observed in the single-site approximation[92, 163]

One question of immediate interest is how the insulating branch is affected by changes of the temperature. This question is being addressed in Fig. 4.5, which shows the filling as a function of the chemical potential for various temperatures, with (a) and without (b) Hund's coupling. Comparing the insulating branches for $J = 0$ with $\beta = 18$ and $\beta = 25$ in Fig. 4.5 (b), one indeed encounters a minor enhancement in doping at the higher temperature, when looking close to the spinoidals. On the other hand, looking at the case of finite J, the change in temperature does not seem to have any significant effect on the nature of the highly doped insulating branch. The position of the spinoidal μ_{C1} remains almost constant for $\beta \in \{50, 100, 200\}$, until the first order transition vanishes at $\beta = 25 < 1/T_c$.

It is interesting to compare the electronic compressibilities $\kappa = \partial n/\partial \mu$ on the metallic and the insulating branch. In the regime under investigation, the metallic branch for $J = 0.25U$ is characterized by an almost perfect linear relation of $n(\mu)$, corresponding to a constant compressibility. In the one-orbital Hubbard model, the compressibility is known to diverge when approaching the critical temperature T_c [92]. Indeed, fitting the slope of $n(\mu)$ in the vicinity of μ_{C2} reveals a slight increase in the compressibility; in order to investigate if this phenomenon can be reproduced in the two-band model, more temperatures between $\mu = 25$ and $\mu = 50$ would have to be examined.

On the insulating branch, the behavior is quite different. Here, as well as for the data points acquired at $\beta = 25$ (above T_c), $n(\mu)$ can be very well fitted to a quadratic function $n(\mu) \sim A(\mu - \mu_0)^2$, indicating a linear $\kappa(\mu)$. Such a property has also been observed in one-orbital models [163]. The fitted parameters are listed in Tab. 4.1 and presented in Fig. 4.6. They are well described by a linear fit in temperature, which in turn corresponds to a linear temperature dependence of the filling close to $T = 0$, different from the Fermi liquid relation $n(T) = n(T = 0) + \alpha T^2$. The non-Fermi liquid character of the solution in this regime could already be anticipated from the strong decoherence displayed by the self-energies in Fig. 4.4. However, the resolution of the Matsubara frequencies at $\beta = 100$ in this case was not high enough to allow for a more detailed analysis.

In the following, we discuss results obtained at $\beta = 200$, the lowest temperature under consideration.

The left panel of Fig. 4.7 shows the self-energies on the branch which is adiabatically connected to

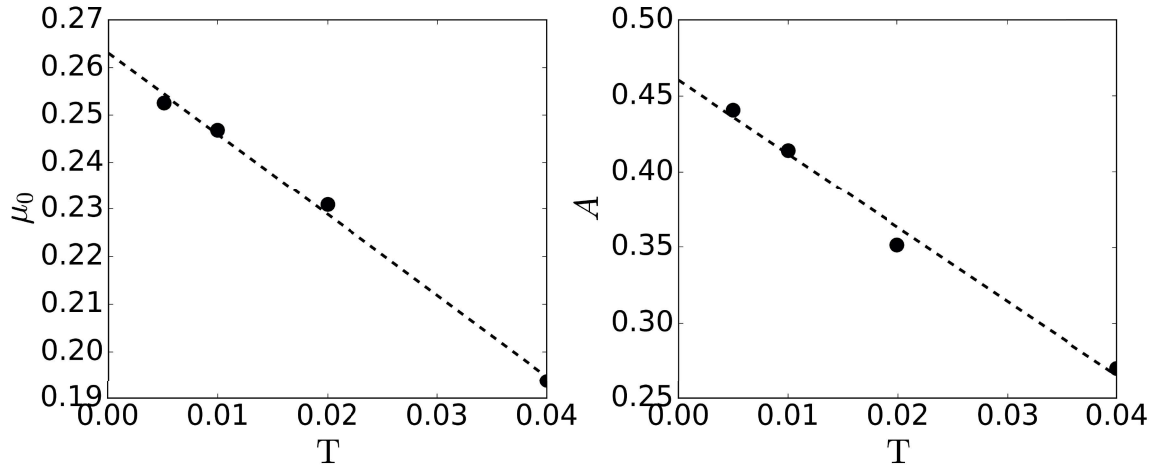

Fig. 4.6 Fit parameters, corresponding to $n(\mu) = A(\mu - \mu_0)^2$, extrapolated to $T = 0$.

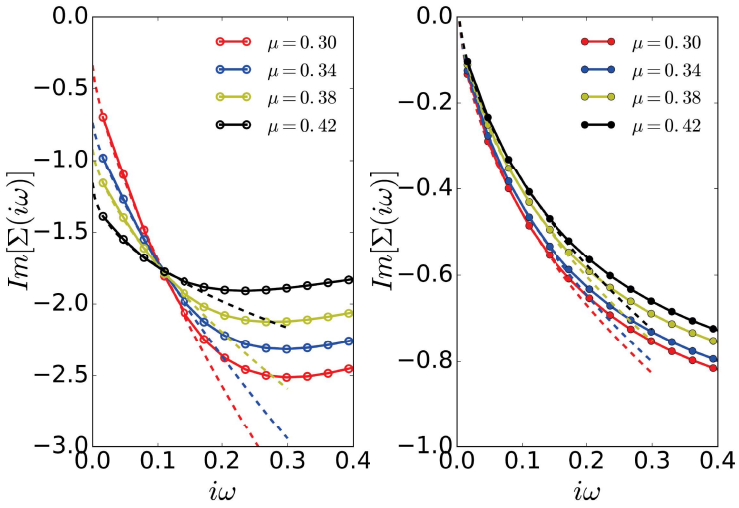

Fig. 4.7 Self-energies of the two-orbital model for several chemical potentials μ, with $U = 3.06$, $J = 0.25U$ and inverse temperature $\beta = 200$. Dashed lines indicate least-square fits to the function $c + b|i\omega|^{\delta}$. Left panel: Imaginary part of the self-energy on the Matsubara axis on the insulating branch of the coexistence region, $\delta = 0.72, 0.75, 0.66, 0.50$ (for $\mu = 0.30, 0.34, 0.38, 0.42$). Right panel: Same quantity on the metallic branch, $\delta = 0.45, 0.46, 0.48, 0.50$ (for $\mu = 0.30, 0.34, 0.38, 0.42$).

the insulator. For small $|i\omega|$, we find the imaginary part of the self-energies to be characterized by a fractional power-law behavior $-\mathrm{Im}[\Sigma(i\omega)] \sim c + b|i\omega|^{\delta}$, with an exponent δ that decreases upon approaching $\mu \to \mu_{c1}$. On this branch, we also find a large finite intercept $c \neq 0$, indicating strong decoherence. This decrease in coherence was already visible in the results shown in Fig. 4.4 for $\beta = 100$: Most interestingly, decoherence gets stronger upon further doping the system, signifying enhanced scattering, while at the same time there is an increase in $|Im[G(iw_0)]|$, testifying a growth in spectral weight at the Fermi level.

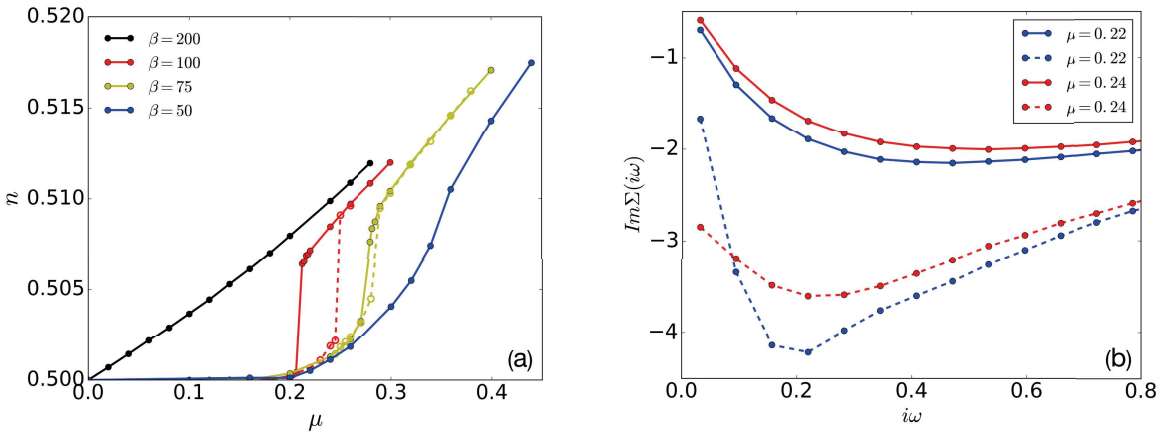

Fig. 4.8 Left panel (a) Filling n per spin as a function of the chemical potential μ for the two-orbital model with spin-flip and pair-hopping terms in the interaction Hamiltonian, i.e. $\alpha = 1$, $U = 3.4$ and $J = 0.25U$. Solid (dashed) lines denote results starting from a metallic (insulating) initial configuration. Imaginary part of the self-energies for the two-orbital model with spin-flip and pair-hopping terms, $U = 3.4$, $J = 0.25U$ and $\beta = 100$. Solid (dashed) lines denote results starting from a metallic (insulating) initial configuration.

The right panel of Fig. 4.7 shows the same quantities on the metallic branch. While the finite intercept of $\mathrm{Im}[\Sigma(i\omega)]$ disappeared, we still find power-law behavior with exponents $\delta \sim 0.5$.

Similar calculations were also performed for the model (4.2) with spin-flip and pair-hopping terms $\alpha = 1$; some of the results are presented in Fig. 4.8.

Panel (a) shows the filling as a function of the chemical potential for the rotationally symmetric model. Compared to the case without Hund's coupling, the insulating branches still extend to significant dopings; the effect is, however, less striking than in the case with Ising spin anisotropy $\alpha = 0$. Another difference is the temperature dependence of the branches. While in the previous case, the insulating branch remained rather stable upon changes of the temperature, we now witness a significant decrease in the extent to finite dopings upon decreasing the temperature. This is rather interesting: If the stability of the peculiar insulating branches in Fig. 4.5 were related to the reduced coherence scale of models with Hund's coupling, one would expect this effect to be even stronger in the rotationally symmetric case, since T_K should be even lower here. A direct comparison is difficult since the presence of spin-flip and pair-hopping terms changes values of the critical interactions. Panel (b) shows the imaginary parts for four self-energies; two of which are on the insulating and two of which are on the metallic branch. Here, the picture is quite similar to the case with density-density interactions. On the metallic branch, the self-energies show coherent, yet non Fermi liquid behavior corresponding to a fractional power law behavior (even though the resolution of the Matsubara-frequencies is too low to appreciate the details). On the insulating branch, the self-energies are increasingly incoherent for bigger chemical potentials.

Now let us go back to the results for the two-orbital model with density-density interactions $\alpha = 0$. The temperature corresponding to $\beta = 200$ is low enough to find a range of dopings $n \approx 0.512 - 0.519$,

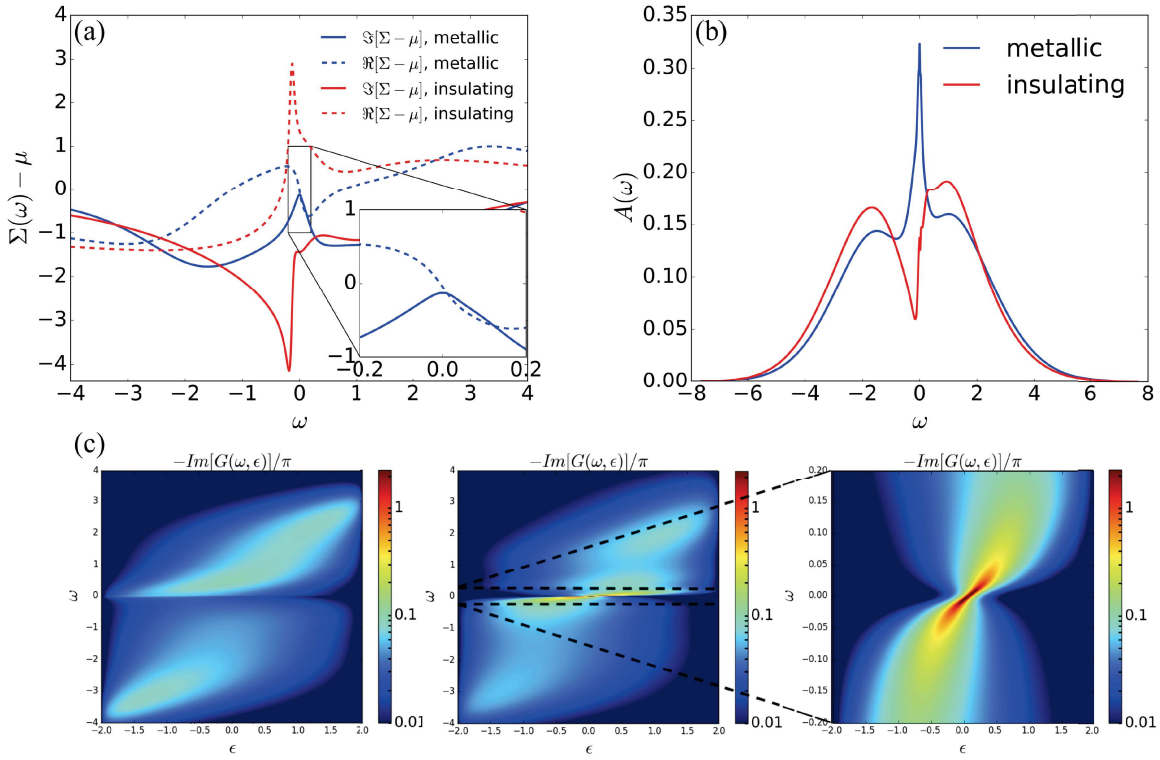

Fig. 4.9 (a) Real and imaginary part of the self-energies on the real-frequency axis for the two-orbital model with $U = 3.06$, $J = 0.25U$ and $\beta = 200$ for doping $n = 0.515$/spin on the metallic (blue) and insulating (red) branch. The inset shows a zoom to the metallic branch around the Fermi level. (b) Spectral functions on the metallic and insulating branch for fixed filling $n = 0.515$/spin, $U = 3.06$, $J = 0.25$ and $\beta = 200$. (c) Spectral functions $A(\omega,\varepsilon) = -Im[G(\omega,\varepsilon)]/\pi$ on the metallic and insulating branch for fixed filling $n = 0.515$/spin, $U = 3.06$, $J = 0.25$ and $\beta = 200$. The Green's functions were calculated as $G(\omega,\varepsilon) = (\omega+\mu-\varepsilon-\Sigma(\omega))^{-1}$ after analytic continuation of the self-energies $\Sigma(i\omega)$.

for which both a metallic and an insulating solution can be stabilized. This allows to perform a direct comparison of the two solutions at constant doping; the results are presented in Fig.4.9 for a filling of $n = 0.515$ per spin. Panel (a) allows to compare the self-energies of the two solutions on the real-frequency axis; panel (b) shows the corresponding spectral functions. The most distinctive feature characterizing the metallic solution in contrast to the insulating one is a sharp resonance at the Fermi level. Such features are commonly found in the Fermi liquid regime, due to the low-energy form of the self-energy in the Fermi liquid: $\Sigma(\omega) \sim \Sigma_0 - (1-Z^{-1})\omega + i(\gamma\omega^2 + \zeta T^2)$ (with real $\Sigma_0, Z, \gamma, \zeta$). On the Matsubara axis, this behavior translates to a linear regime of the imaginary part of the self-energy. Here, the situation is different. Indeed, for the given parameters, the system is not in the Fermi liquid regime, as can be witnessed from the self-energies Fig. 4.7 which do not show Fermi liquid behavior. As in the case of a Fermi liquid, the imaginary parts of the self-energy approach zero up to some finite temperature corrections, leading to long-lived low-energy excitations. Due to the non-linear behavior of $\mathrm{Im}[\Sigma(i\omega)]$ close to the Fermi level, however, no well-defined quasi-particles exist, and a formal

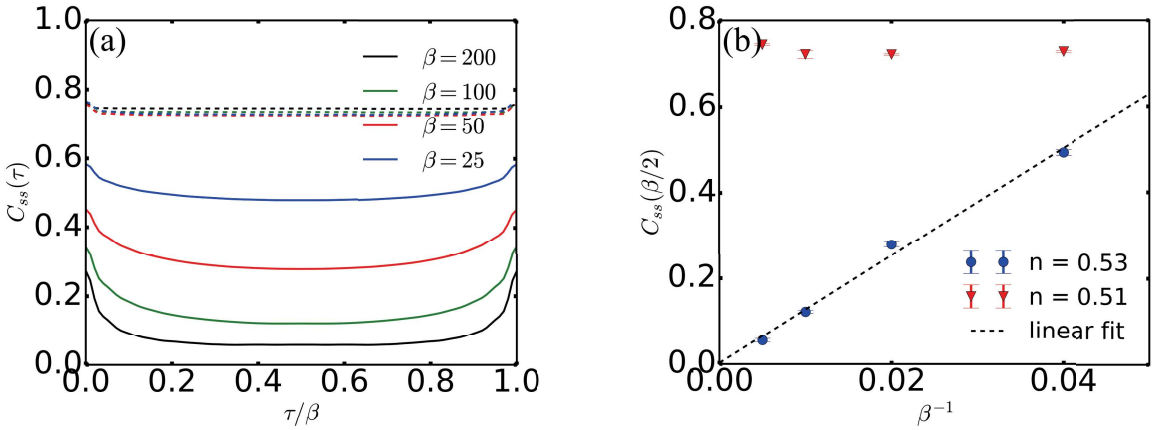

Fig. 4.10 Spin-spin correlations $C_{ss}(\tau) = \langle S_z(\tau)S_z(0)\rangle$ for the two-band model at $U = 3.06$, with $J = 0.25U$. (a) The solid(dashed) lines show the spin-spin correlation functions at fillings $n = 0.53(n = 0.51)$ for different temperatures. (b) Blue dots (red triangles) mark the correlations at $\tau = \beta/2$ for $n = 0.53(n = 0.51)$ as a function of the temperature $T = \beta^{-1}$. The dashed line is a linear fit for $n = 0.53$.

expansion in terms of a quasi-particle residue Z would result in an energy-dependent quantity that vanishes on the Fermi surface.

The pronounced peak of the spectral function of the metallic solution, shown in Fig. 4.9 (b), is due to the vanishing imaginary part of the self-energy at $\omega = 0$, as explained above. The insulating branch is characterized by a pseudo-gap structure, that emerges from the gapped insulator upon doping the system.

4.2.3 Spin-freezing in the vicinity of the Mott transition

We shall now investigate the fate of the spin-spin correlations in the vicinity of the first-order phase transition. Fig. 4.10 (a) shows the spin-spin correlations

$$C_{ss}(\tau) = \langle S_z(\tau)S_z(0)\rangle \tag{4.5}$$

on the metallic and the insulating branch for different temperatures, keeping the particle numbers fixed at $n = 0.53$ and $n = 0.51$, respectively. Fig. 4.10 (b) shows the values of the spin-spin correlations at $\tau = \beta/2$, as a function of temperature $T = \beta^{-1}$. In the Fermi liquid regime, the correlation function takes the form $C_{ss}(\tau) \sim (\beta \sin(\pi\tau/\beta))^{-2}$ (note that this expression looses its validity as $\tau \to 0$ and $\tau \to \infty$, since it would predict diverging correlations). For a Fermi liquid, $C_{ss}(\tau = \beta/2) \sim \beta^{-2} = T^2$ should thus scale quadratically with temperature.

Such Fermi liquid behavior is, in fact, seen on neither of the branches. On the insulating branch, the spin-spin correlations are found to be constant within the error bars, while on the metallic branch, they decay linearly as a function of temperature. According to the definitions of the spin-freezing crossover considered in [160] (onset of incoherence, linear temperature scaling of the correlation

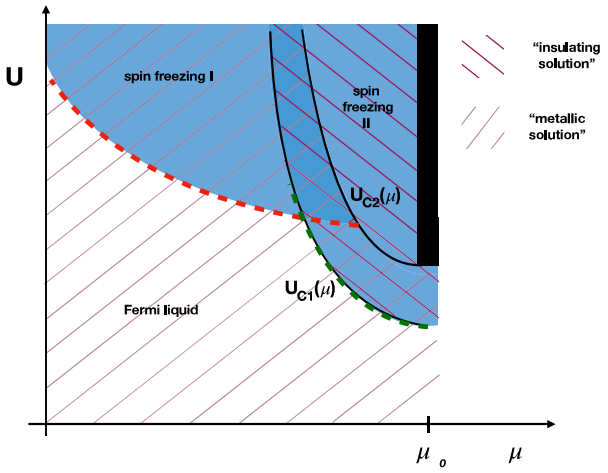

Fig. 4.11 Sketch of the $U-\mu$ phase diagram. The areas of insulating and metallic solutions are marked by lines in different directions; they overlap in the coexistence region, delimited by the critical interaction $U_{C1}(\mu)$ and $U_{C2}(\mu)$. Blue areas mark the spin freezing regime, the crossover is adumbrated by red, dashed lines.

function at $\tau = \beta/2$), only the insulating branch would qualify to belong to the spin-frozen regime. This is interesting, since it is clear from Fig. 3.8 (a), that the phenomenon is observed in a broader region of the phase space. If, as our findings suggest, in the vicinity of the critical interaction at half filling, frozen moments appear only on the insulating branch, this would mean that there are two spin-freezing crossover lines, as sketched in Fig. 4.11. The first one corresponding to the critical interaction $U_{C1}(\mu)$, the other one to the one described in [160], delimiting the Fermi liquid phase from the one of frozen moments.

4.3 Conclusions

Recent years have seen tremendous progress in the understanding of the effect of Hund's coupling on the model level, as well as in realistic systems. This is especially true for the low energy properties of such systems, where it could be demonstrated for the impurity model [77], as within single-site DMFT [148], that the ground state is described by a Fermi liquid. Furthermore,various NRG investigations shed light on the principles underlying the so-called spin-freezing regime.

However, there are still many open questions. Our investigations of the doping-driven Mott insulator revealed the appearance of a novel regime, that is adiabatically connected to the insulator, but yet acquires finite dopings and would be characterized as a "bad metal". This phase was found to exist in all systems with finite Hund's coupling under consideration, i.e. the two-orbital model with and without spin-flip and pair hopping, and the three orbital model with density-density interactions (where the effect is particularly impressive, see Appendix B.2).

We investigated the spin-spin correlations on the metallic and the insulating branches, showing that only the latter one exhibits the spin-freezing phenomenon. This might lead to interesting consequences

in the vicinity of the critical temperature T_C, which constitutes the endpoint of the first order phase transition. Apart from that, it suggests that the spin-freezing boundary is composed of two lines (see the discussion above, as well as Fig. 4.11), that eventually cross.

In a recently conducted slave-spin study [41] a compressibility enhancement and divergence on the metallic branch at low doping due to Hund's coupling was found at T=0 for $U > U_{c2}(T = 0)$, suggesting a tendency of the system towards phase separation in that regime. This effect is not observed in the present study (which is, therefore, consistent with [147]), which however reports mainly results for $U < U_{c2}(T = 0)$ (to the extent we could exactly locate $U_{c2}(T = 0)$, which is very computationally expensive with the present finite-T method). In selected cases, however, as e.g. that of Fig. 4.3, upper panel, we observed a range of densities that could not be stabilized for any of the two branches. This indicates indeed a phase separation, and might be the finite-temperature signature of the physics reported in Ref. [41]. Therefore, chances remain that an effectively diverging compressibility might become visible at lower temperatures, especially if one considers the strong reduction of the effective Fermi-liquid temperature scale upon finite Hund's coupling. Future works might investigate this effect, probing different regimes ($U > U_{c2}(T = 0)$), potentially using methods specifically tailored to treat low-energy regimes.

Part III

The d-p Problem – Phenomenology and Methodology

Chapter 5

The d-p Problem

5.1 Motivation

In the previous chapter, we investigated the physics of multi-orbital systems with Hund's exchange coupling. So far, the discussion was simplified in the sense that we only considered-orbitals from a single electronic shell in our models. Considering calculations for realistic compounds, however, one often finds such a description to be insufficient. This is especially true for materials like the late transition metal oxides (TMOs), such as NiO and the cuprate (materials containing anionic copper complexes) family, where there is considerable charge-transfer from the oxygen ligand-orbitals to the transition metal orbitals.

In the context of DFT+DMFT calculations, the standard approach to this problem is to include the ligand-orbitals in the construction of the low-energy model, but to consider them as uncorrelated. The additional, non-interacting orbitals only slightly increase the complexity of the many-body problem, such that numerical calculations remain feasible.

The description of inter-shell Coulomb interactions, on the other hand, poses a major challenge to theory. In the following, we shall refer to this problem as the "d-p problem", independently of the specific character of the orbitals of interest.

The outline of this chapter is a follows: In the first part, we shall motivate our investigations with a short review on the physics of transition metal oxides. We then continue with a discussion on how to construct d-p low energy models, specifically considering the example of (late) TMOs. In the context of DMFT, emphasis will be put on the nontrivial question of how to derive appropriate single-site impurity models. We then proceed by discussing the physics emerging in systems without inter-shell interactions, focusing on the role of the charge-transfer energy. Finally, we investigate the effect of inter-shell interactions and discuss different schemes of how to take them into account approximately.

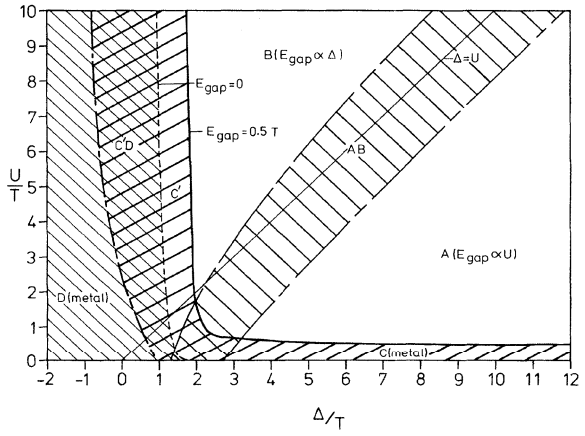

Fig. 5.1 Phase diagram of tranisition metal compounds by Zaanen, Sawatzky and Allen [170]. The phase space is split into four different regimes A,B,C and D; the effective transition metal Coulomb interaction $U = U^{dd}$ and the charge-transfer energy $\Delta = \varepsilon^d - \varepsilon^p$ are expressed in terms of the d-p hybridization T. A corresponds to the Mott insulator, while B is commonly referred to as the "charge-transfer insulating phase". C and D label the metallic phases, with C known as the "d-metal phase" while D being the "p-metal phase"

5.1.1 Transition metal oxides

Historically, transition metal oxides (TMOs) were the first systems for which standard band theory was found to break down. According to band theory, oxides like NiO and a variety of other TMOs should be metallic, due to the partially occupied bands. Experimentally, however, these compounds were well known to be insulating; a fact that was first pointed out in an article published 1937 by J. H. Boer and E. J. W. Verwey[37]. A first explanation for this observation was proposed in the same year in a comment by N. Mott and R. Peierls[118], who argued that the wrong theoretical prediction might be rooted in the neglect of Coulomb interactions. This implies, that correlations between the electrons cannot be neglected anymore.

Since then, the interest in TMOs has hardly declined. On the contrary: Despite the discovery of many other strongly correlated compounds, TMOs still constitute one of the most fascinating classes of solids. Some oxides, such as NiO or $BaTiO_3$, are found to be insulators, while others, like RuO_2 or $LaNiO_3$, are metallic. Other compounds show metal-insulator transitions; as a function of temperature (historically first observed in V_2O_3), pressure or chemical composition (e.g. $(V_{1-x}Cr_x)_2O_3$). Strong correlations also give rise to different types of ordering, like charge density waves and charge ordering, or different types of magnetic states. While materials like CrO_2 or $La_{0.5}Sr_{0.5}MnO_3$ are ferromagnetic, others, like NiO or $LaCrO_3$, are anti-ferromagnetic. The most prominent phenomenon, however, is probably the emergence of high temperature superconductivity within a class of copper based TMOs. While the parent compounds of these "cuprates" are anti-ferromagnetic Mott insulators, they become superconducting upon doping, with critical temperatures of up to $T_c > 130$ for $HgBa_2CuO_{4+\delta}$ (the previous record was $T_c \sim 23K$).

It is evident that this wealth of physical phenomena also constitutes an ideal playground for theory. In particular it raises the question of whether one can find a unified framework in which the physics of these systems can be explained. The Hubbard model[79], was an early success in this respect, since a major part of the physics observed in TMOs is already contained in this simple model. In a famous article[4], Anderson even claimed, that the Hubbard model contains all the relevant physics to explain the remarkable high temperature superconductivity found in the cuprates; this statement, however, was contested in the very same year[48] with proposals to rather use a more refined model. Even earlier, Zaanen, Sawatzky and Allen[170] argued, that especially in the late transition metal oxides (which include copper based oxides), the physics crucially depends on the interplay of the transition metal d-orbitals with the neighboring oxygen p-orbitals. In particular, they identified the effective transition metal Coulomb interaction U^{dd} and the energy difference between the bare transition metal- and ligand states – the charge-transfer energy Δ – as the central quantities to understand the properties of many TMOs. Their corresponding phase diagram, presented in Fig. 5.1, differentiates four different regimes (together with the corresponding intermediate regions). In the insulating phase, they distinguish between *Mott-Hubbard insulators* (A), in which the size of the spectral gap is determined by the effective Coulomb interaction $E_{gap} \propto U^{dd}$ of the TM d-orbitals, and *charge-transfer insulators* (B) in which $U > \Delta$ and the gap is about the charge-transfer energy $E_{gap} \propto \Delta$. In the metallic phase, the differentiation is between "d-metals" (C), in which electrons and holes are heavy due to correlations, and "p-metals" (D), in which carriers are (light) holes in ligand bands.

Apart from transition metal oxides, there are other classes of solids, where inter-shell couplings are of importance. An example are the f-electron systems, such as the lanthanides/actinides and their oxides. Here, it can be the coupling of f- and d-type orbitals (e.g. in Cerium), or the one of f- and p-type orbitals (e.g. UO_2) that is of importance.

5.2 Modeling transition metal oxides

As outlined above, TMOs are commonly modeled by a low energy Hamiltonian that is reduced to the subspace spanned by the transition metal d-orbitals and the oxygen ligand p-orbitals[170]. In general, such a Hamiltonian can be written as

$$H_{dp} = H_0 + H_{kin} + H_{int} \,, \tag{5.1}$$

where H_0 considers the atomic energy levels of the d and p-orbitals

$$H_0 = \sum_{im\sigma} \varepsilon^d_m d^\dagger_{im\sigma} d_{im\sigma} + \sum_{jn\sigma} \varepsilon^p_n p^\dagger_{jn\sigma} p_{jn\sigma} \,, \tag{5.2}$$

with $m \in \{xy, xz, yz, x^2-y^2, 3z^2-r^2\}$ and $n \in \{x, y, z\}$. For the sake of clarity we use different indices "i" and "j" to label the sites of the d and p-orbitals respectively. Furthermore, the chemical potential is

set to zero and we assume that there are no magnetic fields or spatial inhomogeneities in the potential, that would render the energies $\varepsilon_m^{d/p}$ spin or site dependent.
H_{kin} describes the kinetic part of the Hamiltonian

$$H_{kin} = -\sum_{ijmn\sigma} (t_{ijmn}^{dp} d_{im\sigma}^{\dagger} p_{jn\sigma} + h.c.) - \sum_{jj'nn'\sigma} t_{jj'nn'}^{pp} p_{jn\sigma}^{\dagger} p_{j'n'\sigma} \ . \tag{5.3}$$

We neglect any direct hopping between d-type orbitals, assuming the corresponding overlap to be small. In realistic materials calculations, the hopping matrices can for instance be obtained from DFT calculations, by constructing Wannier functions from states within some energy window.
Finally, we have the interaction term

$$H_{int} = \frac{U^{dd}}{2} \sum_{imm'} \hat{N}_d^i (N_d^i - 1) + \frac{U^{pp}}{2} \sum_{jnn'} \hat{N}_p^j (N_p^j - 1) + U^{dp} \sum_{<ij>} \hat{N}_d^i \hat{N}_p^j + H_{Hund} \ , \tag{5.4}$$

with $\hat{N}_d^i = \sum_{m\sigma} n_{im\sigma}^d$ and $\hat{N}_p^j = \sum_{n\sigma} n_{jn\sigma}^p$, where we restrict ourselves to on-site interactions of the d and p-orbitals, as well as nearest neighbor d-p interactions (the factor 1/2 in the last term comes from the double counting implied by the sum over $< ij >$). H_j considers additional "Hund's" interactions, lowering the cost for aligned spins.

Due to the large number of correlated-orbitals, there is little hope to solve Hamiltonian (5.1), even when applying approximate schemes as the dynamical mean-field theory. However, our model is rather general, and simplifications arise when considering more specific systems.

- In realistic materials, the fivefold degeneracy of the 3d-orbitals is lifted by ligand fields. This results in different occupations, with some of the orbitals being (almost) completely filled, while others remain only partly occupied. The filled-orbitals are effectively uncorrelated[1] and will only contribute a static potential shift to the other electrons, while not affecting their dynamics.

  An example would be case of NiO, where the octahedral crystal field splits the 3d-orbitals into two manifolds of smaller degeneracy; referred to as e_g ($x^2 - y^2$ and $3z^2 - r^2$) and t_{2g} (xy, xz, yz). Due to symmetry reasons, the t_{2g} orbitals do not hybridize with the surrounding oxygen ligands. Since they are lower in energy than the e_g orbitals, they will be (almost) completely filled and, therefore, effectively uncorrelated. This leaves us with a simplified, effective model, comprised of two (e_g) d-orbitals, interacting with 3 p-orbitals.

- Usually, the p-orbitals are regarded as non interacting. This constitutes one of the basic assumptions for many studies on realistic systems[65, 70, 157], as well as on the model level[2].

[1] This can be explained due to the fact that the change of filling of orbital m upon varying the bare energy of orbital m' is directly proportional to their mutual correlation. Now if orbital m is almost completely filled, any further change in its bare energy - or that of any other electron - will only cause a small change in its occupation

$$\frac{\partial \langle n_{m\sigma} \rangle}{\partial \varepsilon_{m'\sigma'}} = -\beta (\langle n_{m\sigma} n_{m'\sigma'} \rangle - \langle n_{m\sigma} \rangle \langle n_{m'\sigma'} \rangle) \approx \text{small} \ . \tag{5.5}$$

The orbital is, therefore, only weakly correlated.

In practice, when deriving a low energy Hamiltonian from the results techniques like DFT, this approximation can, however, lead to ambiguities in the evaluation of the effective, screened Coulomb parameters. We shall come back to this problem later.

Making use of these approximations can lead to drastically simplified models. In the case of the cuprate high temperature superconductors, for instance, the relevant physics is believed to be captured by a three-band d-p model comprised of correlated $d_{x^2-y^2}$ orbitals, which hybridize with p_x and p_y orbitals in a quasi two dimensional plane [48].

Of course, we are still dealing with interacting lattice models for which, in general, we cannot find an exact solution. There is a multitude of different approximate approaches to tackle such problems (cluster approximations, auxiliary particle techniques, etc.); here we want to focus on a treatment within dynamical mean-field theory. In this context, one is confronted with the question of how to construct an impurity model for system, in which two species of orbitals "live" on different lattice sites. One possibility would be to use some cluster extension of DMFT. The corresponding cluster impurity models, however, would be a challenge for any of the currently available impurity solvers, and only tractable in the most simple cases (depending on the cluster size and the number of correlated-orbitals). The second strategy is to construct new orbitals, centered on the transition metal sites, as linear combinations of the ligands. In this way, it is possible to construct a single-site impurity that accommodates the transition metal d-orbitals as well as the oxygen p-orbitals.

5.2.1 Zhang-Rice construction

We will follow the latter route. To this means, we shall use a method that goes back to Zhang and Rice[172]. Originally, they applied their construction to transform the three-band Hamiltonian, used to model the CuO_2 planes in La_2CuO_4 high-T_C superconductors, in order to obtain a better starting point for a perturbative expansion. The principles underlying their procedure are rather general and can be applied to a wider class of models (see for instance [141]). Here however, we will demonstrate it on the original system, following the presentation in the lecture notes by Müller-Hartmann[119].

The electronic structure of La_2CuO_4 (and other cuprates) is mainly defined by the physics of the CuO_2 planes. In the undoped case, the copper d-shells are filled with 9 electrons. Six of them inhabit the t_{2g} manifold, the orbitals of which do not hybridize with the surrounding oxygen p-orbitals due to symmetry reasons. Also the Cu d_{z^2} orbital is fully filled and does not hybridize with the oxygen p-orbitals in the CuO_2 planes. This means, that the relevant physics emerges from the interaction of the Cu $d_{x^2-y^2}$ orbital with the p_x and p_y orbitals in the plane, as illustrated in Fig. 5.2. The Hamiltonian of this system is a special case of the model (5.1) introduced before. In the following, we are interested

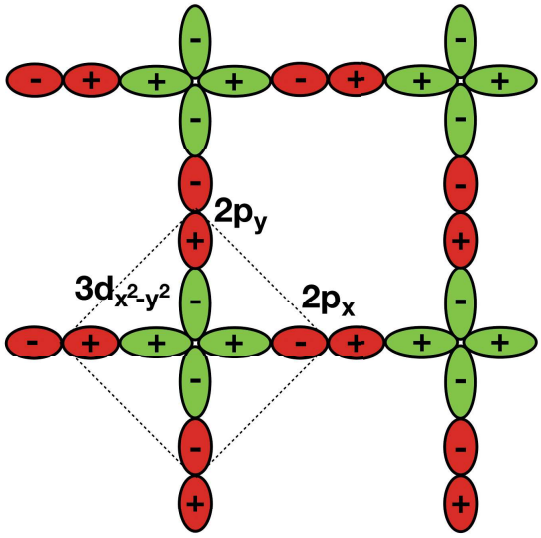

Fig. 5.2 Schematic representation of the CuO_2 plane in La_2CuO_4. The dashed square marks the unit cell composed of the Nickel $3d_{x^2-y^2}$ and the Oxygen $2p_x$ and $2p_y$ orbitals; the signs "+"/"-" represent the phase of the wave functions. Illustration inspired by [172], FIG. 1.

in its kinetic term, which can be written as

$$\begin{aligned} H_{kin} = -t^{dp} \sum_{i\sigma} \Big(& d^{\dagger}_{x^2-y^2,\mathbf{r}_i\sigma} p_{x,\mathbf{r}_i+\Delta\mathbf{x}/2,\sigma} - d^{\dagger}_{x^2-y^2,\mathbf{r}_i\sigma} p_{x,\mathbf{r}_i-\Delta\mathbf{x}/2,\sigma} \\ & + d^{\dagger}_{x^2-y^2,\mathbf{r}_i\sigma} p_{y,\mathbf{r}_i+\Delta\mathbf{y}/2,\sigma} - d^{\dagger}_{x^2-y^2,\mathbf{r}_i\sigma} p_{y,\mathbf{r}_i-\Delta\mathbf{y}/2,\sigma} + h.c. \Big) \ , \end{aligned} \tag{5.6}$$

where we assumed nearest-neighbor interactions only. Using

$$d^{\dagger}_{i\sigma} = \frac{1}{\sqrt{L}} \sum_{\mathbf{k}} e^{-i\mathbf{k}\mathbf{r}_i} d^{\dagger}_{\mathbf{k}\sigma}, \tag{5.7}$$

we can transform (5.6) into momentum space

$$H_{kin} = -t^{dp} \sum_{\mathbf{k}\sigma} \left(2i \sin\frac{k_x}{2} d^{\dagger}_{x^2-y^2,\mathbf{k}\sigma} p_{x,\mathbf{k}\sigma} + 2i \sin\frac{k_y}{2} d^{\dagger}_{x^2-y^2,\mathbf{k}\sigma} p_{y,\mathbf{k}\sigma} + h.c. \right) \ , \tag{5.8}$$

where we have set $|\Delta\mathrm{x}| = |\Delta\mathrm{y}| = 1$, such that $k_x, k_y \in [-\pi, \pi)$.
We proceed by defining our new operators as linear combinations of the p_x and p_y

$$w_{\mathbf{k}\sigma} = 2i \left(\sin\frac{k_x}{2} p_{x,\mathbf{k}\sigma} + \sin\frac{k_y}{2} p_{y,\mathbf{k}\sigma} \right) / f(\mathbf{k}) \tag{5.9}$$

$$v_{\mathbf{k}\sigma} = 2i \left(\sin\frac{k_x}{2} p_{x,\mathbf{k}\sigma} - \sin\frac{k_y}{2} p_{y,\mathbf{k}\sigma} \right) / f(\mathbf{k}) \ , \tag{5.10}$$

which are normalized by the momentum dependent function

$$f(\mathbf{k}) = 2\sqrt{\sin^2\frac{k_x}{2} + \sin^2\frac{k_y}{2}} = 2\sqrt{1 - \frac{1}{2}\left(\cos k_x + \cos k_y\right)}\,. \tag{5.11}$$

The linear combinations were chosen in a way that the hopping Hamiltonian takes the simple form

$$H_{kin} = -t^{dp}\sum_{\mathbf{k}\sigma} f(\mathbf{k})\left(d^{\dagger}_{x^2-y^2,\mathbf{k}\sigma} w_{\mathbf{k}\sigma} + h.c.\right)\,, \tag{5.12}$$

while the $v_{\mathbf{k}\sigma}$ orbital does not hybridize with the $\mathrm{d}_{x^2-y^2}$ electrons anymore. The new orbitals, diagonal in momentum space, can then be transformed back into real space

$$\begin{aligned} w_{i\sigma} &= \frac{1}{\sqrt{L}}\sum_{\mathbf{k}} e^{i\mathbf{k}\mathbf{r}_i} w_{\mathbf{k}\sigma} = 2i\frac{1}{L}\sum_j\sum_{\mathbf{k}} e^{i\mathbf{k}\mathbf{r}_i} e^{i\mathbf{k}\mathbf{r}_j}\frac{1}{f(\mathbf{k})}\left(\sin\frac{k_x}{2}p_{x,\mathbf{r}_j\sigma} + \sin\frac{k_y}{2}p_{y,\mathbf{r}_j\sigma}\right) \\ &= \sum_j \left(W_{x,\mathbf{r}_i-\mathbf{r}_j}p_{x,\mathbf{r}_j\sigma} + W_{y,\mathbf{r}_i-\mathbf{r}_j}p_{y,\mathbf{r}_j\sigma}\right)\,. \end{aligned} \tag{5.13}$$

The absolute value of the weight function depends only on the distance to $\mathbf{r}_i$, thus our new orbitals are centered around the copper site.

Apart from providing a set of transition metal centered-orbitals, the Zhang-Rice transformation comes with a neat "side effect". Transforming the Hamiltonian (5.12) back to real space

$$H_{kin} = -t^{dp}\sum_{ii'} \tilde{f}_{i-i'} d^{\dagger}_{x^2-y^2,i\sigma} w_{i'\sigma} + h.c.\,, \tag{5.14}$$

one realizes that the transformed model includes hoppings to sites at arbitrary distances. The hopping amplitudes, however, reduce drastically when moving away from the central d-orbital: While for the on-site hopping $i = i'$ the effective amplitude is enhanced by almost a factor of 2 $t^{dp}_{on-site} = t^{dp}\tilde{f}_0 \approx 1.916 \times t^{dp}$, the nearest-neighbor amplitude is reduced to $t^{dp}_{NN} \approx -0.280 \times t^{dp}$, and reduces even further for orbitals farther away $t^{dp}_{NNN} \approx -0.047 \times t^{dp}$ (see also [172, 119]).

With this construction, we have achieved two things: First of all, we have derived a Hamiltonian, in which the d- and p-type orbitals are centered on the same site, thus allowing the construction of a single-site impurity model. Secondly, this procedure provides a splendid starting point for a perturbative expansion, since inter-site hopping amplitudes are strongly reduced.

As a side remark it shall be noted that, throughout this derivation, we assumed the p-orbitals to be uncorrelated, i.e. that there was no pp-interaction U^{pp}. In case of such an interaction, transforming the one-body basis as presented would lead to non-local interactions of the w-orbitals. Since handling such interaction can be difficult, one could then either treat them as a perturbation, or, in the context of DMFT, map the problem onto an impurity model with dynamic interactions and apply extended DMFT (EDMFT).

In the following, we shall try to get an intuition for the physics expected to emerge from d-p models. We do this, by considering the most simple realization - a two-band model with one d-type

and one p-type orbital - in the limiting cases of 1) no inter-site hopping (using the Zhang-Rice construction described before) and 2) no interactions.

5.2.2 Limiting cases

Atomic limit

We shall start by considering an atomic two-orbital model, that is a single-site on with both the d- and the p-orbitals are located. From here on, whenever we speak of "p"-orbitals, located on the same site as the d-orbitals, we actually mean linear combinations of the original p-orbitals, like w_σ in (5.13). This being said, we consider the Hamiltonian

$$\begin{aligned} H_{dp} = &\sum_\sigma (\varepsilon^d - \mu) d^\dagger_\sigma d_\sigma + \sum_\sigma (\varepsilon^p - \mu) p^\dagger_\sigma p_\sigma + \sum_\sigma \left(V d^\dagger_\sigma p_\sigma + h.c. \right) \\ &+ U^{dd} n^d_\uparrow n^d_\downarrow + U^{pp} n^p_\uparrow n^p_\downarrow + U^{dp} (n^d_\uparrow + n^d_\downarrow)(n^p_\uparrow + n^p_\downarrow) \, . \end{aligned} \tag{5.15}$$

This model spans a Hilbert space of dimension 16, and has a number of conserved quantities, namely the 1) the total particle number N 2) the spin moment S and 3) the projection of the spin onto its z-component m. In the context of cuprate systems, we would consider copper with a $3d^9$ electronic configuration and filled oxygen orbitals; for our model, this would correspond to the sector with particle number $N = 3$.

For $N = 3$, (5.15) reduces to two Hamiltonians (one for $m = -1$ and one for $m = +1$) each of dimension 2, which act on the basis states

$$|\downarrow, \uparrow\downarrow\rangle \ , \ |\uparrow\downarrow, \downarrow\rangle \ \text{(m = -1) and} \ |\uparrow, \uparrow\downarrow\rangle \ , \ |\uparrow\downarrow, \uparrow\rangle \ \text{(m = + 1)} \, , \tag{5.16}$$

where the first entry is supposed to denote the d- and the second one the p-orbital. In the spin-degenerate case, both of them can be expressed by the same 2×2 matrix

$$H_{N=3,S=1,m=\pm 1} = \begin{bmatrix} U^{pp} + 2U^{dp} + 2\varepsilon_p - 3\mu & -V^* \\ -V & U^{dd} + 2U^{dp} + \varepsilon_p - 3\mu \end{bmatrix} \, , \tag{5.17}$$

where we set $\varepsilon_d = 0$. The eigenvalues of this matrix are

$$\lambda_\pm = \frac{1}{2} \left(U^{dd} + U^{pp} + 4U^{dp} - 6\mu + 3\varepsilon_p \pm \sqrt{(U^{dd} - U^{pp} - \varepsilon_p)^2 + 4|V|^2} \right) \, , \tag{5.18}$$

with the ground state

$$|-\rangle = \cos\alpha \, |\downarrow, \uparrow\downarrow\rangle + \sin\alpha \, |\uparrow\downarrow, \downarrow\rangle \ , \tag{5.19}$$

$$\text{with} \ \frac{\sin\alpha}{\cos\alpha} = -\sqrt{\frac{\lambda_+ - \lambda_- - (U^{dd} - U^{pp} - \varepsilon_p)}{\lambda_+ - \lambda_- + (U^{dd} - U^{pp} - \varepsilon_p)}} \, . \tag{5.20}$$

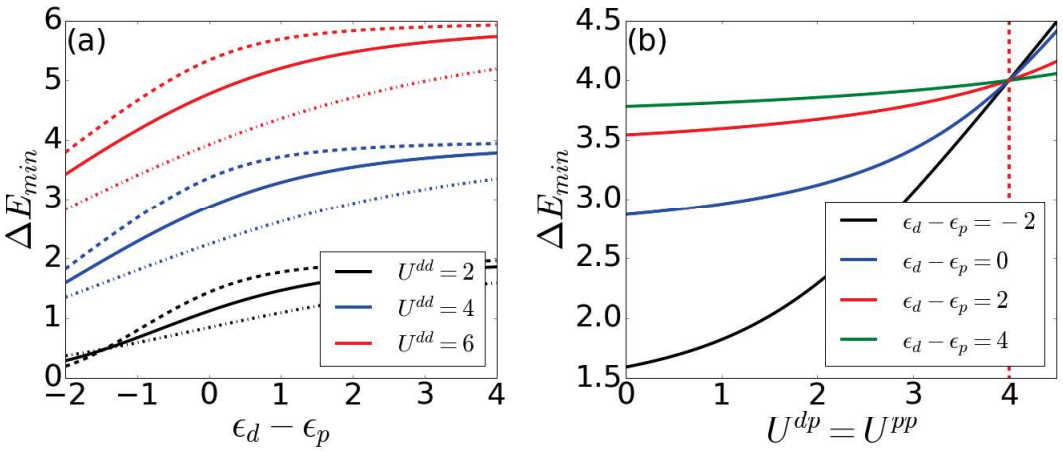

Fig. 5.3 Potential energy diffence ΔE_{min} of the ground states with $N = 4$ & $N = 2$ and two times the ground state with $N = 3$. The left panel (a) shows ΔE_{min} as a function of the bare energy difference $\varepsilon_d - \varepsilon_p$, for different values of U^{dd} with $U^{dp} = U^{pp} = 0$. Solid, dashed and dashed-dotted lines are calculated with $V = 1$,$V = 0.5$ and $V = 2$, respectively. The right panel (b) shows the same quantity as a function of the inter-shell interaction U^{dp}, which is set equal to the ligand interaction U^{pp}, for $U^{dd} = 4$ (marked with a red, dashed line).

For finite hybridization V, this ground state, also known as the Zhang-Rice singlet[172], has a considerable contribution from the state with fully filled d-orbitals $|\uparrow\downarrow,\downarrow\rangle$.

As soon as we go beyond the atomic limit to consider inter-site hoppings, there will necessarily be a mixing of different atomic states. In order to better understand the dynamics of the lattice system, it is therefore instructive to study the atomic multiplet structure, e.g. the energy differences and degeneracies of the different eigenstates. For the sake of compactness, we will not write down the Hamiltonians, eigenvalues and eigenstates for the various electron number and spin sectors; a complete description can be found in Appendix C.1. We shall, however, discuss some illustrative results.

One central phenomenon in the field of correlated electron systems is the appearance of an interaction driven metal-insulator (Mott) transition. In the case of the one orbital Hubbard model (1.8), the energy scale to determine the transition is given by the ratio of the Hubbard U and the bandwidth W. In other words, one has to consider the energy cost U of putting an electron from the half-filled ground state to another site versus the bandwidth of the kinetic energy.

Considering the two orbital d-p model one could imagine that, in the case of $U^{pp} = U^{dp} = 0$, the metal-insulator transition is again mainly determined by the relative strength of the Coulomb interaction U^{dd}/W, since it is the only interaction parameter in the model system. This would be true, if the transition to the insulator would be due to the localization of the correlated d-orbitals. However, it has been shown[2] that it is rather the localization of singlet states, mixing d- with p-holes, that drives the transition.

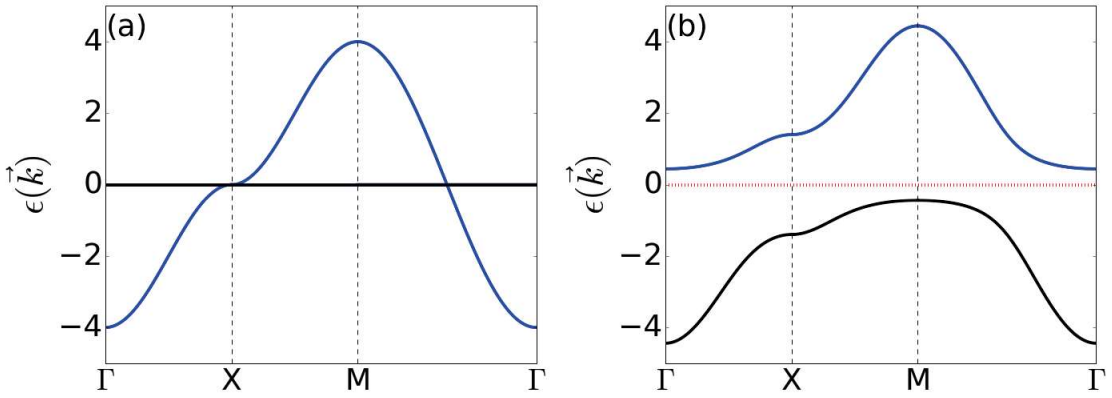

Fig. 5.4 Energy-momentum dispersion $\varepsilon(\vec{k})$ in the non-interacting limit, with $\varepsilon^d = \varepsilon^p = 0$, $t_{ij}^{dp} = 0$ and $t_{ij}^{pp} = \delta_{<ij>}$. In panel (a), the on-site d-p hybridizition is zero $V = 0$; in panel (b), it is set to $V = 1.4$, causing the opening of a gap.

This can be explained with an intuitive argument: Starting from the atomic limit with $N = 3$, the electrons will arrange themselves in ground state (5.19). Adiabatically turning on the inter-site hoppings, the electrons will remain localized until the energetic gain from the hopping exceeds the potential cost from moving an electron from one site to another. This potential cost is the energy difference between the $N = 4$ plus $N = 2$ ground states and two $N = 3$ singlets

$$\Delta E_{pot} = E_{min}[N = 4] + E_{min}[N = 2] - 2E_{min}[N = 3] \,. \tag{5.21}$$

Fig. 5.3 shows this quantity as a function of the bare energy difference $\varepsilon_d - \varepsilon_p$ and the inter-shell interaction U^{dp} for various values of U^{dd} and V.
Some observations: As expected, the potential energy difference grows almost linearly with the interaction U^{dd}, as can be seen by comparing three lines of the same line type in panel (a). At the same time, the gap increases significantly upon increasing $\varepsilon_d - \varepsilon_p$, until it reaches a plateau, defined by the bare value U^{dd}. From panel (b), one expects the inter-shell interaction U^{dp}, which we set to the same value as U^{pp}, to only have a minor influence on the electron localization; at least for $\varepsilon_d - \varepsilon_p > 0$ and realistic values of the interaction ($U^{dp} < U^{dd}$).

Non-interacting limit

The other limiting case is a lattice model, with all interactions set to zero. Again, such a model can take various forms, but for the sake of simplicity we will restrict the discussion to the most simple case of a two-orbital d-p model.

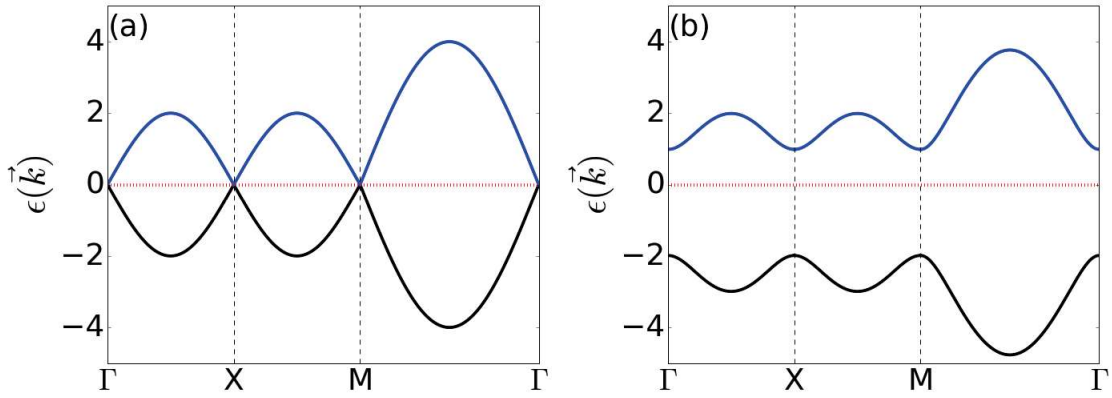

Fig. 5.5 Energy-momentum dispersion $\varepsilon(\vec{k})$ in the non-interacting limit, with $\varepsilon^d = 0$, $\varepsilon^p = -1$, $t_{ij}^{dp} = \delta_{<ij>}$ and $t_{ij}^{pp} = 0$. In panel (a), the on-site d-p hybridizition is zero $V = 0$; in panel (b), it is set to $V = 1.4$, causing the opening of a gap.

Considering a square lattice with d- and p-orbitals labeled by the same site index, our model takes the form

$$\begin{aligned} H_{dp} = &\sum_{i\sigma} \varepsilon^d d_{i\sigma}^\dagger d_{i\sigma} + \sum_{i\sigma} \varepsilon^p p_{i\sigma}^\dagger p_{i\sigma} - \sum_{i\sigma} (V d_{i\sigma}^\dagger p_{i\sigma} + h.c.) \\ &- \sum_{ij\sigma} (t_{ij}^{dp} d_{i\sigma}^\dagger p_{j\sigma} + h.c.) - \sum_{ij\sigma} t_{ij}^{pp} p_{i\sigma}^\dagger p_{j\sigma} \,, \end{aligned} \tag{5.22}$$

where we neglected any direct d-d hopping.
This Hamiltonian can be diagonalized trivially by transforming it into momentum space. For a specific choice of parameters it could, for instance, describe a model of localized d electrons which locally hybridize with p-type valence electrons. Fig. 5.4 shows the energy-momentum dispersion resulting in this case, with $t_{ij}^{dp} = 0$, $t_{ij}^{pp} = \delta_{<ij>}$ and $\varepsilon^d = \varepsilon^p = 0$. In panel (a), the local hybridization is put to zero $V = 0$, and the p-band crosses the Fermi level. Turning on the hybridization, one sees the opening of a gap in panel (b) (for $V = 1.4$); the system becomes insulating.
Fig. 5.5 shows the dispersion for $\varepsilon^d = 0$, $\varepsilon^p = -1$, with $t_{ij}^{dp} = \delta_{<ij>}$ and $t_{ij}^{pp} = 0$. This means, that the d-electrons can only propagate "throught" the p-states, similar to the model (5.14) derived from the Zhang-Rice transformation (there, however, the ratio $V/t^{dp} \mathrel{\hat{=}} t_{on-site}^{dp}/t_{NN}^{dp} = -6.843$ is fixed, and hopping is not restricted to the nearest neighbors). As before, introducing a non-vanishing on-site hybridization $V = 1.4$ results in the opening of a gap.

5.2.3 Realistic low energy models & shell-folding

Throughout most of this chapter, we discuss the d-p problem on a model level, with a focus on the emerging physics and how to effectively tackle such many body systems. Considering the calculation of realistic materials, however, the first challenge lies in how to derive appropriate model parameters, that provide a faithful description of the system's low energy physics.

Nowadays, density functional theory has established itself as an indispensable tool for the calculation of realistic structures. It provides a straightforward way to derive the non-interacting part of a low-energy Hamiltonian, by mapping the original problem onto an effective one-body system which can be fitted by localized Wannier orbitals. In this way, we can derive the parameters of the non-interacting part $H_0 + H_{kin}$ of (5.1).

Constructing the interacting part of a low-energy Hamiltonian is a more delicate issue. Here, immense progress has been made with the development of the *constrained random phase approximation* (cRPA) method[8]. Within cRPA, the partially screened effective Coulomb interactions are calculated by considering screening from degrees of freedom that lie outside the low-energy window of interest. Despite its success[9, 114, 122, 115] however, cRPA leads to ambiguities when considering problems where the original system is down-folded to a correlated subspace that is entangled with bands that lie outside the low-energy window. This is the case, as soon as we consider a model with d-p hybridization, in which only the d-orbitals are regarded as interacting. In order to avoid such ambiguities, interactions of the p-orbitals, as well as inter-shell interactions should, therefore, be treated on the same footing when deriving the low energy model parameters.

This raises the practical issue that, as we shall see, models with inter-shell interactions are computationally much more demanding then those with mere d-interactions.

Recently, an elegant solution to this problem was suggested in the form of an approximate scheme, called *shell-folding*[141]. The scheme is based on the observation that, if both the d- and the p-type orbitals are centered on the same sites (e.g. by a Zhang-Rice transformation, as discussed above), the interaction part (5.4) of the d-p can be re-written as

$$H_{int} = \frac{U^{dd} - U^{dp}}{2} \sum_{imm'} \hat{N}_d^i (N_d^i - 1) + \frac{U^{pp} - U^{dp}}{2} \sum_{inn'} \hat{N}_p^j (N_p^j - 1) + \frac{U^{dp}}{2} \sum_i (\hat{N}_d^i + \hat{N}_p^i)^2 + H_{Hund} \,, \tag{5.23}$$

where additional one-body terms were absorbed in the bare on-site energies in H_0.

So far, we merely performed an algebraic manipulation. The main idea now is based on the assumption, that the dominant screening process for charge fluctuations of the d-orbitals only involves electrons from the surrounding ligands (which we transformed to be centered on the same site as the d orbital). Reminiscent of the *perfect screening* [74] approach by Herring, shell-folding approximates this screening process to be perfect, meaning that any charge fluctuation of the d- orbitals is exactly compensated by fluctuations of the p-type Wannier orbitals on the same site. This implies, that the total charge on each site is a conserved quantity, and the third term in (5.23) is a constant. The shell-folding approximation, therefore, yields the following interaction Hamiltonian

$$H_{int}^{SF} = \frac{U^{dd} - U^{dp}}{2} \sum_{imm'} \hat{N}_d^i (N_d^i - 1) + \frac{U^{pp} - U^{dp}}{2} \sum_{inn'} \hat{N}_p^j (N_p^j - 1) + H_{Hund} \,. \tag{5.24}$$

The validity of this approximation shall be tested for various model parameters.

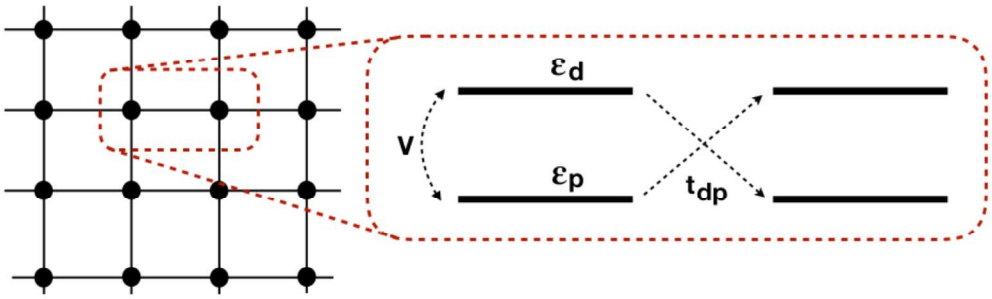

Fig. 5.6 Schematic representation of the two-orbital d-p model under consideration.

5.3 Insights from quantum Monte Carlo

In this section, we present results from numeric calculations performed for the two-orbital d-p model. In order to allow a treatment within single-site DMFT[57], the p-orbitals have been transformed to be centered on the same sites as the d-orbitals (see section 5.2.1), such that the Hamiltonian is of the form

$$\begin{aligned} H_{dp} = &\sum_{i\sigma}(\varepsilon^d-\mu)d^\dagger_{i\sigma}d_{i\sigma}+\sum_{i\sigma}(\varepsilon^p-\mu)p^\dagger_{i\sigma}p_{i\sigma}+\sum_{i\sigma}\left(Vd^\dagger_{i\sigma}p_{i\sigma}+h.c.\right)\\ &+U^{dd}\sum_i n^d_{i\uparrow}n^d_{i\downarrow}+U^{pp}\sum_i n^p_{i\uparrow}n^p_{i\downarrow}+U^{dp}\sum_i(n^d_{i\uparrow}+n^d_{i\downarrow})(n^p_{i\uparrow}+n^p_{i\downarrow})\\ &-t^{dp}\sum_{<ij>}\left(d^\dagger_{i\sigma}p_{j\sigma}+h.c.\right)\ , \end{aligned} \tag{5.25}$$

with on-site hybridization V of the d- and p-orbitals and nearest neighbor hopping t^{dp}. Such a Hamiltonian could, for instance, be derived by applying a Zhang-Rice-type transformation (5.9) and truncating the long-range hopping matrix after nearest neighbor hoppings (which, due the arguments given in section 5.2.2, is a reasonable approximation). For matters of concreteness, we consider a 2-D square lattice; a schematic representation of our model is shown in Fig. 5.6.

As required by the DMFT approximation, the Hamiltonian is then mapped onto a single-site impurity of the form

$$H^{imp}_{dp} = H_{atom}+H_{hyb}\ , \tag{5.26}$$

with

$$\begin{aligned} H_{atom} = &\sum_\sigma(\varepsilon^d-\mu)d^\dagger_\sigma d_\sigma+\sum_\sigma(\varepsilon^p-\mu)p^\dagger_\sigma p_\sigma+\sum_\sigma\left(Vd^\dagger_\sigma p_\sigma+h.c.\right)\\ &+U^{dd}n^d_\uparrow n^d_\downarrow+U^{pp}n^p_\uparrow n^p_\downarrow+U^{dp}(n^d_\uparrow+n^d_\downarrow)(n^p_\uparrow+n^p_\downarrow) \end{aligned} \tag{5.27}$$

and

$$H_{hyb} = \sum_{k\sigma} \left\{ \begin{bmatrix} d^\dagger_\sigma & p^\dagger_\sigma \end{bmatrix} \begin{bmatrix} V_k^{dd} & V_k^{dp} \\ V_k^{pd} & V_k^{pp} \end{bmatrix} \begin{bmatrix} b^d_{k\sigma} \\ b^p_{k\sigma} \end{bmatrix} + h.c. \right\} + \sum_{k\sigma} E_k^d b^{d\dagger}_{k\sigma} b^d_{k\sigma} + \sum_{k\sigma} E_k^p b^{p\dagger}_{k\sigma} b^{p\dagger}_{k\sigma} \,. \tag{5.28}$$

Corresponding to the two orbitals, we introduced two species of bath electrons b_k^d and b_k^p. However, contrary to the cases discussed in the previous chapters, both kinds of bath electrons couple to both impurity orbitals. This is due to the fact that we started out with a lattice model that accommodates inter-shell hoppings and on-site hybridization; an electron has the possibility to start from orbital 1) hop to the bath and then hop back to orbital 2), as it could on the lattice. It can be easily seen from the DMFT equations, that such terms are not only optional, but necessary for the convergence of the self-consistency cycles.

We now switch to a finite temperature Matsubara formulation, in which the model (5.26) corresponds to the following action

$$S_{dp} = S_{atom} + S_{hyb} \,, \tag{5.29}$$

with

$$S_{atom} = \int_0^\beta \mathrm{d}\tau \sum_\sigma \left(d^\dagger_\sigma \partial_\tau d_\sigma + p^\dagger_\sigma \partial_\tau p_\sigma \right) + H_{atom} \tag{5.30}$$

and

$$S_{hyb} = \iint_0^\beta \mathrm{d}\tau \mathrm{d}\tau' \sum_\sigma \begin{bmatrix} d^\dagger_\sigma(\tau) & p^\dagger_\sigma(\tau) \end{bmatrix} \begin{bmatrix} \Delta^{dd}(\tau-\tau') & \Delta^{dp}(\tau-\tau') \\ \Delta^{pd}(\tau-\tau') & \Delta^{pp}(\tau-\tau') \end{bmatrix} \begin{bmatrix} d_\sigma(\tau') \\ p_\sigma(\tau') \end{bmatrix} . \tag{5.31}$$

In this form, the hybridization with the bath states is taken into account implicitly via the hybridization function $\mathbf{\Delta}^{dp}(\tau-\tau')$. This function can be derived in the standard way, yielding its definition

$$\mathbf{\Delta}^{dp}(\tau) = \frac{1}{\beta} \sum_{i\omega} \mathbf{\Delta}^{dp}_{i\omega} e^{-i\omega\tau} \tag{5.32}$$

$$\mathbf{\Delta}^{dp}_{i\omega} = \sum_k \begin{bmatrix} V_k^{dd} & V_k^{dp} \\ V_k^{pd} & V_k^{pp} \end{bmatrix} \begin{bmatrix} i\omega - E_k^d & 0 \\ 0 & i\omega - E_k^p \end{bmatrix}^{-1} \begin{bmatrix} V_k^{dd*} & V_k^{pd*} \\ V_k^{dp*} & V_k^{pp*} \end{bmatrix} . \tag{5.33}$$

Due to the d-p hybridization, the action (5.29) will yield a matrix Greens' function

$$\mathbf{G}^{imp}(\tau) = -\left\langle T \begin{bmatrix} d(\tau)d^\dagger(0) & d(\tau)p^\dagger(0) \\ p(\tau)d^\dagger(0) & p(\tau)p^\dagger(0) \end{bmatrix} \right\rangle \tag{5.34}$$

with non-zeros off-diagonal elements. Within the DMFT self-consistency cycles (see section 1.4.4), this impurity Green's function is then used to generate an update for the hybridization function.

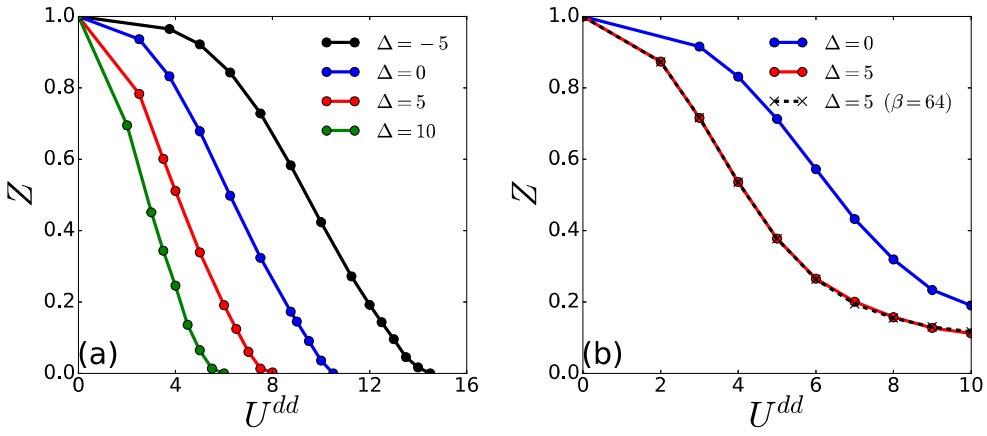

Fig. 5.7 Quasi particle renormalization Z as a function of the d-orbital Coulomb interaction U^{dd} for various values of the charge-transfer energy $\Delta = \varepsilon^d - \varepsilon^p$, with $V = 3.5$ and $\beta = 32$ (unless stated otherwise). Left panel (a) shows $Z(U^{dd})$ for an total filling of $N = 3$, while in the right panel, the total filling is $N = 2.8$.

5.3.1 Results without inter-shell interactions ($U^{dp} = U^{pp} = 0$)

We shall start this section by considering results for the model (5.25), with non-interacting p-orbitals and no inter-shell interaction. For $U^{dp} = U^{pp} = 0$, the model is parametrized by the bare atomic energies ε^d and ε^p, the chemical potential μ, the on-site hybridization V, the intra-shell interaction U^{dd}, as well as the off-diagonal hopping t^{dp}. In the calculations presented in the following, we set $t^{dp} = 1$, such that the bandwidth $W = 8$; all other parameters are given in units of t^{dp}. The on-site hybridization is set to $V = 3.5t^{dp}$, except for if explicitly stated otherwise. Here, we are interested in cases where the energy levels of the ligand-orbitals are close enough to the Fermi level, such that charge-transfer will be important. Together with the Coulomb interaction U^{dd} we will, therefore, consider the charge-transfer energy $\Delta = \varepsilon^d - \varepsilon^p$ (as well as $\tilde{\Delta} = \Delta + U^{dd}/2$ including the Hartree shift from a half-filled d-orbital) as a parameter of major importance.

Fig. 5.7 shows the quasi particle renormalization $Z = \left(1 - \mathrm{Im}\partial\Sigma/\partial\omega\right)^{-1}$ for two different overall fillings $N = 3$ and $N = 2.8$ and various values of the charge-transfer energy. Comparing the different panels (a) and (b), one immediately remarks a striking difference: For $\langle n^{tot} \rangle = 3$ the value of Z goes to zero, indicating a metal-insulator transition. For $\langle n^{tot} \rangle = 2.8$, however, the quasi particle renormalization remains finite, even though correlations increase steadily upon increasing U^{dd}. This is not surprising; although we did not fix the individual occupations of the d- and p- orbitals to an integer value, the metal-insulator transition takes place by localization of Zhang-Rice-type singlets, that constitute the atomic ground state at $\langle n^{tot} \rangle = 3$. This observation is consistent with previous investigations on two-orbital d-p models [2].

Another observation is the general increase of correlations upon increasing the charge-transfer energy Δ. Considering the case of $\langle n^{tot} \rangle = 3$, this can be explained by considering the atomic limit.

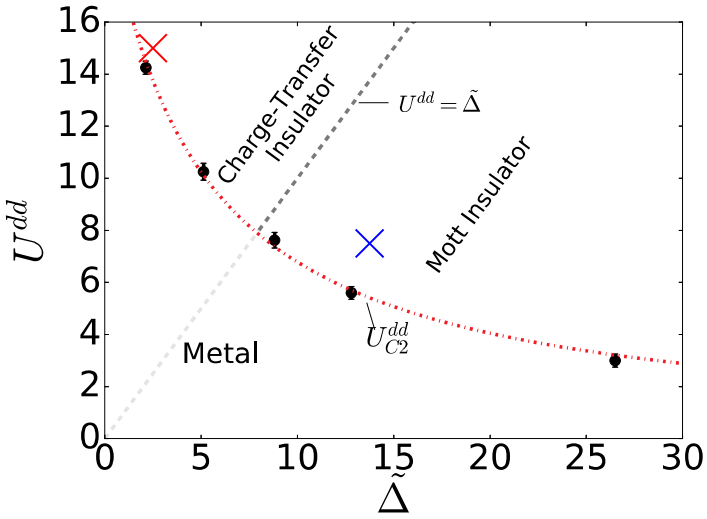

Fig. 5.8 Phase diagram of the two-orbital d-p model (5.25) without inter-shell interactions $U^{dp} = U^{pp} = 0$, showing the critical Coulomb interaction U_{C1}, at which the insulating solution ceases to exist. The red, dashed-dotted line is a fit to the function $f(x) = a/(x+b)+c$. The dashed, grey line is defined as $U^{dd} = \tilde{\Delta}$. In the insulating phase, it indicates the transition from a Mott- to a charge-transfer insulator. Red and blue crosses mark the parameters corresponding to the spectral functions presented in Fig. 5.9 (a) and (b), respectively.

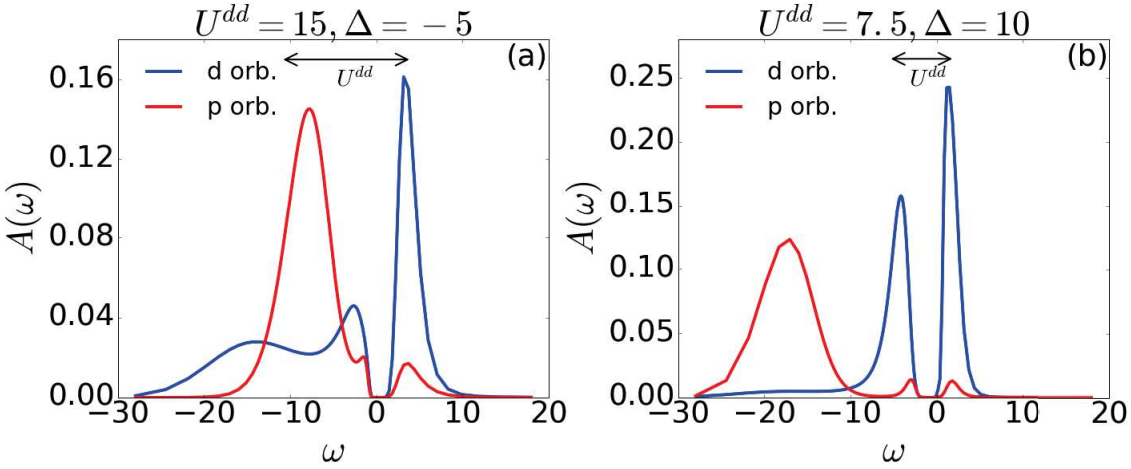

Fig. 5.9 Spectral functions $A(\omega) = -\mathrm{Im}G(\omega)/\pi$ of the d- and the p-orbitals in the insulating regime. In the left panel (a), the interaction parameter U^{dd} is considerably larger than Δ and charge-transfer between orbitals of p- and d-type will thus be important. In the right panel (b), however, the effective charge-transfer energy $\tilde{\Delta} = U^{dd}/2 + \Delta = 13.75$ is much bigger than U^{dd}. The bulk of the spectral weight of the p-orbitals is thus far below the Fermi level, and the size of the gap is mainly determined by U^{dd}.

As can be seen on the right panel of Fig. 5.3, the effective energy difference of the atomic ground state configurations for different electron numbers increases upon increasing $\varepsilon^d - \varepsilon^p$.

Fig. 5.8 shows the metal-insulator phase diagram in the $(U^{dd}, \tilde{\Delta})$ plane, and can be compared to Fig. 5.1, as well as the phase diagram given in [2]. As it could already be anticipated from the previous discussion, the critical interaction strength decreases for increasing charge-transfer energy, which is consistent with the atomic limit considerations. In the insulating regime, the grey, dashed line indicates the crossover from the charge-transfer-insulator to the Mott insulator. Fig. 5.9 shows spectral functions of the d- and p- orbitals for two different sets of parameters, which are marked by crosses in Fig. 5.8. In panel (a), the interaction parameter $U^{dd} = 15$ is much larger than the effective charge-transfer energy $\tilde{\Delta} = 2.5$; the width of spectral gap is close to the latter one. In panel (b), the situation is reversed, with $\tilde{\Delta} = 13.75$ being considerably larger than $U^{dd} = 7.5$. Here, the bulk of the spectral weight corresponding to the p-orbitals is far below the Fermi level, around which we see two Hubbard bands, separated by distance of about U^{dd}.

One technical remark on the calculation of Z. Except for one curve in Fig. 5.7 (b), all calculations were performed at $\beta = 32t^{dp-1}$ i.e. $\beta = 256W^{-1}$. At this temperature, the resolution of the Matsubara frequencies is not fine enough to fit the linear Fermi liquid behavior as $i\omega$ approaches zero, and the renormalization was calculated as $Z \approx (1 - \mathrm{Im}\Sigma[i\omega_0]\beta/\pi)^{-1}$. Calculations at lower temperatures become increasingly costly; for a total filling $N = 2.8$ and $\Delta = 5$, however, we repeated the calculation at $\beta = 64t^{dp-1} = 512W^{-1}$, to check the convergence of the evaluated Z values. The agreement is at least within $\sim 3\%$ (for $U^{dd} > 7$), with a random sign of the deviation (which means, that statistic fluctuations predominate over the expected systematic trend from this method, namely a decrease of Z upon decreasing temperature).

5.3.2 Results with inter-shell interactions ($\mathbf{U^{dp} \neq 0}$ & $\mathbf{U^{dp} \neq 0}$)

In Sec. 5.2.3, we already briefly discussed the issue of constructing low energy models from ab-initio calculations, i.e. the subtleties one has to consider when deriving the effective interaction parameters. More specifically, we evoked the problematics of deriving a low energy model, the correlated subspace of which does not include all the orbitals under consideration. Exactly this was, however, the case that we studied in the last section (and which is most commonly considered in the literature).
In this section, we shall investigate the effect of non-zero inter-shell interactions. The model under consideration is again (5.25), but now we set $U^{dp} \neq 0$ and $U^{pp} \neq 0$. As in the previous calculations, we chose $t^{dp} = 1$ (corresponding to a bandwidth of $W = 8$) as our unit of energy, and set $V = 3.5$. The other parameters will be defined specifically for each calculation.
The very first thing we would like to investigate is the effect that the inter-shell interactions have on the correlation of the d electrons.

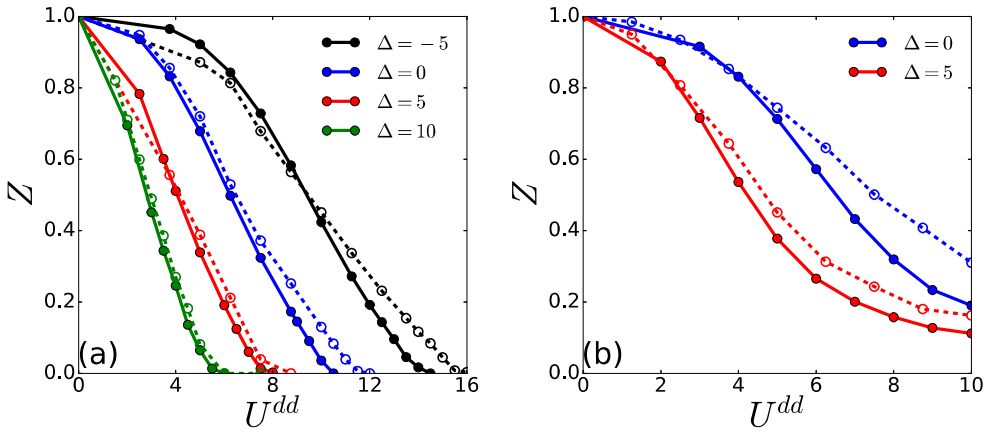

Fig. 5.10 Quasi particle renormalization Z as a function of the d-orbital Coulomb interaction U^{dd} for various values of the charge-transfer energy $\Delta = \varepsilon^d - \varepsilon^p$, with $V = 3.5$ and $\beta = 32$. Solid lines denote results with $U^{dp} = U^{pp} = 0$, dashed-dotted lines correspond to $U^{dp} = U^{pp} = 0.5U^{dd}$. The left panel (a) again shows $Z(U^{dd})$ for a total filling of $N = 3$, while in the right panel, the total filling is $N = 2.8$.

Fig. 5.10 corresponds to Fig. 5.7 presented in the previous section, and compares the d-orbital quasi-particle renormalization for calculations with $U^{dp} = U^{pp} = 0.5U^{dd}$ to those without inter-shell and p-orbital interaction.

The results reveal that the additional interactions consistently lower the correlations of the d electrons (except for some calculations at $\Delta = -5$ in the weakly correlated regime, which would require a more careful investigation). At a first glance, this might seem counter-intuitive, since interactions are supposed to enhance correlations. However, one can give some simple arguments, why this is to be expected.

1. The *Hartree contribution* of the inter-shell and p orbital interaction to the self-energy constitutes a constant, real shift, that can be absorbed in the on-site energies

$$\tilde{\varepsilon}^d_\sigma = \varepsilon^d_\sigma + U^{dp}\left\langle n^p_\uparrow + n^p_\downarrow \right\rangle \tag{5.35}$$

$$\tilde{\varepsilon}^p_\sigma = \varepsilon^p_\sigma + U^{dp}\left\langle n^d_\uparrow + n^d_\downarrow \right\rangle + U^{pp}\left\langle n^p_{\bar{\sigma}} \right\rangle . \tag{5.36}$$

This means, that the bare charge-transfer energy will be changed by

$$\delta\Delta = U^{dp}\left(\left\langle n^p_\uparrow + n^p_\downarrow \right\rangle - \left\langle n^d_\uparrow + n^d_\downarrow \right\rangle\right) - U^{pp}\left\langle n^p_{\bar{\sigma}} \right\rangle , \tag{5.37}$$

which, for $U^{dp} = U^{pp}$, as well as $N^d > 1$ and $N^p < 2$ will necessarily be negative $\delta\Delta < 0$. Considering the arguments put forward in the previous section on the results with d interactions only (i.e. the considerations from the atomic limit) we know that this leads to a decrease in correlations.

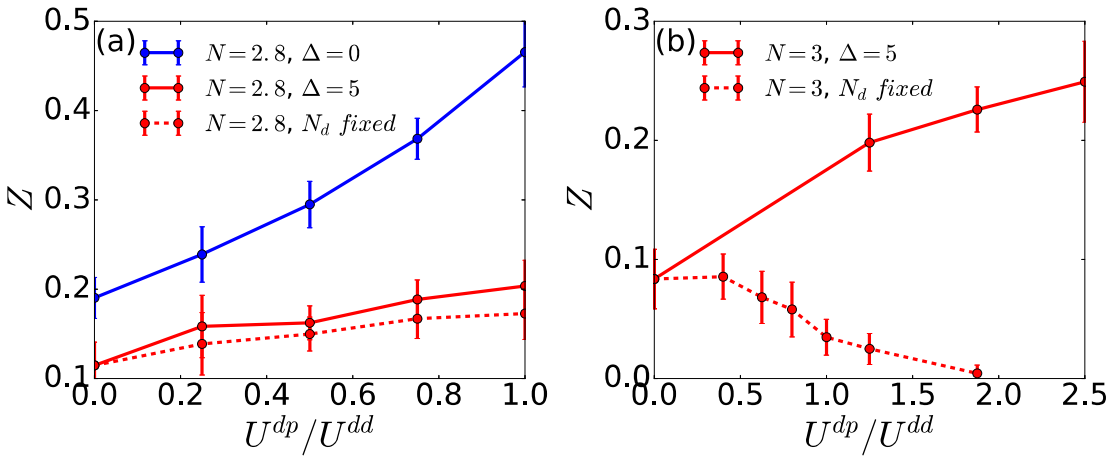

Fig. 5.11 Quasiparticle renormalization Z as a function of $U^{dp} = U^{pp}$. The solid lines in panel (a) show Z at average total filling $N = 2.8$ for two different values of the charge-transfer energy and $U^{dd} = 4$. The dashed, red line shows Z from fixing the indivual fillings $N_d = N_d(U^{dp} = 0, \Delta = 5)$, keeping $N = 2.8$ and $U^{dd} = 10$. Panel (b) shows the same quantity for total filling $N = 3$ and $U^{dd} = 6.25$; the red, solid line for fixed Δ, and the red, dashed line for fixing individual fillings $N_d = N_d(U^{dp} = 0, \Delta = 5)$. In all calculations, we set $V = 3.5$ and $\beta = 32$.

2. The decrease in correlations can also be explained by considering the *shell-folding* approximation, explained in Sec. 5.2.3. According to this approximation, the inter-shell interaction renormalizes the intra-shell interactions as $\tilde{U}^{dd} = U^{dd} - U^{dp}$ and $\tilde{U}^{pp} = U^{pp} - U^{dp}$. For the parameters under consideration, i.e. $U^{dp} = U^{pp} = 0.5U^{dd}$, this means that the effective p interactions cancels exactly to zero, while the d interaction is diminished to half its original value. Looking at Fig. 5.10, it is clear that this approximation strongly overestimates the reduction of correlations due to the inter-shell interaction, since if it was exact, the dashed-dotted curves should be equivalent to the solid lines, at double the value of U^{dd}.

Let us reconsider these two points more carefully. If the decrease in correlation was due to the Hartree contribution of the self-energy, this would mean that this effect should become ever stronger upon decreasing the charge-transfer energy Δ. This is because $\delta\Delta$ in Eq. (5.37) decreases for increasing filling of the d-orbitals; which is exactly the effect of decreasing Δ.

That this is indeed the case can already be seen in Fig. 5.10 (b), and becomes even clearer when contemplating Fig. 5.11 (a), which shows the evolution of the quasi particle renormalization upon increasing $U^{dp} = U^{pp}$. Indeed, comparing the solid lines in panel (a), we see that the slope of $Z(U^{dp})$ is strongly enhanced for the blue curve, calculated with a smaller charge-transfer energy of $\Delta = 0$. This raises the question of whether the decrease of correlations is only due to the Hartree shift. To investigate this issue, we added the dashed, red line, which shows the evolution of Z for constant individual occupations, such that $N_d = N_d(U^{dp} = 0, \Delta = 5)$ is fixed to the value it takes for the red, solid curve at $U^{dp} = 0$. Most interestingly, even though the slope of the dashed curve is smaller than the one of the solid curve, it is still positive, indicating a decrease in correlations.

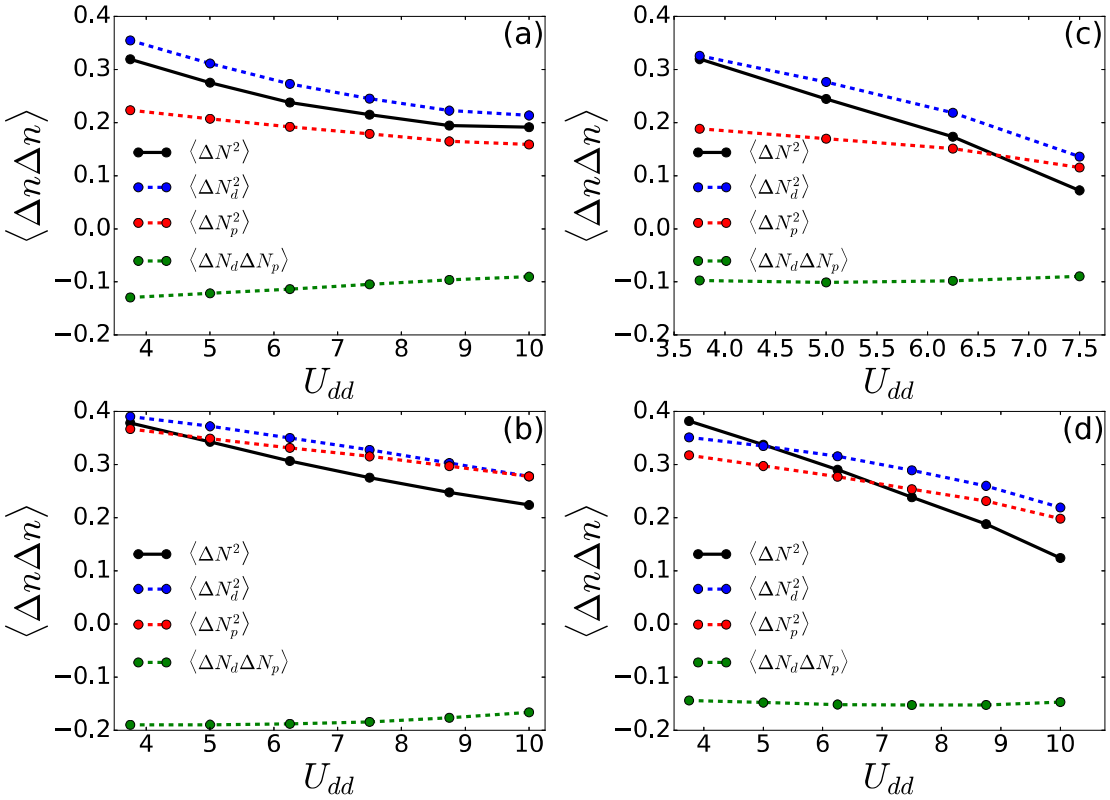

Fig. 5.12 Charge correlations in the metallic regime for (a) $N = 2.8$, $\Delta = 5$, (b) $N = 2.8$, $\Delta = 0$, (c) $N = 3$, $\Delta = 5$, (d) $N = 3$, $\Delta = 0$, as a function of the d orbital interaction U^{dd} with $U^{dp} = U^{pp} = 0.5U^{dd}$, $V = 3.5$ and $\beta = 32$. Black, solid lines denote fluctuations of total charge $\langle \Delta N^2 \rangle = \langle (\Delta N_d + \Delta N_p)^2 \rangle = \langle \Delta N_d^2 \rangle + \langle \Delta N_p^2 \rangle + 2 \langle \Delta N_d \Delta N_p \rangle$, dashed lines its different components.

That this behavior is, however, not universal, can be seen in the right panel (b) of Fig. 5.11. It shows the quasi-particle renormalization for total filling $N = 3$; once for fixed charge-transfer energy $\Delta = 5$, and once for fixed individual fillings $N_d = N_d(U^{dp} = 0, \Delta = 5)$ at $U^{dd} = 6.25$ (which is supposed to be close to the critical value of the metal-insulator transition at $U_C^{dd} \approx 7.25$) . While for fixed Δ the correlations decrease as before, they increase when keeping the individual fillings fixed.

The second argument to explain the decrease in correlations followed the reasoning of the *shell-folding* approximation. Here, we can use the results from the numerous calculations performed to generate Fig. 5.10 to actually test the assumption on which this approximation is based. As it has already been mentioned in Sec. 5.2.3, shell-folding can be thought of as a generalization of the *perfect screening* approximation [74], assuming that charge fluctuations of the correlated d-electrons would be perfectly compensated by fluctuations of the surrounding ligands (which, by means of Zhang-Rice-type transformation, we centered on the same site).

Fig. 5.12 shows the charge fluctuations of and between different orbitals. According to the shell-folding approximation, $N = N_d + N_p$ should be approximately constant, and thus $\langle \Delta N^2 \rangle = \langle (N_d + N_p - \langle N_d + N_p \rangle)^2 \rangle$ should be close to zero. Indeed, for all panels (a) - (d), fluctuations of the

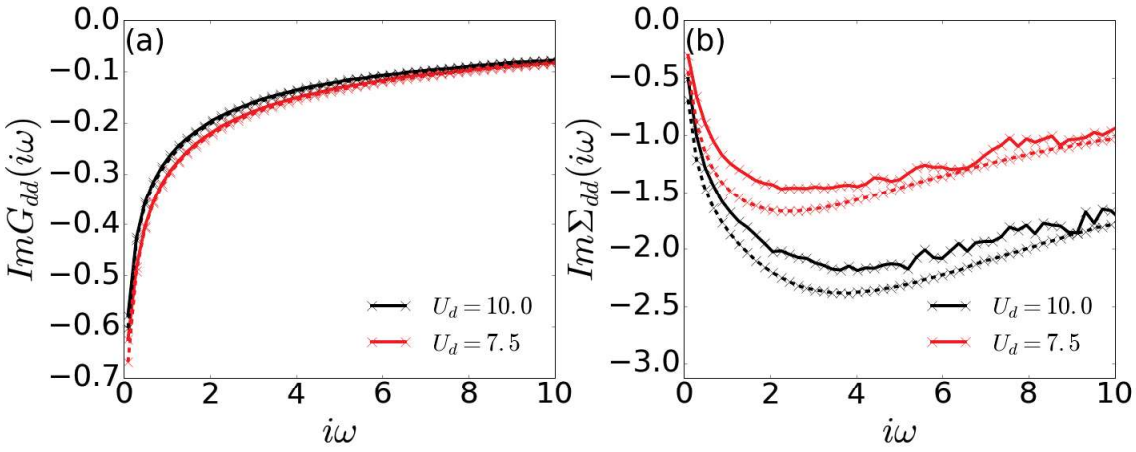

Fig. 5.13 Imaginary part of the Green's function (a) and self energy (b) for total filling $N = 2.8$, $U^{dp} = U^{pp} = 0.5U^{dd}$ and two different values of U^{dd}. Solid lines denote results from the full two orbital calculation, while dashed lines consider results using the Hartree approximation. In all calculations we set $V = 3.5$ and $\beta = 32$.

total charge are smaller than the fluctuations of the d electrons alone. However it is only in graphs (c) and (d) with $N = 3$, and considerably large U^{dd}, that $\langle \Delta N^2 \rangle$ actually comes close to zero. This might seem in contradiction with the results from Fig. 5.11, where for fixed individual fillings (thus eliminating the effect from the Hartree correction) an increase in correlations can only be seen for the calculations performed at an overall filling $N = 2.8$.

So how can we make sense of these different observations? Fig. 5.11 suggests, that for incommensurate fillings, a shell-folding like renormalization of U^{dd} and U^{pp} explains the decrease of correlations upon increasing the inter-shell interaction U^{dp}. While this effect should persist for the commensurate filling $N = 3$, the physics in the strongly correlated regime is dominated by the formation of Zhang-Rice like singlets (which finally cause the metal-insulator transition), for which the atomic energy gap increases with increasing U^{dp} (see Sec. 5.2.2, Fig. 5.3 (b)).

This also results in different descriptions of how to approximately treat the effect of inter-shell interactions in the calculations.

- For incommensurate fillings (and also for commensurate fillings at sufficiently weak correlations), and significantly large and positive charge-transfer energy Δ, the effect of the inter-shell interaction $U^{dp} < U^{dd}$ is, to a substantial degree, due to the Hartree correction to the self-energy, which can be used as a starting point for further approximations, as can be seen in Fig. 5.13.

- For commensurate fillings in the strongly correlated regime, the influence of inter-shell interactions can be rather strong, with significant effects beyond the Hartree correction. This can be witnessed in Fig. 5.14, which shows the imaginary part of the d-orbital Green's functions and self-energies for various values of the inter-shell interaction, that is set to be equal to the p orbital interaction $U^{dp} = U^{pp}$. Upon increasing U^{dp}, the system undergoes a metal-insulator

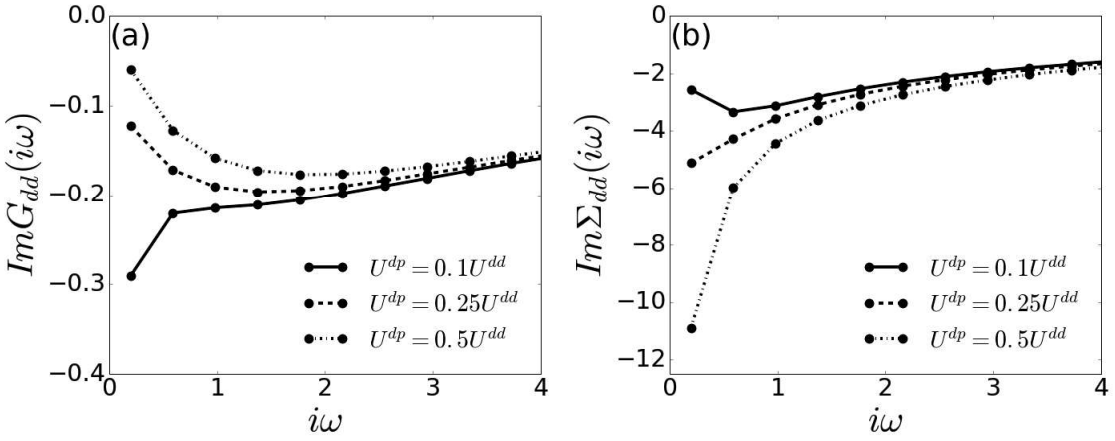

Fig. 5.14 Imaginary part of the Green's function (a) and self energy (b) for total filling $N = 3$, fixed individual fillings $N_d = 1.1$, $U^{dd} = 6.5$ and various strengths of the inter-shell interaction $U^{dp} = U^{pp}$. In all calculations we used $V = 3.5$ and $\beta = 16$.

transition, as can be seen from the behavior of the Green's function around the Fermi level: For the biggest inter-shell interaction under consideration $U^{dp} = U^{pp} = 0.5U^{dd} = 3.25$, the imaginary part of the Green's function extrapolates to zero, indicating vanishing spectral weight i.e. a gap at the Fermi level. Note that this effect is strictly beyond the Hartree correction, since the individual fillings have been kept constant.

One simple way to improve upon the Hartree approximation discussed in the first point, is to reconsider the mean-field decoupling of the interaction terms on which the self-energy correction is based. Considering the Hamiltonian (5.25), we can decouple the terms depending on U^{dp} and U^{pp} as

$$\begin{aligned} U^{pp} n^p_\uparrow n^p_\downarrow + U^{dp}(n^d_\uparrow + n^d_\downarrow)(n^p_\uparrow + n^p_\downarrow) \approx\ & U^{pp}\left\{ n^p_\uparrow \left\langle n^p_\downarrow \right\rangle + \left\langle n^p_\uparrow \right\rangle n^p_\downarrow + \left\langle n^p_\uparrow \right\rangle \left\langle n^p_\downarrow \right\rangle \right\} \\ & + U^{dp}\left\{ (n^d_\uparrow + n^d_\downarrow)\left\langle n^p_\uparrow + n^p_\downarrow \right\rangle + \left\langle n^d_\uparrow + n^d_\downarrow \right\rangle (n^p_\uparrow + n^p_\downarrow) + \left\langle n^d_\uparrow + n^d_\downarrow \right\rangle \left\langle n^p_\uparrow + n^p_\downarrow \right\rangle \right\} \\ & - U^{dp}\left\{ d^\dagger_\uparrow p_\uparrow \left\langle p^\dagger_\uparrow d_\uparrow \right\rangle + \left\langle d^\dagger_\uparrow p_\uparrow \right\rangle p^\dagger_\uparrow d_\uparrow + \left\langle d^\dagger_\uparrow p_\uparrow \right\rangle \left\langle p^\dagger_\uparrow d_\uparrow \right\rangle \right\} \\ & - U^{dp}\left\{ d^\dagger_\downarrow p_\downarrow \left\langle p^\dagger_\downarrow d_\downarrow \right\rangle + \left\langle d^\dagger_\downarrow p_\downarrow \right\rangle p^\dagger_\downarrow d_\downarrow + \left\langle d^\dagger_\downarrow p_\downarrow \right\rangle \left\langle p^\dagger_\downarrow d_\downarrow \right\rangle \right\} , \end{aligned} \tag{5.38}$$

where we neglected any spin-flipping terms. Fixing the individual occupations of the orbitals also fixes the energy corrections, due to the Hartree contributions in the first two lines of (5.38). However, we have not yet exploited the corrections from the Fock contributions in the 3^{rd} and 4^{th} line.

Fig. 5.15 compares the results from applying the Hartree and Hartree-Fock approximations to the system with total filling $N = 2.8$. Indeed, a major improvement is achieved by adding the additional off-diagonal terms. The rather small deviation of the Hartree-Fock Z from the reference results suggests that the contribution from higher-order corrections are merely small in this parameter range.

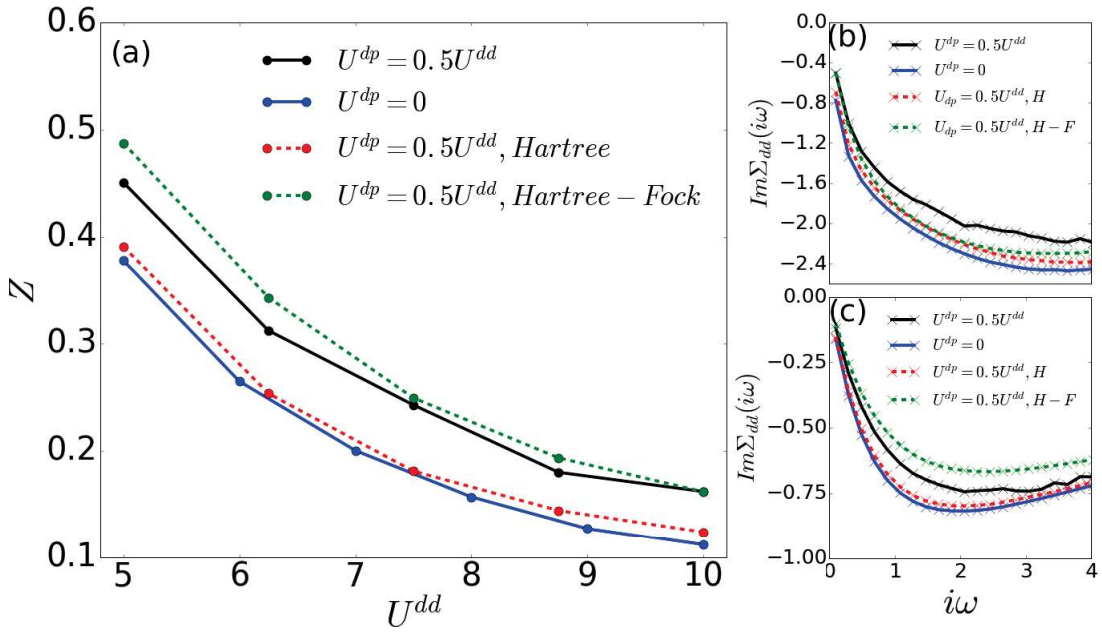

Fig. 5.15 Comparison of different approximation schemes for total filling $N = 2.8$. Panel (a) shows the d orbital quasi-particle renormalization Z as a function of U^{dd}. Solid lines show the exact results from quantum Monte Carlo; the black lines for $U^{dp} = U^{pp} = 0.5U^{dd}$ and the blue lines for $U^{dp} = U^{pp} = 0$. The red and green, dashed lines show the results from applying the Hartree and the Hartree-Fock approximation, respectively. Panel (b) and (c) show the imaginary part of the d orbital self-energies, comparing the results with and without inter-shell interaction, as well as with different approximation schemes (with "H" standing Hartree, "H-F" for Hartree-Fock). The d orbital interaction strength is $U^{dd} = 5$ (b) and $U^{dd} = 10$ (c). In all calculations, we set $V = 3.5$ and $\beta = 32$.

In the scenario discussed in the second point, effects from the inter-shell interaction are significant, and cannot be captured by simply adding a constant Hartree shift to the self-energy. On the other hand, the increasing difficulty of performing calculations for a growing number of orbitals motivates us to seek different ways to treat the effect of U^{dp} on an approximative level. This will be the topic of the next chapter.

5.4 Conclusions

In this chapter, we have discussed the physics of models with two different, interacting shells – the d-p problem. To this end, we focused on the most simple model realization for such a system – the two orbital Hubbard model with off-diagonal (in orbital space) intra- and inter-site hopping. The specific form of the model under consideration corresponds to the model emerging from the Zhang-Rice construction, truncated to nearest-neighbor hoppings.

In the case without inter-shell interactions, we studied the different solutions realized in the phase space spanned by the Hubbard interaction and the charge-transfer energy (U^{dd}, $\tilde{\Delta}$), reproducing a

phase diagram of Zaanen-Sawatzky-Allen type in the case for 3/4 filling $N = N_d + N_p = 3$. In the metallic phase, we discussed how the charge-transfer energy $\Delta = \varepsilon^d = \varepsilon^p$ influences correlations. In the insulating phase, we demonstrated how this parameter changes the character of the spectral gap, resulting in a transition from a *charge-transfer insulator* at small Δ to a Mott insulator at large Δ.

We then proceeded to discussing how inter-shell interactions influence the correlations of the model system. Our results, obtained for different parameter-sets, suggest that inter-shell interactions generally *decrease* the correlations of the system. We explain this observation with the decrease of the effective charge-transfer energy, as well as a reduction of the effective interaction due to screening (see Sec. 5.2.3).

Our results for fixed individual fillings N_d and N_p demonstrate that the effect of inter-shell interactions, after compensating for interaction-induced charge-transfer, is more subtle. In particular, we still find a decrease in correlations in the metallic regime away from commensurate filling. On the other hand, at $N = 3$ and fixed N_d, N_p, we find that U^{dp}, U^{pp} make the system more strongly correlated, even inducing a phase transition.

Since inter-shell interactions are notoriously hard to handle in calculations, we investigated the efficiency of simple mean-field approximations to treat these interactions in an effective manner. We find that in the metallic regime, Hartree-Fock-type approximations provide reasonable results, at negligible computational cost. However, in the strongly correlated regime, where the additional interactions can lead to a phase transition, they fail, emphasizing the necessity of more sophisticated approximations.

Chapter 6

Slave Rotor Approach to the d-p Problem

6.1 Motivation & outline

In the previous section 2.3, we introduced the slave rotor technique. The reason for this is, that we would like to apply it to the d-p model. In section 5.3 we discussed some of the physics emerging from models with inter-shell coupling, by considering the most simple case of a "1+1"-orbital system. While the two orbital model constitutes a special case of the systems of interest, it is clear that the difficulties encountered in the corresponding Monte Carlo simulations (especially due to the negative sign problem) would increase drastically with every additional orbital.

In section 5.2.3, we already discussed the shell-folding approximation[141] as a simple scheme to derive an effective Hamiltonian in which the inter-shell interaction is eliminated and only serves to re-normalize the other interactions. The shell-folding approximation is based on the physical assumption, that the dominant screening process for charge fluctuations of the d-electrons is mediated by the surrounding ligands. This means, that shell-folding would become exact in the limit of "perfect-screening", in which every d-charge fluctuation is perfectly canceled by a compensating fluctuation of a p-charge, making the sum of the local charges $N_i^{tot} = \sum_{m\sigma} n^d_{im\sigma} + \sum_{n\sigma} n^p_{in\sigma}$ a constant on each cell.

We have seen that in most parameter regimes, the inter-shell interaction U^{dp} effectively reduces correlations, as predicted by shell-folding. However, it is also clear that the efficiency of the screening by the electrons on the same site is, in general, far from perfect. It is for this reason, that we would like to incorporate charge fluctuations into our theory. As announced, this shall be done making use of the slave rotor formalism introduced in the previous section; this time, however, we shall work in a functional integral formalism (a corresponding derivation of the slave rotor technique can be found in [50]).

6.2 Rotorization of the action

To keep the discussion as simple as possible, we shall again consider the minimal two-orbital impurity model, which serves us as a test case for the general d-p problem (we emphasize, however, that the following derivation is general and not restricted to two-orbital models). The action reads

$$S_{dp} = S_{atom} + S_{hyb} \,, \tag{6.1}$$

with

$$\begin{aligned} S_{atom} = \int_0^\beta \mathrm{d}\tau \, \Bigg\{ & \sum_\sigma \left(d_\sigma^\dagger \partial_\tau d_\sigma + p_\sigma^\dagger \partial_\tau p_\sigma \right) \\ & + \sum_\sigma (\varepsilon^d - \mu) d_\sigma^\dagger d_\sigma + \sum_\sigma (\varepsilon^p - \mu) p_\sigma^\dagger p_\sigma + \sum_\sigma \left(V d_\sigma^\dagger p_\sigma + h.c. \right) \\ & + (U^{dd} - U^{dp}) n_\uparrow^d n_\downarrow^d + (U^{pp} - U^{dp}) n_\uparrow^p n_\downarrow^p + \frac{U^{dp}}{2} (N_d + N_p - 2)^2 \Bigg\} \end{aligned} \tag{6.2}$$

and

$$S_{hyb} = \iint_0^\beta \mathrm{d}\tau \mathrm{d}\tau' \sum_\sigma \begin{bmatrix} d_\sigma^\dagger(\tau) & p_\sigma^\dagger(\tau) \end{bmatrix} \mathbf{\Delta}^{dp}(\tau - \tau') \begin{bmatrix} d_\sigma(\tau') \\ p_\sigma(\tau') \end{bmatrix} \,, \tag{6.3}$$

where the matrix quantity $\mathbf{\Delta}^{dp}(\tau - \tau')$ is defined by (5.32). Note that in (6.2), we used the shell-folding rewriting in which U^{dp} renormalizes the other interactions, but we kept the interaction of the total charge (the additional -2 corresponds to the number of orbitals and was introduced for later convenience; the energy shift it induces is supposed to be absorbed in the chemical potential μ).

The goal is to incorporate fluctuations of the term $(N_d + N_p - 2)^2$. To achieve this, we proceed by decoupling it using a Hubbard-Stratonovich (HS) transformation

$$\frac{U^{dp}}{2} (N_d + N_p - 2)^2 \xrightarrow[\text{HS trans.}]{} \frac{1}{2U^{dp}} \phi^2 + i\phi (N_d + N_p - 2) \,. \tag{6.4}$$

After this transformation, the atomic action becomes

$$\begin{aligned} S_{atom} = \int_0^\beta \mathrm{d}\tau \, \Bigg\{ & \sum_\sigma \left(d_\sigma^\dagger \partial_\tau d_\sigma + p_\sigma^\dagger \partial_\tau p_\sigma \right) \\ & + \sum_\sigma (\varepsilon^d + i\phi - \mu) d_\sigma^\dagger d_\sigma + \sum_\sigma (\varepsilon^p + i\phi - \mu) p_\sigma^\dagger p_\sigma + \sum_\sigma \left(V d_\sigma^\dagger p_\sigma + h.c. \right) \\ & + (U^{dd} - U^{dp}) n_\uparrow^d n_\downarrow^d + (U^{pp} - U^{dp}) n_\uparrow^p n_\downarrow^p + \frac{1}{2U^{dp}} \phi^2 - 2i\phi \Bigg\} . \end{aligned} \tag{6.5}$$

The price for eliminating the interaction term is the emergence of a HS field ϕ that couples directly to the electron density. We will, therefore, apply a gauge transformation to the electronic fields[1]

$$d(\tau) = \tilde{d}(\tau)e^{-i\theta(\tau)} \tag{6.6}$$

$$p(\tau) = \tilde{p}(\tau)e^{-i\theta(\tau)} \tag{6.7}$$

$$\theta(\tau) = \int_0^\tau \mathrm{d}\tau' \phi(\tau') - \tau\frac{\phi_0}{\beta}\,, \tag{6.8}$$

with $\phi_0 = \int_0^\beta \mathrm{d}\tau\ \phi(\tau)[2\pi]$. With this transformation, the coupling to the dynamic part of the HS field is encoded in a U(1) variable $e^{\pm i\theta}$, leaving only an explicit coupling to the static component ϕ_0. The atomic part of the action then reads

$$\begin{aligned} S_{atom} = \int_0^\beta \mathrm{d}\tau\ \Bigg\{ & \sum_\sigma \left(\tilde{d}^\dagger_\sigma(\partial_\tau + i\phi_0/\beta)\tilde{d}_\sigma + \tilde{p}^\dagger_\sigma(\partial_\tau + i\phi_0/\beta)p_\sigma\right) \\ & + \sum_\sigma(\varepsilon^d - \mu)\tilde{d}^\dagger_\sigma\tilde{d}_\sigma + \sum_\sigma(\varepsilon^p - \mu)\tilde{p}^\dagger_\sigma\tilde{p}_\sigma + \sum_\sigma\left(V\tilde{d}^\dagger_\sigma\tilde{p}_\sigma + h.c.\right) \\ & + (U^{dd} - U^{dp})\tilde{n}^d_\uparrow\tilde{n}^d_\downarrow + (U^{pp} - U^{dp})\tilde{n}^p_\uparrow\tilde{n}^p_\downarrow + \frac{1}{2U^{dp}}\phi^2 - 2i\phi \Bigg\}\,, \end{aligned} \tag{6.9}$$

where the coupling $i\phi(\tilde{N}_d + \tilde{N}_p)$ was canceled by the terms emerging from the time derivatives acting on the transformed electron fields $\partial_\tau d(\tau) = -i(\phi - \phi_0/\beta)\tilde{d}(\tau)e^{-i\theta(\tau)} + (\partial_\tau\tilde{d}(\tau))e^{-i\theta(\tau)}$. While we could almost entirely decouple the electrons from the HS field in the atomic action, we introduced an explicit coupling in the hybridization term

$$S_{hyb} = \iint_0^\beta \mathrm{d}\tau\mathrm{d}\tau' \sum_\sigma \begin{bmatrix}\tilde{d}^\dagger_\sigma(\tau) & \tilde{p}^\dagger_\sigma(\tau)\end{bmatrix} \mathbf{\Delta}^{dp}(\tau - \tau') \begin{bmatrix}\tilde{d}_\sigma(\tau') \\ \tilde{p}_\sigma(\tau')\end{bmatrix} e^{i(\theta(\tau) - \theta(\tau'))}\,. \tag{6.10}$$

The form of the transformed action is reminiscent of the slave rotor formulation of Ref. [50] introduced in 2.3 and indeed, we can retrieve the original formulation by performing a second transformation $1/(2U^{dp})\phi^2 \to (U^{dp}/2)L^2 - iL\phi = (U^{dp}/2)L^2 - iL(\partial_\tau\theta + \phi_0/\beta)$. While this doesn't change the form of the hybridization part(6.11), the atomic action becomes

$$\begin{aligned} S_{atom} = \int_0^\beta \mathrm{d}\tau\ \Bigg\{ & \sum_\sigma \left(\tilde{d}^\dagger_\sigma(\partial_\tau + i\phi_0/\beta)\tilde{d}_\sigma + \tilde{p}^\dagger_\sigma(\partial_\tau + i\phi_0/\beta)p_\sigma\right) \\ & + \sum_\sigma(\varepsilon^d - \mu)\tilde{d}^\dagger_\sigma\tilde{d}_\sigma + \sum_\sigma(\varepsilon^p - \mu)\tilde{p}^\dagger_\sigma\tilde{p}_\sigma + \sum_\sigma\left(V\tilde{d}^\dagger_\sigma\tilde{p}_\sigma + h.c.\right) \\ & + (U^{dd} - U^{dp})\tilde{n}^d_\uparrow\tilde{n}^d_\downarrow + (U^{pp} - U^{dp})\tilde{n}^p_\uparrow\tilde{n}^p_\downarrow + \frac{U^{dp}}{2}L^2 - iL\left(\frac{\partial\theta}{\partial\tau} + \frac{\phi_0}{\beta}\right) - 2i\frac{\phi_0}{\beta} \Bigg\}\,. \end{aligned} \tag{6.11}$$

[1] This transformation leaves the measure invariant, so we will not encounter any additional difficulties when calculating the path integral.

We recognize the angular momentum variable L, corresponding to the operator $\hat{L}$, as well as the phase variable θ, which is conjugate to L. The static field component ϕ_0/β corresponds to the Lagrange multiplier. We will restrict ourselves to its saddle-point value of $h = -i\phi_0/\beta$ (which again, we allow to be complex), defined by

$$\langle L \rangle \stackrel{!}{=} \sum_\sigma \langle \tilde{d}_\sigma^\dagger \tilde{d}_\sigma \rangle + \sum_\sigma \langle \tilde{p}_\sigma^\dagger \tilde{p}_\sigma \rangle - 2 \,, \tag{6.12}$$

or, equivalently

$$\frac{1}{U^{dp}} i \left(\left\langle \frac{\partial \theta}{\partial \tau} \right\rangle + ih \right) \stackrel{!}{=} \sum_\sigma \langle \tilde{d}_\sigma^\dagger \tilde{d}_\sigma \rangle + \sum_\sigma \langle \tilde{p}_\sigma^\dagger \tilde{p}_\sigma \rangle - 2 \,, \tag{6.13}$$

(the second expression can be derived by considering the saddle-point corresponding to action (6.2)). To make the problem tractable, we then perform a mean-field decoupling of the action. Since in the atomic action (6.11), fermionic and rotor variables are only coupled via ϕ_0, the mean-field decoupling only affects the hybridization term (6.10) and we get

$$S_{dp}^{MF} = S_{atom} + S_{hyb}^f + S_{hyb}^\theta \,, \tag{6.14}$$

with

$$S_{hyb}^f = \iint_0^\beta \mathrm{d}\tau \mathrm{d}\tau' \sum_\sigma \begin{bmatrix} \tilde{d}_\sigma^\dagger(\tau) & \tilde{p}_\sigma^\dagger(\tau) \end{bmatrix} \mathbf{\Delta}_f^{dp}(\tau - \tau') \begin{bmatrix} \tilde{d}_\sigma(\tau') \\ \tilde{p}_\sigma(\tau') \end{bmatrix} \,, \tag{6.15}$$

$$S_{hyb}^\theta = \iint_0^\beta \mathrm{d}\tau \mathrm{d}\tau' \, \Delta_\theta^{dp}(\tau - \tau') e^{i(\theta(\tau) - \theta(\tau'))} \,. \tag{6.16}$$

By using the Feynman-Peierls variational principle, we define the functions $\mathbf{\Delta}_f^{dp}(\tau)$ and Δ_θ^{dp} to optimize the functional

$$\varepsilon[\mathbf{\Delta}_f^{dp}(\tau), \Delta_\theta^{dp}] = \left\langle S_{dp} - S_{dp}^{MF} \right\rangle_{S_{dp}^{MF}} - \ln Z^{MF} + \ln Z \,. \tag{6.17}$$

Furthermore, we introduced Z^{MF} and Z as the partition functions corresponding to S_{dp}^{MF} and S_{dp}, respectively. Not surprisingly, the functional is optimized by

$$\mathbf{\Delta}_f^{dp}(\tau - \tau') = \left\langle e^{i(\theta(\tau) - \theta(\tau'))} \right\rangle_{S_{dp}^{MF}} \mathbf{\Delta}^{dp}(\tau - \tau') \tag{6.18}$$

$$\Delta_\theta^{dp}(\tau - \tau') = \sum_\sigma \left\langle \begin{bmatrix} \tilde{d}_\sigma^\dagger(\tau) & \tilde{p}_\sigma^\dagger(\tau) \end{bmatrix} \mathbf{\Delta}^{dp}(\tau - \tau') \begin{bmatrix} \tilde{d}_\sigma(\tau') \\ \tilde{p}_\sigma(\tau') \end{bmatrix} \right\rangle_{S_{dp}^{MF}} \,. \tag{6.19}$$

After these functions have been evaluated self-consistently, any physical observable can be evaluated as an expectation value with respect to the mean-field action S_{dp}^{MF}. Analogously to (2.39), the impurity

Green's function factorizes to

$$\mathbf{G}^{imp}(\tau-\tau') = -\left\langle T\begin{bmatrix}\tilde{d}(\tau)\tilde{d}^{\dagger}(\tau') & \tilde{d}(\tau)\tilde{p}(\tau')\\ \tilde{p}(\tau)\tilde{d}^{\dagger}(\tau') & \tilde{p}(\tau)\tilde{p}(\tau')\end{bmatrix}\right\rangle \left\langle e^{-i(\theta(\tau)-\theta(\tau'))}\right\rangle = \tilde{\mathbf{G}}^{imp}(\tau-\tau')G^{\theta}(\tau-\tau')\,. \tag{6.20}$$

6.2.1 DMFT self-consistency

Assuming that we have a way to calculate $\tilde{\mathbf{G}}^{imp}(\tau-\tau')$ and $G^{\theta}(\tau-\tau')$, we can use the DMFT approximation to incorporate the effect of the lattice. In practice, the self-consistency conditions (6.18) and (6.19) will be updated during the DMFT cycles, such that the overall scheme becomes the following.
Starting from an initial guess for $\mathbf{\Delta}_f^{dp}$ and Δ_{θ}^{dp} (or, equivalently, $\mathbf{\Delta}^{dp}$, $\tilde{\mathbf{G}}^{imp}$ and G^{θ}),

1. solve the impurity model S_{dp}^{MF} to obtain $\tilde{\mathbf{G}}^{imp}(\tau-\tau')$ and $G^{\theta}(\tau-\tau')$.

2. Use the Dyson equation to calculate the local self energy $\mathbf{\Sigma}_{i\omega} = \left[\mathbf{G}^0_{i\omega}\right]^{-1} - \left[\mathbf{G}^{imp}_{i\omega}\right]^{-1}$. Here $\mathbf{G}^0_{i\omega}$ is the non-interacting Green's function corresponding to the non-interacting part of (6.1).

3. Calculate the local Green's function

$$\mathbf{G}^{loc}_{i\omega} = \frac{1}{N}\sum_{\mathbf{k}}\left(\mathbb{1}(i\omega+\mu) - \varepsilon(\mathbf{k}) - \mathbf{\Sigma}_{i\omega}\right)^{-1} \tag{6.21}$$

   and use the result to calculate the new Weiss field, i.e. free Green's function

$$\left[\mathbf{G}^0_{i\omega}\right]^{-1} = \left[\mathbf{G}^{loc}_{i\omega}\right]^{-1} + \mathbf{\Sigma}_{i\omega}\,. \tag{6.22}$$

4. Derive the hybridization function

$$\mathbf{\Delta}^{dp}_{i\omega} = \mathbb{1}(i\omega+\mu) - \begin{bmatrix}\varepsilon^d & V\\ V* & \varepsilon^p\end{bmatrix} - \left[\mathbf{G}^0_{i\omega}\right]^{-1}\,, \tag{6.23}$$

   and calculate $\mathbf{\Delta}_f^{dp}$ and Δ_{θ}^{dp} (using $\tilde{\mathbf{G}}^{imp}$ and G^{θ}) to construct the new action S_{dp}^{MF}.

5. Iterate until $\mathbf{G}^{imp}_{i\omega} = \mathbf{G}^{loc}_{i\omega}$ and the self-consistency equations (6.18) & (6.19) are fulfilled.

Even though we eliminated the inter-shell interactions in the fermionic part of the action, we still have to deal with interactions within the d- and the p- shells. In case of the p-orbitals, this interaction is supposed to be rather weak and will be even further decreased upon subtracting U^{dp}. Thus, we can hope that the effect of the p-p Coulomb interaction can be well described by a Hatree approximation. The d-orbitals, however, will remain correlated, and we will have to apply numerical methods (see section C.2) in order to solve the impurity model.

On the other hand, we have to evaluate $G^\theta(\tau-\tau')$, which poses a non-trivial problem by itself. We shall discuss several approaches in the following.

6.3 Evaluating the rotor Green's function

Our goal is to calculate the Green's function

$$G^\theta(\tau-\tau') = \left\langle e^{-i(\theta(\tau)-\theta(\tau'))} \right\rangle_{S^\theta_{dp}} , \tag{6.24}$$

corresponding to the mean-field decoupled rotor action

$$S^\theta_{dp} = \int_0^\beta \mathrm{d}\tau \left\{ -iL\frac{\partial\theta}{\partial\tau} + hL + \frac{U^{dp}}{2}L^2 \right\} + \iint_0^\beta \mathrm{d}\tau\mathrm{d}\tau' \, \Delta^{dp}_\theta(\tau-\tau') e^{i(\theta(\tau)-\theta(\tau'))} . \tag{6.25}$$

6.3.1 The atomic limit

In the atomic limit, the rotor hybridization function $\Delta^{dp}_\theta(\tau-\tau')$ (which can be shown to correspond to the kinetic energy of the fermions, see Appendix D.2) approaches zero, and we can find an analytic expression (see Appendix D.1) for the Green's function

$$G^\theta_0(\tau) = \frac{\sum_n \cos\{2n\pi(\frac{h}{U^{dp}}-2+\tau/\beta)\} e^{-\frac{2n^2\pi^2}{U^{dp}\beta}}}{\sum_n \cos\{2n\pi(\frac{h}{U^{dp}}-2\} e^{-\frac{2n^2\pi^2}{U^{dp}\beta}}} \exp\left\{ \sum_\nu \left\{ \frac{U^{dp}}{\beta\nu^2}(\cos(\nu\tau)-1) \right\} \right\} , \tag{6.26}$$

where $\nu_m = m\frac{2\pi}{\beta}$ and the sum $\sum_\nu$ runs over all ν_m with m being an integer $m \in (-\infty,\infty)$.
Using a Green's function formalism, the saddle-point constraint (6.12) e.g. (6.13), translates into

$$\frac{1}{U^{dp}}\left(-\frac{\partial_\tau G^\theta(\tau=0^-) + \partial_\tau G^\theta(\tau=0^+)}{2} - h \right) \stackrel{!}{=} \sum_\sigma \langle \tilde{d}^\dagger_\sigma \tilde{d}_\sigma \rangle + \sum_\sigma \langle \tilde{p}^\dagger_\sigma \tilde{p}_\sigma \rangle - 2 , \tag{6.27}$$

which can be derived from (6.13) and by considering that

$$i\left\langle \frac{\partial\theta}{\partial\tau} \right\rangle = -\frac{1}{2}\left(\frac{\partial}{\partial\tau}\left\langle e^{-i[\theta(\tau=0^+)-\theta(0)]} \right\rangle + \frac{\partial}{\partial\tau}\left\langle e^{-i[\theta(\tau=0^-)-\theta(0)]} \right\rangle \right) , \tag{6.28}$$

where one has to care about the discontinuity of the first derivative.

Comparing expressions (6.27) and (6.26), this means that

- For $h=0$, G^θ_0 is symmetric around $\tau=0$, therefore $\partial_\tau G^\theta(\tau=0^-) = -\partial_\tau G^\theta(\tau=0^+)$ and the left side of (6.27) vanishes: The system is at half filling $N=2$.
- For $h\neq 0$, the system departs from half filling. Note that a finite rotor filling can only be achieved due to the summation over the integer winding number n in (6.26): If one only considered the $n=0$ contribution, the rotor system would be stuck at half filling.

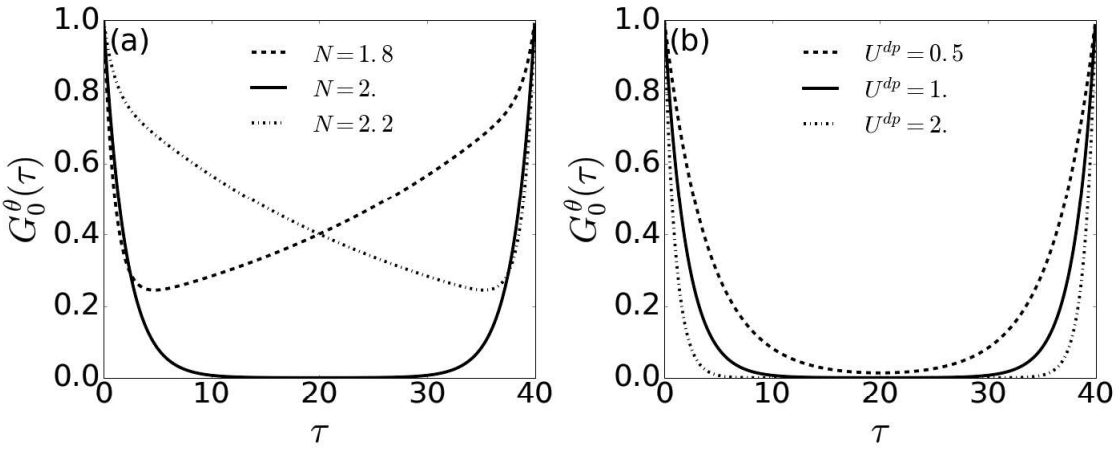

Fig. 6.1 Rotor Green's function in the atomic limit for (a) different fillings and (b) different values of the interaction U^{dp}.

Fig. 6.1 shows the rotor Green's function in the atomic limit for various fillings N (left panel (a)) and various interaction strengths U^{dp} (right panel (b)). Yet another important point has to be clarified. When deriving the mean-field formalism in Sec. 2.3.2, we identified the expectation value

$$\langle \cos\theta \rangle_\theta^2 = \lim_{\beta\to\infty} \langle \cos(\theta(\beta/2))\cos(\theta(0)) \rangle_\theta = \lim_{\beta\to\infty} G_0^\theta(\beta/2) \tag{6.29}$$

as the quasi-particle renormalization Z of the auxiliary fermions. In the atomic limit, this value will always be zero, as it is already adumbrated by Fig. 6.1 (b). This means, that the atomic limit approximation can only be expected to be of relevance in the insulating phase, which is in contrast with similar implementations, e.g. to describe models with dynamic interactions [95]. A more detailed derivation can be found in Appendix D.1.2.

6.3.2 Beyond the atomic limit

In principle, one could perform a perturbative expansion of the Green's function in the hybridization term (the resulting analytic expressions can be found in Appendix D.1.3). In practice, however, it is more convenient to consider non-perturbative methods to calculate the rotor Green's function.
The only reason why the rotor action (6.25) is hard to tackle is because of the hybridization term, which is non-local in imaginary time. One way to circumvent this proxblem is to consider a Hamiltonian formalism, and apply the slave rotor transformation to Hamiltonian (5.26)

$$H_{imp}^{SR} = H_{atom}^{SR} + H_{hyb}^{SR} , \tag{6.30}$$

such that

$$\begin{aligned} H^{SR}_{atom} = &\sum_\sigma (\varepsilon^d - \mu - h)\tilde{d}^\dagger_\sigma \tilde{d}_\sigma + \sum_\sigma (\varepsilon^p - \mu - h)\tilde{p}^\dagger_\sigma \tilde{p}_\sigma + \sum_\sigma \left(V \tilde{d}^\dagger_\sigma \tilde{p}_\sigma + h.c.\right) \\ &+ (U^{dd} - U^{dp})\tilde{n}^d_\uparrow \tilde{n}^d_\downarrow + (U^{pp} - U^{dp})\tilde{n}^p_\uparrow \tilde{n}^p_\downarrow + \frac{U^{dp}}{2}\hat{L}^2 + h\hat{L}\,, \end{aligned} \tag{6.31}$$

where we used the shell-folding (see Sec. 5.2.3) form, and

$$H^{SR}_{hyb} = \sum_{k\sigma} \left\{ \begin{bmatrix} \tilde{d}^\dagger_\sigma & \tilde{p}^\dagger_\sigma \end{bmatrix} \begin{bmatrix} V^{dd}_k & V^{dp}_k \\ V^{pd}_k & V^{pp}_k \end{bmatrix} \begin{bmatrix} b^d_{k\sigma} \\ b^p_{k\sigma} \end{bmatrix} e^{i\theta} + h.c. \right\} + \sum_{k\sigma} E^d_k b^{d\dagger}_{k\sigma} b^d_{k\sigma} + \sum_{k\sigma} E^p_k b^{p\dagger}_{k\sigma} b^{p\dagger}_{k\sigma}\,. \tag{6.32}$$

A mean-field decoupling of (6.30) leads to

$$H^{SR}_{imp} = H^f_{imp} + H^\theta_{imp}\,, \tag{6.33}$$

with

$$\begin{aligned} H^f_{imp} = &\sum_\sigma (\varepsilon^d - \mu - h)\tilde{d}^\dagger_\sigma \tilde{d}_\sigma + \sum_\sigma (\varepsilon^p - \mu - h)\tilde{p}^\dagger_\sigma \tilde{p}_\sigma + \sum_\sigma \left(V \tilde{d}^\dagger_\sigma \tilde{p}_\sigma + h.c.\right) \\ &+ (U^{dd} - U^{dp})\tilde{n}^d_\uparrow \tilde{n}^d_\downarrow + (U^{pp} - U^{dp})\tilde{n}^p_\uparrow \tilde{n}^p_\downarrow \\ &+ \sum_{k\sigma} \left\{ \begin{bmatrix} \tilde{d}^\dagger_\sigma & \tilde{p}^\dagger_\sigma \end{bmatrix} \begin{bmatrix} V^{dd}_k & V^{dp}_k \\ V^{pd}_k & V^{pp}_k \end{bmatrix} \begin{bmatrix} b^d_{k\sigma} \\ b^p_{k\sigma} \end{bmatrix} \left\langle e^{i\theta} \right\rangle + h.c. \right\} + \sum_{k\sigma} E^d_k b^{d\dagger}_{k\sigma} b^d_{k\sigma} + \sum_{k\sigma} E^p_k b^{p\dagger}_{k\sigma} b^{p\dagger}_{k\sigma} \end{aligned} \tag{6.34}$$

and

$$\begin{aligned} H^\theta_{imp} &= \frac{U^{dp}}{2}\hat{L}^2 + h\hat{L} + \sum_{k\sigma} \left\{ \left\langle \begin{bmatrix} \tilde{d}^\dagger_\sigma & \tilde{p}^\dagger_\sigma \end{bmatrix} \begin{bmatrix} V^{dd}_k & V^{dp}_k \\ V^{pd}_k & V^{pp}_k \end{bmatrix} \begin{bmatrix} b^d_{k\sigma} \\ b^p_{k\sigma} \end{bmatrix} \right\rangle e^{i\theta} + h.c. \right\} \\ &= \frac{U^{dp}}{2}\hat{L}^2 + h\hat{L} + \frac{1}{2}E^f_{kin}\left(e^{i\theta} + e^{-i\theta}\right)\,, \end{aligned} \tag{6.35}$$

where E^f_{kin} is the kinetic energy of the auxiliary fermions (for a derivation see Appendix D.2). After this decoupling, we can proceed as in Sec. 6.2.1, using the DMFT self-consistency. For the auxiliary fermions, we can integrate out the bath states, such that one retrieves (6.15), with the only difference that now the rotor expectation value in (6.18) factorizes

$$\Delta^{dp}_f(\tau - \tau') = \left\langle e^{i\theta} \right\rangle^2 \Delta^{dp}(\tau - \tau')\,. \tag{6.36}$$

Otherwise, nothing changes and $\tilde{\mathbf{G}}^{imp}$ still has to be calculated using numerical methods.
On the other hand, the calculation of G^θ simplifies drastically, since Hamiltonian (6.35) can be diagonalized by truncating its spectrum and mapping it onto a matrix, as explained in Appendix A.1. The Green's function G^θ can then simply be calculated by evolving the operator $e^{i\theta(\tau)}$ in time.

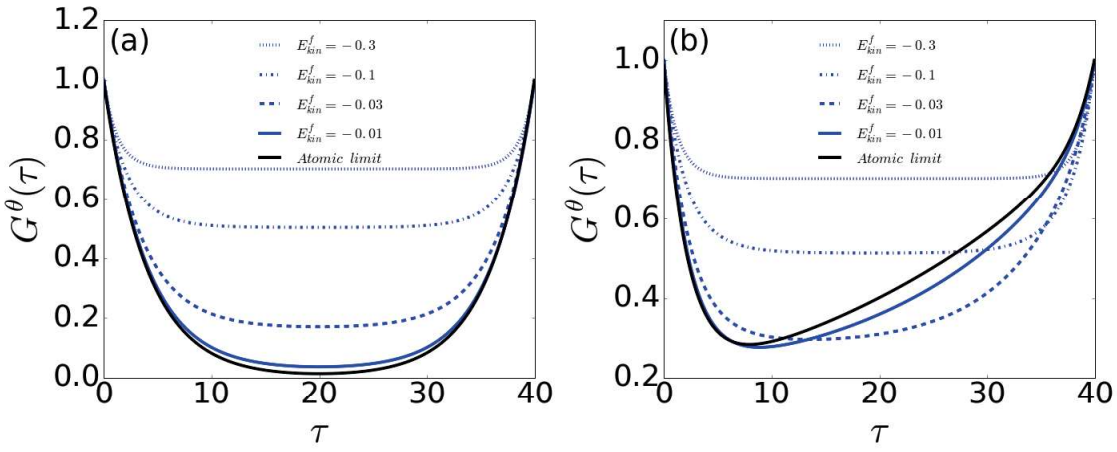

Fig. 6.2 Rotor Green's functions for various values of the kinetic energy E^f_{kin} corresponding to the auxiliary fermions. The black lines mark the Green's function in the atomic limit, i.e. $E_{kin} = 0$. Panel (a) shows the Green's functions at half filling $N = 2$, while panel (b) shows the same quantities for $N = 1.8$.

Fig. 6.2 shows the rotor Green's function for different values of the auxiliary fermion kinetic energy E^f_{kin}. For kinetic energy $E^f_{kin} > 0$, the imaginary time Green's functions form a plateau characterized by $G^\theta(\beta/2) \approx \langle e^{i\theta} \rangle^2$. Upon increasing the magnitude of E^f_{kin}, this value approaches one $\langle e^{i\theta} \rangle \xrightarrow[|E_{kin}|\to\infty]{} 1$, and the physical Green's function (6.20) approaches the auxiliary fermionic one $\mathbf{G}^{imp}(\tau) \xrightarrow[|E_{kin}|\to\infty]{} \tilde{\mathbf{G}}^{imp}(\tau)$.
Looking at the right panel 6.2 (b), it is remarkable to see how even small values of $|E^f_{kin}|$ counteract the asymmetry that characterizes the rotor Green's function away from half filling.

6.4 Numerical results for the d-p problem

In the following, we present some results obtained by the slave-rotor technique, as derived in the previous section, applied to the d-p problem.

6.4.1 The insulating phase

We start by considering the insulating regime, where we expect reasonable results from the atomic limit approximation to the rotor problem. Fig. 6.3 shows the imaginary part of the d orbital Green's function and self-energy, comparing results obtained from the slave rotor and shell-folding approximations to those from the full numerical two orbital calculations. Looking at the Green's functions in panels (a), (c) and (e), we see that the results from the slave rotor scheme stay rather close to the reference calculations, while those obtained from shell-folding deviate more strongly upon increasing the inter-shell interaction. This goes up to the point where the strong shell-folding renormalization of the

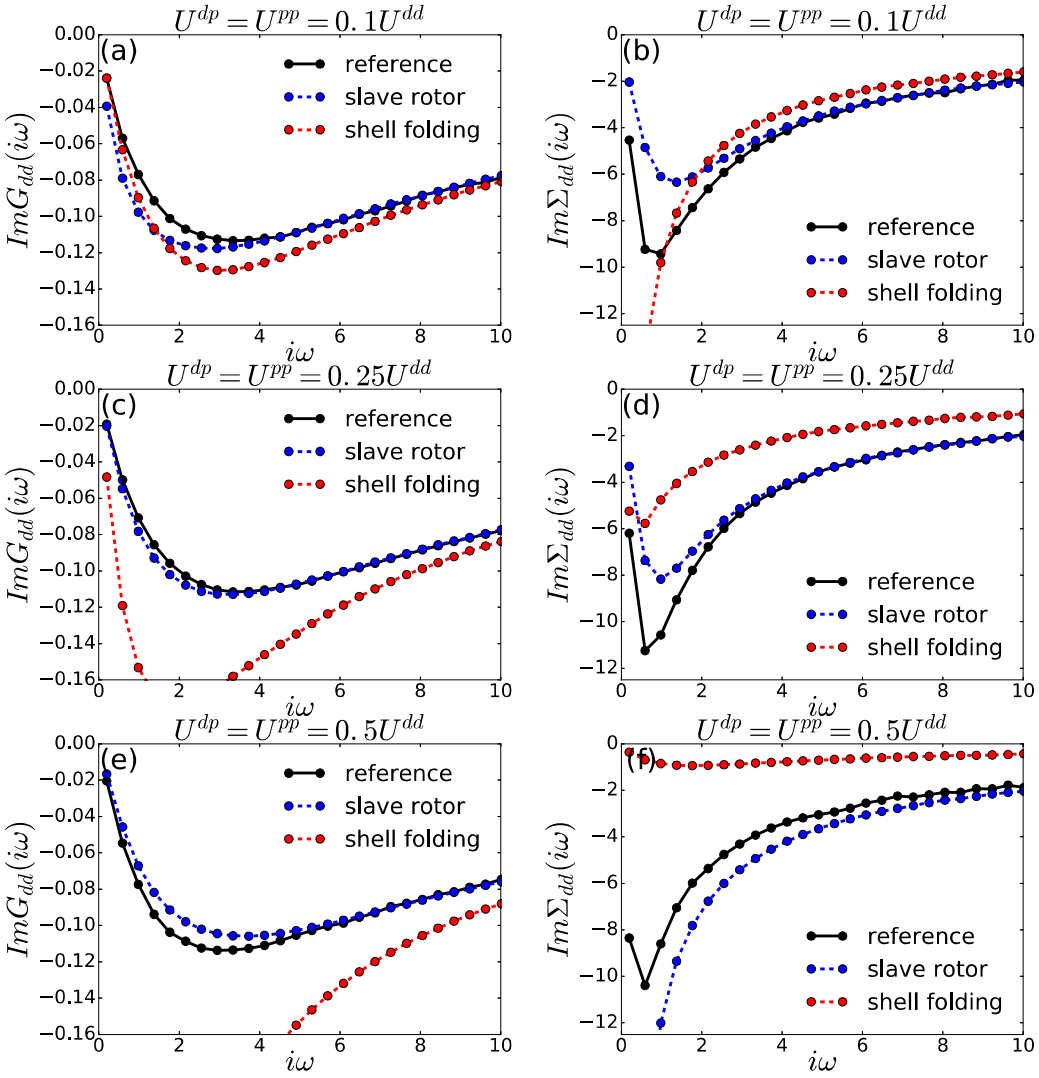

Fig. 6.3 Imaginary part of the d orbital Green's function and self energy for total filling $N = 3$, $U^{dd} = 10$, $V = 3.5$, $\beta = 16$ and various values of $U^{dp} = U^{pp}$. Solid, black lines denote results from the full model; blue and red dashed lines correspond to the solutions from the slave rotor and shell-folding approximation, respectively.

bare interaction $\tilde{U^{dd}} = U^{dd} - U^{dp}$ turns the system metallic (as can be seen from the behavior of the red curve in panels (e) and (f)).

The breakdown of the shell-folding approximation is also apparent from looking at the self-energies in panels (b), (d) and (f). For increasing U^{dp}, the curves deviate more and more from the reference calculation, even recovering the typical Fermi-liquid behavior for the biggest inter-shell interaction under consideration.

The self-energies also reveal a significant deviation between the slave rotor approximation and the reference calculations. This difference is particularly pronounced for small Matsubara frequencies;

contrary to the shell-folding approximation, however, the slave rotor solution follows the general trend of the reference calculation.

Another striking difference concerns the behavior of the high-frequency tails of the self energies. While the high-frequency behavior of the shell-folding solution is completely off the reference of high inter-shell interactions, the tail from the slave rotor solution remains rather close to the correct result. That such a behavior is indeed expected, can be confirmed by analytical considerations (see Sec. D.4.2).

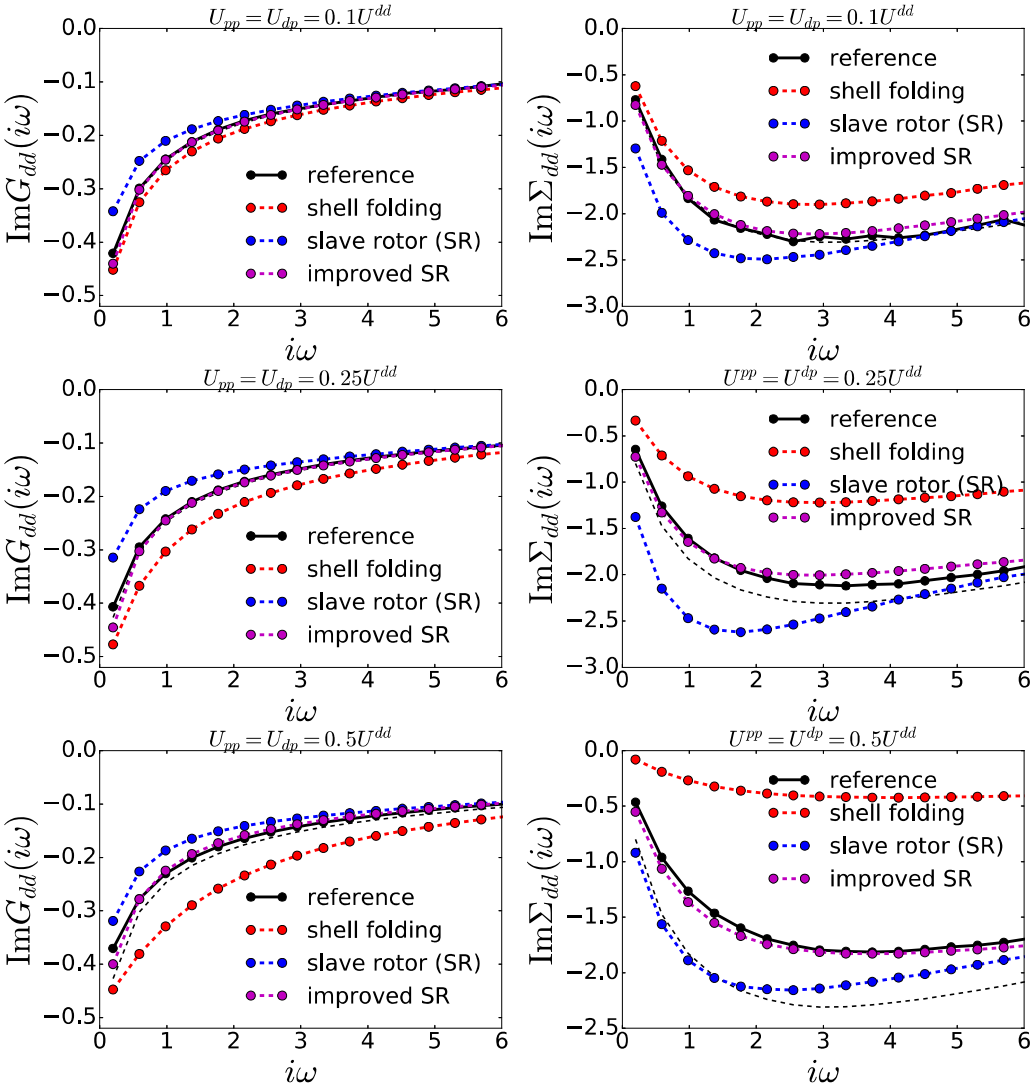

Fig. 6.4 Imaginary part of the d orbital Green's function and self energy for total filling $N_{tot} = 2.8$, d-d interaction $U^{dd} = 10$, charge-transfer energy $\Delta = 0$, $V = 3.5$, $\beta = 16$ and various values of $U^{dp} = U^{pp}$. Solid, black lines denote results from the full model; red, blue and magenta-colored dashed lines correspond to the solutions from the shell-folding, slave rotor and the improved slave rotor approximations, respectively. The results may be compared to the solution for $U^{dp} = U^{pp} = 0$, which is marked by black, dashed lines.

6.4.2 The metallic phase

We now turn to the metallic phase. Fig. 6.4 shows the results for Green's functions and self-energies for different values of inter-shell interactions, for a total filling of $N_{tot} = 2.8$, and parameters $U^{dd} = 10$, $V = 3.5$, $\beta = 16$ (all in units of t). In this regime, the slave rotor approximation (blue) yields only slightly better results than the shell-folding scheme (red), mainly at strong values of $U^{dp} = U^{pp}$.

Again, the slave rotor method is clearly superior in the high-frequency regime; however, close to $i\omega = 0$, the simple shell-folding is mostly closer to the reference solution. This might be explained by the following considerations. First, it is known that the slave rotor method overestimates correlations in the weak to intermediate interaction range (as can be seen from Fig. 2.2). This leads to a stronger depletion of the reconstructed, physical Green's function (6.20) – which, close to $\beta/2$ is approximately $\mathbf{G}^{imp}(\beta/2) = \tilde{\mathbf{G}}^{imp}(\beta/2)G^{\theta}(\beta/2) \approx \tilde{\mathbf{G}}^{imp}(\beta/2)Z_{rot}^2$ – therefore reducing the absolute value of the Green's function for small Matsubara frequencies. On the other hand, it is well known [50, 29], that the slave rotor solution in the low temperature limit is characterized by $\lim_{T\to 0} \mathrm{Im}[\Sigma_{phys}(\omega = 0)] \neq 0$, and therefore does not describe a Fermi liquid.

In [29], this issue motivated the authors to consider a hybrid approach, combining their slave rotor based method (used to treat dynamic interactions) with results for $\mathrm{Im}G(\omega = 0)$ from analytic considerations, such that the resulting Green's functions displayed the correct low-energy behavior.

In the single-site DMFT description of the one-orbital or orbitally degenerate Hubbard models, the Fermi-liquid condition $\lim_{T\to 0} \mathrm{Im}[\Sigma(\omega = 0)] = 0$ pins the Green's function at the Fermi-level to

$$\mathrm{Im}[G(\omega = 0)] = \mathrm{Im} \int \mathrm{d}\varepsilon \frac{D(\varepsilon)}{\mu - \varepsilon - \mathrm{Re}\Sigma(0) - i0^-} = D(\mu - \mathrm{Re}\Sigma(0)) \,, \tag{6.37}$$

since the value of $\mu - \mathrm{Re}\Sigma(0)$ is uniquely defined for a fixed filling. Unfortunately, this is not the case anymore for non-degenerate multi-orbital systems – fixing the filling N_{tot} does not fix $\mu\mathbb{1} - \mathrm{Re}\mathbf{\Sigma}(0)$ (which is now a matrix), and therefore we cannot evaluate the spectral weight at $\omega = 0$.

In lack of a simple, exact method to evaluate the spectral weight at the Fermi-level, we considered a more pragmatic approach to improve upon the original method. Acknowledging, that for intermediate inter-shell interaction strengths, the shell-folding approach gives better results close to the Fermi-level, we use this information for a minimal modification of the rotor Green's function G^{θ}. Analogously to [29], we consider the improved expression

$$G^{\theta+SF}(i\nu) = \begin{cases} a & \text{if } i\nu = 0 \\ \left(1 - be^{-\nu/c}\right) G^{\theta}(i\nu) & \text{if } i\nu \neq 0 \,. \end{cases} \tag{6.38}$$

Two of the three parameters – a and b – are fixed by the conditions that 1) the (physical) Green's function $G_{dd}^{imp}(\tau) = \tilde{G}_{dd}^{imp}(\tau)G^{\theta+SF}(\tau)$ yields the same spectral weight as the shell-folding Green's function at the Fermi level $\mathrm{Im}G_{dd}^{imp}(\omega = 0) = \mathrm{Im}G_{dd}^{SF}(\omega = 0)$ and 2) that $G^{\theta+SF}(0) = G^{\theta+SF}(\beta) = 1$, which ensures that the expectation number of the pseudo-fermions matches the one of the physical

electrons. The third parameter c is a crossover frequency between the shell-folding and the slave rotor behavior. Its optimal value was found to be about the bandwidth $\approx W = 2D$ of the system.

Results from this hybrid method can also be seen in Fig. 6.4, where they are labeled as "improved SR". Indeed, the Green's functions and self-energies obtained from this method are much closer to the reference solution, for all parameters under consideration.

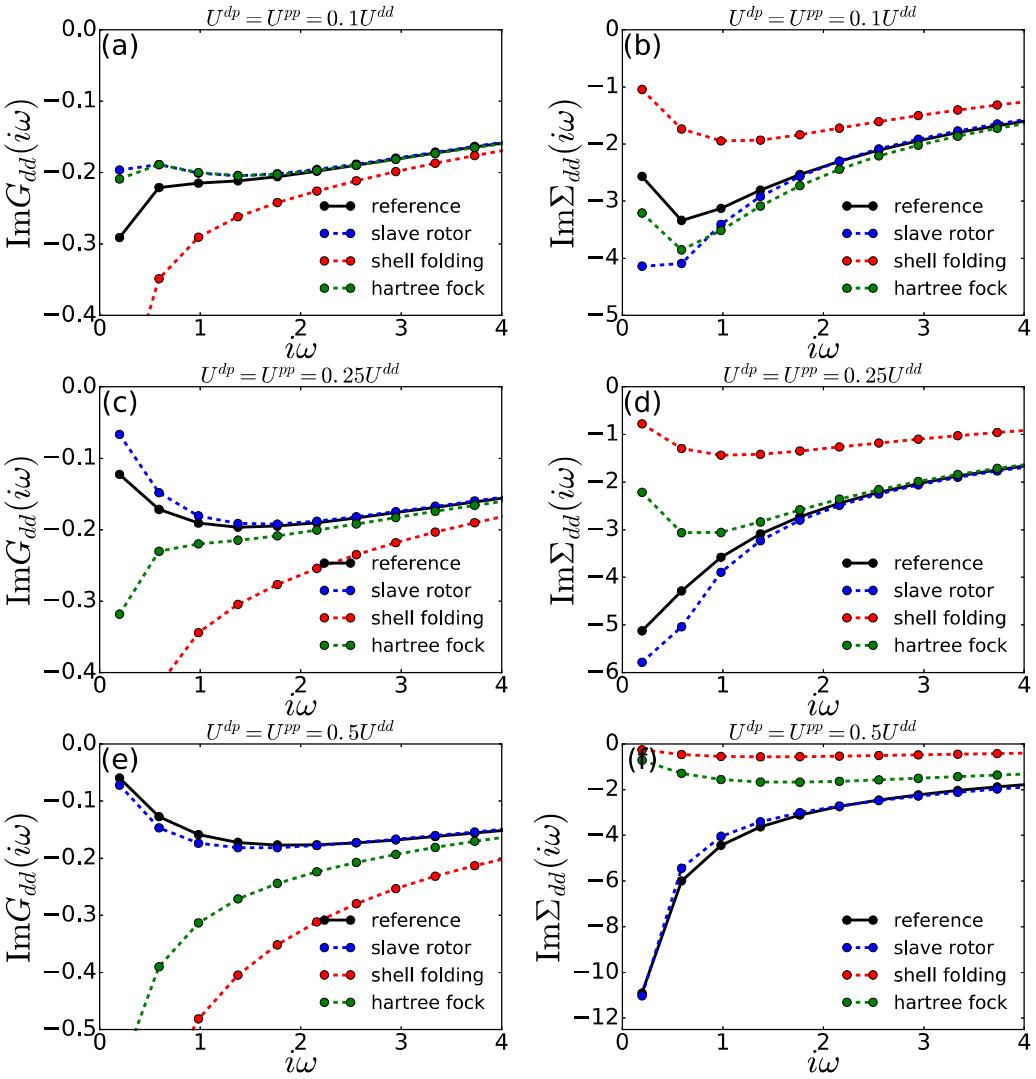

Fig. 6.5 Imaginary part of the d orbital Green's function and self energy for total filling $N_{tot} = 3$, fixed $N_d = 1.1$, interactions $U^{dd} = 6.5$, $V = 3.5$, $\beta = 16$ and various values of $U^{dp} = U^{pp}$. Solid, black lines denote results from the full model; blue, green and red dashed lines correspond to the solutions from the slave rotor, Hartree-Fock and shell-folding approximations, respectively.

The hybrid method is expected to work fine, as long as both the physical- and the shell-folding solution belong to the same (weakly to moderately correlated, metallic) regime. Unfortunately, this must not necessarily be the case, as it became clear by our investigations in the insulating phase,

where strong inter-shell interactions caused the shell-folding solution to undergo a phase-transition to the metallic regime.

6.4.3 The metal-insulator transition

Finally, we shall consider a regime where inter-shell interactions can trigger a phase transition. As discussed in the previous chapter 5.3.2, inter-shell interactions usually decrease the correlations on the transition metal ions. A major reason for this was found in the lowering of the effective charge-transfer energy, facilitating d-p hopping.

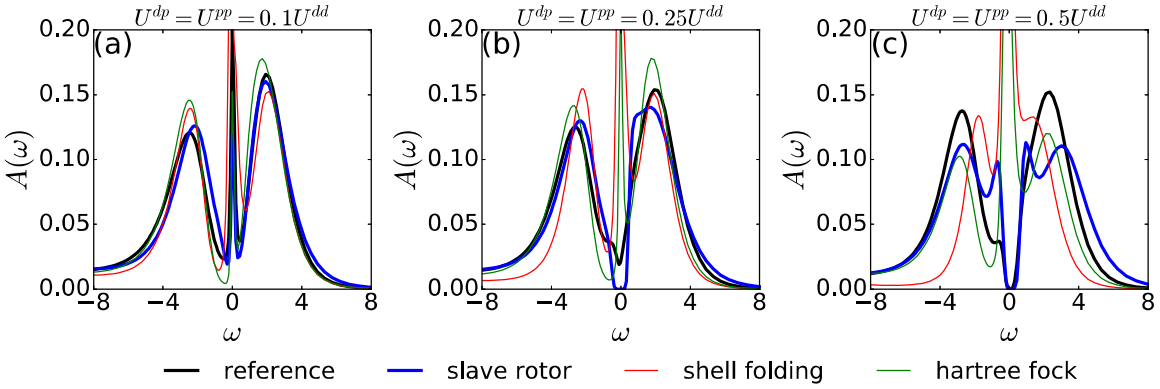

Fig. 6.6 Spectral functions of the d orbital for total filling $N_{tot} = 3$, fixed $N_d = 1.1$, interactions $U^{dd} = 6.5$, $V = 3.5$, $\beta = 16$ and various values of $U^{dp} = U^{pp}$. Solid, black lines denote results from the full model; blue, green and red dashed lines correspond to the solutions from the slave rotor, Hartree-Fock and shell-folding approximations, respectively.

In the following calculations, we eliminate any form of charge-transfer, by fixing the fillings of the individual orbitals to $N_d = 1.1$ and $N_p = 1.9$, respectively. As before, we consider three different values of the inter-shell interaction (which we set equal to the ligand interaction $U^{dp} = U^{pp}$), at constant $U^{dp} = 6.5$ and inverse temperature $\beta = 16$.

As in the previous section on the metallic phase, we consider three different approximate methods and compare them to the exact solution of the model. These methods include the slave rotor approximation and the shell-folding scheme. The hybrid method Eq. (6.38) derived before is not expected to work at a phase transition; therefore, we rather consider the Hartree Fock (HF) approximation (5.38), which we showed to provide a good approximation in the metallic phase (see Fig. 5.15).

Our results are presented in Fig. 6.5 and Fig. 6.6. At small $U^{dp} = U^{pp} = 0.1U^{dd}$, the Green's functions and self energies of both the slave rotor and the HF results are rather close to the reference solution, in contrast to the result obtained from the shell-folding scheme, which already shows a significant deviation. The HF method gives a slightly better result at small Matsubara frequencies, while the slave rotor approach gives a better description of the high-frequency tail. The latter point is due to the fact that the HF approximation treats the many-body inter-shell interactions merely

as shifts of the bare one-body energies, which are not taken into account in the calculation of the high-frequency tail of the self energies.

Upon increasing the inter-shell interactions, the curves corresponding to the shell-folding method deviate increasingly from the reference solutions; describing a weakly correlated metal where the solution of the full two-orbital system is an insulator (panels (e) and (f), for $U^{dp} = U^{pp} = 0.5U^{dd}$). Nevertheless, this is to be expected, since the basic assumption of this scheme is perfect screening of the U^{dd} interaction by charge-transfer from the ligands, thus decreasing the effective d-orbital interaction proportional to U^{dp}. Here, also the Hartree Fock methods fails to follow the correct trend, also predicting a decrease in correlations and increasing coherence. In the case of fixed fillings, the metal-insulator transition is due to interaction-induced correlations, which are not captured by the Hartree-Fock approximation. The solution from the slave rotor method, on the other hand remains close to the reference one, reproducing the correct behavior.

This is further emphasized by Fig. 6.6, which shows the spectral functions $A(\omega) = -\frac{1}{\pi}\mathrm{Im}G(\omega)$ corresponding to the d-orbitals. Within the slave rotor method, increasing correlations caused by inter-shell interactions induce the opening of a spectral gap, thus following the trend of the reference calculations. The middle panel (b) shows a slight difference in the critical interaction values – the qualitative trend, however is preserved.

6.5 Summary & Outlook

Motivated by the difficulty of performing simulations on quantum impurity models with inter-shell interactions, we derived a computationally light-weight technique which treats such interactions on an effective level. The method can be seen as an extension of the *shell-folding* (introduced in [141] and described in chapter 5.2.3) and is designed to be applied in the framework of dynamical mean-field theory.

Our method is based on the slave rotor technique (see 2.3) using an exact reformulation of the original model in terms of auxiliary variables. After deriving the general formalism, we discussed different approximation schemes and provided a detailed description of how to embed the method into DMFT self-consistency cycles.

After discussing the details of the derivation, we give a proof-of-concept, by testing our method in different parameter regimes. In the insulating phase, we find the slave rotor technique to be superior to the shell-folding scheme. In the metallic regime, however, the quality of both approximations is found to be similar at small to intermediate inter-shell interactions; the slave rotor method only trumps at higher values of U^{dp}. To improve upon these results, we proposed a modification of the rotor Green's function, which takes into account information from the shell-folding solution. While this hybrid scheme gives much better results than the other methods, it has the drawback, that it can only work if the expected solution is in the metallic regime. Finally, we test our method in the description of the metal-insulator transition, driven by correlations due to inter-shell interactions. Here, the slave rotor technique is compared to the shell-folding and Hartree Fock approximations. While both of the latter

methods fail to give an accurate description of the transition, the results from the slave rotor technique remain close to the reference solutions.

Our calculations considered only the most simple case of a two-orbital d-p model. However, the considerations that flew into the derivation our method were general and not restricted to any specific number of orbitals. Finally, the purpose of our work is to provide a light-weight tool that allows to treat inter-shell interactions in the context of realistic systems. A potential application would be the three-band Emery model, for which the importance of d-p interaction was already investigated on the level of a Hartree approximation[66]. Finally, one could also consider more complex systems, like a full five-orbital d-shell, interacting with three p-orbitals. Such models are relevant for a variety of realistic systems (e.g. many iron based superconductors); due to the enormous computational cost, inter-shell interactions are commonly neglected in such calculations. Our new method provides a path to include them in the future.

Part IV

Molecular Spintronics Modeling

Chapter 7

The Hybridization-Induced Spin Transition in Metal-Organic Molecules

7.1 Motivation and Introduction

In this final chapter we shall leave the realm of solid-state physics and focus on some aspects of *molecular spintronics*. Work presented in this chapter was done in collaboration with Sumanta Bhandary, who contributed all density functional theory calculations.

Before we consider the specifics of our project, we shall start with a short motivation in the form of a brief overview over the subject. For more detailed reviews, we refer to [80] (fundamentals and applications of spintronics) and [136] (molecular spintronics).

7.1.1 Spintronics

Molecular spintronics was preceded by "conventional spintronics", which emerged in the 1980's with the development of methods allowing the *injection and detection of spin magnetization in metals*[81] and, most prominently, the discovery of the giant magnetoresitance (GMR)[14, 25], which was honored with the Nobel Prize in physics in 2007. The general principle underlying the GMR is the spin dependence of the resistivity in ferromagnetic materials; an effect which – as the "two current" model[117] – had already been suggest in 1936 by N.F. Mott. Apart from numerous technical applications – most notably the application of GMR materials as magnetic field sensors in hard-disc drives – these advances paved the way for the genesis of a new discipline. The main principle of spintronics is the manipulation of the electron spin degree of freedom in solid-state systems[80]. In this sense, the aim is to exploit the electron spin for applications in information storage, transport and processing.

Spin-related effects were first studied in the context of transition metal compounds; the system under consideration in the original paper on the GMR[14] comprised stacked layers of iron and chromium. Since, however, most of our current electronics technology is based on semiconductors,

the exploration of semiconductor spintronics[86, 11] promised a better integration within existing solid-state devices. In the framework of semiconductor spintronics, information storage, transport and processing is accomplished within a single materials platform. Furthermore, the electronic properties of semiconductors can be easily modified (e.g. by doping to introduce additional charge carriers), and the characteristic spin-relaxation time in such compounds is usually longer than in metals.

Recent efforts in experiment and theory were focused on the exploration of yet another route to creating spin-devices, considering organic materials. As compared to their inorganic counterparts, organic compounds offer a practically infinite number of different variations and structures, allowing for very specific applications. Moreover, low atomic numbers Z of the atomic constituents result in a weak spin-orbit coupling, enhancing the lifetime of excited spin-states.

7.1.2 Molecular spintronics and the spin crossover

Molecular spintronics, based on single molecular structures offer various advantages over their bulk counterparts. In the context of solid-state systems, one usually talks about magnetism as a collective phenomenon, which includes a large number of atoms. In molecular spintronics, on the other hand, magnetism is considered on the level of individual molecules. This leads to an enormous potential in miniaturization and efficiency, surpassing the limits of bulk devices. As in organic spintronics, there is an enormous variety of molecules that can be considered for usage in spin devices.

These prospects spurred the efforts that led to the rapid advances the field has seen over the last two decades; from the realization of stable single ion magnets[109], to spin valves[152], switches and storage devices.

One of the key ingredients for many applications is magnetic bi-stability. This term denotes the possibility of realizing two stable states characterized by different spin configurations. In bulk systems, magnetic bistability can, for instance, manifest itself as the magnetization in ferromagnets. In the context of molecules, different spin-states can correspond to different eigenstates (light-induced excited spin-state trapping (LIESST)[40]), to modifications of the molecular structure/coordination[155], or – for molecules on surfaces – correspond to changes of the molecule/surface interface[128]. One is usually interested in systems with a high- (HS) and a low-spin (LS) state, the transition between which is referred to as the spin crossover (SCO). Changes in the spin-state can be hinged naturally by external stimuli, such as temperature, light, pressure, electric fields etc. Considering technical applications in devices, it is crucial to gain control over the spin crossover (SCO).

Many organometallic complexes, hosting transition metal ions such as Fe^{2+}, Fe^{3+}, Co^{2+}, Ni^{2+}, Mn^{2+} or Mn^{3+} are well suited for spin-state switching, due to a subtle balance of ligand field and spin-pairing energy. The latter is fundamentally caused by Hund's exchange coupling, which was discussed in detail in Chapter 3. An effective way to control the SCO is to manipulate the ligand fields of the molecules. This can be achieved in several ways, e.g. a SCO can be induced by temperature, light or by imparting strain on the metal-molecule nano-junctions.

In [121], a light-induced spin change was for the first time observed in thin films of iron based SCO complexes. To this day, this remains one of the most effective ways to trigger a SCO [15]. Recent efforts were put into investigating the SCO in molecules on surfaces. Here, Warner et al. achieved a spin-state switching in molecules on Au[158] and graphite surfaces[19, 87] both using temperature and light as stimulators. While these observations were made at low temperatures, room temperature spin-state switching has recently been observed in iron molecular complexes[113].

An efficient way to switch spin-states is to alter the isomeric structure of molecules by ligand association or dissociation. Coordination-induced spin-state switching was investigated by Herges et al. [73], who proposed a light-driven modification in the coordination of Ni-porphyrin molecules[44].

Yet another way to induce a SCO considers the usage of scanning tunnel microscopy (STM), which allows for a manipulation of atoms/molecules with unprecedented precision. The feasibility of this approach has been demonstrated by Miyamachi et al.[116], who achieved a spin-crossover in Fe-complexes, adsorbed on a metallic surface. Furthermore, an STM tip can be used to induce voltage pulses which can trigger a SCO[69].

Describing spin-crossover phenomena theoretically is a challenging task. Different approaches, such as density functional theory (DFT) with several forms of exchange-correlation functionals[171, 63], DFT+U[21, 101, 20], DFT+many-body theory[30, 22], full configuration interaction quantum Monte Carlo[105] methods, etc. have been used in the literature. On the specific example of nickel porphyrin[131], time-dependent density functional theory techniques have been used to explicitly characterize the singlet and triplet excited states.

7.2 The hybridization-induced spin crossover

In this project, we have focused on the spin crossover in organometallics, and, more specifically in Ni-porphyrin (Ni-TPP) molecules. As outlined above, the spin-state of such molecules depends on the hybridization of the transition-metal (TM) ion with the surrounding ligands. Thus a SCO mechanism requires a controlled manipulation thereof. The aim of the following investigations is to explore the scenario of a hybridization induced SCO.

7.2.1 Structure of the molecules

Ni-porphyrin molecules contain a Ni^{2+} ion that is located at the center of a porphyrin macrocycle. The porphyrin complex itself is often connected to various peripheral substituents, such as phenyl groups. Fig. 7.1 shows two different Ni-porphyrin molecules, of which the structures were obtained by relaxing the atomic positions within density functional theory + “U”[107, 45]. Panel (a) shows the “planar” Ni-TPP molecule, in which the central nickel atom is surrounded by 4 nitrogen ligands, resulting in a quasi-square planar ligand field (“quasi”, since this neglects the rest of the molecular structure, which is supposed to have only a weak influence on the central transition metal ion). The Ni-TPP (Im_2) structure shown in panel (b) is characterized by two additional pyridine structures, that

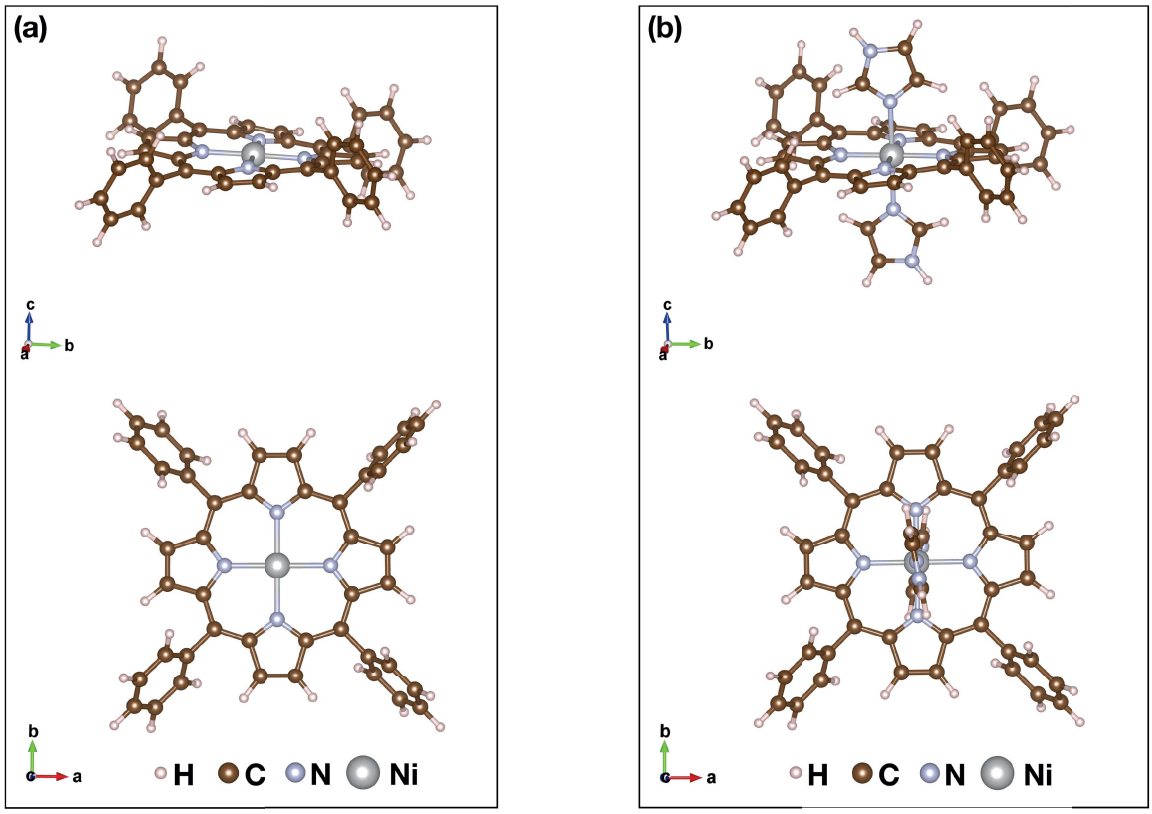

Fig. 7.1 Relaxed structures of the Ni-TPP (a) and the Ni-TPP(Im_2) (b) molecules, from two different perspectives.

attach to the nickel atom along the vertical axis. This changes the central ligand field to be "quasi" octahedral.

These are only two out of a multitude of stable structures that could be conceived; another possibility would be a Ni-TPP molecule with only one additional pyridine structure (a similar structure is considered in [44]). Experimentally, it is well-known[46], that the "planar", four-fold coordinate structure (a) exhibits a $S = 0$ low-spin (LS) configuration, while the "octahedral", six-fold coordinate structure (b) is characterized by a $S = 1$ high-spin (HS) state.

A naive explanation for this can be given by considering a crystal-field picture, as presented in Fig. 7.2. The magnetic moment is mainly determined by the central TM ion. In the square-planar case the bare energy levels of the nickel d-orbitals are split as shown in panel (a). In this configuration, one could think that the 8 valence electrons of the nickel ion fill the d-shell, except for the $d_{x^2-y^2}$ orbital, resulting in a low-spin-state $S = 0$. In an octahedral crystal field, however, the orbitals of the e_g manifold would be degenerate, and therefore be occupied by two parallel spins, due to Hund's coupling. While these simple considerations give an intuitive explanation for the formation of two different spin-states, we shall see in the following that the expected physics is a bit more

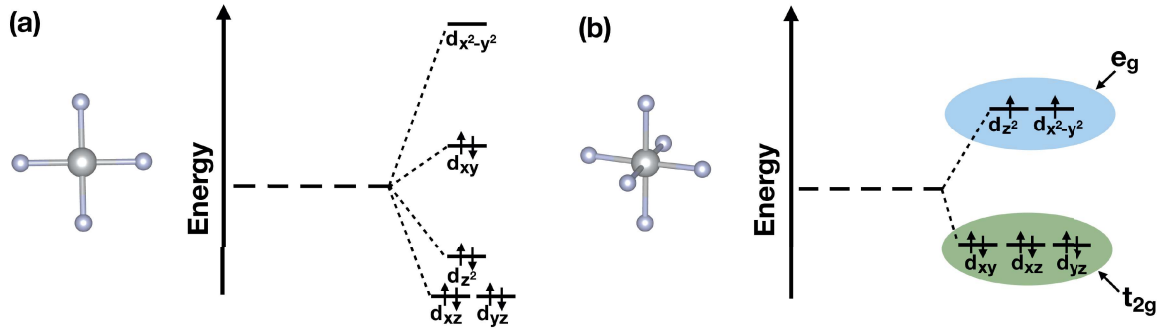

Fig. 7.2 Crystal field splitting of the d-orbital manifold. (a) Shows the splitting of the bare energy levels in a square-planar crystal field. (b) Shows the bare levels in a octahedral crystal field, splitting the d-orbitals into the three-fold degenerate t_{2g}- and the two-fold degenerate e_g manifolds. Arrows indicate the distribution of 8 electron spins, considering the influence of Hund's exchange coupling.

complicated. Most importantly, this simplistic picture does not consider the effect of hybridization with the surrounding nitrogen ligands, which plays an important role.

7.2.2 A minimal model to capture the spin-crossover

Our goal is to describe the changes in the spin-state of a transition metal ion brought about by a modification of the ligand-to-transition metal hybridization strength. To this effect, we construct a model, in which the transition metal ion and the ligands are represented by two orbitals each. A minimal number of two orbitals is necessary to incorporate the effect of Hund's exchange coupling, which is at the heart of any high-spin configuration.

Our generic model for the description of the SCO, illustrated in Fig. 7.3, is defined by the following Hamiltonian

$$\begin{aligned} H = & \sum_{m=1,2,\sigma} (\varepsilon_m - \varepsilon_H) n_{m\sigma} + \sum_{m=1,2} E_m^b \sum_{\sigma} n_{m\sigma}^b \\ & + \sum_{m=1,2} \sum_{\sigma} \left(V_m d_{m\sigma}^{\dagger} b_{m\sigma} + h.c. \right) \\ & + U \sum_{m=1,2} n_m n_m + \sum_{\sigma\sigma'} (U' - \delta_{\sigma\sigma'} J) n_{1\sigma} n_{2\sigma'} \\ & - \mu \sum_{m=1,2} \sum_{\sigma} (n_{m\sigma} + n_{m\sigma}^b) \,, \end{aligned} \tag{7.1}$$

where $d_{m\sigma}^{\dagger}(d_{m\sigma})$ create (annihilate) an electron at the correlated orbital m (of energy ε_m) with spin σ, while $b_{m\sigma}^{\dagger}(b_{m\sigma})$ denote the creation (annihilation) operators of the electrons at the ligand orbitals m (of energy E_m^b). The number operators are defined as $n_{m\sigma} = d_{m\sigma}^{\dagger} d_{m\sigma}$ and $n_{m\sigma}^b = b_{m\sigma}^{\dagger} b_{m\sigma}$. V_m is the hybridization between correlated and bath orbitals, U and J represent on-site Coulomb- and exchange interactions, respectively, with $U' = U - 2J$. The chemical potential, μ fixes the overall occupation (correlated orbitals+ligands); Throughout this chapter, it will be fixed to 6. The parameter ε_H shifts

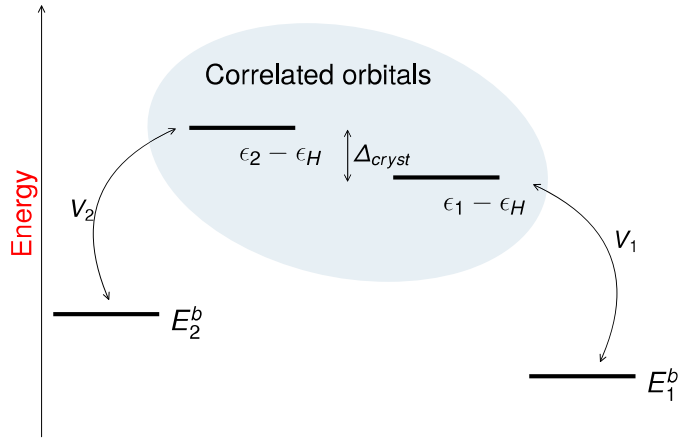

Fig. 7.3 Schematic illustration of our model. The system consists of two correlated orbitals with bare energies $\varepsilon_1/\varepsilon_2$ (minus a shift ε_H, that compensates for the Hartree contribution from the interaction), interacting via Coulomb repulsion and Hund's exchange coupling. The difference of the impurity energy levels is denoted by $\Delta_{cryst} = \varepsilon_2 - \varepsilon_1$. Each impurity orbital couples to an uncorrelated bath site with a hybridization strength V_1/V_2; the energy levels of the bath sites are E_1^b/E_2^b. All bare energy levels will be shifted by a chemical potential defined by fixing the overall filling.

the energy levels ε_m and is explicitly added to cancel the Hartree contribution from the interaction. In the context of our model, we shall define the crystal field splitting as the difference of the energy levels of the correlated orbitals $\Delta_{cryst} = \varepsilon_2 - \varepsilon_1$.

In realistic systems, external stimuli such as strain would typically change several model parameters at the same time. Nevertheless, with the present model, we can explore the whole parameter space spanned by crystal field strength and hybridization. A spin-crossover can then be realized in two ways – either by crystal field modification, i.e. changing the relative energies of the correlated orbitals or by tuning the metal-ligand hybridization.

The quantity of central interest is the spin moment $\left\langle \vec{S}^2 \right\rangle$, defined as

$$\vec{S}_{tot} = \frac{1}{2} \sum_{m=1,2} \sum_{\sigma\sigma'} \left(d^\dagger_{m\sigma} \vec{\sigma}_{\sigma\sigma'} d_{m\sigma'} + b^\dagger_{m\sigma} \vec{\sigma}_{\sigma\sigma'} b_{m\sigma'} \right) \tag{7.2}$$

$$\vec{S}_{corr} = \frac{1}{2} \sum_{m=1,2} \sum_{\sigma\sigma'} d^\dagger_{m\sigma} \vec{\sigma}_{\sigma\sigma'} d_{m\sigma'} \,, \tag{7.3}$$

where $\vec{\sigma}_{\sigma\sigma'}$ is the vector of Pauli matrices. Here, $\vec{S}_{tot}$ and $\vec{S}_{corr}$ describe the spin moment of the total molecule and the correlated subspace only, respectively. The occupations of the correlated orbitals $n_m = \sum_\sigma n_{m\sigma}$ will provide information about the charge transfer from the bath sites to the correlated orbitals. Furthermore, we consider the free energy $F = \langle H \rangle - ST$, to analyze the energetics of the different spin configurations.

These quantities will be calculated as a function of the crystal field Δ_{cryst} and the ratio of the hybridization strengths V_1/V_2, for fixed $V_2 = \sqrt{8}eV$. Throughout the following model study, we take $U = 5.14$eV and $J = 0.89$eV[1]. Furthermore, we consider the parameters $E_1^b = E_2^b = -2eV$, while the bare e_g levels will be set to $\varepsilon_1 = -\Delta_{cryst} - \varepsilon_H$ and $\varepsilon_2 = +\Delta_{cryst} - \varepsilon_H$. The Hartree potential, corresponding to a homogeneous charge distribution, reads $\varepsilon_H = \frac{N}{4}(3U - 5J)$. In principle, N should be the total occupation of the correlated orbitals. However, inspired by the fully localized limit double-counting of electronic structure theory[108], we rather choose the integer values $N = 2$ or $N = 3$.

In the case without hybridization, the correlated orbitals would have an occupation of $N = 2$, while for the above parameters, the ligands would be completely filled. The high-spin-state would then be associated with having one electron per correlated orbital, while the low-spin-state would correspond to the orbitally-polarized configuration. In this case, $\left\langle \vec{S}^2_{tot} \right\rangle = \left\langle \vec{S}^2_{corr} \right\rangle$, with $\left\langle \vec{S}^2_{corr} \right\rangle = 2$ and 0, respectively in the high-spin and low-spin configurations.

Model results

Fig. 7.4 shows the spin moment $\left\langle \vec{S}^2 \right\rangle$ as a function of Δ_{cryst} and V_1 for $\varepsilon_H(N = 2)$ (panel (a)) and $\varepsilon_H(N = 3)$ (panel (b)). Both figures exhibit two low-spin regions (blue), separated by a band-like high-spin region (yellow) with a width that decreases from about $\sim 5.5J$ to $\sim 4.5J$ upon increasing V_1/V_2. Qualitatively, the shape of the high-spin region is easily explained: In the *atomic limit*, in which both hybridizations vanish $V_1 = V_2 = 0$, the energy levels of the eigenstates would have a linear dependence on the crystal field and a high-spin to low-spin transition would be induced as soon as $|\varepsilon_2 - \varepsilon_1| = |\Delta_{cryst}| > 3J$, therefore resulting in a width of $6J$. While in the absence of hybridizations this region should be symmetric around $\Delta_{cryst} = 0$, a finite $V_2 > 0$ will lead to two molecular orbitals; a bonding orbital with an energy below E_2^b and an anti-bonding one with an energy above ε_2. Within our convention, we therefore need a negative crystal field to move the energy of the anti-bonding state down to ε_1, and thus move back to the center of the high-spin region where the energy levels are degenerate. The bend of the high-spin region is simply due to the fact that, upon increasing V_1, the energy level of the anti-bonding $m = 1$ orbital-bath state is pushed up, therefore reducing the energy difference to the corresponding $m = 2$ orbital-bath state.

In order to get a better insight in the physics of the SCO, we can take a look at the transition along two different paths in parameter space, marked as horizontal and vertical dashed lines in Fig. 7.4, respectively. The results are presented in Fig. 7.5. Panels (a)-(c) show the results for the hybridization driven SCO, with vanishing crystal field $\Delta_{cryst} = 0$; panels (d)-(f) explore the crystal-field driven SCO, with constant $V_1 = V_2/2$. Furthermore, we differentiate between results obtained for $\varepsilon_H(N = 3)$ (solid lines) and those for $\varepsilon_H(N = 2)$ (dashed lines).
The upper panels (a) and (d) show the spin moment along the cuts marked as dashed lines in Fig. 7.4.

[1]These values correspond to the interaction parameters for the e_g manifold (see Eqs. (3.22) and (3.21)), for $U_{avg} = 4$ and $J_{avg} = 1$. Even though the model depends only on the ratio of the parameters e.g. with respect to V_2, we prefer here to introduce electron Volts as a unit, to enable an easier comparison with the following chapters.

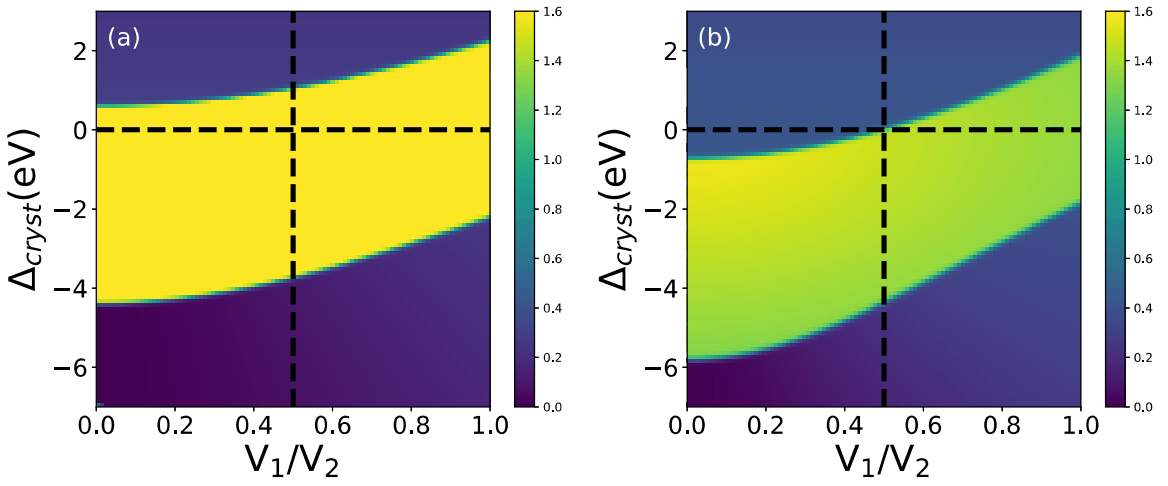

Fig. 7.4 Spin moment $\left\langle \vec{S}^2 \right\rangle$ of the correlated orbitals as a function of the crystal field $\Delta_{cryst} = (\varepsilon_2 - \varepsilon_1)$ and the d_{z^2} hybridization for $\varepsilon_H(N=2)$ (a) and $\varepsilon_H(N=3)$ (b). Fig. 7.5 shows different quantities for constant V_1 along the dashed line.

Red lines mark the spin moment of the full system $\left\langle \vec{S}^2_{tot} \right\rangle$, black lines correspond to the correlated orbitals $\left\langle \vec{S}^2_{corr} \right\rangle$ only. Panel (d) shows that a crystal-field driven SCO can be achieved for both values of ε_H under consideration; changing its numerical value merely leads to shift of the transition points and a change of the absolute values of the spin moment, due to the change in the hybridization with the ligands. Panel (a), however, makes clear that a hybridization driven SCO cannot be realized for $\varepsilon_H(N=2)$ – for which we remain in the high-spin regime for all V_1 under consideration – but rather requires a bigger energy shift, as given by $\varepsilon_H(N=3)$.

In general, a comparison between the black and red lines reveals that only the spin moment of the full system $\left\langle \vec{S}^2_{tot} \right\rangle$ exhibits a clear low-spin to high-spin transition. It is also the molecular spin moment, that is of experimental interest.

In the high-spin regime, one would expect the electrons to be (more or less) equally distributed among the two orbitals, while the low-spin regimes should be characterized by strong orbital polarization. Such behavior is indeed reflected in the middle panels (b) and (e) of Fig. 7.5, which show the occupations of the different orbitals along the dashed lines drawn in Fig. 7.4. The roughly constant dashed lines in panel (b) again witness the fact that no hybridization driven SCO is found for $\varepsilon_H(N=2)$. Looking at the overall occupation $\langle n_1 + n_2 \rangle$ in panel (e), one sees a "staircase" like behavior when changing the configuration from low- to high-spin and back to low-spin. This can be understood as a consequence of the different hybridization strengths V_1/V_2, resulting in a different charge transfer to the correlated orbitals.

In the lower panels (c) and (f) of Fig. 7.5 we see the difference in free energy $F = E - TS$ between the lowest lying (in terms of their energy) high/low-spin eigenstates $\Delta F = F[low] - F[high]$, as they are calculated along the cuts in Fig. 7.4. The point where this difference is zero marks the phase

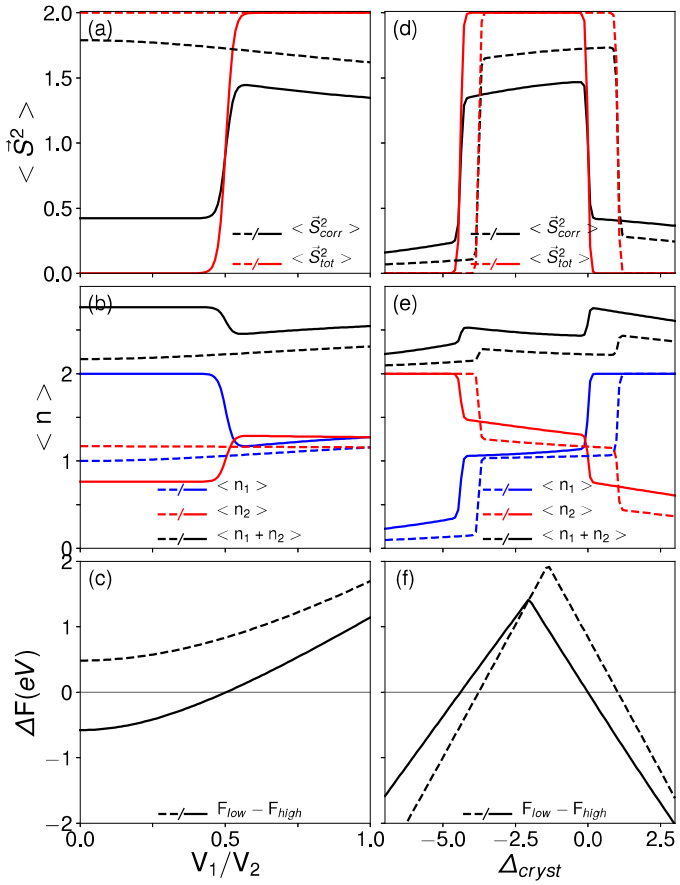

Fig. 7.5 Spin moment $\left\langle \vec{S}^2 \right\rangle$ (panels (a) and (d)), occupations n of the correlated orbitals (panels (b) and (e)) and the difference in free energy between high and low-spin-states (panels (c) and (f)) along the cuts indicated in Fig 7.4 for $\varepsilon_H(N=3)$ (solid lines) and $\varepsilon_H(N=2)$ (dashed lines). Left side: Results along the cut with constant $\Delta_{cryst} = 0$. Right side: Results along the cut with constant $V_1 = V_2/2 = \sqrt{2}eV$.

transition. The entropy is calculated from the degeneracy of the eigenstate; while the high-spin-state is two-fold degenerate with $S = \ln(2)$, the low-spin-state is non degenerate with $S = \ln(1) = 0$. Since $\beta = 40$, this yields $TS \approx 0.017eV$, which means that in our case the difference between energy and free energy is rather small. Comparing the solid and dashed lines in panel (c) and (f) illustrates how ε_H shifts the energy difference between the high-spin and low-spin-states, therefore underlining the different electron occupations of the correlated orbitals in the two regimes. Finally, we shall clarify the peculiar shape of the curves in panel (f): If again we restricted ourselves to a simple two-electron system without any hybridization, this difference would read $\Delta F = (U - |\Delta_{cryst}|) - (U' - J - T\ln(2))$, explaining the almost linear slopes as found in the low-spin regions in the panel (f) of Fig. 7.5.

Conclusions

This leads us to the following conclusions. The results of this model study indicate, that a purely hybridization-induced ($\Delta_{cryst} = 0$) SCO cannot be accomplished in the naive scenario considering a static Hartree shift $\varepsilon_H(N = 2)$, corresponding to a half-filled e_g manifold. However, as it can be seen from panels (b) and (e) of Fig. 7.5, this assumption underestimates the actual average filling of the correlated orbitals. On the other hand, a SCO is found when considering a larger energy shift $\varepsilon_H(N = 3)$. This leads to the conclusion that the hybridization driven SCO, in the molecular setup under consideration, is intimately related to a charge-transfer from the ligands to the correlated orbitals. However, from Fig. 7.5 (b) and (e), it is clear that an energy correction corresponding to fixed electron numbers is at odds with the changing average occupations presented in these plots. In the following, when using parameters from realistic molecular structures, we shall improve on this inconsistency by applying a self-consistent double-counting scheme.

7.3 Ab initio description of the spin crossover

7.3.1 Density functional theory and the double counting problem

The following pages will be used to give a "micro-introduction" into density functional theory. For the sake of compactness, we shall not go into details about this very rich topic, but only focus on informations needed for the following discussion. Detailed introductions can be found in[28, 7, 67]; for a general overview consider[82].

Density functional theory is based on the Hohenberg-Kohn[76] theorems, that state that the ground state energy of a system can be uniquely expressed as a functional of the electronic density only. This functional consists of several terms: The form of the kinetic and potential energy is well-known, and it can be easily written in terms of the electron density. On the other hand, the exact functionals for the exchange- and correlation terms are, in general, not known. In practice, the validity of any DFT calculation is limited by the quality of the approximations employed to describe these terms.

In the often used local density approximation (LDA), the exchange-correlation energy functional is written as

$$E_{XC}^{LDA}[n] = \int \mathrm{d}^3 r \, \varepsilon_{XC}(n) n(\vec{r}) \, , \tag{7.4}$$

where the exchange-correlation potential $\varepsilon_{XC}(n)$ only takes in to account the local electron density. In the context of this project, we applied the more sophisticated general gradiant approximation (GGA)[100, 17, 132]. GGA is a direct generalization of LDA, in which the approximated exchange correlation functional also considers the local gradient of the electron density

$$E_{XC}^{GGA}[n] = \int \mathrm{d}^3 r \, \varepsilon_{XC}(n, \nabla n) n(\vec{r}) \, . \tag{7.5}$$

Both of these functionals can be easily generalized to account for spin polarization, by substituting $\varepsilon_{XC}(n) \to \varepsilon_{XC}(n_\uparrow, n_\downarrow)$ in (7.4) and $\varepsilon_{XC}(n, \nabla n) \to \varepsilon_{XC}(n_\uparrow, n_\downarrow, \nabla n_\uparrow, \nabla n_\downarrow)$ in (7.5).

Since these DFT approximations do not properly take into account the exchange-correlation, it is poorly suited for the description of strongly correlated electron systems. Furthermore, it does not provide any information about the spectrum of excited states (even though the energy spectrum of the Kohn-Sham equations[89] is often "abused" to this means).

It is for this reasons, that nowadays DFT is often used in combination with many-body techniques. In this spirit, DFT can be used to extract bare energy levels $\varepsilon(\mathbf{k})$ for the many-body Hamiltonian, by assuming

$$\varepsilon(\mathbf{k}) \approx \varepsilon^{DFT}(\mathbf{k}) \; . \tag{7.6}$$

The many-body Hamiltonian is then solved with appropriate techniques.

This leads to the following problem: Even though the DFT result deviates from the true ground state solution, it still contains contributions of electronic correlations from the Coulomb interaction. On the other hand, this two-body interaction is explicitly treated by solving the many-body Hamiltonian. This leads to a double counting (DC) of the same effect, which we have to compensate for in order to ensure a faithful description of the physics.

Several schemes have been suggested to compensate for this double counting. The "around mean-field" (AMF) approximation was originally derived in the context of the "LDA+U" scheme. It is based on the assumption that the LDA solution corresponds to some kind of mean-field approximation to the fully interacting quantum problem. In this spirit, the LDA energy functional can be extended "around the mean-field" by considering

$$E^{LDA+AMF} = E^{LDA} + \hat{H}_{int} - \left\langle \hat{H}_{int} \right\rangle \; , \tag{7.7}$$

where we consider $\hat{H}_{int}$ for a d-orbital system (see Eq. (3.31), without spin-flip and pair-hopping interactions

$$\hat{H}_{int} = \sum_{mm'} U_{mm'} \hat{n}_{m\uparrow} \hat{n}_{m'\downarrow} + \sum_{m>m',\sigma} (U_{mm'} - J_{mm'}) \hat{n}_{m\sigma} \hat{n}_{m'\sigma} \; . \tag{7.8}$$

It is then easily shown (see [36]), that averaging over the occupation numbers ($\langle \hat{n}_{m\sigma} \rangle = n^0_\sigma$) leads to

$$E^{AMF}_{DC} = \left\langle \hat{H}_{int} \right\rangle = U_{avg} N_\uparrow N_\downarrow + \frac{1}{2} \frac{2\ell}{2\ell+1} (U_{avg} - J_{avg}) \sum_\sigma N^2_\sigma \; , \tag{7.9}$$

with U_{avg} and J_{avg} defined as in Eq. (3.23) and (3.24), and $N_\sigma = (2\ell+1) n^0_\sigma$. For a d-orbital system, the angular momentum variable is $\ell = 2$.

Another approach to correct for double counting is the "fully localized limit" (FLL)[36, 108] approximation. It was proposed in the context of correcting the LDA in the description of localized d-

or f-electrons, where it was argued that one should rather subtract the energy from the N-degenerate atomic limit

$$E_{DC}^{FLL} = \frac{1}{2}U_{avg}N(N-1) - \frac{1}{2}J_{avg}\sum_{\sigma}N_{\sigma}(N_{\sigma}-1)\,, \tag{7.10}$$

with $N = \sum_{\sigma} N_{\sigma}$.

Upon differentiating these energy functionals with respect to the electron density, one obtains the double counting potentials

$$\frac{\partial E_{DC}^{AMF}}{\partial n_{\sigma}} = V_{DC,\sigma}^{AMF} = U_{avg}\left(N - \frac{N_{\sigma}}{2\ell+1}\right) - J_{avg}\left(N_{\sigma} - \frac{N_{\sigma}}{2\ell+1}\right) \tag{7.11}$$

$$\frac{\partial E_{DC}^{FLL}}{\partial n_{\sigma}} = V_{DC,\sigma}^{FLL} = U_{avg}\left(N - \frac{1}{2}\right) - J_{avg}\left(N_{\sigma} - \frac{1}{2}\right)\,, \tag{7.12}$$

which are used to shift the bare energy levels of the electrons to account for the double counting. More explicitly, this is done by adding an additional term to the Hamiltonian

$$\hat{H}_{int} \rightarrow \hat{H}_{int} - \sum_{m\sigma} V_{DC,\sigma}^{AMF/FFL}\hat{n}_{m\sigma}\,. \tag{7.13}$$

In the molecular spintronic system under consideration, electrons are supposed to be strongly localized. For this reason, we will in the following consider the FLL approach to correct for double counting.

7.3.2 Results from density functional theory

The goal of this section is to study the SCO in nickel porphyrin molecules, by employing our model (7.1) with parameters obtained from realistic *ab initio* caluculations. To calculate the non-interacting electronic structure of the systems, we perform DFT calculations using the Vienna ab initio simulation package (VASP)[94]. We use a plane wave projector augmented wave basis with the Perdew-Burke-Ernzerhof (PBE) -generalised gradient approximation[132] of the exchange correlation potential. To treat the isolated molecule, we consider a 30x30x30 Å^3 simulation cell which yields a minimum separation of 17.58Å between the molecule and its periodic image. The plane-wave energy cut-off is 400 eV, which is used for all the calculations. In order to obtain the molecular structures (see Fig. 7.1), the internal atomic positions are relaxed until the Hellman Feynman forces were minimized up to 0.01 eV/Å. To account for the narrow Ni-3*d* states, the relaxation of the molecules are done within DFT+U formalism with the Coulomb parameter U_{avg} = 4 eV and exchange parameter J_{avg} = 1 eV (corresponding to the parameters chosen in the model investigation presented in the previous sections).

In contrast to the DFT calculations for the relaxation of the structures, input for the model (7.1) was obtained from DFT calculations "sans U". Specifically, we are interested in the extraction of the bare energies of the correlated orbitals e_m, the energies of the bath orbitals E_m^b and the hybridization

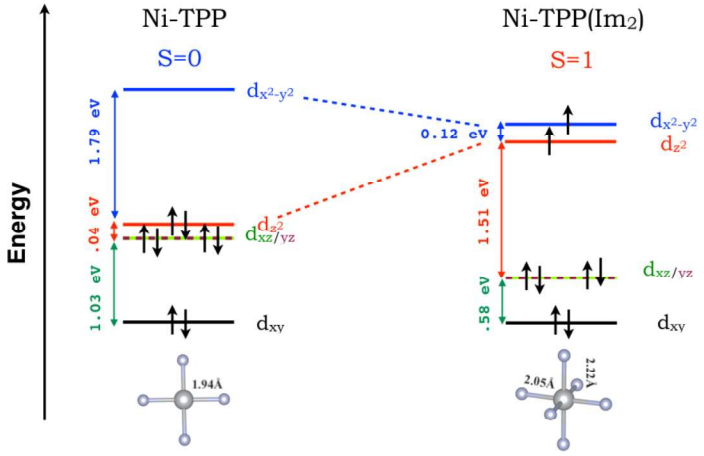

Fig. 7.6 Orbital energies of Ni-3d orbitals in Ni-TPP (left) and Ni-TPP(Im_2) (right). The t_{2g} orbitals are completely filled in both conformations, hence the magnetism is governed by the partially filled eg orbitals.

strengths V_m. The latter two are interconnected by the hybridization function

$$\Delta(i\omega) = \sum_m \frac{V_m V_m^*}{\omega + i\delta - E_m^b}, \tag{7.14}$$

which we assume (due to the geometry of the molecule) to be diagonal to a good approximation. In order to calculate the hybridization function, we first consider the Kohn-Sham Green's function G_{KS}, which is calculated from the Lehmann representation using

$$G_{KS}(\omega) = \sum_{nk} \frac{|\psi_{nk}\rangle\langle\psi_{nk}|}{\omega + i\delta - \varepsilon_{nk}}, \tag{7.15}$$

where ψ_{nk}'s and ε_{nk}'s are the Kohn-Sham eigenstates and eigenvalues for band n and reciprocal space point k. The full Green's function then needs to be projected onto an atom-centered local Green's function $G_{imp}^{mm'}$; in our case, the localized orbitals are chosen as cubic harmonics (χ_m). To this means, we write

$$G_{imp}^{mm'}(\omega) = \sum_{nk} \frac{P_{nk}^m P_{nk}^{m'*}}{\omega + i\delta - \varepsilon_{nk}} \tag{7.16}$$

where $P_{nk}^m = \langle \chi_m \mid \psi_{nk} \rangle$ and $P_{nk}^{m'*} = \langle \psi_{nk} \mid \chi_{m'} \rangle$. Finally, the hybridization function is calculated from the local impurity Green's function using the expression

$$G_{imp}^{-1}(\omega) = \omega + i\delta - V_{cryst} - \Delta(\omega). \tag{7.17}$$

In the above expression, G_{imp} is the projected Green's function on local orbitals and Δ, V_{cryst} are the hybridization function and static crystal field, respectively.

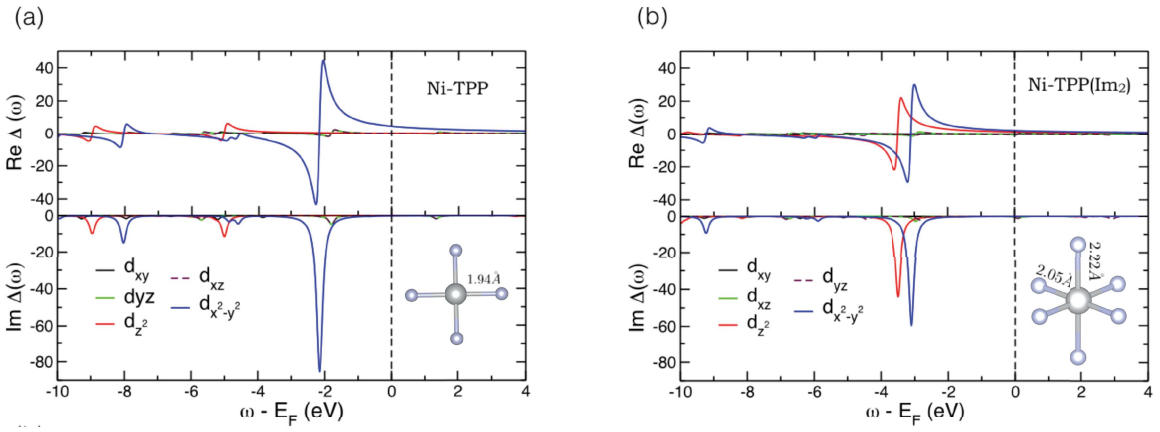

Fig. 7.7 The real and imaginary parts of the energy-dependent hybridization functions of Ni in Ni-TPP (a) and in Ni-TPP (Im_2) (b). A smearing parameter of 0.1 eV has been used for these plots for the sake of visualization. In the inset, the corresponding co-ordination geometries of Ni atoms in Ni-TPP and Ni-TPP(Im2) are shown, with axial Ni-N bond lengths.

Fig. 7.6, shows the relative energies of the molecular orbitals (formed by the Ni-3*d* orbitals, hybridizing with the ligands), for Ni-TPP (left) and Ni-TPP(Im_2) (right) isomers. In Ni-TPP, the highest occupied molecular orbital (HOMO) and the lowest unoccupied molecular orbital (LUMO) are of $d_{x^2-y^2}$ and d_{z^2} character, with an energy separation of 1.79 eV. The degenerate d_{xz} and d_{yz} orbitals are close to d_{z^2} (the energy difference being 0.04 eV), which itself is separated from the lowest-lying d_{xy} orbital by about 1 eV. These energies are in qualitative agreement with those from previous theoretical studies[131]. A small quantitative difference is expected due to the different descriptions of the DFT exchange-correlation potentials. In Ni-TPP (Im_2), the Ni-N bond length is extended by ∼6%. Due to this core expansion, the energy of the $d_{x^2-y^2}$ orbital is reduced, while the axial ligand bonding raises the orbital energy of d_{z^2}, reducing the corresponding energy separation to 0.12 eV. In accordance with the literature, this results in both orbitals being half filled, such that a high-spin triplet state is formed. The change of coordination has a crucial impact on the charge transfer between the porphyrin ring and the Ni ion. Within the DFT+U formalism (used to relax the molecular structures), the projected total charge on the Ni 3*d* orbitals is 8.16 in the Ni-TPP (Im_2) molecule, while it is 8.4 in Ni-TPP. This charge transfer is enhanced in the many-body calculations, as will be described below.

Fig. 7.7 (a), (b) show the real and imaginary parts of the hybridization functions of the five d-orbitals for Ni-TPP and Ni-TPP (Im_2), respectively. The peaks of the functions are smoothed out by a smearing parameter of 0.1 eV, which has been added for the sake of visualization. Every feature of the hybridization function indicates the position of a bath-state eigen energy E_b^m. The intensity of these features are dictated by the hybridization strength $|V_m|^2$.

There are several things to remark. In both cases – with and without the pyridine structures – the hybridization of the t_{2g} orbitals is rather weak. This à posteriori justifies the choice of our minimal model, in which we neglected the t_{2g} manifold completely: Indeed, Fig. 7.6 shows that in both cases

under consideration, the t_{2g} orbitals remain energetically below the e_g orbitals and are completely filled. The major qualitative difference between the two configurations concerns the hybridization of the d_{z^2} orbital. While for Ni-TPP(Im_2), d_{z^2} and d_{x^2-y2} hybridize almost equally strong, for Ni-TPP the hybridization of the d_{z^2} orbital is negligible. This is due to the geometry of the orbitals. The d_{x^2-y2} orbital overlaps with the p-type ligands in the x-y plane, while the hybridization with the out-of-plane ligands is negligible. On the other hand, the d_{z^2} orbital hybridizes strongly with the out-of-plane ligands, while there is basically no hybridization with in-plane ligands.

Putting together all of these results, we end up with the following table of parameters for our minimal model.

Table 7.1 Parameters as calculated from DFT calculations (using VASP) by projection onto Wannier orbitals.

	4-coordinated Ni-TPP	6-coordinated Ni-TPP(Im_2)
ε_1 (d_{z^2})	-0.90	-1.44
ε_2 ($d_{x^2-y^2}$)	-1.69	-2.10
$\lvert V_1\rvert^2$	0	4.39
$\lvert V_2\rvert^2$	8.85	5.92
E_1^b	-	-3.5
E_2^b	-2.1	-3.1

It shall be noted that in both molecules, the porphyrin structures were found to be slightly non-planar. This "ruffling" is stronger for the four-fold co-ordinated Ni-TPP, and was found in [144] to decrease the affinity of additional pyridine structures to attach to the Ni center. This provides an interesting outlook on potential applications in which Ni-porphyrin molecules are deposited on surfaces. The contact with a surface is supposed to decrease the ruffling, therefore enhancing the affinity of the molecule to bind with pyridine structures. This effect might increase the suitability of these molecules to be applied as spin-switches in spintronics applications.

7.3.3 Combining DFT and many-body theory

We now proceed by incorporating the parameters obtained from the DFT calculations and listed in Tab. 7.1 into our Hamiltonian (7.1). In contrast to the pure model study presented before, the energy shift ε_H will now be used to correct for double counting. For the reason mentioned before, the fully localized limit approach is most suited for the application molecular systems. We, therefore, set ε_H to the double counting potential (7.12)

$$\varepsilon_H[N] = U_{avg}^{e_g}\left(N-\frac{1}{2}\right) - J_{avg}^{e_g}\left(\frac{N}{2}-\frac{1}{2}\right), \tag{7.18}$$

where we assumed the absence of spin-polarization, implying $N_\sigma = N/2$. Since we are not dealing with the fully degenerate d-manifold, we use the averaged interaction parameters corresponding to the

e_g manifold only. The averaged Hubbard interaction reads

$$U_{avg}^{e_g} = \frac{1}{4} \sum_{m,m' \in e_g} U_{mm'} = U_0 - J_2 \,, \tag{7.19}$$

from which we further deduce the averaged Hund's coupling

$$J_{avg}^{e_g} = U_{avg}^{e_g} - \frac{1}{2} \sum_{m \neq m' \in e_g} (U_{mm'} - J_{mm'}) = 2J_2 \,. \tag{7.20}$$

For the form of the interaction matrix, consider Eqs. (3.22), (3.21).

By using ε_H as our double counting potential, it becomes a function of the filling of the correlated orbitals $\varepsilon_H = \varepsilon_H(n_{corr})$. Since this energy-shift has itself an influence on the electron occupation $n_{corr} = n_{corr}(\varepsilon_H)$, we evaluate it self-consistently, such that

$$n_{corr}(\varepsilon_H(n)) = n \,. \tag{7.21}$$

After these technicalities, let us proceed to the results. We will start by discussing the outcomes for the two set of parameters listed in Tab. 7.1, before we consider the scenario of a strain-induced spin crossover.

Four-fold coordinated Ni-TPP

The model Hamiltonian (7.1), provides a description of the physics of the four-fold coordinated Ni-TPP molecule, provided the parameters in the left column of Tab. 7.1 are used. In this case, we find the ground state to be characterized by a low-spin moment, with $\langle S^2 \rangle_{corr} = 0.45$ for the correlated subspace and $\langle S^2 \rangle_{tot} = 0.0$. Keeping only Fock states with a weight $> 10^{-10}$, the ground state is spanned by only 4 Fock states, and can be written as

$$\begin{aligned} |\mathbf{GS}\rangle_L = 0.55\,|{\uparrow\downarrow},{\uparrow}\rangle_c\,|{\uparrow\downarrow},{\downarrow}\rangle_b + 0.55|{\uparrow\downarrow},{\downarrow}\rangle_c|{\uparrow\downarrow},{\uparrow}\rangle_b \\ +0.45|{\uparrow\downarrow},0\rangle_c|{\uparrow\downarrow},{\uparrow\downarrow}\rangle_b + 0.44|{\uparrow\downarrow},{\uparrow\downarrow}\rangle_c|{\uparrow\downarrow},0\rangle_b \,. \end{aligned} \tag{7.22}$$

In this notation, the subscript c corresponds to the correlated orbitals, while b designates the bath states; the order for the two orbital indices $m = 1,2$ is $|1,2\rangle$. Clearly, this ground state is characterized by a major charge transfer from the ligands to the correlated orbitals, such that the effective filling of the latter ones is close to three. The left panel of Fig. 7.8 shows the energies of the ten lowest lying, non-degenerate eigenstates, relative to the ground state, together with their spin-moment $\left\langle \vec{S}_{tot}^2 \right\rangle$ and their degeneracy.

It shall be mentioned, that the states corresponding to the two lowest lying eigenenergies can be faithfully reproduced by a simplified Hamiltonian that considers only the Fock basis states that make up the ground state (7.22). A detailed discussion is found in Appendix E.1, together with an explicit matrix representation of the corresponding Hamiltonian.

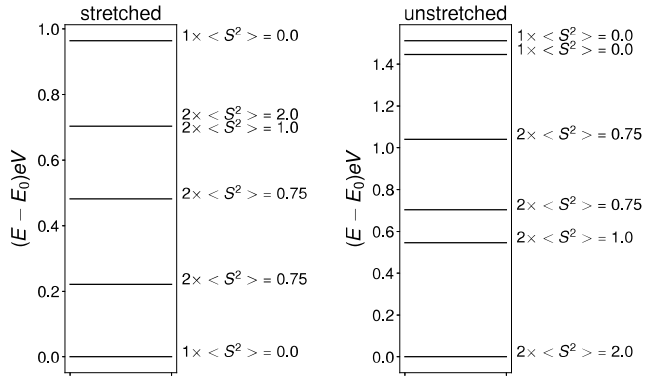

Fig. 7.8 Energy diagram of the infinitely stretched (Ni-TPP) molecule (left panel) and of the unstretched (Ni-TPP(Im$_2$)) molecule (right panel). All energy values are given relative to their ground-state; they are labeled according to their degeneracy and the corresponding spin value of the full system, e.g. $2\times < S^2 >= 2.0$ means that the energy is $2\times$ degenerate with a spin moment $< S^2 >= 2.0$.

Six-fold coordinated Ni-TPP(Im$_2$)

Using the parameters of the right column of Tab. 7.1, we describe the physics of the molecule with Ni-TPP(Im$_2$) configuration. Here, the ground state is a two-fold degenerate high-spin state with $\left\langle \vec{S}^2_{corr} \right\rangle = 1.54$ and $\left\langle \vec{S}^2_{tot} \right\rangle = 2.0$. The two states are spanned by 4 Fock states each, and are related by spin-flip symmetry

$$\begin{aligned} |\mathbf{GS}\rangle^{(1)}_H = {} & 0.81\,|\uparrow,\uparrow\rangle_c\,|\uparrow\downarrow,\uparrow\downarrow\rangle_b + 0.34\,|\uparrow\downarrow,\uparrow\rangle_c\,|\uparrow,\uparrow\downarrow\rangle_b \\ & + 0.46\,|\uparrow,\uparrow\downarrow\rangle_c\,|\uparrow\downarrow,\uparrow\rangle_b + 0.16\,|\uparrow\downarrow,\uparrow\downarrow\rangle_c\,|\uparrow,\uparrow\rangle_b \ , \end{aligned} \tag{7.23}$$

$$\begin{aligned} |\mathbf{GS}\rangle^{(2)}_H = {} & 0.81\,|\downarrow,\downarrow\rangle_c\,|\uparrow\downarrow,\uparrow\downarrow\rangle_b + 0.34\,|\uparrow\downarrow,\downarrow\rangle_c\,|\downarrow,\uparrow\downarrow\rangle_b \\ & + 0.46\,|\downarrow,\uparrow\downarrow\rangle_c\,|\uparrow\downarrow,\downarrow\rangle_b + 0.16\,|\uparrow\downarrow,\uparrow\downarrow\rangle_c\,|\downarrow,\downarrow\rangle_b \ . \end{aligned} \tag{7.24}$$

The filling of the correlated orbitals is $\langle n_1 + n_2 \rangle = 2.38$; much closer to half filling then in the low-spin configuration. However, the charge transfer from the ligands is still considerable. The energies of the eigenstates, relative to the ground state, as well as the corresponding degeneracies and spin-states can be found in the right panel of Fig. 7.8.

Again, the two lowest lying, non-degenerate energy levels are faithfully described by a simplified Hamiltonian, that acts on a truncated Hilbert space, spanned by the Fock basis states that make up the ground states (7.23). As before, we refer to Appendix E.1 for a more detailed discussion.

Spin-crossover: Strain on the axial ligands

In order to mimic the effect on the electronic structure introduced by strain, we linearly interpolate between the two structural configurations corresponding to Ni-TPP and Ni-TPP(Im$_2$). To this effect, we introduce a parameter x, that linearly blends the parameters of the Ni-TPP configuration ($x = 0$)

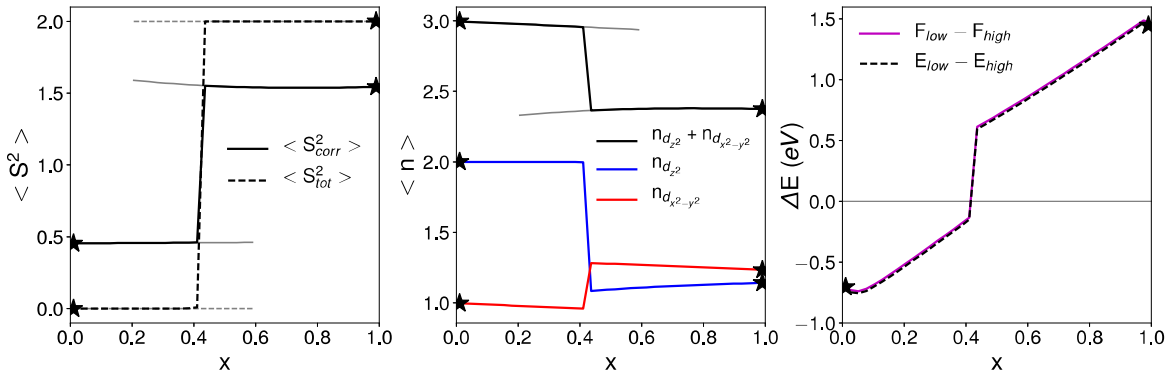

Fig. 7.9 Spin moment $\langle S^2 \rangle$ (left panel) , impurity occupations n (middle panel) and the difference in free energy and energy between the lowest lying low and high-spin-states (right panel), obtained from linearly changing the parameter set of the infinitely stretched P[Ni-TPP] to the one of the unstretched $P[unstretched]$ configuration $P[x] = (1-x) \cdot P[\text{Ni-TPP}] + x \cdot P[\text{Ni-TPP(Im}_2)]$. Black dots indicate the values at $P[x=0] = P[\text{Ni-TPP}]$ and $P[x=1] = P[\text{Ni-TPP(Im}_2)]$. Grey lines correspond to results obtained from simplified models valid in the asymtotic regimes (Appendix E.1).

into those of the Ni-TPP(Im$_2$) ($x = 1$) one, and therefore simulates "stretching" of the axial ligand. The Hamiltonian is then diagonalized at each point of x.

The results are shown in Fig. 7.9, which presents the variation of the spin moment $\left\langle \vec{S}^2 \right\rangle$ (left panel), individual occupations of the correlated orbitals (middle panel), and the free energy of the spin configurations as a function of x. In the left panel of Fig. 7.9, solid and dashed lines correspond to the spin moment for the correlated orbitals $\left\langle \vec{S}^2_{corr} \right\rangle$ and the whole molecule $\left\langle \vec{S}^2_{tot} \right\rangle$, respectively. Our calculations predict a spin moment transition appearing at $x \approx 0.4$. The exact position of the transition is sensitive to the parameters from the ab initio calculations, as well as the way one corrects for double-counting. It must, however, be stressed that the values in between $x = 0$ and $x = 1$ are not based on actual DFT calculations, and merely serve to illustrate the mechanism that mimics the stretching of the molecule.

As the spin-state changes, a jump is observed in the occupations (middle panel). In the low-spin state, the total occupation of the correlated orbitals is $\langle n \rangle \approx 3$ with the d_{z^2} orbital completely filled and the $d_{x^2-y^2}$ orbital carrying ≈ 1 electron, owing to a strong hybridization with N ligand. In the high-spin state, both orbitals hybridize strongly with the N ligands, such that the occupation of the individual orbitals is $\sim$1.2, reducing the total occupation to $\langle n \rangle \sim 2.4$.

The grey lines in Fig. 7.9 (left and middle panels) were obtained from simplified models described before (see Appendix E.1), describing the physics in the two limiting cases. The spin-moment, as well as the occupations are almost perfectly reproduced within these models; they fail, however, to predict the spin-moment transition, since the low-spin-state remains energetically favored within the whole parameter range under consideration.

The right panel of Fig. 7.9 shows the difference in free energy and energy (both as defined above) between the lowest lying low and high-spin-states as a function of x. Compared to Fig. 7.5 (c), one

notes an additional feature in the region of the SCO, i.e. where the lines cross zero. This jump is due to the different occupations of the correlated orbitals corresponding to the different spin-states, and can be attributed to subtleties in the application of the double counting correction (see Appendix E.2).

7.4 Conclusion

In summary, we have presented a minimal two-orbital model, that is able to capture the relevant physics of the spin-state transition in a generic parameter space. We deduced a spin phase diagram which depicts the inter-dependence of hybridization and crystal field in order to bring in a spin-crossover. The model is complemented with the parameters derived from DFT calculations in order to study the realistic scenario of a spin crossover in Ni-TPP isomers. Our calculations show a robust low-spin-state in Ni-TPP and a high-spin-state in six-fold coordinated Ni-TPP(Im_2). As indicated in the results of the model study, we modified the hybridization between axial ligands and Ni-ion in Ni-TPP(Im_2) by imparting a mechanical strain of the imidazole ligands. The situation is mimicked by an interpolation between the parameters sets corresponding to six-fold coordinated Ni-TPP(Im_2) and four-fold coordinated Ni-TPP molecules. The spin-state transition appears at an intermediate strain, corresponding to the interpolating parameter $x \approx 0.4$. The ligand to metal charge transfer is significantly enhanced as the molecular spin-state changes from the high- to the low-spin state. In this respect, we have discussed the importance of a charge self-consistent double counting scheme in order to properly account for the metal-ligand charge transfer. Finally, our results suggest that a mechanical strain-induced SCO can be achieved in hexacoordinated Ni-TPP(Im_2), which would potentially pave the way for its integration in mechanically controlled or scanning tunneling microscopy break junctions.

Conclusion and Outlook

In this thesis, we have treated several topics belonging to the field of correlated electron systems.

In the first part, have presented results for the two- and three orbital Hubbard model obtained from finite-temperature DMFT calculations, comparing the case with and without Hund's exchange coupling. In particular, we focused on the doping-driven metal-insulator transition around half filling, where we found Hund's coupling to give rise to a regime of bad-metallic character that reaches to large dopings, while being adiabatically connected to the insulator. This regime was also found to be related to the emergence of the spin-freezing phenomenon, which recently received attention due to its potential significance for superconductivity.

The findings presented in this chapter pose many new questions, for instance concerning the implications of the bad-metallic phase in the context of realistic systems, its fate at lower temperatures and the underlying connection to spin-freezing.

In the second part of the thesis, we discussed the importance and implications of metal-ligand interactions – the d-p problem. We have presented results for a minimal two-orbital d-p system, obtained from DMFT. In the case of vanishing inter-shell interaction, we presented a phase-diagram á la Zaanen-Sawatzky-Allen, and discussed the different insulating regimes. We then introduced inter-shell metal-ligand– as well as ligand-ligand interactions, studying their effect in various parameter regimes. We show that these additional interactions generally decrease correlations on the transition metal ions due to an induced shift of the charge transfer energies. Finally, we demonstrate that Hartree and Hartree-Fock schemes can be an effective tool to approximately take into account inter-shell interactions.

We derived and tested a novel method for an effective treatment of inter-shell interactions in the context of d-p models. The method is an extension of the shell-folding scheme and based on a slave-rotor description of charge fluctuations. The first sections of this chapter were spent on the derivation of the formalism, followed by a description of how to embed it the framework of DMFT, as well as various approximation schemes.

This part was closed with a proof-of-principle, applying our method in the insulating and metallic regimes, where it compared to results from reference calculations and other approximation schemes. Here, an exciting outlook is to apply our slave-rotor method to realistic systems, where an exact consideration of the metal-ligand interactions is rarely feasible.

In the last part of the thesis, we left the realm of lattice models to study problems related to molecular systems. We considered a minimal many-body model that is able to capture the relevant physics of the spin-crossover (SCO) in organometallic molecules. We then demonstrated the hybridization driven SCO by incorporating parameters from the DFT calculations into our model. To this means, we mimicked the effect of strain on the axial ligands by interpolating between the parameter sets corresponding to the two different molecular structures.

Our results suggest Ni-porphyrin as a promising candidate for a molecular spin-state switch, that could for instance be applied in the context of a mechanically controlled break junction.

Acknowledgements

Of course, this thesis could not have been realized without the help and support of many people.

In particular I want to thank my *directrice* Silke Biermann, who provided guidance and advice, shared her ideas with me and introduced me to other members of the scientific community. Most importantly, she gave me the freedom to explore and to pursue my own ideas.

In this spirit, I also want to thank my collaborators Luca de' Medici and Sumanta Bhandary for sharing their expertise and excitement, introducing me to new concepts and even new fields.

I want to thank all the members of CPHT, for making the last three years a wonderful, stimulating experience. Specifically, I want to thank Sophie Chauvin and Pascal Delange, the "germanic gang" including Steffen Backes, Benjamin Lenz, Maximilian Schemmer, Anna Galler and Jan Maelger, les Français Julien Despres, Louis Villa, Alexandre Lazarescu (also for sharing their valuable frexpertise), il mafioso Marcello Turtulici, Yao Hepeng, Swarup Panda, my friend Alaska Subedi (also for amazing food) and anyone that I could have forgotten.

Apart from life at University I want to thank my friends and flatmates Roberto Raschetti, Damien Bellon and, especially, Justine Houille for making my time in Paris truly wonderful.

Finally, I would not have enjoyed my time in Paris the way I did without the support of my family in Austria – my mother, my father, Teresa, Alex, my grandparents Ludwig, Melitta, Margaretha and Johann, and the cat Coco (for her soft fur and wild spirit) – who did not expel me despite my long periods of absence. I'm particularly grateful to all of friends back home, for keeping the contact regardless of the distance.

References

[1] (1992). Electronic structure of metallic oxides: Band-gap closure and valence control. *Journal of Physics and Chemistry of Solids*, 53(12):1595 – 1602. Special Issue Elecronic Structure and Fermiology of High-T.

[2] Amaricci, A., de' Medici, L., and Capone, M. (2017). Mott transitions with partially filled correlated orbitals. *Europhysics Letters*, 118.

[3] Anderson, P. W. (1961). Localized magnetic states in metals. *Phys. Rev.*, 124:41–53.

[4] ANDERSON, P. W. (1987). The resonating valence bond state in la2cuo4 and superconductivity. *Science*, 235(4793):1196–1198.

[5] Anderson, P. W. and Yuval, G. (1969). Exact results in the kondo problem: Equivalence to a classical one-dimensional coulomb gas. *Phys. Rev. Lett.*, 23:89–92.

[6] Anisimov, V. I., Zaanen, J., and Andersen, O. K. (1991). Band theory and mott insulators: Hubbard u instead of stoner i. *Phys. Rev. B*, 44:943–954.

[7] Argaman, N. and Makov, G. (2000). Density functional theory: An introduction. *American Journal of Physics*, 68(1):69–79.

[8] Aryasetiawan, F., Imada, M., Georges, A., Kotliar, G., Biermann, S., and Lichtenstein, A. I. (2004). Frequency-dependent local interactions and low-energy effective models from electronic structure calculations. *Phys. Rev. B*, 70:195104.

[9] Aryasetiawan, F., Karlsson, K., Jepsen, O., and Schönberger, U. (2006). Calculations of hubbard *u* from first-principles. *Phys. Rev. B*, 74:125106.

[10] Auerbach, A. and Arovas, D. P. (2011). Schwinger bosons approaches to quantumantiferromagnetism. In Lacroix, C., Mendels, P., and Mila, F., editors, *Introduction to Frustrated Magnetism*, chapter 14. Springer-Verlag Berlin Heidelberg.

[11] Awschalom, D. D. and Flatté, M. E. (2007). Challenges for semiconductor spintronics. *Nature Physics*, 3:153 EP –.

[12] Ayral, T. and Parcollet, O. (2015). Mott physics and spin fluctuations: A unified framework. *Phys. Rev. B*, 92:115109.

[13] Backes, S. (2017). *Density functional theory and dynamical mean-field theory: A way to model strongly correlated systems*. PhD thesis, Goethe-Universitrankfurt in Frankfurt am Main.

[14] Baibich, M. N., Broto, J. M., Fert, A., Van Dau, F. N., Petroff, F., Etienne, P., Creuzet, G., Friederich, A., and Chazelas, J. (1988). Giant magnetoresistance of (001)fe/(001)cr magnetic superlattices. *Phys. Rev. Lett.*, 61:2472–2475.

[15] Bairagi, K., Iasco, O., Bellec, A., Kartsev, A., Li, D., Lagoute, J., Chacon, C., Girard, Y., Rousset, S., Miserque, F., Dappe, Y. J., Smogunov, A., Barreteau, C., Boillot, M.-L., Mallah, T., and Repain, V. (2016). Molecular-scale dynamics of light-induced spin cross-over in a two-dimensional layer. *Nature Communications*, 7:12212 EP –.

[16] Barnes, S. E. (1976). New method for the anderson model. *Journal of Physics F: Metal Physics*, 6(7):1375–1383.

[17] Becke, A. D. (1988). Density-functional exchange-energy approximation with correct asymptotic behavior. *Phys. Rev. A*, 38:3098–3100.

[18] Bednorz, J. G. and Müller, K. A. (1986). Possible hightc superconductivity in the balacuo system. *Zeitschrift für Physik B Condensed Matter*, 64(2):189–193.

[19] Bernien, M., Naggert, H., Arruda, L. M., Kipgen, L., Nickel, F., Miguel, J., Hermanns, C. F., Krüger, A., Krüger, D., Schierle, E., Weschke, E., Tuczek, F., and Kuch, W. (2015). Highly efficient thermal and light-induced spin-state switching of an fe(ii) complex in direct contact with a solid surface. *ACS Nano*, 9(9):8960–8966. PMID: 26266974.

[20] Bhandary, S., Brena, B., Panchmatia, P. M., Brumboiu, I., Bernien, M., Weis, C., Krumme, B., Etz, C., Kuch, W., Wende, H., Eriksson, O., and Sanyal, B. (2013). Manipulation of spin state of iron porphyrin by chemisorption on magnetic substrates. *Phys. Rev. B*, 88:024401.

[21] Bhandary, S., Ghosh, S., Herper, H., Wende, H., Eriksson, O., and Sanyal, B. (2011). Graphene as a reversible spin manipulator of molecular magnets. *Phys. Rev. Lett.*, 107:257202.

[22] Bhandary, S., Schüler, M., Thunström, P., di Marco, I., Brena, B., Eriksson, O., Wehling, T., and Sanyal, B. (2016). Correlated electron behavior of metal-organic molecules: Insights from density functional theory combined with many-body effects using exact diagonalization. *Phys. Rev. B*, 93:155158.

[23] Biedenharn, H. and Van Dam, H. (1965). *J. Schwinger: Quantum Theory of Angular Momentum*. Academic, New York.

[24] Biermann, S., Aryasetiawan, F., and Georges, A. (2003). First-principles approach to the electronic structure of strongly correlated systems: Combining the *gw* approximation and dynamical mean-field theory. *Phys. Rev. Lett.*, 90:086402.

[25] Binasch, G., Grünberg, P., Saurenbach, F., and Zinn, W. (1989). Enhanced magnetoresistance in layered magnetic structures with antiferromagnetic interlayer exchange. *Phys. Rev. B*, 39:4828–4830.

[26] Blandin, A. and Friedel, J. (1959). Propriétés magnétiques des alliages dilués. interactions magnétiques et antiferromagnétisme dans les alliages du type métal noble-métal de transition. *J. Phys. Radium*, 20:160.

[27] Born, M. and Oppenheimer, R. (1927). Zur quantentheorie der molekeln. *Annalen der Physik*, 389(20):457–484.

[28] Burke, K. and Wagner, L. O. (2013). Dft in a nutshell. *International Journal of Quantum Chemistry*, 113(2):96–101.

[29] Casula, M., Rubtsov, A., and Biermann, S. (2012). Dynamical screening effects in correlated materials: Plasmon satellites and spectral weight transfers from a green's function ansatz to extended dynamical mean field theory. *Phys. Rev. B*, 85:035115.

[30] Chen, J., Millis, A. J., and Marianetti, C. A. (2015). Density functional plus dynamical mean-field theory of the spin-crossover molecule fe(phen)$_2$(ncs)$_2$. *Phys. Rev. B*, 91:241111.

[31] Clogston, A. M., Matthias, B. T., Peter, M., Williams, H. J., Corenzwit, E., and Sherwood, R. C. (1962). Local magnetic moment associated with an iron atom dissolved in various transition metal alloys. *Phys. Rev.*, 125:541–552.

[32] Coleman, P. (1984). New approach to the mixed-valence problem. *Phys. Rev. B*, 29:3035–3044.

[33] Coleman, P. (2015). *Introduction to Many-Body Physics*. Cambridge University Press.

[34] Coqblin, B. and Schrieffer, J. R. (1969). Exchange interaction in alloys with cerium impurities. *Phys. Rev.*, 185:847–853.

[35] Czyżyk, M. T. and Sawatzky, G. A. (1994a). Local-density functional and on-site correlations: The electronic structure of la$_2$cuo$_4$ and lacuo$_3$. *Phys. Rev. B*, 49:14211–14228.

[36] Czyżyk, M. T. and Sawatzky, G. A. (1994b). Local-density functional and on-site correlations: The electronic structure of la$_2$cuo$_4$ and lacuo$_3$. *Phys. Rev. B*, 49:14211–14228.

[37] de Boer, J. H. and Verwey, E. J. W. (1937). Semi-conductors with partially and with completely filled3d-lattice bands. *Proceedings of the Physical Society*, 49(4S):59–71.

[38] de Haas, W., de Boer, J., and van dën Berg, G. (1934). The electrical resistance of gold, copper and lead at low temperatures. *Physica*, 1(7):1115 – 1124.

[39] de' Medici, L., Mravlje, J., and Georges, A. (2011). Janus-faced influence of hund's rule coupling in strongly correlated materials. *Phys. Rev. Lett.*, 107:256401.

[40] Decurtins, S., Gütlich, P., Köhler, C., Spiering, H., and Hauser, A. (1984). Light-induced excited spin state trapping in a transition-metal complex: The hexa-1-propyltetrazole-iron (ii) tetrafluoroborate spin-crossover system. *Chemical Physics Letters*, 105(1):1 – 4.

[41] de'Medici, L., Georges, A., and Biermann, S. (2005). Orbital-selective mott transition in multiband systems: Slave-spin representation and dynamical mean-field theory. *Phys. Rev. B*, 72:205124.

[42] Dirac, P. A. M. and Fowler, R. H. (1928). The quantum theory of the electron. *Proceedings of the Royal Society of London. Series A, Containing Papers of a Mathematical and Physical Character*, 117(778):610–624.

[43] Dodge, J. S., Weber, C. P., Corson, J., Orenstein, J., Schlesinger, Z., Reiner, J. W., and Beasley, M. R. (2000). Low-frequency crossover of the fractional power-law conductivity in srruo$_3$. *Phys. Rev. Lett.*, 85:4932–4935.

[44] Dommaschk, M., Schütt, C., Venkataramani, S., Jana, U., Näther, C., Sönnichsen, F. D., and Herges, R. (2014). Rational design of a room temperature molecular spin switch. the light-driven coordination induced spin state switch (ld-cisss) approach. *Dalton Trans.*, 43:17395–17405.

[45] Dudarev, S. L., Botton, G. A., Savrasov, S. Y., Humphreys, C. J., and Sutton, A. P. (1998). Electron-energy-loss spectra and the structural stability of nickel oxide: An lsda+u study. *Phys. Rev. B*, 57:1505–1509.

[46] Duval, H., Bulach, V., Fischer, J., and Weiss, R. (1999). Four-coordinate, low-spin (s = 0) and six-coordinate, high-spin (s = 1) nickel(ii) complexes of tetraphenylporphyrins with -pyrrole electron-withdrawing substituents: Porphyrin-core expansion and conformation. *Inorganic Chemistry*, 38(24):5495–5501. PMID: 11671276.

[47] Eckern, U., Schön, G., and Ambegaokar, V. (1984). Quantum dynamics of a superconducting tunnel junction. *Phys. Rev. B*, 30:6419–6431.

[48] Emery, V. J. (1987). Theory of high-t_c superconductivity in oxides. *Phys. Rev. Lett.*, 58:2794–2797.

[49] Fanfarillo, L. and Bascones, E. (2015). Electronic correlations in hund metals. *Phys. Rev. B*, 92:075136.

[50] Florens, S. and Georges, A. (2002). Quantum impurity solvers using a slave rotor representation. *Phys. Rev. B*, 66:165111.

[51] Florens, S. and Georges, A. (2004). Slave-rotor mean-field theories of strongly correlated systems and the mott transition in finite dimensions. *Phys. Rev. B*, 70:035114.

[52] Foulkes, W. (2012). Tight-binding models and coulomb interactions for s, p, and d electrons. In Pavarini, E., Koch, E., Anders, F., and Jarrell, M., editors, *Correlated Electrons: From Models to Materials Modeling and Simulation, Vol. 2*, chapter 6. Verlag des Forschungszentrum Jlich.

[53] Foulkes, W. (2016). Tight-binding models and coulomb interactions for s, p, and d electrons. In E. Pavarini, E. Koch, J. v. d. B. and Sawatzky, G., editors, *Quantum Materials: Experiments and Theory Modeling and Simulation Vol. 6*, chapter 3. Verlag des Forschungszentrum Jlich.

[54] Frésard, R. and Wolfle, P. (1992). Unified slave boson representation of spin and charge degrees of freedom for strongly correlated fermi systems. *International Journal of Modern Physics B*, 06(05n06):685–704.

[55] Georges, A. and Kotliar, G. (1992). Hubbard model in infinite dimensions. *Phys. Rev. B*, 45:6479–6483.

[56] Georges, A., Kotliar, G., and Krauth, W. (1993). Superconductivity in the two-band hubbard model in infinite dimensions. *Zeitschrift für Physik B Condensed Matter*, 92(3):313–321.

[57] Georges, A., Kotliar, G., Krauth, W., and Rozenberg, M. J. (1996). Dynamical mean-field theory of strongly correlated fermion systems and the limit of infinite dimensions. *Rev. Mod. Phys.*, 68:13–125.

[58] Georges, A., Kotliar, G., and Si, Q. (1992). Strongly correlated systems in infinite dimensions and their zero dimensional counterparts. *International Journal of Modern Physics B*, 06(05n06):705–730.

[59] Georges, A., Medici, L. d., and Mravlje, J. (2013). Strong correlations from hund's coupling. *Annual Review of Condensed Matter Physics*, 4(1):137–178.

[60] Georgescu, A. B. and Ismail-Beigi, S. (2015). Generalized slave-particle method for extended hubbard models. *Phys. Rev. B*, 92:235117.

[61] Gross, D. J. and Wilczek, F. (1973). Ultraviolet behavior of non-abelian gauge theories. *Phys. Rev. Lett.*, 30:1343–1346.

[62] Gross, R. and Marx, A. (2012). *Festkörperphysik*. Oldenbourg Wissenschaftsverlag.

[63] Gueddida, S. and Alouani, M. (2013). Spin crossover in a single $fe(phen)_2(ncs)_2$ molecule adsorbed onto metallic substrates: An ab initio calculation. *Phys. Rev. B*, 87:144413.

[64] Gull, E., Millis, A. J., Lichtenstein, A. I., Rubtsov, A. N., Troyer, M., and Werner, P. (2011). Continuous-time monte carlo methods for quantum impurity models. *Rev. Mod. Phys.*, 83:349–404.

[65] Han, M. J., Wang, X., Marianetti, C. A., and Millis, A. J. (2011). Dynamical mean-field theory of nickelate superlattices. *Phys. Rev. Lett.*, 107:206804.

[66] Hansmann, P., Parragh, N., Toschi, A., Sangiovanni, G., and Held, K. (2014). Importance of d–p Coulomb interaction for high TC cuprates and other oxides. *New Journal of Physics*, 16(3):033009.

[67] Harrison, N. M. (2006). An introduction to density functional theoryl.

[68] Hartree, D. R. (1928). The wave mechanics of an atom with a non-coulomb central field. part ii. some results and discussion. *Mathematical Proceedings of the Cambridge Philosophical Society*, 24(1):111?132.

[69] Harzmann, G. D., Frisenda, R., van der Zant, H. S. J., and Mayor, M. (2015). Single-molecule spin switch based on voltage-triggered distortion of the coordination sphere. *Angewandte Chemie International Edition*, 54(45):13425–13430.

[70] Haule, K., Birol, T., and Kotliar, G. (2014). Covalency in transition-metal oxides within all-electron dynamical mean-field theory. *Phys. Rev. B*, 90:075136.

[71] Haule, K. and Kotliar, G. (2009). Coherence–incoherence crossover in the normal state of iron oxypnictides and importance of hund's rule coupling. *New Journal of Physics*, 11(2):025021.

[72] Haule, K., Shim, J. H., and Kotliar, G. (2008). Correlated electronic structure of $lao_{1-x}f_xFeAs$. *Phys. Rev. Lett.*, 100:226402.

[73] Herges, R., Dommaschk, M., Gutzeit, F., Boretius, S., and Haag, R. (2014). Coordination-induced spin-state-switch (cisss) in water. *Chem. Commun.*, 50.

[74] Herring, C. (1966). *Magnetism: Exchange Interactions Among Itinerant Electrons*, volume 4. Academic Press, New York.

[75] Hettler, M. H., Mukherjee, M., Jarrell, M., and Krishnamurthy, H. R. (2000). Dynamical cluster approximation: Nonlocal dynamics of correlated electron systems. *Phys. Rev. B*, 61:12739–12756.

[76] Hohenberg, P. and Kohn, W. (1964). Inhomogeneous electron gas. *Phys. Rev.*, 136:B864–B871.

[77] Horvat, A., Žitko, R., and Mravlje, J. (2016). Low-energy physics of three-orbital impurity model with kanamori interaction. *Phys. Rev. B*, 94:165140.

[78] Hoshino, S. and Werner, P. (2015). Superconductivity from emerging magnetic moments. *Phys. Rev. Lett.*, 115:247001.

[79] Hubbard, J. and Flowers, B. H. (1963). Electron correlations in narrow energy bands. *Proceedings of the Royal Society of London. Series A. Mathematical and Physical Sciences*, 276(1365):238–257.

[80] utić et al.spintronics$_r$*eviewŽuti ć*,*I*.,*Fabian*,*J*.,*andDas Sarma*,*S*.(2004). *Spintronics* : *Fundamentalsandapplications*.*Rev*.*Mod*.*Phys*.,76 : 323 − −410.

[81] Johnson, M. and Silsbee, R. H. (1985). Interfacial charge-spin coupling: Injection and detection of spin magnetization in metals. *Phys. Rev. Lett.*, 55:1790–1793.

[82] Jones, R. O. (2015). Density functional theory: Its origins, rise to prominence, and future. *Rev. Mod. Phys.*, 87:897–923.

[83] Kamihara, Y., Hiramatsu, H., Hirano, M., Kawamura, R., Yanagi, H., Kamiya, T., and Hosono, H. (2006). Iron-based layered superconductor: laofep. *Journal of the American Chemical Society*, 128(31):10012–10013. PMID: 16881620.

[84] Kamihara, Y., Watanabe, T., Hirano, M., and Hosono, H. (2008). Iron-based layered superconductor la[o1-xfx]feas (x = 0.050.12) with tc = 26 k. *Journal of the American Chemical Society*, 130(11):3296–3297. PMID: 18293989.

[85] Kanamori, J. (1963). Electron correlation and ferromagnetism of transition metals. *Progress of Theoretical Physics*, 30(3):275.

[86] Kikkawa, J. M. and Awschalom, D. D. (1999). Lateral drag of spin coherence in gallium arsenide. *Nature*, 397(6715):139–141.

[87] Kipgen, L., Bernien, M., Ossinger, S., Nickel, F., Britton, A. J., Arruda, L. M., Naggert, H., Luo, C., Lotze, C., Ryll, H., Radu, F., Schierle, E., Weschke, E., Tuczek, F., and Kuch, W. (2018). Evolution of cooperativity in the spin transition of an iron(ii) complex on a graphite surface. *Nature Communications*, 9(1):2984.

[88] Koga, A., Inaba, K., and Kawakami, N. (2005). Mott transitions in two-orbital hubbard systems. *Progress of Theoretical Physics Supplement*, 160:253–273.

[89] Kohn, W. and Sham, L. J. (1965). Self-consistent equations including exchange and correlation effects. *Phys. Rev.*, 140:A1133–A1138.

[90] Kondo, J. (1964). Resistance Minimum in Dilute Magnetic Alloys. *Progress of Theoretical Physics*, 32(1):37–49.

[91] Kostic, P., Okada, Y., Collins, N. C., Schlesinger, Z., Reiner, J. W., Klein, L., Kapitulnik, A., Geballe, T. H., and Beasley, M. R. (1998). Non-fermi-liquid behavior of $SrRuO_3$: Evidence from infrared conductivity. *Phys. Rev. Lett.*, 81:2498–2501.

[92] Kotliar, G., Murthy, S., and Rozenberg, M. J. (2002). Compressibility divergence and the finite temperature mott transition. *Phys. Rev. Lett.*, 89:046401.

[93] Kotliar, G. and Ruckenstein, A. E. (1986). New functional integral approach to strongly correlated fermi systems: The gutzwiller approximation as a saddle point. *Phys. Rev. Lett.*, 57:1362–1365.

[94] Kresse, G. and Furthmüller, J. (1996). Efficient iterative schemes for ab initio total-energy calculations using a plane-wave basis set. *Phys. Rev. B*, 54:11169–11186.

[95] Krivenko, I. S. and Biermann, S. (2015). Slave rotor approach to dynamically screened coulomb interactions in solids. *Phys. Rev. B*, 91:155149.

[96] Kuramoto, Y. (1983). Self-consistent perturbation theory for dynamics of valence fluctuations. *Zeitschrift für Physik B Condensed Matter*, 53(1):37–52.

[97] Lanczos, C. (1950). An iteration method for the solution of the eigenvalue problem of linear differential and integral operators. *Journal of Research of the National Bureau of Standards*, 45:255.

[98] Landau, L. D. (1957a). Oscillations in a fermi liquid. *JETP*, 5:101.

[99] Landau, L. D. (1957b). The theory of a fermi liquid. *JETP*, 3:920.

[100] Langreth, D. C. and Mehl, M. J. (1983). Beyond the local-density approximation in calculations of ground-state electronic properties. *Phys. Rev. B*, 28:1809–1834.

[101] Lebègue, S., Pillet, S., and Ángyán, J. G. (2008). Modeling spin-crossover compounds by periodic DFT + U approach. *Phys. Rev. B*, 78:024433.

[102] Lechermann, F., Georges, A., Kotliar, G., and Parcollet, O. (2007). Rotationally invariant slave-boson formalism and momentum dependence of the quasiparticle weight. *Phys. Rev. B*, 76:155102.

[103] Lee, Y. S., Yu, J., Lee, J. S., Noh, T. W., Gimm, T.-H., Choi, H.-Y., and Eom, C. B. (2002). Non-fermi liquid behavior and scaling of the low-frequency suppression in the optical conductivity spectra of $caruo_3$. *Phys. Rev. B*, 66:041104.

[104] Li, T., Wölfle, P., and Hirschfeld, P. J. (1989). Spin-rotation-invariant slave-boson approach to the hubbard model. *Phys. Rev. B*, 40:6817–6821.

[105] Li Manni, G., Smart, S. D., and Alavi, A. (2016). Combining the complete active space self-consistent field method and the full configuration interaction quantum monte carlo within a super-ci framework, with application to challenging metal-porphyrins. *Journal of Chemical Theory and Computation*, 12(3):1245–1258.

[106] Lieb, E. H. and Wu, F. Y. (1968). Absence of mott transition in an exact solution of the short-range, one-band model in one dimension. *Phys. Rev. Lett.*, 20:1445–1448.

[107] Liechtenstein, A. I., Anisimov, V. I., and Zaanen, J. (1995a). Density-functional theory and strong interactions: Orbital ordering in mott-hubbard insulators. *Phys. Rev. B*, 52:R5467–R5470.

[108] Liechtenstein, A. I., Anisimov, V. I., and Zaanen, J. (1995b). Density-functional theory and strong interactions: Orbital ordering in mott-hubbard insulators. *Phys. Rev. B*, 52:R5467–R5470.

[109] Liu, J., Chen, Y.-C., Liu, J.-L., Vieru, V., Ungur, L., Jia, J.-H., Chibotaru, L. F., Lan, Y., Wernsdorfer, W., Gao, S., Chen, X.-M., and Tong, M.-L. (2016). A stable pentagonal bipyramidal dy(iii) single-ion magnet with a record magnetization reversal barrier over 1000 k. *Journal of the American Chemical Society*, 138(16):5441–5450. PMID: 27054904.

[110] Makino, H., Inoue, I. H., Rozenberg, M. J., Hase, I., Aiura, Y., and Onari, S. (1998). Bandwidth control in a perovskite-type $3d^1$-correlated metal $ca_{1-x}sr_xvo_3$. ii. optical spectroscopy. *Phys. Rev. B*, 58:4384–4393.

[111] Mattuck, R. (1992). *A Guide to Feynman Diagrams in the Many-body Problem*. Dover Books on Physics Series. Dover Publications.

[112] Metzner, W. and Vollhardt, D. (1989). Correlated lattice fermions in $d = \infty$ dimensions. *Phys. Rev. Lett.*, 62:324–327.

[113] Milek, M., Heinemann, F. W., and Khusniyarov, M. M. (2013). Spin crossover meets diarylethenes: Efficient photoswitching of magnetic properties in solution at room temperature. *Inorganic Chemistry*, 52(19):11585–11592. PMID: 24063424.

[114] Miyake, T. and Aryasetiawan, F. (2008). Screened coulomb interaction in the maximally localized wannier basis. *Phys. Rev. B*, 77:085122.

[115] Miyake, T., Pourovskii, L., Vildosola, V., Biermann, S., and Georges, A. (2008). d- and f-orbital correlations in the refeaso compounds. *Journal of the Physical Society of Japan*, 77(Suppl.C):99–102.

[116] Miyamachi, T., Gruber, M., Davesne, V., Bowen, M., Boukari, S., Joly, L., Scheurer, F., Rogez, G., Yamada, T. K., Ohresser, P., Beaurepaire, E., and Wulfhekel, W. (2012). Robust spin crossover and memristance across a single molecule. *Nature communications*, 3:938.

[117] Mott, N. F. and Fowler, R. H. (1936). The electrical conductivity of transition metals. *Proceedings of the Royal Society of London. Series A - Mathematical and Physical Sciences*, 153(880):699–717.

[118] Mott, N. F. and Peierls, R. (1937). Discussion of the paper by de boer and verwey. *Proceedings of the Physical Society*, 49(4S):72–73.

[119] Müller-Hartmann (2006). Theoretische festkrperphysik ii.

[120] Müller-Hartmann, E. (1989). Correlated fermions on a lattice in high dimensions. *Zeitschrift für Physik B Condensed Matter*, 74(4):507–512.

[121] Naggert, H., Bannwarth, A., Chemnitz, S., von Hofe, T., Quandt, E., and Tuczek, F. (2011). First observation of light-induced spin change in vacuum deposited thin films of iron spin crossover complexes. *Dalton Trans.*, 40:6364–6366.

[122] Nakamura, K., Arita, R., and Imada, M. (2008). Ab initio derivation of low-energy model for iron-based superconductors lafeaso and lafepo. *Journal of the Physical Society of Japan*, 77(9):093711.

[123] Nevidomskyy, A. H. and Coleman, P. (2009a). Kondo resonance narrowing in d- and f-electron systems. *Phys. Rev. Lett.*, 103:147205.

[124] Nevidomskyy, A. H. and Coleman, P. (2009b). Kondo resonance narrowing in d- and f-electron systems. *Phys. Rev. Lett.*, 103:147205.

[125] Nozières, Ph. and Blandin, A. (1980). Kondo effect in real metals. *J. Phys. France*, 41(3):193–211.

[126] Okada, I. and Yosida, K. (1973). Singlet Ground State of the Localized d-Electrons Coupled with Conduction Electrons in Metals. *Progress of Theoretical Physics*, 49(5):1483–1502.

[127] Okimoto, Y., Katsufuji, T., Okada, Y., Arima, T., and Tokura, Y. (1995). Optical spectra in (la,y)tio$_3$: Variation of mott-hubbard gap features with change of electron correlation and band filling. *Phys. Rev. B*, 51:9581–9588.

[128] Ormaza, M., Abufager, P., Verlhac, B., Bachellier, N., Bocquet, M. L., Lorente, N., and Limot, L. (2017). Controlled spin switching in a metallocene molecular junction. *Nature Communications*, 8(1):1974.

[129] Parcollet, O., Ferrero, M., Ayral, T., Hafermann, H., Krivenko, I., Messio, L., and Seth, P. (2015). Triqs: A toolbox for research on interacting quantum systems. *Computer Physics Communications*, 196:398 – 415.

[130] Park, H., Haule, K., and Kotliar, G. (2008). Cluster dynamical mean field theory of the mott transition. *Phys. Rev. Lett.*, 101:186403.

[131] Patchkovskii, S., Kozlowski, P. M., and Zgierski, M. Z. (2004). Theoretical analysis of singlet and triplet excited states of nickel porphyrins. *The Journal of Chemical Physics*, 121(3):1317–1324.

[132] Perdew, J. P., Burke, K., and Ernzerhof, M. (1996). Generalized gradient approximation made simple. *Phys. Rev. Lett.*, 77:3865–3868.

[133] Politzer, H. D. (1973). Reliable perturbative results for strong interactions? *Phys. Rev. Lett.*, 30:1346–1349.

[134] Potthoff, M. (2012). Self-Energy-Functional Theory. In: Avella A., Mancini F. (eds) Strongly Correlated Systems. Springer Series in Solid-State Sciences, vol 171. Springer, Berlin, Heidelberg.

[135] Pruschke, T. and Bulla, R. (2005). Hund's coupling and the metal-insulator transition in the two-bandhubbard model. *The European Physical Journal B - Condensed Matter and Complex Systems*, 44(2):217–224.

[136] Sanvito, S. (2011). Molecular spintronics. *Chem. Soc. Rev.*, 40:3336–3355.

[137] Sarachik, M. P., Corenzwit, E., and Longinotti, L. D. (1964). Resistivity of mo-nb and mo-re alloys containing 1*Phys. Rev.*, 135:A1041–A1045.

[138] Schollwöck, U. (2005). The density-matrix renormalization group. *Rev. Mod. Phys.*, 77:259–315.

[139] Schrieffer, J. R. and Wolff, P. A. (1966). Relation between the anderson and kondo hamiltonians. *Phys. Rev.*, 149:491–492.

[140] Schrodinger, E. (1926). Quantisierung als eigenwertproblem. *Annalen der Physik*, 385(13):437–490.

[141] Seth, P., Hansmann, P., van Roekeghem, A., Vaugier, L., and Biermann, S. (2017). Towards a first-principles determination of effective coulomb interactions in correlated electron materials: Role of intershell interactions. *Phys. Rev. Lett.*, 119:056401.

[142] Shinaoka, H., Nomura, Y., Biermann, S., Troyer, M., and Werner, P. (2015). Negative sign problem in continuous-time quantum monte carlo: Optimal choice of single-particle basis for impurity problems. *Phys. Rev. B*, 92:195126.

[143] Shortley, G. and Condon, E. (1935). *The theory of atomic spectra*. Cambridge.

[144] Song, Y., Haddad, R. E., Jia, S.-L., Hok, S., Olmstead, M. M., Nurco, D. J., Schore, N. E., Zhang, J., Ma, J.-G., Smith, K. M., Gazeau, S., Pécaut, J., Marchon, J.-C., Medforth, C. J., and Shelnutt, J. A. (2005). Energetics and structural consequences of axial ligand coordination in nonplanar nickel porphyrins. *Journal of the American Chemical Society*, 127(4):1179–1192. PMID: 15669857.

[145] Sordi, G., Haule, K., and Tremblay, A.-M. S. (2010). Finite doping signatures of the mott transition in the two-dimensional hubbard model. *Phys. Rev. Lett.*, 104:226402.

[146] Sordi, G., Sémon, P., Haule, K., and Tremblay, A. M. S. (2012). Pseudogap temperature as a widom line in doped mott insulators. 2.

[147] Stadler, K., Kotliar, G., Weichselbaum, A., and von Delft, J. (2018). Hundness versus mottness in a three-band hubbard-hund model: On the origin of strong correlations in hund metals. *Annals of Physics*.

[148] Stadler, K. M., Yin, Z. P., von Delft, J., Kotliar, G., and Weichselbaum, A. (2015). Dynamical mean-field theory plus numerical renormalization-group study of spin-orbital separation in a three-band hund metal. *Phys. Rev. Lett.*, 115:136401.

[149] Sugiyama, G. and Koonin, S. (1986). Auxiliary field monte-carlo for quantum many-body ground states. *Annals of Physics*, 168(1):1 – 26.

[150] Toschi, A., Katanin, A. A., and Held, K. (2007). Dynamical vertex approximation: A step beyond dynamical mean-field theory. *Phys. Rev. B*, 75:045118.

[151] Umrigar, C. J., Wilson, K. G., and Wilkins, J. W. (1988). Optimized trial wave functions for quantum monte carlo calculations. *Phys. Rev. Lett.*, 60:1719–1722.

[152] Urdampilleta, M., Klyatskaya, S., Cleuziou, J.-P., Ruben, M., and Wernsdorfer, W. (2011). Supramolecular spin valves. *Nature Materials*, 10:502 EP –.

[153] van der Marel, D. and Sawatzky, G. A. (1988). Electron-electron interaction and localization in d and f transition metals. *Phys. Rev. B*, 37:10674–10684.

[154] van Dongen, P. G. J., Gebhard, F., and Vollhardt, D. (1989). Variational evaluation of correlation functions for lattice electrons in high dimensions. *Zeitschrift für Physik B Condensed Matter*, 76(2):199–210.

[155] Venkataramani, S., Jana, U., Dommaschk, M., Sönnichsen, F. D., Tuczek, F., and Herges, R. (2011). Magnetic bistability of molecules in homogeneous solution at room temperature. *Science*, 331(6016):445–448.

[156] Vučičević, J., Tanasković, D., Rozenberg, M. J., and Dobrosavljević, V. (2015). Bad-metal behavior reveals mott quantum criticality in doped hubbard models. *Phys. Rev. Lett.*, 114:246402.

[157] Wang, X., Han, M. J., de' Medici, L., Park, H., Marianetti, C. A., and Millis, A. J. (2012). Covalency, double-counting, and the metal-insulator phase diagram in transition metal oxides. *Phys. Rev. B*, 86:195136.

[158] Warner, B., Oberg, J. C., Gill, T. G., El Hallak, F., Hirjibehedin, C. F., Serri, M., Heutz, S., Arrio, M.-A., Sainctavit, P., Mannini, M., Poneti, G., Sessoli, R., and Rosa, P. (2013). Temperature- and light-induced spin crossover observed by x-ray spectroscopy on isolated fe(ii) complexes on gold. *The Journal of Physical Chemistry Letters*, 4(9):1546–1552. PMID: 26282313.

[159] Werner, P., Casula, M., Miyake, T., Aryasetiawan, F., Millis, A., and Biermann, S. (2012). Satellites and large doping and temperature dependence of electronic properties in hole-doped bafe2as2. *Nature Physics*, 8:331.

[160] Werner, P., Gull, E., Troyer, M., and Millis, A. J. (2008). Spin freezing transition and non-fermi-liquid self-energy in a three-orbital model. *Phys. Rev. Lett.*, 101:166405.

[161] Werner, P., Hoshino, S., and Shinaoka, H. (2016). Spin-freezing perspective on cuprates. *Phys. Rev. B*, 94:245134.

[162] Werner, P. and Millis, A. J. (2006). Hybridization expansion impurity solver: General formulation and application to kondo lattice and two-orbital models. *Phys. Rev. B*, 74:155107.

[163] Werner, P. and Millis, A. J. (2007). Doping-driven mott transition in the one-band hubbard model. *Phys. Rev. B*, 75:085108.

[164] White, S. R. (1992). Density matrix formulation for quantum renormalization groups. *Phys. Rev. Lett.*, 69:2863–2866.

[165] White, S. R., Scalapino, D. J., Sugar, R. L., Loh, E. Y., Gubernatis, J. E., and Scalettar, R. T. (1989). Numerical study of the two-dimensional hubbard model. *Phys. Rev. B*, 40:506–516.

[166] Wilson, K. G. (1975). The renormalization group: Critical phenomena and the kondo problem. *Rev. Mod. Phys.*, 47:773–840.

[167] Yanase, Y. and Yamada, K. (1997). Effect of hund's rule coupling on the kondo effect. *Journal of the Physical Society of Japan*, 66(11):3551–3557.

[Yin et al.] Yin, Z. P., Haule, K., and Kotliar, G. Kinetic frustration and the nature of the magnetic and paramagnetic states in iron pnictides and iron chalcogenides. *Nature Materials*, 10:932.

[169] Yuval, G. and Anderson, P. W. (1970). Exact results for the kondo problem: One-body theory and extension to finite temperature. *Phys. Rev. B*, 1:1522–1528.

[170] Zaanen, J., Sawatzky, G. A., and Allen, J. W. (1985). Band gaps and electronic structure of transition-metal compounds. *Phys. Rev. Lett.*, 55:418–421.

[171] Zein, S., Borshch, S. A., Fleurat-Lessard, P., Casida, M. E., and Chermette, H. (2007). Assessment of the exchange-correlation functionals for the physical description of spin transition phenomena by density functional theory methods: All the same? *The Journal of Chemical Physics*, 126(1):014105.

[172] Zhang, F. C. and Rice, T. M. (1988). Effective hamiltonian for the superconducting cu oxides. *Phys. Rev. B*, 37:3759–3761.

Appendix A

Appendix A

A.1 Solving the rotor Hamiltonian & "slave-matrix" techniques

In order to solve the slave rotor mean-field equations, we still have to find a way to calculate expectation values with respect to the rotor Hamiltonian. In case of (2.41), the corresponding Schrödinger equation constitutes a simple ordinary differential equation of second order, and a solution is obtained most easily, for instance by employing standard numerical approaches such as the shooting method.
The most simple and practical approach probably consists in writing the rotor Hamiltonian as a matrix in the basis of the angular momentum eigenstates (2.24). In this basis, we can write the rotor operators as

$$\hat{L} \rightarrow \begin{bmatrix} Q_{cut}/2 & 0 & \cdots & 0 & 0 \\ 0 & \ddots & & & 0 \\ & & 1 & & \\ \vdots & & 0 & & \vdots \\ & & & -1 & \\ 0 & & & \ddots & 0 \\ 0 & 0 & \cdots & 0 & -Q_{cut}/2 \end{bmatrix} \tag{A.1}$$

and

$$e^{i\theta} \to \begin{bmatrix} 0 & 1 & & \cdots & & 0 & 0 \\ 0 & \ddots & \ddots & & & & 0 \\ & & 0 & 1 & & & \\ \vdots & & & 0 & 1 & & \vdots \\ & & & & \ddots & \ddots & \\ 0 & & & & & 0 & 1 \\ C & 0 & & \cdots & & & 0 \end{bmatrix} . \tag{A.2}$$

Since the original Hilbert space is of infinite size, we had to introduce a cut-off Q_{cut} for the angular momentum, leaving us with matrices of the size $(Q_{cut}+1)\times(Q_{cut}+1)$. It is clear, that we retrieve a faithful representation of the slave rotor operators as we let $Q_{cut}\to\infty$. The number C was introduced as some gauge degree of freedom, the meaning of which will be explained in the following.

The possibility to write the rotor operators as (A.1) and (A.2) raises the following question: *Considering that the physical Hilbert space is restricted to a maximum total electron number* $2N$ *per site, such that* $Q\in -N\ldots N$*, why did we have to introduce an infinite number of auxiliary states that are, a priori, unphysical?*

This question was the main motivation for the development of a "Generalized slave-particle" method[60]. The principle of this technique is identical to the slave rotor method; but the operators $\hat{L}$ and $e^{i\theta}/e^{-i\theta}$ are replaced by matrices of the form (A.1) and (A.2) with a cut-off angular momentum equal to the number of electron states $Q_{cut}=2N$.

Applying this method allows to reduce the error made by using the saddle point approximation (2.31) for the Lagrange multiplier, since a large (actually infinite) number of unphysical states is excluded right away. However, this advantage comes along with a couple of problems, that can not all be solved simultaneously

1. When considering the non-interacting limit $U=0$, the slave rotor mean-field method reproduces the correct result with quasi-particle renormalization $\mathscr{Z}=1$. In the truncated matrix formulation, we can achieve this by adjusting the parameter C in (A.2). At half filling, for instance, $C=1$ gives the desired result.

2. The two rotor ladder operators cancel each other to unity $e^{i\theta}e^{-i\theta}=1$, which implies that the auxiliary fermionic density equals the one of the physical electrons $d^\dagger d = f^\dagger f e^{i\theta}e^{-i\theta} = f^\dagger f$. This is an important detail of the theory and leads to complications (for instance in the calculation of the Greens' function (2.39)) if it is violated. In the truncated matrix formulation, this property is only preserved case for $C=1$.

3. The truncated matrix formulation lacks the canonical commutation relation $\left[\hat{L}, e^{i\theta}\right] = e^{i\theta}$, except for $C=0$.

Depending on the parameter regime, these issues might be outweighed by the benefits from reducing the number of unphysical states (at half filling, for instance, we avoid the first two problems of the list). It is clear, however, that one should only use such a method with care.

Appendix B

Appendix B

B.1 Schrieffer-Wolff transformation of the Anderson impurity model

B.1.1 The Transformation

The following derivation closely follows the presentation given in [33], for the original reference consider [139]. We're starting with a Hamiltonian of the form

$$H = H_0 + \lambda H_{hyb} = \begin{bmatrix} H_L & \lambda V^\dagger \\ \lambda V & H_H \end{bmatrix} , \tag{B.1}$$

with designated low and high energy subspaces, that are connected by an off-diagonal hybridization H_{hyb}. The parameter λ is used to emphasize that this hybridization will be treated as a perturbation. The goal of the Schrieffer-Wolf transformation[139] is to derive an effective low energy Hamiltonian by eliminating the off-diagonal elements of (B.1) with a unitary transformation $U = e^S$

$$H_{eff} = e^S(H_0 + H_{hyb})e^{-S} = e^S \begin{bmatrix} H_L & \lambda V^\dagger \\ \lambda V & H_H \end{bmatrix} e^{-S} = \begin{bmatrix} H_L^{eff} & 0 \\ 0 & H_H^{eff} \end{bmatrix} . \tag{B.2}$$

Due to the unitarity of U, the operator $S^\dagger = -S$ must be anti-hermitian. It is implicitly defined by the hybridization H_{hyb}, and can therefore be expanded in λ as

$$S = \lambda S_1 + \lambda^2 S_2 + \mathcal{O}(\lambda^3) . \tag{B.3}$$

We will now use the identity

$$e^A B e^{-A} = B + [A,B] + \frac{1}{2}[A,[A,B]] + \dots , \tag{B.4}$$

to expand (B.2) as

$$e^S(H_0+H_{hyb})e^{-S} = H_0+\lambda\left(H_{hyb}+[S_1,H_0]\right)+\lambda^2\left(\frac{1}{2}[S_1,[S_1,H]]+[S_1,H_{hyb}]+[S_2,H_0]\right)+\dots\ . \tag{B.5}$$

By setting

$$[S_1,H_0] = -H_{hyb}, \tag{B.6}$$

off-diagonal terms can be eliminated up to first order. Plugging this into the second term in (B.5), we get

$$e^S(H_0+H_{hyb})e^{-S} = H_0+\lambda^2\left(\frac{1}{2}[S_1,H_{hyb}]+[S_2,H_0]\right)+\dots\ . \tag{B.7}$$

The last term $[S_2,H_0]$ would contain off-diagonal elements, but it can be eliminated by chosing $S_2=0$. We therefore arrive at

$$H_L^{eff} = H_L+\lambda^2\Delta H_L = H_L+\lambda^2\frac{1}{2}P_L[S_1,H_{hyb}]P_L \tag{B.8}$$

$$H_H^{eff} = H_H+\lambda^2\Delta H_H = H_H+\lambda^2\frac{1}{2}P_H[S_1,H_{hyb}]P_H\ , \tag{B.9}$$

where P_L, P_H are projectors on the low/high energy subspace.
The term we're interested in is ΔH_L, which can be shown to be

$$\Delta H_L = \frac{1}{2}\sum_H \left|L'\right\rangle\left\langle L'\right|H_{hyb}\left|H\right\rangle\left\langle H\right|H_{hyb}\left|L\right\rangle\left\langle L\right|\left(\frac{1}{E_{L'}-E_H}+\frac{1}{E_L-E_H}\right)\ . \tag{B.10}$$

B.1.2 Deriving the Kondo model

We can now apply the Schrieffer-Wolff transformation to the Anderson impurity model (3.36)

$$H = \sum_{k\sigma}\varepsilon_k b^\dagger_{k\sigma}b_{k\sigma}+\sum_{k\sigma}(V_k d^\dagger_\sigma b_{k\sigma}+h.c.)+\varepsilon^d n^d+U\left(n^d_\uparrow-\frac{1}{2}\right)\left(n^d_\downarrow-\frac{1}{2}\right)\ . \tag{B.11}$$

In this case, the low energy subspace is spanned by the states in which the correlated orbital is inhabited by a single electron of spin up or down.
We can then think of two different processes that take us from the low energy to high energy subspace and then back to the low energy one.

1. In the first one, a bath electron of energy ε_k jumps onto the impurity, forming an intermediate state with two electrons. The energy difference of the two states is thus $E_L-E_H=\varepsilon_k-(\varepsilon^d+U)$. Eventually, one of the electrons jumps back to inhibit a bath state of energy $\varepsilon_{k'}$, resulting in the energy difference $E_{L'}-E_H=\varepsilon_{k'}-(\varepsilon^d+U)$.

2. In the second process, the electron on the impurity "jumps" into the sea of conduction states, such that the difference of energies is $E_L - E_H = \varepsilon^d - \varepsilon_k$. Afterwards, a conduction electron jumps back to the impurity; the energy difference being $E_{L'} - E_H = \varepsilon^d - \varepsilon_{k'}$.

Considering these processes in (B.10) leads us to

$$\begin{aligned}\Delta H_L = &\frac{1}{2}\sum_{k,k'} V_k V_{k'}^* (b_{k'\sigma'}^\dagger d_{\sigma'})(d_\sigma^\dagger b_{k\sigma}) \left(\frac{1}{\varepsilon_k - (\varepsilon^d + U)} + \frac{1}{\varepsilon_{k'} - (\varepsilon^d + U)}\right) \\ &+ \frac{1}{2}\sum_{k,k'} V_k V_{k'}^* (d_{\sigma'}^\dagger b_{k\sigma'})(b_{k'\sigma}^\dagger d_\sigma) \left(\frac{1}{\varepsilon^d - \varepsilon_{k'}} + \frac{1}{\varepsilon^d - \varepsilon_k}\right)\end{aligned} . \tag{B.12}$$

Now using the identity $\delta_{\alpha\beta}\delta_{\gamma\eta} = \frac{1}{2}(\delta_{\alpha\eta}\delta_{\beta\gamma} + \vec{\sigma}_{\alpha\eta}\cdot\vec{\sigma}_{\gamma\beta})$, we can re-write

$$\begin{aligned}(b_{k'\sigma'}^\dagger d_{\sigma'})(d_\sigma^\dagger b_{k\sigma}) &= (b_{k'\alpha}^\dagger d_\beta)(d_\gamma^\dagger b_{k\eta})\delta_{\alpha\beta}\delta_{\gamma\eta} \\ &= \frac{1}{2} b_{k\alpha}^\dagger b_{k'\alpha} \underbrace{d_\beta^\dagger d_\beta}_{=1} - b_{k\alpha}^\dagger \vec{\sigma}_{\alpha\beta} b_{k'\beta} \cdot \underbrace{d_\gamma^\dagger \frac{\vec{\sigma}_{\gamma\eta}}{2} d_\eta}_{=\vec{S}_d} ,\end{aligned} \tag{B.13}$$

$$(d_{\sigma'}^\dagger b_{k\sigma'})(b_{k'\sigma}^\dagger d_\sigma) = -\frac{1}{2} b_{k'\alpha}^\dagger b_{k\alpha} - b_{k'\alpha}^\dagger \vec{\sigma}_{\alpha\beta} b_{k\beta} \cdot \underbrace{d_\gamma^\dagger \frac{\vec{\sigma}_{\gamma\eta}}{2} d_\eta}_{=\vec{S}_d} . \tag{B.14}$$

To simplify the expressions, we will assume that $|\varepsilon_k|, |\varepsilon_{k'}| << |\varepsilon^d|, |\varepsilon^d + U|$, such that we can ignore these energies in the denominators. We then end up with

$$\begin{aligned}\Delta H_L = &\sum_{k,k'} V_k V_{k'}^* b_{k'\alpha}^\dagger \vec{\sigma}_{\alpha\beta} b_{k\beta} \cdot \vec{S}_d \left(\frac{1}{\varepsilon^d + U} - \frac{1}{\varepsilon^d}\right) \\ &- \frac{1}{2}\sum_{k,k'} V_k V_{k'}^* b_{k'\sigma}^\dagger b_{k\sigma} \left(\frac{1}{\varepsilon^d + U} - \frac{1}{\varepsilon^d}\right) .\end{aligned} \tag{B.15}$$

The first term corresponds to the famous Kondo spin-spin interaction, while the second term represents an additional potential for the conduction electrons.

B.2 Three-orbital case

Fig. B.1 shows the equivalent to Fig. 4.3 for the three-band model. In contrast to models without Hund's coupling (where $T_K/D \sim (T_K^{N=1}/D)^{1/N}$, with $D = 2t$ being the half bandwidth), T_K is rather decreased for more orbitals in the case of $J > 0$. However, the increased cost of performing numerical simulations yet prevented us from exploring very low temperatures. While the coexistence region is smaller than in the two-band case, the metal-insulator transition is characterized by an insulating branch that can be stabilized to even higher dopings. In general, the phenomenology seems to be the same, more extensive research would, however, be of interest.

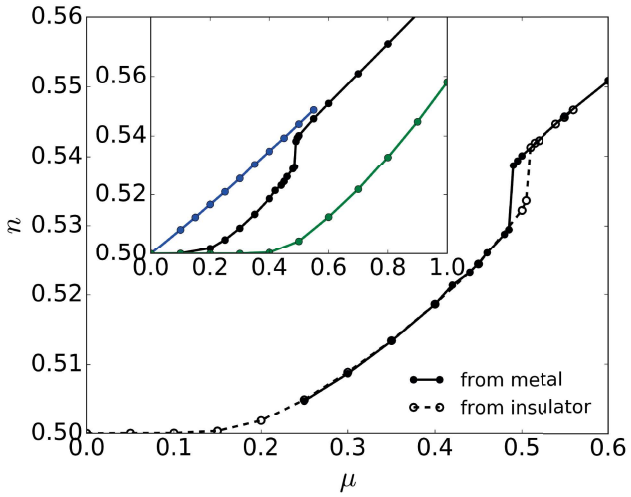

Fig. B.1 Filling n per spin as a function of the chemical potential μ for a three-band model with $U = 2.3$, $J = 0.25U$ and $\beta = 50$. Solid (dashed) lines denote results starting from a metallic (insulating) initial configuration. Inset: $n(\mu)$ per spin for $U = 2.25, 2.3, 2.6$ (blue, black, green) for $J = 0.25$, starting from a metallic configuration.

Appendix C

Appendix C

C.1 Diagonalization of the two orbital d-p atomic model

We start out with the Hamiltonian

$$H = U^{dd} n_{\uparrow}^{d} n_{\downarrow}^{d} - \mu \sum (n^{d} + n^{p}) + \sum (V d^{\dagger} p + V^{*} p^{\dagger} d) + \varepsilon_{p} \sum p^{\dagger} p \ , \tag{C.1}$$

which can be cast in the matrix form

$$\begin{bmatrix} H_{N\ 0,S_z\ 0} & 0 & 0 & 0 & 0 & 0 & 0 & 0 & 0 \\ 0 & H_{N=1,S_z=-1/2} & 0 & 0 & 0 & 0 & 0 & 0 & 0 \\ 0 & 0 & H_{N=1,S_z=+1/2} & 0 & 0 & 0 & 0 & 0 & 0 \\ 0 & 0 & 0 & H_{N=2,S_z=-1} & 0 & 0 & 0 & 0 & 0 \\ 0 & 0 & 0 & 0 & H_{N=2,S_z=0} & 0 & 0 & 0 & 0 \\ 0 & 0 & 0 & 0 & 0 & H_{N=2,S_z=+1} & 0 & 0 & 0 \\ 0 & 0 & 0 & 0 & 0 & 0 & H_{N=3,S_z=-1/2} & 0 & 0 \\ 0 & 0 & 0 & 0 & 0 & 0 & 0 & H_{N=3,S_z=+1/2} & 0 \\ 0 & 0 & 0 & 0 & 0 & 0 & 0 & 0 & H_{N=4,S_z=0} \end{bmatrix} \tag{C.2}$$

where the Block Matrices are categorized by total total number of particles N and spin S_z. We will now proceed by diagonalizing each block-matrix individually.

Particle number $N = 0$

Here, we have only one matrix

$$H_{N=0,S_z=0} = 0|0,0\rangle\langle 0,0| \text{ acts on the state } |0,0\rangle \tag{C.3}$$

with eigenvalue

$$\varepsilon = 0 \ . \tag{C.4}$$

Particle number $N = 1$

The two matrices are

$$H_{N=1,S_z=-1/2} = \begin{bmatrix} -\mu & V \\ V^* & \varepsilon_p - \mu \end{bmatrix} \text{ acting on } \begin{bmatrix} |\downarrow, 0\rangle \\ |0, \downarrow\rangle \end{bmatrix} \tag{C.5}$$

and

$$H_{N=1,S_z=+1/2} = \begin{bmatrix} -\mu & V \\ V^* & \varepsilon_p - \mu \end{bmatrix} \text{ acting on } \begin{bmatrix} |\uparrow, 0\rangle \\ |0, \uparrow\rangle \end{bmatrix} , \tag{C.6}$$

both having the same eigenvalues

$$\varepsilon = \frac{1}{2}\left((\varepsilon_p - 2\mu) \pm \sqrt{\varepsilon_p^2 + 4V^2} \right) , \tag{C.7}$$

Particle number $N = 2$

Here, we have three matrices, the first one being

$$H_{N=2,S_z=-1} = (-2\mu + \varepsilon_p)|\downarrow, \downarrow\rangle\langle\downarrow, \downarrow| \text{ acting on } |\downarrow, \downarrow\rangle \tag{C.8}$$

with the eigenvalue

$$\varepsilon = -2\mu + \varepsilon_p \, . \tag{C.9}$$

The second one is the 4×4 matrix

$$H_{N=2,S_z=0} = \begin{bmatrix} (-2\mu + \varepsilon_p) & 0 & -V & -V^* \\ 0 & (-2\mu + \varepsilon_p) & V & V^* \\ -V^* & V^* & 2\varepsilon_p - 2\mu & 0 \\ -V & V & 0 & U^{dd} - 2\mu \end{bmatrix} \text{ acting on } \begin{bmatrix} |\downarrow, \uparrow\rangle \\ |\uparrow, \downarrow\rangle \\ |0, \uparrow\downarrow\rangle \\ |\uparrow\downarrow, 0\rangle \end{bmatrix} . \tag{C.10}$$

In case that the hoppings are real $V = V^*$, this matrix can be split up further by rotating the basis

$$\mathbf{R}\vec{v}_0 = \begin{bmatrix} \frac{1}{\sqrt{2}} & \frac{1}{\sqrt{2}} & 0 & 0 \\ \frac{1}{\sqrt{2}} & -\frac{1}{\sqrt{2}} & 0 & 0 \\ 0 & 0 & 1 & 0 \\ 0 & 0 & 0 & 1 \end{bmatrix} \begin{bmatrix} |\downarrow, \uparrow\rangle \\ |\uparrow, \downarrow\rangle \\ |0, \uparrow\downarrow\rangle \\ |\uparrow\downarrow, 0\rangle \end{bmatrix} = \begin{bmatrix} \frac{1}{\sqrt{2}}(|\downarrow, \uparrow\rangle + |\uparrow, \downarrow\rangle) \\ \frac{1}{\sqrt{2}}(|\downarrow, \uparrow\rangle - |\uparrow, \downarrow\rangle) \\ |0, \uparrow\downarrow\rangle \\ |\uparrow\downarrow, 0\rangle \end{bmatrix} . \tag{C.11}$$

Applying this unitary transformation to the Hamiltonian matrix yields

$$\mathbf{R}^T H_{N=2,S_z=0}\mathbf{R} = \begin{bmatrix} (-2\mu+\varepsilon_p) & 0 & 0 & 0 \\ 0 & (-2\mu+\varepsilon_p) & -\sqrt{2}V & -\sqrt{2}V \\ 0 & -\sqrt{2}V & 2\varepsilon_p - 2\mu & 0 \\ 0 & -\sqrt{2}V & 0 & U^{dd} - 2\mu \end{bmatrix} . \tag{C.12}$$

This means, that the $N = 2$, $S_z = 0$ manifold splits into a singlet state

$$\frac{1}{\sqrt{2}}(|\downarrow,\uparrow\rangle + |\uparrow,\downarrow\rangle) \tag{C.13}$$

with energy

$$\varepsilon = -2\mu + \varepsilon_p \, , \tag{C.14}$$

and a triplet, corresponding to the eigenstates of the 3×3 matrix

$$\begin{bmatrix} (-2\mu+\varepsilon_p) & -\sqrt{2}V & -\sqrt{2}V \\ -\sqrt{2}V & 2\varepsilon_p - 2\mu & 0 \\ -\sqrt{2}V & 0 & U^{dd} - 2\mu \end{bmatrix} \text{ acting on } \begin{bmatrix} \frac{1}{\sqrt{2}}(|\downarrow,\uparrow\rangle - |\uparrow,\downarrow\rangle) \\ |0,\uparrow\downarrow\rangle \\ |\uparrow\downarrow,0\rangle \end{bmatrix} . \tag{C.15}$$

The eigenvalues and eigenstates can be easily obtained by diagonalization of this matrix.
Finally, we have the matrix corresponding to $N = 2$, $S_z = +1$

$$H_{N=2,S_z=+1} = (-2\mu+\varepsilon_p)|\uparrow,\uparrow\rangle\langle\uparrow,\uparrow| \text{ acting on } |\uparrow,\uparrow\rangle \tag{C.16}$$

with the eigenvalue

$$-2\mu + \varepsilon_p \, . \tag{C.17}$$

Particle number $N = 3$
The Hamiltonians are

$$H_{N=3,S_z=-1/2} = \begin{bmatrix} -3\mu+2\varepsilon_p & -V^* \\ -V & U^{dd} - 3\mu + \varepsilon_p \end{bmatrix} \text{ acting on } \begin{bmatrix} |\downarrow,\uparrow\downarrow\rangle \\ |\uparrow\downarrow,\downarrow\rangle \end{bmatrix} \tag{C.18}$$

and

$$H_{N=3,S_z=+1/2} = \begin{bmatrix} -3\mu+2\varepsilon_p & -V^* \\ -V & U^{dd} - 3\mu + \varepsilon_p \end{bmatrix} \text{ acting on } \begin{bmatrix} |\uparrow,\uparrow\downarrow\rangle \\ |\uparrow\downarrow,\uparrow\rangle \end{bmatrix} \tag{C.19}$$

both having the same eigenvalues

$$\varepsilon = \frac{1}{2}\left((U^{dd} - 6\mu + 3\varepsilon_p) \pm \sqrt{(U^{dd} - \varepsilon_p)^2 + 4V^2}\right) . \tag{C.20}$$

Particle number $N = 4$
The Hamiltonian is

$$H_{N=4,S_z=0} = (U^{dd} - 4\mu + 2\varepsilon_p)|\uparrow\downarrow,\uparrow\downarrow\rangle\langle\uparrow\downarrow,\uparrow\downarrow| \tag{C.21}$$

with eigenvalues

$$\varepsilon = U^{dd} - 4\mu + 2\varepsilon_p . \tag{C.22}$$

C.2 Solving the two-orbital d-p impurity model – remarks and approximations

To solve the quantum impurity model, we applied a hybridization expansion continuous time quantum Monte Carlo (CT-hyb) algorithm, using the implementation provided by the TRIQS[129] toolbox. The algorithm works by sampling the partition function Z, which is expanded in the hybridization part of the action S_{hyb} (5.31). In principle, this algorithm can be applied to solve impurity model (5.29) for arbitrary interactions U^{dd}, U^{dp} and U^{pp}. We distinguish two cases:

C.2.1 First case: $\mathbf{U^{dp} = U^{pp} = 0}$

If the p-orbitals do not interact with themselves or with the other orbitals, we can integrate them out, reducing the effective degrees of freedom to the d-manifold only. We shall demonstrate this explicitly for model (5.29).

In the following, it will be more practical to re-write the action in Matsubara frequency space. This gives us

$$S_{dp} = -\sum_{i\omega} \begin{bmatrix} d^\dagger_{i\omega\sigma} & p^\dagger_{i\omega\sigma} \end{bmatrix} \left[\mathbf{G}^0_{i\omega}\right]^{-1} \begin{bmatrix} d_{i\omega\sigma} \\ p_{i\omega\sigma} \end{bmatrix} + S_{int} , \tag{C.23}$$

where $\left[\mathbf{G}^0_{i\omega}\right]^{-1}$ is the inverse of the non-interacting Greens' function

$$\left[\mathbf{G}^0_{i\omega}\right]^{-1} = \begin{bmatrix} i\omega + \mu - \varepsilon^d - \Delta^{dd}_{i\omega} & -V - \Delta^{dp}_{i\omega} \\ -V^* - \Delta^{pd}_{i\omega} & i\omega + \mu - \varepsilon^p - \Delta^{pp}_{i\omega} \end{bmatrix} , \tag{C.24}$$

and S_{int} accounts for the interacting parts of the action. From (C.23), we can retrieve the interacting Greens' function by deriving the partition function Z with respect to the hybridization function. For

$G^{dd}_{i\omega\sigma}$, e.g. we get

$$G^{dd}_{i\omega\sigma} = \left\langle d^\dagger_{i\omega\sigma} d_{i\omega\sigma} \right\rangle = \frac{1}{Z} \int \mathrm{D}[d^\dagger_\sigma, d_\sigma, p^\dagger_\sigma, p_\sigma] d^\dagger_{i\omega\sigma} d_{i\omega\sigma} e^{-S_{dp}} = -\frac{1}{Z} \frac{\partial Z}{\partial \Delta^{dd}_{i\omega\sigma}} \,, \tag{C.25}$$

(we explicitly added a spin label to the hybridization function, to avoid ambiguities concerning the derivative) with

$$Z = \int \mathrm{D}[d^\dagger_\sigma, d_\sigma, p^\dagger_\sigma, p_\sigma] e^{-S_{dp}} \,. \tag{C.26}$$

Likewise, the other elements of the matrix Greens's function (5.34) can be calculated by deriving Z with respect to Δ^{dp}, Δ^{pd} and Δ^{pp}.
In order to "get rid" of the p-orbitals, we start by re-arranging the action as

$$\begin{aligned} S_{dp} = &- \sum_{i\omega\sigma} d^\dagger_{i\omega\sigma} \left[\mathbf{G}^0_{i\omega}\right]^{-1}_{dd} d_{i\omega\sigma} - \left(p^\dagger_{i\omega\sigma} + \frac{\left[\mathbf{G}^0_{i\omega}\right]^{-1}_{dp}}{\left[\mathbf{G}^0_{i\omega}\right]^{-1}_{pp}} d^\dagger_{i\omega\sigma} \right) \left[\mathbf{G}^0_{i\omega}\right]^{-1}_{pp} \left(p_{i\omega\sigma} + \frac{\left[\mathbf{G}^0_{i\omega}\right]^{-1}_{pd}}{\left[\mathbf{G}^0_{i\omega}\right]^{-1}_{pp}} d_{i\omega\sigma} \right) \\ &+ d^\dagger_{i\omega\sigma} \frac{\left[\mathbf{G}^0_{i\omega}\right]^{-1}_{dp} \left[\mathbf{G}^0_{i\omega}\right]^{-1}_{pd}}{\left[\mathbf{G}^0_{i\omega}\right]^{-1}_{pp}} d_{i\omega\sigma} + S_{int} \,. \end{aligned} \tag{C.27}$$

If $U^{dp} = U^{pp} = 0$, the action is quadratic in the p-fields and factorizes to

$$Z = \int \mathrm{D}[d^\dagger_\sigma, d_\sigma] e^{-S_{dd}} Z_p = Z_d Z_p \,, \tag{C.28}$$

with

$$S_{dd} = - \sum_{i\omega\sigma} d^\dagger_{i\omega\sigma} \left[\mathbf{G}^0_{i\omega}\right]^{-1}_{dd} d_{i\omega\sigma} + d^\dagger_{i\omega\sigma} \frac{\left[\mathbf{G}^0_{i\omega}\right]^{-1}_{dp} \left[\mathbf{G}^0_{i\omega}\right]^{-1}_{pd}}{\left[\mathbf{G}^0_{i\omega}\right]^{-1}_{pp}} d_{i\omega\sigma} + S_{int} \,. \tag{C.29}$$

For Z_p, we can get a simple, analytic expression, which depends only on $\left[\mathbf{G}^0_{i\omega}\right]^{-1}_{pp}$

$$\begin{aligned} Z_p &= \int \mathrm{D}[p^\dagger_\sigma, p_\sigma] \exp\left\{ \sum_{i\omega\sigma} \left(p^\dagger_{i\omega\sigma} + \frac{\left[\mathbf{G}^0_{i\omega}\right]^{-1}_{dp}}{\left[\mathbf{G}^0_{i\omega}\right]^{-1}_{pp}} d^\dagger_{i\omega\sigma} \right) \left[\mathbf{G}^0_{i\omega}\right]^{-1}_{pp} \left(p_{i\omega\sigma} + \frac{\left[\mathbf{G}^0_{i\omega}\right]^{-1}_{pd}}{\left[\mathbf{G}^0_{i\omega}\right]^{-1}_{pp}} d_{i\omega\sigma} \right) \right\} \\ &= \prod_{i\omega\sigma} \left[\mathbf{G}^0_{i\omega}\right]^{-1}_{pp} \,. \end{aligned} \tag{C.30}$$

Due to (C.25), the d-d Greens' function $G^{dd}_{i\omega\sigma}$ is independent of Z_p, and can therefore be calculated by solving a one-orbital impurity model corresponding to the action (C.29).

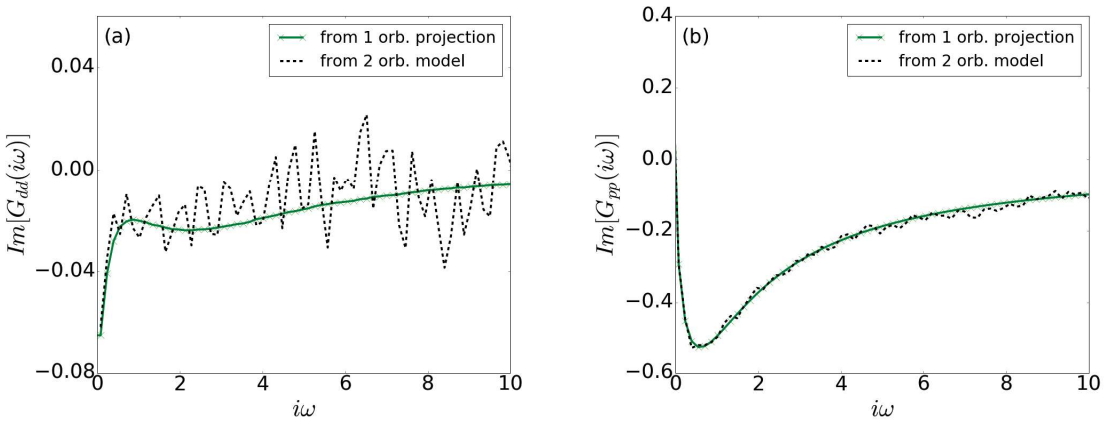

Fig. C.1 Imaginary part of the Green's functions, comparing the results from Monte Carlo calculations for the full two-orbital impurity model (black dashed lines) and from using the projection to the one-orbital model (green solid lines), as described in the main text.

The other components of $\mathbf{G}^{imp}$ can be evaluated by deriving the partition function

$$G^{dp}_{i\omega\sigma} = -\frac{1}{Z}\frac{\partial Z}{\partial \Delta^{dp}_{i\omega\sigma}} = G^{dd}_{i\omega\sigma}\frac{\left[\mathbf{G}^0_{i\omega}\right]^{-1}_{pd}}{\left[\mathbf{G}^0_{i\omega}\right]^{-1}_{pp}}\,, \tag{C.31}$$

$$G^{pd}_{i\omega\sigma} = -\frac{1}{Z}\frac{\partial Z}{\partial \Delta^{pd}_{i\omega\sigma}} = G^{dd}_{i\omega\sigma}\frac{\left[\mathbf{G}^0_{i\omega}\right]^{-1}_{dp}}{\left[\mathbf{G}^0_{i\omega}\right]^{-1}_{pp}}\,, \tag{C.32}$$

$$G^{pp}_{i\omega\sigma} = -\frac{1}{Z}\frac{\partial Z}{\partial \Delta^{pp}_{i\omega\sigma}} = \left(\left[\mathbf{G}^0_{i\omega}\right]^{-1}_{pp}\right)^{-1} + G^{dd}_{i\omega\sigma}\frac{\left[\mathbf{G}^0_{i\omega}\right]^{-1}_{dp}\left[\mathbf{G}^0_{i\omega}\right]^{-1}_{pd}}{\left(\left[\mathbf{G}^0_{i\omega}\right]^{-1}_{pp}\right)^2}\,, \tag{C.33}$$

where the first term in (C.25) comes from the $\left[\mathbf{G}^0_{i\omega}\right]^{-1}_{pp}$ dependence of Z_p.
Using the Dyson equation to calculate the self energy confirms the obvious fact that only the dd-element is non zero

$$\left[\mathbf{G}^0_{i\omega}\right]^{-1} - \mathbf{G}^{imp\,-1} \equiv \Sigma = \begin{bmatrix} \Sigma^{dd} & 0 \\ 0 & 0 \end{bmatrix}\,. \tag{C.34}$$

It is not hard to see, that projecting the problem onto an effective one-band calculation is way more effective than solving the original two-band model with off-diagonal hybridization. A comparison of the efficiency is presented in Fig. C.1, which shows the results from a "single-shot" (i.e. no DMFT self-consistency) Monte Carlo calculations with the two methods, using the same number of measurements (8×10^6). The drastic difference in quality is mainly due to the sign problem, that emerges in the two-band calculation: Here, the average sign $\langle \mathrm{sign} \rangle_{MC} = 0.244$, which means that the error is increased by a factor of $1/\langle \mathrm{sign} \rangle^2_{MC} \approx 16$.

C.2.2 Second case: $U^{dp}, U^{pp} \neq 0$

If the U^{dp} and/or U^{pp} are non zero, the p-orbitals are correlated and cannot simply be integrated out as before. If interactions (or hybridizations) are small, one can use a Hartree approach - treating the additional interactions in a mean-field fashion - and then apply the method presented for the $U^{dp} = U^{pp} = 0$ case.

If neither of these approximations works, the full multi-orbital model has to be solved numerically. We already dealt with 2- and 3-band models in the previous chapter; in these cases, however, the hybridization function was diagonal in the single-particle basis. Here, the hybridization function (5.31) has off-diagonal elements, which gives rise to a negative sign problem.

The negative sign problem arises in Monte Carlo simulations of fermionic systems, as a consequence of the fermionic anti-commutation relations. More specifically, it appears since the weight w_c of the sampled configurations $\{c\}$ can have a negative sign.

The appearance of a sign problem is problematic, since it drastically reduces the efficiency of the algorithm. For constant precision of the result, the number of Monte Carlo measurements has to be increased by $1/\langle sign \rangle_{MC}$.

However, the sign problem is not a gauge invariant quantity and can thus be improved by optimizing the single-particle basis [142]. This is achieved by means of an unitary transformation to the electron operators

$$\begin{bmatrix} \tilde{d}_\sigma \\ \tilde{p}_\sigma \end{bmatrix} = U \begin{bmatrix} d_\sigma \\ p_\sigma \end{bmatrix} \tag{C.35}$$

(note that applying such a transformation will inevitably lead to rather complicated interaction terms; depending on the implementation of the hybridization expansion solver, however, this is not a cause of further problems).

In our calculations, we have chosen the basis that diagonalizes the local Hamiltonian of the system

$$\begin{bmatrix} \varepsilon_d & V \\ V* & \varepsilon_p \end{bmatrix} , \tag{C.36}$$

which significantly reduced the severity of the sign problem.

Since the negative sign problem gets exponentially worse upon decreasing the temperature

$$\langle sign \rangle_{MC} \sim e^{-\alpha\beta} , \tag{C.37}$$

it also prohibited us from reaching very low temperatures. In practice, the lowest temperatures for which we could obtain reasonable results were $\beta W = 256$, with W being the bandwidth of the system.

In section 5.3, we discuss results from Monte Carlo calculations considering both the cases $U^{dp} = U^{pp} = 0$ and $U^{dp}, U^{pp} \neq 0$.

Appendix D

Appendix D

D.1 Slave rotor propagator: Atomic limit and perturbative expansion

In this section, we shall derive the rotor Green's function in the atomic limit and describe how a perturbative expansion in the hybridization term can be performed. We consider the rotor part of the atomic action (6.2), together with the mean-field hybridization (6.16)

$$S^{\theta} = \frac{1}{U^{dp}} \int_0^{\beta} \mathrm{d}\tau \left(\frac{\partial \theta}{\partial \tau} + \frac{\phi_0}{\beta} \right)^2 + \iint_0^{\beta} \mathrm{d}\tau \mathrm{d}\tau' \, \Delta_{\theta}^{dp}(\tau - \tau') e^{i(\theta(\tau) - \theta(\tau'))} \,, \tag{D.1}$$

where we substituted $\phi = \partial_\tau \theta + \phi_0/\beta$.
The rotor Green's function is defined as

$$G^{\theta}(\tau) = \frac{1}{Z^{\theta}} \int \mathscr{D}[\theta] e^{-i(\theta(\tau) - \theta(0))} e^{-S^{\theta}} \,, \tag{D.2}$$

with $Z^{\theta} = \int \mathrm{D}[\theta] e^{-S^{\theta}}$.

D.1.1 Atomic limit

In the atomic limit, Δ_{θ}^{dp} vanishes, so apart from the normalization, calculating the $G^{\theta}(\tau)$ requires a functional integration over an exponential with the following argument A

$$A = -i(\theta(\tau) - \theta(0)) - \frac{1}{U^{dp}} \int_0^{\beta} \mathrm{d}\tau \left\{ \left(\frac{\partial \theta}{\partial \tau} \right)^2 + 2 \frac{\phi_0}{\beta} \frac{\partial \theta}{\partial \tau} + \frac{\phi_0^2}{\beta^2} \right\} . \tag{D.3}$$

By parametrizing the rotor fields θ as[1]

$$\theta(\tau) = \frac{2n\pi}{\beta}\tau + \frac{1}{\beta}\sum_{\nu}\tilde{\theta}(\nu)e^{-i\nu\tau}\,, \tag{D.4}$$

we can re-write the exponent A as

$$A = A_1 + A_2\,, \tag{D.5}$$

with

$$\begin{aligned} A_1 &= -\frac{1}{U^{dp}}\frac{2n^2\pi^2}{\beta} - i2n\pi(h\frac{1}{U^{dp}} - N/2) - i\frac{2n\pi}{\beta}\tau \\ A_2 &= -\frac{1}{\beta}\sum_{\nu}\left\{-\frac{1}{2}\frac{1}{U^{dp}}\nu(-\nu)\underbrace{\tilde{\theta}(\nu)\tilde{\theta}(-\nu)}_{=\tilde{\theta}(\nu)\tilde{\theta}^*(\nu)} + \underbrace{i\tilde{\theta}(\nu)\left(e^{-i\nu\tau}-1\right)}_{=\frac{i}{2}\left[\tilde{\theta}(\nu)(e^{-i\nu\tau}-1)+\tilde{\theta}^*(\nu)(e^{i\nu\tau}-1)\right]}\right\} - \beta\frac{1}{2}\frac{1}{U^{dp}}(\frac{\phi_0}{\beta})^2\,. \end{aligned} \tag{D.6}$$

The path integral is now evaluated by integrating over the $\tilde{\theta}(\nu)$ as well as summing over n. These operations can be factorized and evaluated independently: The contribution corresponding to A_1 reads

$$\sum_n e^{A_1} = \sum_n \cos\{2n\pi(\frac{h}{U^{dp}} - N/2 + \tau/\beta)\}e^{-\frac{2n^2\pi^2}{U^{dp}\beta}}\,, \tag{D.7}$$

(since imaginary contributions cancel each other under the summation) and must be normalized by the corresponding contribution to the partition function

$$Z^{\theta}_{A1} = \sum_n \cos\{2n\pi(\frac{h}{U^{dp}} - N/2)\}e^{-\frac{2n^2\pi^2}{U^{dp}\beta}}\,. \tag{D.8}$$

The evaluation of the second contribution requires integration over all $\tilde{\theta}(\nu)$. Since A_2 is only of quadratic order in $\tilde{\theta}(\nu)$, we can proceed by completing the square

$$\begin{aligned} A_2 \to -\sum_{\nu}\Bigg\{&\frac{1}{2\beta}U^{dp-1}\nu^2\left[\tilde{\theta}(\nu) + i\frac{U^{dp}}{\nu^2}\left(e^{i\nu\tau}-1\right)\right]\left[\tilde{\theta}^*(\nu) + i\frac{U^{dp}}{\nu^2}\left(e^{-i\nu\tau}-1\right)\right] \\ &+\frac{1}{2\beta}\frac{U^{dp}}{\nu^2}\left(e^{i\nu\tau}-1\right)\left(e^{-i\nu\tau}-1\right)\Bigg\} - \beta\frac{1}{2}U^{dp-1}(\frac{\phi_0}{\beta})^2\,. \end{aligned} \tag{D.9}$$

[1] Note that the coefficients are restricted by two constrants: 1) The field $\theta(\tau)$ must be real, therefore $\tilde{\theta}(\omega) = \tilde{\theta}(-\omega)^*$ and 2) $\theta(0) = \theta(\beta)\ [2\pi]$, from which we can deduce $\Re[\tilde{\theta}] = 0$.

The terms in first line, as well as the last term in the second line will be canceled by the corresponding terms in the partition function, such that finally, we arrive at

$$G_0^\theta(\tau) = \frac{\sum_n \cos\{2n\pi(\frac{h}{U^{dp}} - N/2 + \tau/\beta)\} e^{-\frac{2n^2\pi^2}{U^{dp}\beta}}}{\sum_n \cos\{2n\pi(\frac{h}{U^{dp}} - N/2)\} e^{-\frac{2n^2\pi^2}{U^{dp}\beta}}} \exp\left\{\sum_\nu \left\{\frac{U^{dp}}{\beta\nu^2}(\cos(\nu\tau) - 1)\right\}\right\} . \tag{D.10}$$

D.1.2 Quasi particle renormalization

Analogously to the definition used in the mean-field formalism in Sec. 2.3.2, we can derive a auxiliary fermion renormalization $\mathscr{Z}_{dp}$ as

$$\mathscr{Z}_{dp} = \langle\cos\theta\rangle_\theta^2 = \lim_{\beta\to\infty} \langle\cos(\theta(\beta/2))\cos(\theta(0))\rangle_\theta = \lim_{\beta\to\infty} G_0^\theta(\beta/2) . \tag{D.11}$$

It must be emphasized, that in the context of our slave-rotor method for the d-p model $\mathscr{Z}_{dp}$ does not correspond to the full quasi-particle renormalization $\mathscr{Z}$, but only to the contribution from the inter-shell interaction U^{dp}.

To evaluate this expression for (D.10), it is sufficient to consider the exponential part at $\tau = \beta/2$

$$\sum_\nu \left\{\frac{U^{dp}}{\beta\nu^2}(\cos(\nu\beta/2) - 1)\right\} . \tag{D.12}$$

Considering that $\nu = 2\pi m/\beta$, and that the summation of m runs over all integers except 0, this gives

$$2\frac{U^{dp}}{\Delta\nu\beta} \sum_{\nu>0} \left\{\frac{\Delta\nu}{\nu^2}(-1-1)\right\} = -\frac{\beta U^{dp}}{\pi^2} \sum_{n=1}^{\infty} \frac{1}{n^2} = -\frac{\beta U^{dp}}{6} , \tag{D.13}$$

which diverges to $-\infty$, as $\beta \to \infty$. For this reason, G_0^θ, as defined in (D.10) always yields a vanishing $\mathscr{Z}_{dp}$.

This is in contrast to similar implementation by Krivenko et al. [95], where the atomic limit Green's function results in a non vanishing $\mathscr{Z}$. The reason for this difference, is the form of the interaction. While here, we consider an instantaneous interaction $U^{dp}(\tau) = \delta(\tau)U^{dp}$, corresponding to a constant interaction in Matsubara space $U^{dp}(i\nu) = U^{dp}$, the interaction considered in [95] is of form $\bar{U}(i\nu) = -\sum_\alpha 2\lambda_\alpha^2 \left(\frac{\omega_\alpha}{\nu^2+\omega_\alpha^2} - \frac{1}{\omega_\alpha}\right)$. For an interaction of this form, the parts diverging under the infinite summation will cancel each other, such that $\lim_{\beta\to\infty} G_0^\theta(\beta/2)$, and therefore Z, remains finite.

D.1.3 Hybridization expansion

If we expand the action (D.1) around $\Delta_\theta^{dp}(\tau-\tau')$, we can write the rotor propagator as

$$\begin{aligned}
G^\theta(\tau) &= \frac{1}{Z^\theta}\int \mathscr{D}[\theta] e^{-i(\theta(\tau)-\theta(0))}\Bigg(1 \\
&\quad + \sum_{n=1}^{\infty}\frac{(-1)^n}{n!}\iint_0^\beta \mathrm{d}\tau_1\mathrm{d}\tau_1'\cdots\iint_0^\beta \mathrm{d}\tau_n\mathrm{d}\tau_n'\prod_{j=1}^n \Delta_\theta^{dp}(\tau_j-\tau_j')e^{i(\theta(\tau_j)-\theta(\tau_j'))}\Bigg)e^{-\bar{S}} \\
&= \frac{1}{Z^\theta}\Big\{G_0^\theta(\tau)+\sum_{n=1}^{\infty}\frac{(-1)^n}{n!}\iint_0^\beta \mathrm{d}\tau_1\mathrm{d}\tau_1'\cdots\iint_0^\beta \mathrm{d}\tau_n\mathrm{d}\tau_n'\, G_0^\theta(\tau,0,\tau_1,\tau_1',...,\tau_n,\tau_n')\prod_{j=1}^n\Delta_\theta^{dp}(\tau_j-\tau_j') \\
&= \frac{1}{Z^\theta}\Big\{G_0^\theta(\tau)+\sum_{n=1}^{\infty}(-1)^n(n!)\iint_0^\beta \mathrm{d}\tau_1\mathrm{d}\tau_1'\cdots\iint_0^{\tau_{n-1}} \mathrm{d}\tau_n\mathrm{d}\tau_n'\, G_0^\theta(\tau,0,\tau_1,\tau_1',...,\tau_n,\tau_n')\prod_{j=1}^n\Delta_\theta^{dp}(\tau_j-\tau_j')\,,
\end{aligned} \tag{D.14}$$

with

$$Z^\theta = 1+\sum_{n=1}^{\infty}(-1)^n(n!)\iint_0^\beta \mathrm{d}\tau_1\mathrm{d}\tau_1'\cdots\iint_0^{\tau_{n-1}} \mathrm{d}\tau_n\mathrm{d}\tau_n'\, G_0^\theta(\tau_1,\tau_1',...,\tau_n,\tau_n')\prod_{j=1}^n\Delta_\theta^{dp}(\tau_j-\tau_j') \tag{D.15}$$

where $G_0^\theta(\tau,0,\tau_1,\tau_1',...,\tau_n,\tau_n')$ can be calculated analogously to $G_0^\theta(\tau)$, and has the simple analytic expression

$$\begin{aligned}
G_0^\theta(\tau,0,\tau_1,\tau_1',...,\tau_n,\tau_n') &= \sum_n \cos\{2n\pi(hU_{dp}^{-1}+\tau/\beta+\sum_n(\tau_n-\tau_n')/\beta)\}e^{-\frac{2n^2\pi^2}{U_{dp}\beta}} \\
&\quad\times\exp\sum_\nu\frac{U_{dp}}{2\nu^2}\{(2\cos(\nu\tau)-2) \\
&\quad-2\sum_n\left[\cos(\nu(\tau_n-\tau))-\cos(\nu(\tau_n'-\tau))-\cos(\nu\tau_n)+\cos(\nu\tau_n')\right] \\
&\quad-\left(\sum_n\cos(\nu\tau_n)-\cos(\nu\tau_n')\right)^2-\left(\sum_n(\nu\tau_n)-(\nu\tau_n')\right)^2\Bigg\}\,.
\end{aligned} \tag{D.16}$$

D.2 Kinetic energy of the impurity model

In this section, we shall proof that

$$\sum_{k\sigma}\left\langle\begin{bmatrix}d_\sigma^\dagger & p_\sigma^\dagger\end{bmatrix}\begin{bmatrix}V_k^{dd} & V_k^{dp}\\ V_k^{pd} & V_k^{pp}\end{bmatrix}\begin{bmatrix}b_{k\sigma}^d\\ b_{k\sigma}^p\end{bmatrix}\right\rangle = \frac{1}{\beta}\sum_{i\omega}\mathrm{Tr}\left\{\mathbf{G}_{i\omega}^{imp}\Delta_{i\omega}\right\} = \frac{1}{2}E_{kin}\,. \tag{D.17}$$

The expectation value, as well as the impurity Green's function are calculated with respect to the impurity action

$$S = S_{atom} + S_{hyb} \,, \tag{D.18}$$

with the hybridization part

$$\begin{aligned} S_{hyb} = \int_0^\beta \mathrm{d}\tau \sum_{k\sigma} \left(\begin{bmatrix} d_\sigma^\dagger & p_\sigma^\dagger \end{bmatrix} \begin{bmatrix} V_k^{dd} & V_k^{dp} \\ V_k^{pd} & V_k^{pp} \end{bmatrix} \begin{bmatrix} b_{k\sigma}^d \\ b_{k\sigma}^p \end{bmatrix} + h.c. \right) \\ + \sum_{k\sigma} \begin{bmatrix} b_{k\sigma}^{d\dagger} & b_{k\sigma}^{p\dagger} \end{bmatrix} \begin{bmatrix} -i\omega + E_k^d & 0 \\ 0 & -i\omega + E_k^p \end{bmatrix} \begin{bmatrix} b_{k\sigma}^d \\ b_{k\sigma}^{p\dagger} \end{bmatrix} \,, \end{aligned} \tag{D.19}$$

which is equivalent to

$$S_{hyb} = \sum_{i\omega} \sum_{\sigma} \begin{bmatrix} d_{\sigma i\omega}^\dagger & p_{\sigma i\omega}^\dagger \end{bmatrix} \begin{bmatrix} \Delta_{i\omega}^{dd} & \Delta_{i\omega}^{dp} \\ \Delta_{i\omega}^{pd} & \Delta_{i\omega}^{pp} \end{bmatrix} \begin{bmatrix} d_{\sigma i\omega} \\ p_{\sigma i\omega} \end{bmatrix} \,, \tag{D.20}$$

with

$$\begin{bmatrix} \Delta_{i\omega}^{dd} & \Delta_{i\omega}^{dp} \\ \Delta_{i\omega}^{pd} & \Delta_{i\omega}^{pp} \end{bmatrix} = \sum_k \begin{bmatrix} V_k^{dd} & V_k^{dp} \\ V_k^{pd} & V_k^{pp} \end{bmatrix} \begin{bmatrix} i\omega - E_k^d & 0 \\ 0 & i\omega - E_k^p \end{bmatrix}^{-1} \begin{bmatrix} V_k^{dd*} & V_k^{pd*} \\ V_k^{dp*} & V_k^{pp*} \end{bmatrix} \,. \tag{D.21}$$

Since S_{atom} does not depend on the bath states, we can express the expectation value in (D.17) as

$$\begin{aligned} \sum_{k\sigma} \left\langle \begin{bmatrix} d_\sigma^\dagger & p_\sigma^\dagger \end{bmatrix} \begin{bmatrix} V_k^{dd} & V_k^{dp} \\ V_k^{pd} & V_k^{pp} \end{bmatrix} \begin{bmatrix} b_{k\sigma}^d \\ b_{k\sigma}^p \end{bmatrix} \right\rangle &= -\frac{1}{\beta} \sum_{k\sigma} \frac{1}{Z} \left(\frac{\partial Z}{\partial V_k^{dd}} V_k^{dd} + \frac{\partial Z}{\partial V_k^{dp}} V_k^{dp} + \frac{\partial Z}{\partial V_k^{pd}} V_k^{pd} + \frac{\partial Z}{\partial V_k^{pp}} V_k^{pp} \right) \\ &= \frac{1}{\beta} \sum_{i\omega} \sum_{\sigma} \left\langle \begin{bmatrix} d_{\sigma i\omega}^\dagger & p_{\sigma i\omega}^\dagger \end{bmatrix} \begin{bmatrix} \Delta_{i\omega}^{dd} & \Delta_{i\omega}^{dp} \\ \Delta_{i\omega}^{pd} & \Delta_{i\omega}^{pp} \end{bmatrix} \begin{bmatrix} d_{\sigma i\omega} \\ p_{\sigma i\omega} \end{bmatrix} \right\rangle \,, \end{aligned} \tag{D.22}$$

which follows from the definition of the partition function $Z = \int \mathscr{D}[d,p] \exp\{-(S_{atom} + S_{hyb})\}$. This proves the first equivalence of (D.17).

D.3 Truncated Matsubara sums

If we want to calculate the Fourier transform of some bosonic quantity, we have to evaluate

$$G^\theta(\tau) = \frac{1}{\beta} \sum_{n=\infty}^{\infty} G_{i\nu_n}^\theta e^{-i\nu\tau} \,. \tag{D.23}$$

In practice this sum has to be truncated at some finite frequency ν_N, which is problematic if $G^\theta(\tau)$ is not a differentiable function. Therefore, it is useful to consider the high-frequency behaviour of $G^\theta_{i\nu}$

$$G^\theta_{i\nu\to\infty} \sim \frac{A}{\nu^2} \tag{D.24}$$

and rewrite

$$G^\theta(\tau) \approx \frac{G^\theta_{i\nu_0}}{\beta} + \frac{1}{\beta}\sum_{n=-N,n\neq 0}^{N}\left(G^\theta_{i\nu_n} - \frac{A}{\nu_n^2}\right)e^{-i\nu_n\tau} + \frac{1}{\beta}\sum_{n=\infty,n\neq 0}^{\infty}\frac{A}{\nu_n^2}e^{-i\nu_n\tau}\,. \tag{D.25}$$

Making use of the identity $\sum_{n=1}^{\infty}\frac{\cos(nx)}{n^2} = \frac{\pi^2}{6} - \frac{\pi|x|}{2} + \frac{x^2}{4} + \ldots$, we get

$$G^\theta(\tau) \approx \frac{G^\theta_{i\nu_n}}{\beta} + \frac{1}{\beta}\sum_{n=N,n\neq 0}^{N}\left(G^\theta_{i\nu_n} - \frac{A}{\nu_n^2}\right)e^{-i\nu_n\tau} + A\frac{1}{\beta}\frac{\beta^2}{2\pi^2}\left(\frac{\pi^2}{6} - \frac{\pi^2|\tau|}{\beta} + \frac{\pi^2\tau^2}{\beta^2}\right)\,. \tag{D.26}$$

Evaluating the Green's function at $\tau = 0$, we therefore get

$$G^\theta(\tau=0) = \frac{1}{\beta}\sum_\nu\left(G^\theta_\nu - \frac{U_{dp}^{-1}}{2}\frac{1}{\nu^2}\right) + \frac{U_{dp}^{-1}}{2}\frac{\beta}{12}\,, \tag{D.27}$$

while for the derivative, relevant for constraint (6.13), the summation is straight forward

$$\frac{1}{2U_{dp}}\left(\partial_\tau G^\theta(\tau=0^-) + \partial_\tau G^\theta(\tau=0^+)\right) = -\frac{i}{\beta U_{dp}}\sum_\nu\left(\nu G^\theta_\nu - \frac{U_{dp}^{-1}}{2}\frac{1}{\nu}\right) + 0 = -\frac{i}{\beta U_{dp}}\sum_\nu \nu G^\theta_\nu\,. \tag{D.28}$$

D.4 High-frequency tails

While lots of the physical properties of the many body system are encoded in the self-energy. Nevertheless, most Monte Carlo algorithms only sample the Green's function, such that the self-energy has to be obtained from solving the Dyson equation

$$\Sigma_{i\omega} = (\mathscr{G}^0_{i\omega})^{-1} - (\mathbf{G}_{i\omega})^{-1}\,, \tag{D.29}$$

which, for multi orbital systems will be a matrix equation.
Since both $\mathscr{G}^0_{i\omega}$ and $\mathbf{G}_{i\omega}$ decay as $\sim 1/(i\omega)$ for large Matsubara frequencies, it is clear that this inversion is numerically unstable. It is for this reason, that is can be useful to have an analytic expression for the tail of the self-energy, which we shall derive in the following (for a detailed discussion see also [64]). We start by formally expanding the Green's function in the high-frequency

regime

$$\mathbf{G}_{i\omega} = \frac{1}{i\omega}\mathbf{G}_0 + \frac{1}{(i\omega)^2}\mathbf{G}_1 + \frac{1}{(i\omega)^3}\mathbf{G}_2 + \mathscr{O}\left(\frac{1}{(i\omega)^4}\right) , \tag{D.30}$$

where the first coefficient is already defined by a sum-rule to be equal to unity $\mathbf{G}_0 = \mathbb{1}$. The expansion of $\mathscr{G}^0_{i\omega}$ is analogous to the one of $\mathbf{G}_{i\omega}$.
For the self-energy, we can proceed likewise, giving

$$\Sigma_{i\omega} = \Sigma_\infty + \Sigma_1 \frac{1}{i\omega} + \mathscr{O}\left(\frac{1}{(i\omega)^2}\right) ; \tag{D.31}$$

contrary to the Green's function, however, the coefficients Σ_∞ and Σ_1 can take arbitrary values.
Due to the Dyson equation (D.29), the coefficients of the self-energy can be related to those of the free and the dressed Green's function. Inverting the Green's function (D.30), dropping the terms $\mathscr{O}\left(\frac{1}{(i\omega)^4}\right)$, we get

$$(\mathbf{G}_{i\omega})^{-1} \approx i\omega \left(\mathbf{G}_0^{-1} - \mathbf{G}_0^{-2}\left(\frac{1}{i\omega}\mathbf{G}_1 + \frac{1}{(i\omega)^2}\mathbf{G}_2\right) + \mathbf{G}_0^{-3}\left(\frac{1}{(i\omega)^2}\mathbf{G}_1^2\right)\right) , \tag{D.32}$$

and likewise

$$(\mathbf{G}^0_{i\omega})^{-1} \approx i\omega \left(\mathbf{G}_0^{0-1} - (\mathbf{G}_0^0)^{-2}\left(\frac{1}{i\omega}\mathbf{G}_1^0 + \frac{1}{(i\omega)^2}\mathbf{G}_2^0\right) + (\mathbf{G}_0^0)^{-3}\left(\frac{1}{(i\omega)^2}(\mathbf{G}_1^0)^2\right)\right) . \tag{D.33}$$

These expressions simplify considerably when we consider that $\mathbf{G}_0 = \mathbf{G}_0^0 = \mathbb{1}$. Plugging them back into the Dyson equation we get

$$\Sigma_{i\omega} = \left(\mathbf{G}_1 - \mathbf{G}_1^0\right) + \frac{1}{i\omega}\left((\mathbf{G}_1^0)^2 - (\mathbf{G}_1)^2 - (\mathbf{G}_2^0 - \mathbf{G}_2)\right) , \tag{D.34}$$

which can be compared with (D.31) to retrieve the parameters of interest

$$\Sigma_\infty = \left(\mathbf{G}_1 - \mathbf{G}_1^0\right) \tag{D.35}$$

$$\Sigma_1 = \left((\mathbf{G}_1^0)^2 - (\mathbf{G}_1)^2 - (\mathbf{G}_2^0 - \mathbf{G}_2)\right) . \tag{D.36}$$

But how can we calculate the coefficients for the Green's functions? It can be shown that the high-frequency coefficients are related to the discontinuity of the n^{th} derivative of the Green's function at $\tau = 0$

$$\mathbf{G}_n = \partial_\tau^{(n)}\mathbf{G}(\tau = 0^+) - \partial_\tau^{(n)}\mathbf{G}(\tau = 0^-) . \tag{D.37}$$

These derivatives can be simply calculated from the definition of the Green's function

$$G(\tau) = -\left\langle T d(\tau) d^{\dagger}(0) \right\rangle \ , \tag{D.38}$$

which, for matter of convenience, we wrote in scalar notation. The time derivative of the Greens function depends on the time derivative of the electron operators

$$\partial_{\tau} d(\tau) = \left[\hat{H}, d(\tau)\right] \ , \tag{D.39}$$

such that finally, we get

$$G_1 = -\left\langle \left\{ \left[\hat{H}, d\right], d^{\dagger} \right\} \right\rangle \ , \tag{D.40}$$

$$G_2 = \left\langle \left\{ \left[\hat{H}, \left[\hat{H}, d\right]\right], d^{\dagger} \right\} \right\rangle \ . \tag{D.41}$$

In case of a matrix Green's function, these expressions have to be evaluated for each matrix component.

D.4.1 High-frequency tail of the d-p problem

We can now use the expressions derived in the previous section to calculate the self-energy high-frequency tail for the d-p problem.
For models with density-density interaction, evaluating expressions (D.35), (D.36), (D.40) and (D.41) yields

$$\Sigma_{\infty}^{mn} = \delta_{mn} \sum_{l} U^{ml} \left\langle n^{l} \right\rangle \tag{D.42}$$

$$\Sigma_{1}^{mn} = \sum_{lk} U^{ml} U^{nk} \left(\left\langle n^{l} n^{k} \right\rangle - \left\langle n^{l} \right\rangle \left\langle n^{k} \right\rangle \right), \tag{D.43}$$

where the indices m, n, k, l label spin and orbital degrees of freedom at the same time.
Considering the d-p Hamiltonian (5.25), this translates into the following expressions for the moments of the d orbital self-energy

$$\Sigma_{\infty}^{dd\uparrow\uparrow} = U^{dd} \left\langle n_{\downarrow}^{d} \right\rangle + U^{dp} \left\langle n_{\uparrow}^{p} + n_{\downarrow}^{p} \right\rangle \tag{D.44}$$

$$\begin{aligned} \Sigma_{1}^{dd\uparrow\uparrow} = {} & (U^{dd})^2 \left\langle n_{\downarrow}^{d} \right\rangle \left(1 - \left\langle n_{\downarrow}^{d} \right\rangle \right) + 2 U^{dd} U^{dp} \left(\left\langle n_{\downarrow}^{d} (n_{\uparrow}^{p} + n_{\downarrow}^{p}) \right\rangle - \left\langle n_{\downarrow}^{d} \right\rangle \left\langle n_{\uparrow}^{p} + n_{\downarrow}^{p} \right\rangle \right) \\ & + (U^{dp})^2 \left(\left\langle (n_{\uparrow}^{p} + n_{\downarrow}^{p})^2 \right\rangle - \left\langle n_{\uparrow}^{p} + n_{\downarrow}^{p} \right\rangle \left\langle n_{\uparrow}^{p} + n_{\downarrow}^{p} \right\rangle \right) \ , \end{aligned} \tag{D.45}$$

(and likewise for the opposite spin). The high-frequency tail corresponding to the shell-folding method (see Sec. 5.2.3), on contrast, are given by

$$\Sigma_{\infty}^{dd\uparrow\uparrow} = (U^{dd} - U^{dp}) \left\langle n_{\downarrow}^{d} \right\rangle \tag{D.46}$$

$$\Sigma_{1}^{dd\uparrow\uparrow} = (U^{dd} - U^{dp})^2 \left\langle n_{\downarrow}^{d} \right\rangle \left(1 - \left\langle n_{\downarrow}^{d} \right\rangle\right) . \tag{D.47}$$

D.4.2 High-frequency tail using the slave rotor method

Of course, the methodology derived above can also be used to evaluate the high-frequency tail when using the slave rotor method, derived in Sec. 6.
As before, the high-frequency moments are determined by the discontinuity of the nth time derivative of the Green's function, with the difference, that now

$$\tilde{G} = -\left\langle T\tilde{d}(\tau)\tilde{d}^{\dagger}(0)e^{-i(\theta(\tau)-\theta(0))} \right\rangle . \tag{D.48}$$

We shall now consider the slave rotor mean-field Hamiltonian (6.33), to derive the high frequency moments. To keep a better overview, let us evoke the Hamiltonian, which writes

$$\hat{H}_{imp}^{SR} = \hat{H}_{imp}^{f} + \hat{H}_{imp}^{\theta} , \tag{D.49}$$

with

$$\begin{aligned}
\hat{H}_{imp}^{f} = &\sum_{\sigma}(\varepsilon^{d} - \mu - h)\tilde{d}_{\sigma}^{\dagger}\tilde{d}_{\sigma} + \sum_{\sigma}(\varepsilon^{p} - \mu - h)\tilde{p}_{\sigma}^{\dagger}\tilde{p}_{\sigma} + \sum_{\sigma}\left(V\tilde{d}_{\sigma}^{\dagger}\tilde{p}_{\sigma} + h.c.\right) \\
&+ (U^{dd} - U^{dp})\tilde{n}_{\uparrow}^{d}\tilde{n}_{\downarrow}^{d} + (U^{pp} - U^{dp})\tilde{n}_{\uparrow}^{p}\tilde{n}_{\downarrow}^{p} \\
&+ \sum_{k\sigma}\left\{ \begin{bmatrix} \tilde{d}_{\sigma}^{\dagger} & \tilde{p}_{\sigma}^{\dagger} \end{bmatrix} \begin{bmatrix} V_k^{dd} & V_k^{dp} \\ V_k^{pd} & V_k^{pp} \end{bmatrix} \begin{bmatrix} b_{k\sigma}^{d} \\ b_{k\sigma}^{p} \end{bmatrix} \left\langle e^{i\theta} \right\rangle + h.c. \right\} + \sum_{k\sigma} E_k^{d} b^{d\dagger}{}_{k\sigma} b_{k\sigma}^{d} + \sum_{k\sigma} E_k^{p} b^{p\dagger}{}_{k\sigma} b_{k\sigma}^{p}
\end{aligned} \tag{D.50}$$

and

$$\begin{aligned}
\hat{H}_{imp}^{\theta} &= \frac{U^{dp}}{2}\hat{L}^2 + h\hat{L} + \sum_{k\sigma}\left\{ \left\langle \begin{bmatrix} \tilde{d}_{\sigma}^{\dagger} & \tilde{p}_{\sigma}^{\dagger} \end{bmatrix} \begin{bmatrix} V_k^{dd} & V_k^{dp} \\ V_k^{pd} & V_k^{pp} \end{bmatrix} \begin{bmatrix} b_{k\sigma}^{d} \\ b_{k\sigma}^{p} \end{bmatrix} \right\rangle e^{i\theta} + h.c. \right\} \\
&= \frac{U^{dp}}{2}\hat{L}^2 + h\hat{L} + \frac{1}{2}E_{kin}^{f}\left(e^{i\theta} + e^{-i\theta}\right) .
\end{aligned} \tag{D.51}$$

To calculate G_1 (D.40) and G_2 (D.41) in this case, we need the commutators $\left[\hat{H}^{SR}_{imp}, \tilde{d}_\sigma e^{-i\theta}\right]$ and $\left[\hat{H}^{SR}_{imp}, \tilde{d}^\dagger_\sigma e^{i\theta}\right]$. The first one reads

$$\begin{aligned}\left[\hat{H}^f_{imp}+\hat{H}^\theta_{imp}, \tilde{d}_\sigma e^{-i\theta}\right] &= -\left((\varepsilon^d-\mu-h)\tilde{d}_\sigma + V\tilde{p}_\sigma + (U^{dd}-U^{dp})\tilde{d}_\sigma\tilde{n}^d_{\bar{\sigma}}\right)e^{-i\theta} \\ &\quad -\sum_{k\sigma}\left(V^{dd}_k b^d_{k\sigma}+V^{dp}_k b^p_{k\sigma}\right)\left\langle e^{i\theta}\right\rangle e^{-i\theta} - \left(\frac{U^{dp}}{2}+h+U^{dp}\hat{L}\right)\tilde{d}_\sigma e^{-i\theta} \\ &= \hat{A}+\hat{B}\,,\end{aligned} \tag{D.52}$$

which we split into two parts

$$\hat{A} = -\left(\varepsilon^d-\mu+(U^{dd}-U^{dp})\tilde{n}^d_{\bar{\sigma}}+\frac{U^{dp}}{2}+U^{dp}\hat{L}\right)\tilde{d}_\sigma e^{-i\theta} \tag{D.53}$$

$$\hat{B} = -\left(V\tilde{p}_\sigma+\sum_{k\sigma}\left(V^{dd}_k b^d_{k\sigma}+V^{dp}_k b^p_{k\sigma}\right)\left\langle e^{i\theta}\right\rangle\right)e^{-i\theta}\,, \tag{D.54}$$

for a more systematic evaluation of the second one. We then get

$$\begin{aligned}\left[\hat{H}^f_{imp}+\hat{H}^\theta_{imp}, \hat{A}\right] &= \left(\varepsilon^d-\mu+(U^{dd}-U^{dp})\tilde{n}^d_{\bar{\sigma}}+\frac{U^{dp}}{2}+U^{dp}\hat{L}\right) \\ &\quad\times\left((\varepsilon^d-\mu-h)\tilde{d}_\sigma+V\tilde{p}_\sigma+(U^{dd}-U^{dp})\tilde{d}_\sigma\tilde{n}^d_{\bar{\sigma}}+\sum_{k\sigma}\left(V^{dd}_k b^d_{k\sigma}+V^{dp}_k b^p_{k\sigma}\right)\left\langle e^{i\theta}\right\rangle\right)e^{-i\theta} \\ &\quad+\left(\varepsilon^d-\mu+(U^{dd}-U^{dp})\tilde{n}^d_{\bar{\sigma}}+\frac{U^{dp}}{2}\right)\times\left(\frac{U^{dp}}{2}+h+U^{dp}\hat{L}\right)\tilde{d}_\sigma e^{-i\theta} \\ &\quad+\left(\frac{(U^{dp})^2}{2}(\hat{L}+2\hat{L}^2)+hU^{dp}\hat{L}\right)\tilde{d}_\sigma e^{-i\theta}+\frac{1}{2}E^f_{kin}U^{dp}\left(1-e^{-2i\theta}\right)\tilde{d}_\sigma\end{aligned} \tag{D.55}$$

and

$$\begin{aligned}\left[\hat{H}^f_{imp}+\hat{H}^\theta_{imp}, \hat{B}\right] &= |V|^2\tilde{d}_\sigma+\sum_{k\sigma}\left(V^{dd}_k(V^{dd}_k\tilde{d}_\sigma+V^{dp}_k\tilde{p}_\sigma)+V^{dp}_k(V^{dp}_k\tilde{d}_\sigma+V^{pp}_k\tilde{p}_\sigma)\right)\left\langle e^{i\theta}\right\rangle^2 e^{-i\theta} \\ &\quad+\sum_{k\sigma}\left(V^{dd}_k E^d_k b^d_{k\sigma}+V^{dp}_k E^p_k b^p_{k\sigma}\right)\left\langle e^{i\theta}\right\rangle e^{-i\theta} \\ &\quad+\left(V\tilde{p}_\sigma+\sum_{k\sigma}\left(V^{dd}_k b^d_{k\sigma}+V^{dp}_k b^p_{k\sigma}\right)\left\langle e^{i\theta}\right\rangle\right)\times\left(\frac{U^{dp}}{2}+h+U^{dp}\hat{L}\right)e^{-i\theta}\,.\end{aligned} \tag{D.56}$$

Here, we made use of the relations

$$\left[d^\dagger d, d\right] = -d \tag{D.57}$$
$$\left[d^\dagger d, d^\dagger\right] = +d^\dagger \tag{D.58}$$
$$\left[\hat{L}, e^{i\theta}\right] = +e^{i\theta} \tag{D.59}$$
$$\left[\hat{L}, e^{-i\theta}\right] = -e^{-i\theta} \tag{D.60}$$
$$\left[\hat{L}^2, e^{i\theta}\right] = -e^{i\theta} + 2\hat{L}e^{i\theta} \tag{D.61}$$
$$\left[\hat{L}^2, e^{-i\theta}\right] = -e^{-i\theta} - 2\hat{L}e^{-i\theta}\ . \tag{D.62}$$

We can now calculate the anti-commutators for (D.40) and (D.41). For the one corresponding to G_1, we get

$$\begin{aligned}\left\{\left[\hat{H}^{SR}_{imp}, \tilde{d}_\sigma e^{-i\theta}\right], \tilde{d}^\dagger_\sigma e^{i\theta}\right\} = &-\left((\varepsilon^d - \mu - h) + (U^{dd} - U^{dp})\tilde{n}^d_{\bar{\sigma}}\right) \\ &-\left(\frac{U^{dp}}{2} + h + U^{dp}\hat{L}\right)\ .\end{aligned} \tag{D.63}$$

The expressions for G_2 are slightly more complicated, since we have to evaluate the anti-commutator for $\hat{A}$ and $\hat{B}$. Fortunately, however, all the terms which are not $\sim \tilde{d}_\sigma$ cancel, thus simplifying the (otherwise even more complicated) expressions to

$$\begin{aligned}\left\{\left[\hat{H}^{SR}_{imp}, \hat{A}\right], \tilde{d}^\dagger_\sigma e^{i\theta}\right\} = &\left(\varepsilon^d - \mu + (U^{dd} - U^{dp})\tilde{n}^d_{\bar{\sigma}}\right)^2 + \left(\frac{U^{dp}}{2} + U^{dp}\hat{L}\right)\left(\varepsilon^d - \mu + (U^{dd} - U^{dp})\tilde{n}^d_{\bar{\sigma}}\right) \\ &\cancel{-\left(\varepsilon^d - \mu + (U^{dd} - U^{dp})\tilde{n}^d_{\bar{\sigma}} + \frac{U^{dp}}{2} + \cancel{U^{dp}\hat{L}}\right)h} \\ &\cancel{+\left(\varepsilon^d - \mu + (U^{dd} - U^{dp})\tilde{n}^d_{\bar{\sigma}} + \frac{U^{dp}}{2}\right)h} \\ &+\left(\frac{U^{dp}}{2} + U^{dp}\hat{L}\right)\left(\varepsilon^d - \mu + (U^{dd} - U^{dp})\tilde{n}^d_{\bar{\sigma}} + \frac{U^{dp}}{2}\right) \\ &+\frac{U^{dp}}{2}\left(\hat{L} + 2\hat{L}^2\right) + \cancel{hU^{dp}\hat{L}} + \frac{1}{2}E^f_{kin}U^{dp}\left(e^{i\theta} - e^{-i\theta}\right)\end{aligned} \tag{D.64}$$

and

$$\left\{\left[\hat{H}^{SR}_{imp}, \hat{B}\right], \tilde{d}^\dagger_\sigma e^{i\theta}\right\} = |V|^2 + \sum_{k\sigma}\left(|V^{dd}_k|^2 + |V^{dp}_k|^2\right)\left\langle e^{-i\theta}\right\rangle^2\ . \tag{D.65}$$

Using these expressions, we can evaluate

$$\begin{aligned} G_2^{dd\sigma\sigma} - (G_1^{dd\sigma\sigma})^2 &= \left\langle \left\{ \left[\hat{H}_{imp}^{SR}, \hat{A}+\hat{B}\right], \tilde{d}_\sigma^\dagger e^{i\theta} \right\} \right\rangle - \left\langle \left\{ \left[\hat{H}_{imp}^{SR}, \tilde{d}_\sigma e^{-i\theta}\right], \tilde{d}_\sigma^\dagger e^{i\theta} \right\} \right\rangle^2 \\ &= (U^{dd}-U^{dp})^2 \left\langle \tilde{n}_{\bar{\sigma}}^d \right\rangle \left(1 - \left\langle \tilde{n}_{\bar{\sigma}}^d \right\rangle\right) + (U^{dp})^2 \left(\left\langle \hat{L}^2 \right\rangle - \left\langle \hat{L} \right\rangle^2\right) \\ &\quad + |V|^2 + \sum_{k\sigma} \left(|V_k^{dd}|^2 + |V_k^{dp}|^2\right) \left\langle e^{-i\theta} \right\rangle^2 , \end{aligned} \tag{D.66}$$

where we assumed that $\left\langle e^{i\theta} \right\rangle = \left\langle e^{-i\theta} \right\rangle$. Remarkably, most terms cancel, leading to a rather simple form. However, we still have to subtract the terms corresponding to the non-interacting Green's function.

The equivalent expressions for the non-interacting Hamiltonian follow trivially by setting U^{dd}, U^{pp} and U^{dp} to zero and $\left\langle e^{i\theta} \right\rangle$ to one. However, care must be taken when comparing the bare energies $\varepsilon^d/\varepsilon^p$ in the interacting and non-interacting limit: When bringing the Hamiltonian to its shell folding form, the bare energy levels obtained a shift of $\varepsilon^{d/p} \to \varepsilon^{d/p} + U^{dp}(N/2) - U^{dp}/2 = \varepsilon^{d/p} + U^{dp}(N-1)/2$, which is absent in the non-interacting case. Taking this shift into account, and using (D.35) and (D.36), as well as (D.40) and (D.41), we can then calculate the coefficients of the high-energy tail. Eventually, this leads us to

$$\Sigma_\infty^{dd\sigma\sigma} = G_1^{dd\sigma\sigma} - G_1^{dd\sigma\sigma 0} = (U^{dd}-U^{dp}) \left\langle \tilde{n}_{\bar{\sigma}}^d \right\rangle + U^{dp} \left(\left\langle \hat{L} \right\rangle + 1/2 + (N-1)/2\right) , \tag{D.67}$$

which, using the constraint (2.33) reads

$$\Sigma_\infty^{dd\sigma\sigma} = G_1^{dd\sigma\sigma} - G_1^{dd\sigma\sigma 0} = U^{dd} \left\langle \tilde{n}_{\bar{\sigma}}^d \right\rangle + U^{dp} \left(\left\langle \tilde{n}_\sigma^d + \tilde{n}_\uparrow^p + \tilde{n}_\downarrow^p \right\rangle\right) , \tag{D.68}$$

and should be compared to the exact expression (D.42).

For the $1/(i\omega)$ term, we get

$$\begin{aligned} \Sigma_1^{dd\sigma\sigma} &= (G_1^{dd\sigma\sigma 0})^2 - (G_1^{dd\sigma\sigma})^2 + (G_2^{dd\sigma\sigma} - G_2^{dd\sigma\sigma 0}) \\ &= (U^{dd}-U^{dp})^2 \left\langle \tilde{n}_{\bar{\sigma}}^d \right\rangle \left(1 - \left\langle \tilde{n}_{\bar{\sigma}}^d \right\rangle\right) + (U^{dp})^2 \left(\left\langle \hat{L}^2 \right\rangle - \left\langle \hat{L} \right\rangle^2\right) \\ &\quad + \sum_{k\sigma} \left(|V_k^{dd}|^2 + |V_k^{dp}|^2\right) \left(\left\langle e^{-i\theta} \right\rangle^2 - 1\right) . \end{aligned} \tag{D.69}$$

In contrast to the high-frequency tails from the shell-folding approximation Eq. (D.46), these expressions take into account the effect of the inter-shell interactions, explaining the improved results.

Appendix E

Appendix E

E.1 Simplified asymptotic models

In the limiting cases of the bi-pyramidal and (infinitely stretched) square planar configurations, corresponding to the parameter set (Tab. 7.1) obtained from our DFT calculations, the results obtained from Hamiltonian (7.1) correspond to those obtained from two very simple models, which shall be described in the following.

Low spin model. In the infinitely stretched case, the orbital does not hybridize any more with its ligand, therefore making the filling a good quantum number. The Coulomb repulsion acting on the orbital will therefore manifest itself as a mere shift of the bare energy. Due to the strong hybridization of the orbital with the ligand, the effective energy will lie above the one of the , justifying the assumption that the orbital (and it's ligand) are completely filled. Since our system contains 6 electrons, this leaves us with a strongly reduced Hilbert space, spanned by the 4 states

$$\begin{aligned} &|\uparrow\downarrow,\uparrow\rangle_c\,|\uparrow\downarrow,\downarrow\rangle_b \;,\; |\uparrow\downarrow,\downarrow\rangle_c\,|\uparrow\downarrow,\uparrow\rangle_b \;, \\ &|\uparrow\downarrow,0\rangle_c\,|\uparrow\downarrow,\uparrow\downarrow\rangle_b \;,\; |\uparrow\downarrow,\uparrow\downarrow\rangle_c\,|\uparrow\downarrow,0\rangle_b \;. \end{aligned} \tag{E.1}$$

Using these as our basis states, we can write the corresponding Hamiltonian as a matrix

$$H_{\text{low}} = \begin{pmatrix} 2U-5J+\Delta/2-\mu+E_2^b & 0 & -V_2 & -V_2 \\ 0 & 2U-5J+\Delta/2-\mu+E_2^b & V_2 & V_2 \\ -V_2 & V_2 & 2E_2^b & 0 \\ -V_2 & V_2 & 0 & 5U-10J+\Delta-2\mu \end{pmatrix}, \tag{E.2}$$

which can be easily diagonalized.

High spin model. In the bi-pyramidal configuration, Hund's coupling will strongly favour the states

$$|\uparrow,\uparrow\rangle_c\,|\uparrow\downarrow,\uparrow\downarrow\rangle_b \;,\; |\downarrow,\downarrow\rangle_c\,|\uparrow\downarrow,\uparrow\downarrow\rangle_b \;. \tag{E.3}$$

Since the second state can be generated from the first one by applying a global spin-flip transformation (which, without any external magnetic field leaves the system invariant), it suffices to consider only the first one in the following. Due to the considerable hybridization V_1, V_2 with the ligands, we also have to consider the states

$$|\uparrow\downarrow,\uparrow\rangle_c\,|\uparrow,\uparrow\downarrow\rangle_b \;,\; |\uparrow,\uparrow\downarrow\rangle_c\,|\uparrow\downarrow,\uparrow\rangle_b \;,\; |\uparrow\downarrow,\uparrow\downarrow\rangle_c\,|\uparrow,\uparrow\rangle_b \;. \tag{E.4}$$

Thus, our Hilbert space is again of dimension 4, and we can write down the Hamiltonian as a matrix

$$H_{\text{high}} = \begin{pmatrix} U-3J-2\mu+2(E_1^b+E_2^b) & -V_1 & -V_2 & 0 \\ -V_1 & 3U-5J-\Delta/2-3\mu+E_1^b+2E_2^b & 0 & -V_2 \\ -V_2 & 0 & 3U-5J+\Delta/2-3\mu+2E_1^b+E_2^b & -V_1 \\ 0 & -V_2 & -V_1 & 6U-10J-4\mu+(E_1^b+E_2^b) \end{pmatrix}, \tag{E.5}$$

which can be diagonalized without effort.

E.2 Subtleties of the Double Counting self-consistency

As we already mentioned before, evaluating the double counting potential (7.18) in a self-consistent way corresponds to solving an equation $n_{corr}(\varepsilon_{HF}(n)) = n$. This equation can have multiple solutions, among which we chose the one with the lowest energy as the physical solution. For a continuously changing set of model parameters $P[x]$, however, we find that some solutions only exist within a certain range of parameters $P[x < x_c]$ and then disappear in the vicinity of the spin crossover. This is visualized in Fig. E.1, which shows the occupation of the correlated subspace as a function of the bare energy shift from the double counting. This energy shift itself depends on the filling (black line), such that self-consistent solutions correspond to the positions, where the black line crosses the $n_{corr}(\varepsilon_{HF})$ lines. We see that for $x = 0.1, 0.2, 0.3, 0.4$, we have three crossings, corresponding to three solutions. For $x = 0.5 > x_c$, however, only one crossing persists, meaning that there is only one solution left. This is what we mean by "disappearing solutions". Since the solution that is lost is precisely the one previously minimizing the energy, this leads to a "jump" of the energies.

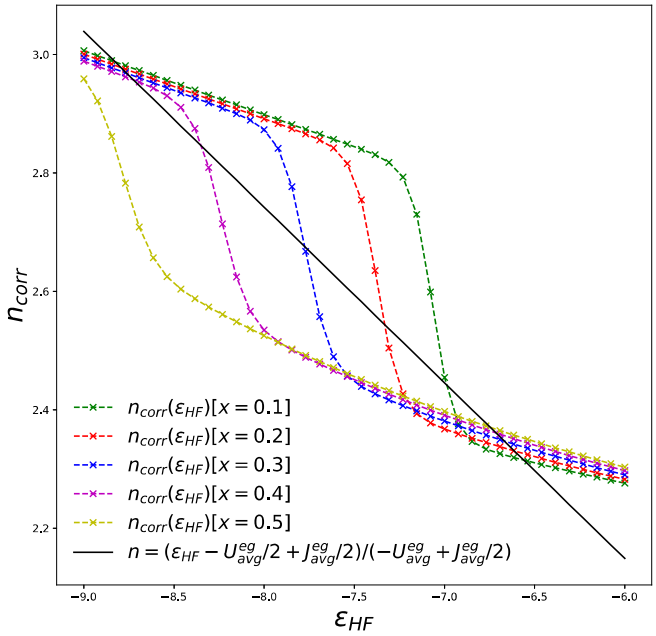

Fig. E.1 Visual representation of the double counting self-consistency equations, for different set of parameters $P[x] = (1-x) \cdot P[\text{Ni-TPP}] + x \cdot P[\text{Ni-TPP(Im}_2)]$. Colored lines mark the occupations of the correlated orbitals as a function of the energy shift ε_{HF}, while the black line is the inversion of the double-counting potential as a function of the filling. Crossings of the black- with the colored lines correspond to solutions of the self-consistency equation.

université PARIS-SACLAY
ÉCOLE DOCTORALE
Physique en Île-de-France (EDPIF)

Titre : Physique multi-orbitalaire dans les matériaux corrélés: Couplage de Hund et interactions inter-couches

Mots clés : électrons fortement corrélés, théorie du champ moyen dynamique, rotateurs esclaves, développement de méthodes

Résumé : Les matériaux corrélés offrent une richesse de nouveaux phénomènes, dont beaucoup ne sont pas encore – ou seulement partiellement – compris. Cette thèse se concentre sur les modèles multi-orbitalaires que j'etudie à travers une palette de méthodes, dont la théorie du champ moyen dynamique. Dans le modèle de Hubbard multi-orbitalaire proche de la transition de Mott, je mets en évidence un régime de mauvais métal induit par le couplage de Hund. Les propriétés de la transition de Mott dans ce système sont analysées. Dans un deuxième temps, je traite un modèle élargi pour inclure des degrés de liberté des ligands dans les oxydes. Plus spécifiquement, cette thèse étudie les effets des interactions inter-couches entre orbitales corrélés d'un atome de métal de transition et les orbitales p des ligands. Une partie du travail est dédiée au développement de nouvelles méthodes dont une approche de rotateurs esclaves à ce problème. Le dernier chapitre concerne la domaine de la spintronique moléculaire, où j'étudie la physique du "spin-state switching" en fonction de l'hybridation d'un ion de métal de transition avec ses ligands dans les molecules organométalliques du type porphyrine de nickel.

Title : Multi-Orbital Physics in Materials with Strong Electronic Correlations: Hund's Coupling and Inter-Shell Interactions

Keywords : strongly correlated electrons, dynamical mean-field theory, slave rotor, method development

Abstract : Strongly correlated materials offer a wealth of fascinating phenomena, many of which are not yet – or only partially – understood. In this thesis, I concentrate on the study of multi-orbital lattice models, to get a better insight into the physics of such systems. The models are investigated with a range of different methods, in particular, the dynamical mean-field theory (DMFT). In multi-orbital Hubbard models close to the Mott transition, I find that Hund's coupling gives rise to a bad metal phase, which extends to surprisingly large dopings. Here, I analyze the properties of the metal-insulator transition, investigating the fate of spin-spin correlations and the electronic compressibility. In the second part of my thesis, I consider an extended model that includes additional degrees of freedom associated with the orbitals of the oxygen ligands in transition metal oxides. More specifically, I focus on the effect of inter-shell interactions between the transition metal d orbitals and the ligand p orbitals. An important part of my thesis is dedicated to the development of a new slave rotor method, to treat such models efficiently. In the last chapter, I leave the realm of solid-state physics to study strong correlations in the context of molecular spintronics. Here, I investigate the effect of "spin-state switching" as a function of the hybridization of a transition metal ion with its ligands in organometallic nickel porphyrin molecules.

Université Paris-Saclay
Espace Technologique / Immeuble Discovery
Route de l'Orme aux Merisiers RD 128 / 91190 Saint-Aubin, France